USING AMS TO HELP INTERPRET GLACIOGENIC DEPOSITS OF THE LATE PALEOZOIC ICE AGE IN THE PARANÁ BASIN, BRAZIL

by

James Anthony Amato

A Thesis Submitted in
Partial Fulfillment of the
Requirements for the Degree of

Master of Science
in Geosciences

at
The University of Wisconsin-Milwaukee
August 2017

ABSTRACT

USING AMS TO HELP INTERPRET GLACIOGENIC DEPOSITS OF THE LATE PALEOZOIC ICE AGE IN THE PARANÁ BASIN, BRAZIL

by

James Anthony Amato

The University of Wisconsin-Milwaukee, 2017
Under the Supervision of Professor John L. Isbell and Professor Julie A. Bowles

The term 'diamictite' is used as a lithologic descriptive term without assigning a particular origin to a rock unit as either glacial deposits (till), proglacial, glacially influenced deposits (resulting from meltwater plumes and ice rafted debris), or mass transport deposits (glacial or non-glacial related). While in some cases, it is possible to delineate between the origins of diamictites, in other instances, weathering and lack of exposures make it difficult to determine. In general, the occurrence of diamictites within the Gondwana succession has been traditionally used to indicate the occurrence of subglacial deposition despite the potential occurrence of other depositional modes. Thus, the extent of glaciation during the Late Paleozoic Ice Age is interpreted to be much greater than it actually was. . One area of interest in Gondwana where interpretation of these deposits is problematic, and hence has resulted in problems determining ice extent, is the Paraná Basin in Brazil. The ability to better differentiate subglacial processes from proglacial, subaqueous mass transport, glaciomarine/glaciolacustrine rainout, and/or ice rafting, in addition to determining glacier flow or mass transport directions, will allow researchers studying these deposits to more accurately reconstruct the environments timing and extent of glaciation during the LPIA.

In sedimentary fabrics, anisotropy of magnetic susceptibility (AMS) is a geophysical method, which depicts the preferred orientation of magnetic particles during the final stages of transport and/or synsedimentary deformation. The technique is used to determine the preferred orientation of the constituent grains, therefore a useful indicator to help determine the mode of deposition, direction of sediment transport, and the nature of stress and strain during deformation. In August of 2016, samples were collected from deposits assigned to the Itararé Group, which outcrop along the southern and eastern margins of the Paraná Basin, Brazil. 19 fabrics were analyzed from seven different locations (Alfredo Wagner, Aurora, Cachoeira do Sul, Campo do Tenente, Ibaré, Porto Amazonas, and São Gabriel), stretching across the states of Rio Grande do Sul, Santa Catarina, and Paraná. While in most cases, AMS allowed us to delineate between the origins of diamictites, in other cases, it proved to be more difficult. In most cases, AMS measurements were beneficial in determining the direction of sediment transport. Our findings are consistent with past studies in which AMS was used to infer a variety of glaciogenic deposits, but also acts as a study case for the different types of fabrics that may develop as a result of Newtonian vs non-Newtonian sediment gravity flows.

While flow directions along the southern margin of the basin are consistent with the inferred N/NW ice movement into the basin, some of the flow directions along the eastern margin are not, revealing deviations in topography. Flow directions obtained from mass transport deposits in the area stretching from Campo do Tenente to Porto Amazonas (an area in which different stratigraphic levels of glaciation are exposed) tend to show uniform flow to the south. This observation is consistent with other AMS studies of similar deposits within the area, suggesting the existence of a southward paleoslope, which strongly influenced subaqueous deposition throughout the extent of the Itararé Group.

TABLE OF CONTENTS

LIST OF FIGURES

LIST OF TABLES

LIST OF TERMS AND ABBREVIATIONS

AMS	anisotropy of magnetic susceptibility
Ar	argon
B	magnetic induction [T]
B_c	coercivity
B_{cr}	coercivity of remanence
°C	degrees Celsius
dX/dT	first derivative minima
H	magnetic field [A/m], $B = \mu_0 H$
LHEAS	lower-hemisphere equal-area stereogram
LPIA	late Paleozoic ice age
M	magnetization [A/m]
MD	multi-domain
M_r	saturation remanent magnetization
M_s	saturation magnetization
MTD	mass transport deposit
N	number of measurements
N_b	number of mean measurements
PSD	pseudo-single domain
SD	single-domain
SE	standard error
SI	international system of units
SP	superparamagnetic
T	tesla [kg/A^1s^2]
T_C	Curie temperature [°C]
UFPR	Universidade Federal do Paraná, Brazil
UFRGS	Universidade Federal do Rio Grande do Sul
UWM	University of Wisconsin-Milwaukee
VSM	vibrating sample magnetometer

$\boldsymbol{k}_1$	eigenvector of maximum (long) susceptibility axis
$\boldsymbol{k}_2$	eigenvector of intermediate susceptibility axis
$\boldsymbol{k}_3$	eigenvector of minimum (short) susceptibility axis
τ_1	eigenvalue of maximum (long) susceptibility axis
τ_2	eigenvalue of intermediate susceptibility axis
τ_3	eigenvalue of minimum (short) susceptibility axis
μ_0	permeability of free space (constant) [H/m]
χ	magnetic susceptibility [SI]
χ_0	low-field susceptibility
χ_b	bulk susceptibility
χ_{hf}	high-field susceptibility
χ_{ij}	susceptibility tensor

ACKNOWLEDGEMENTS

From nightlife guru to Master of Science, there are many people to whom I owe thanks. Not only for their help in completing this graduate thesis, but for their continual support throughout this five-year endeavor of going back to school. My sincere gratitude goes out:

First and foremost to my parents Dominic and Diane Amato, if it weren't for their continual love and support, I may not have had such a great second shot at life.

To Gina Seegers-Szablewski, for her friendship throughout my academic studies. If it weren't for her guidance, advice, and support, I would not be standing where I am today.

To my truly amazing advisors: Dr. John Isbell and Dr. Julie Bowels for their patience, guidance, and assistance throughout this project.

To my Brazilian colleagues: Dr. Fernando Vesely, Dr. Barbara Trzaskos, Dr. Roberto Iannuzzi, Eduardo Luiz Menozzo da Rosa, and Bruno Gomes de Souza for their expertise, support, and gracious hospitality.

To the faculty, staff, graduate students and alumni of UW-Milwaukee who assisted me in one way or another as I juggled writing this thesis, being a teaching assistant, pursuing a graduate certificate in GIS, and landing a job. In particular, special thanks to; Brett Ketter, Rob Graziano, Dr. Barry Cameron, Dr. Elmo Rawling, Dr. Bill Kean, Dr. Bill Jacobson, Libby Ives, Nick Fedorchuk and Kate Pauls.

To the institutions and organizations that supported this project thru research grants from: National Science Foundation (OISE #1444181 and EAR #1729219), UWM Graduate School Research Growth Initiative, Society of Sedimentary Geology, Center for Latin American & Caribbean Studies, Wisconsin Geological Society, and Institute of Rock Magnetism.

Lastly, to Dr. Thomas S. Hooyer; a school mentor who passed away in 2016 due to unfortunate circumstances, to whom I dedicate this thesis. Thank you Tom for inspiring me!

CHAPTER 1. INTRODUCTION

1.1 The Late Paleozoic Ice Age

The Late Paleozoic Ice Age (LPIA) can be broadly defined as the interval of time from the late Devonian until the late Permian, during which glaciation occurred across the south polar and mid-latitude areas of Gondwana (Frakes et al., 1992; Crowell, 1999). The LPIA was an important climatic event in Earth's history as it represents a time when Earth shifted from an icehouse to a greenhouse state. There were many paleoenvironmental aspects of the LPIA that are still unknown, including the timing, extent, style, and duration of glaciation (Crowell and Frakes, 1970; Isbell et al., 2003, 2012; Fielding et al., 2008b). Traditionally, the LPIA has been modeled as a single, massive ice sheet (Fig 1-1A), that nucleated at the paleo-South pole and radiated outwards into the mid-latitudes (e.g. Veevers and Powell, 1987; Frakes and Francis, 1988; Frakes et al., 1992; Scotese 1997; Ziegler et al., 1997; Buggisch, et al., 2011). However, recent work has found evidence that rather than one massive ice sheet, numerous ice sheets, ice caps and alpine glaciers were most likely spread across the supercontinent (Fig 1-1B) (Isbell et al., 2012; Montañez and Poulsen, 2013). These smaller, but still relatively large ice sheets waxed and waned through multiple million year plus glacial intervals with alternating glacial minima or non-glacial periods of approximately equal duration (Crowell and Frakes, 1970; Caputo and Crowell, 1985; Dickins, 1997; López-Gamundí, 1997; Isbell et al., 2003; Fielding et al., 2008a, 2008c, 2008d; Gulbranson et al., 2010; Limarino et al., 2014). Scientists are in the process of reconstructing the distribution and timing of these events in hopes of better understanding environmental changes associated with deep time climate change.

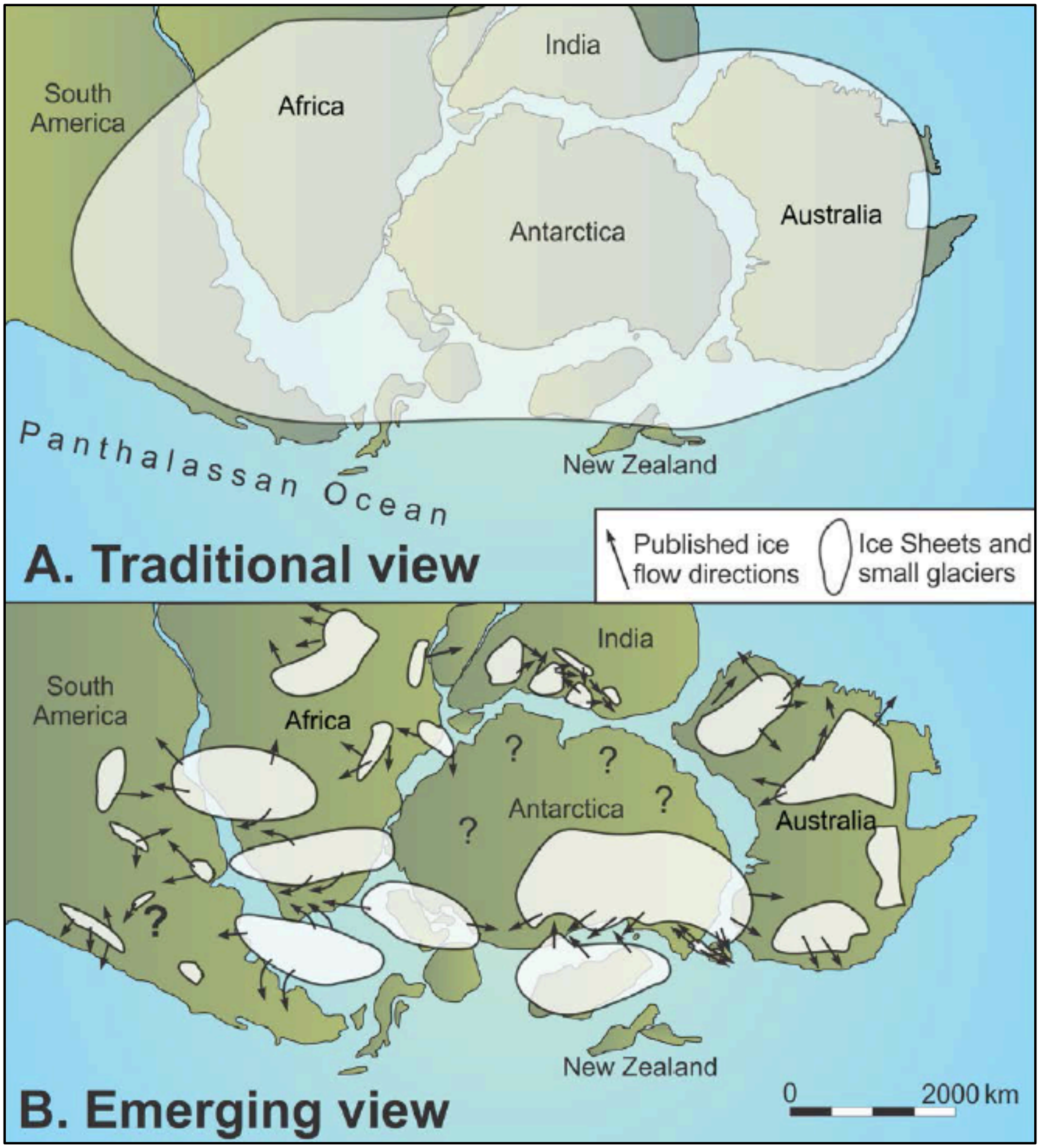

Fig 1-1. (A) *Traditional and* ***(B)*** *emerging views of glaciation during the Late Paleozoic Ice Age on Gondwana. Figure after Moxness (2016); modified from Isbell et al. (2012).*

1.2 Paraná Basin, Brazil

One of the major ice accumulation centers of the LPIA was interpreted to be located in south-central Africa in the highlands of Namibia referred to as the Windhoek ice sheet (Visser, 1987; Santos et al., 1996; Rocha-Campos et al., 2008). On the West African margin, glacial lobes were interpreted to have extended towards the W/NW into the subsiding, intracratonic Paraná Basin of southeastern Brazil (Santos et al., 1996; Rocha-Campos et al., 2008; Vesely et al, 2015). This basin was located in mid-latitudes during the Pennsylvanian and Early Permian and was thus sensitive to changing climatic conditions (Ziegler et al., 1997; Blakey, 2008; Torsvik et al., 2013). Roche moutonnée, striae, crescntic gouges and grooved surfaces on the underlying, unconformable Precambrian and Devonian rocks indicate the direction of ice movement, and in general imply that the ice was grounded as it flowed across to the basin margins (Gravenor and Rocha-Campos, 1983; Santos et al., 1996; Rocha-Campos et al., 2008; Vesely et al, 2015). As the glacier penetrated deeper into the basin, there is little evidence that the ice remained grounded, but rather was partially grounded and/or floating (Gravenor and Rocha-Campos, 1983). However, these glaciers were most likely temperate glaciers, based on their paleolatitude, the amount of debris transported, and the grooved surfaces left behind (Boulton, 1972; Evans et al., 2006;), suggesting that the ice would have been too weak to have formed floating ice shelves but rather developed a calving front, dispersing icebergs into more distal areas in the basin (Rocha-Campos et al., 2008; Vesely et al, 2015). The existence of widespread marine beds, interbedded with glaciogenic deposits, suggest that the south and eastern edge of the Paraná Basin was a low-lying irregular coastal area (Eyles et al., 1993; Vesely et al, 2015).

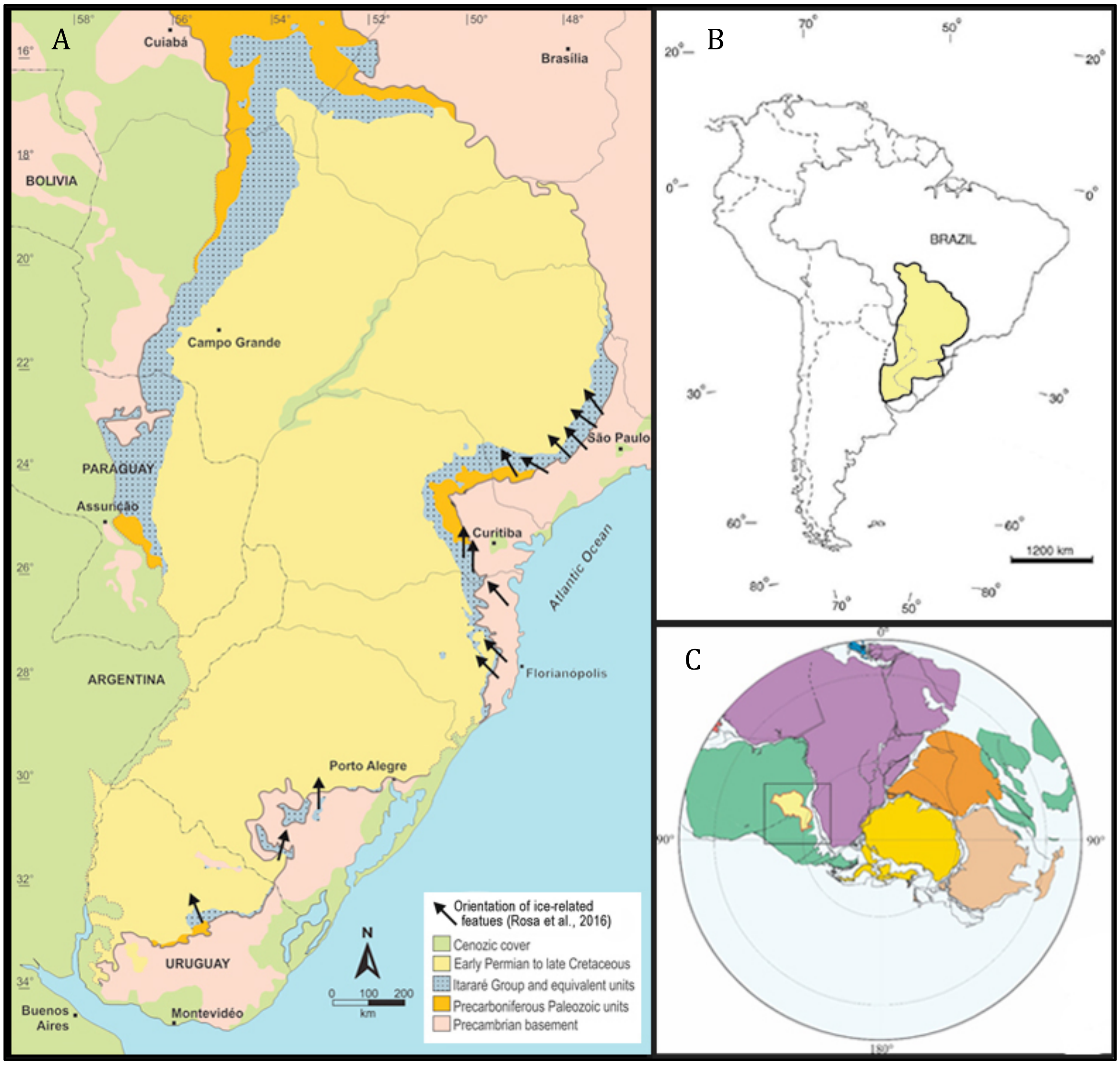

Fig 1-2. ***(A)*** *Undifferentiated deposits of the Itararé Group (see Rosa et al., 2016).* ***(B)*** *Location of the Paraná Basin in present day South America. Figure modified from Goldberg and Humayun (2010).* ***(C)*** *Orientation of Gondwana and the Paraná Basin in relation to the paleo-South pole during the late Carboniferous. Figure provided from University of Texas-Austin, Institute of Geophysics, PLATES Project.*

1.2.1 Itararé Group

The present Paraná Basin (Fig 1-2B) is more than a million square kilometers and covers parts of the states of Mato Grosso, Mato Grosso do Sul, Goiás, São Paulo, Paraná, Santa Catarina, and Rio Grande do Sul in Brazil and parts of Paraguay, Argentina, and Uruguay (Gravenor and Rocha-Campos, 1983). The glaciogenic deposits which outcrop around the basin margins have been assigned to the Itararé Group (Fig 1-2A) and are most likely Pennsylvanian in age (Souza, 2006; Cagliari et al., 2016), but the base may have extended into the Mississippian. The group is an important succession in Gondwana in terms of paleogeographic position, stratigraphic thickness, and geographical extent (Rocha-Campos et al., 2008). The 1300 m thick succession of the Itararé is composed primarily of sandstone, siltstone, shales, rhythmites and diamictites (Fig 1-3) (Eyles et al., 1993; Rocha-Campos et al., 2008). Different nomenclatures have been used to divide the Itararé Group into formations. Schneider et al. (1974) separated the Itararé into 3 formations based on outcrop sections along the eastern margin of the basin, Campo do Tenente, Mafra and Rio do Sul formations, oldest to youngest respectively. Whereas, França and Potter (1988) also separated the Itararé into 3 formations, but based on well-log data, the Lagoa Azul, Campo Mourao and Taciba formations, oldest to youngest respectively (Fig 1-4).

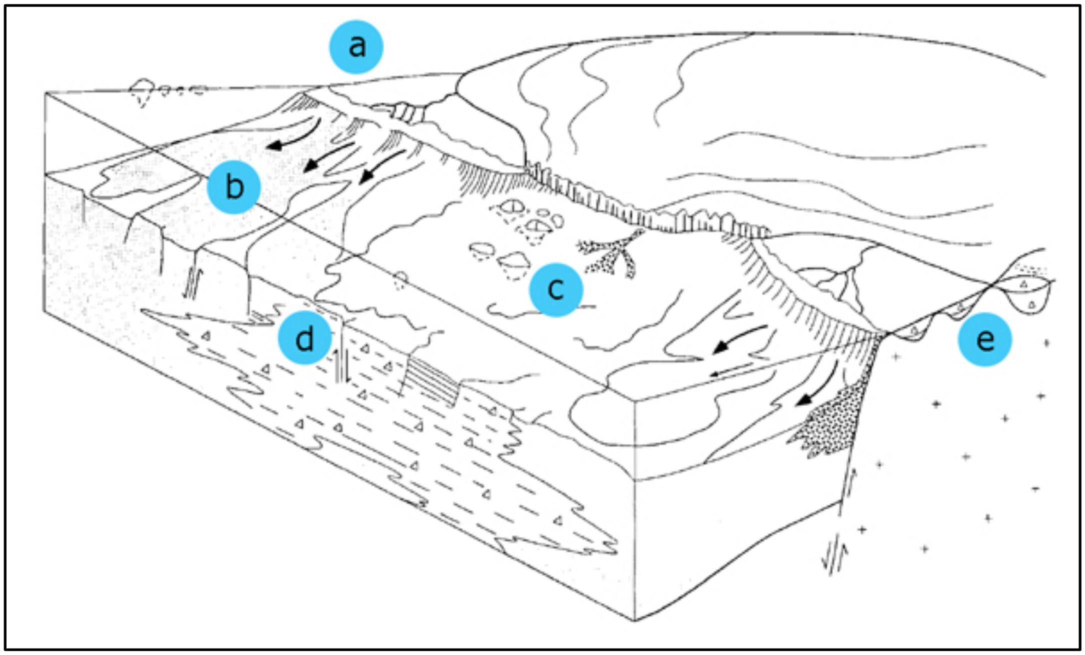

Fig 1-3. *Depositional model and sedimentary facies for the Itararé Group along the southern and eastern margins of the Paraná Basin (a) melt-water deltas (b) subaqueous MTD's resulting from an unstable shelf margin, (c) ice rafted debris producing 'rain out' diamictites, interbedded with mudstones and rhythmites, (d) fine grained marine beds (e) terrestrial subglacial deposits. Figure modified after Eyles et al. (1993).*

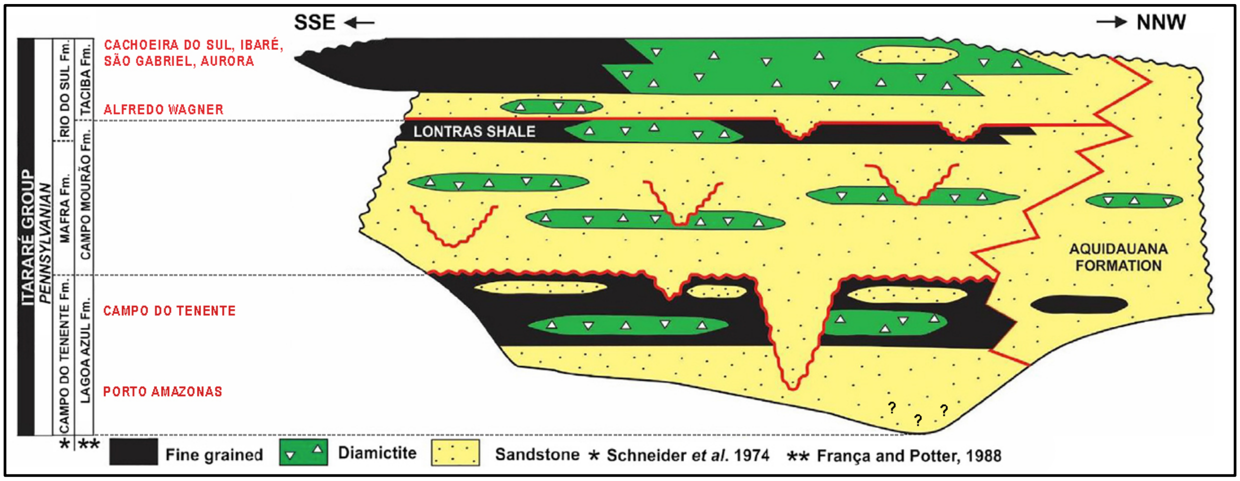

Fig 1-4. *Stratigraphic chart of the Itararé Group with nomenclature from both Schneider et al. (1974) and França and Potter (1988). Location of sample sites in relation to stratigraphic position in red text. '?' towards the bottom of the stratigraphic chart indicate the lowest part of the Itararé Group may have extended into the Mississippian. Figured modified from Fallgatter and Paim (2017).*

Numerous depositional sequences bounded by disconformities have been identified throughout the basin, suggesting multiple glaciations and/or glacial advances and retreats (França and Potter, 1991; Santos et al., 1996; Canuto et al., 2001; Vesely and Assine, 2006). A variety of diamictites are interpreted to have formed in terrestrial and subaquatic environments along the margins of the basin. Diamictites are sedimentary rocks made up of poorly-sorted terrigenous material, containing variously sized clasts (granule to boulders) suspended in a mudstone to sandstone matrix (Flint et al., 1960; Moncrieff, 1989; Hambrey and Glasser, 2012). The term 'diamictite' is used as a lithologic descriptive term without assigning a particular origin to the rock unit as either glacial deposits (till), proglacial, glaciomarine (e.g., two component system of fines settling from meltwater plumes and clast transported as ice rafted debris), glacially influenced marine deposits (marine deposits with ice rafted debris) or mass transport deposits (glacial or non-glacial related) (Jenner et al., 2007; Posamentier and Martinsen, 2011). The ISSMGE Technical Committee on landslides classifies subaqueous mass transport into five categories; slides (translational or rotational), topples, spreads, falls and flows (Locat, 2001). Mulder and Alexander (2001) further subdivide subaqueous flowing material into four categories: density flows (cohesive matrix strength), hyperconcentrated density flows (non-cohesive, grain-to-grain support), concentrated density flows (non-cohesive, grain-to-grain support), and turbidity flows (turbulent support). The difference between concentrated density flows and hyperconcentrated density flows is the upper part of a concentrated density flow will be fully turbulent (Mulder and Alexander, 2001). While the classification of the ISSMGE Technical Committee group's slumps and slides together, many would make a distinction between the two based on the presence of internal deformation, or the lack of, respectively,

respectively. While some schemes do not include turbidites in the spectrum of mass transport deposits, for the scope of this study we consider them genetically related unless noted.

While in some cases, it is possible to delineate between the origins of diamictites, in other instances, weathering and lack of exposures make it difficult to determine the associated mechanism of deposition (e.g., subglacial, rain out, mass transport) (Benn and Evans, 2010; Eyles et al., 1993; Rocha Campos et al., 2008). The complication of diamictites being misclassified, along with the possibility that some diamictites were removed by erosion, could explain the inconsistent interpretations for sequence boundaries of the Itararé Group (subglacial erosion vs. subaerial exposure) (França and Potter, 1988; Canuto et al., 2001; Vesely and Assine, 2006). The way a diamictite is interpreted will impact the inferred origin of these boundaries and, by consequence, on the nature of related cyclicity. This discrepancy points out the need to identify diamictites according to origin to avoid the possibility that certain deposits resulting from non-ice-contact processes (rainout, mass transport) from a single glacial advance and retreat and are not counted as evidence of multiple advances (Kilfeather et al., 2010; Boulton, 1972; Gravenor and Rocha-Campos, 1983), and to correctly identify the extent of glaciation.

1.2.1.1 Past Magnetic Studies

Only two other studies have examined the magnetic fabrics of the Itararé Group in the Paraná Basin. Gravenor and von Brunn (1987) conducted a magnetic fabric analysis on a massive diamictite located in Lapa Quarry, 65 km southwest of Curitiba. Strata in the exposure are interpreted to be glaciomarine and stratigraphically correlated to the middle part of the Campo do Tenente Formation (Gravenor and Rocha-Campos, 1983). Archanjo et al. (2006) conducted a magnetic fabric analysis on similar massive diamictites interpreted to be glaciomarine in the region of Rio do Sul between Mafra and Alfredo Wagner, but stratigraphically correlated to the younger Rio do Sul Formation.

1.3 Motivation and objective

In general, the occurrence of diamictites within the Gondwana succession has been traditionally used to indicate the occurrence of subglacial deposition despite the potential occurrence of other depositional modes. Thus, the extent of glaciation is interpreted to be much greater than it actually was (e.g., Isbell et al., 2003; González, and Saravia, 2010). One area of interest in Gondwana where interpretations of these deposits is problematic, and hence have resulted in problems determining ice extent, is in the Paraná Basin in Brazil (Eyles et al., 1993; Rocha Campos et al., 2008; Vesely et al, 2015).

The ability to better differentiate subglacial processes from subaqueous mass transport, proglacial glaciomarine/glaciolacustrine rainout, and/or ice rafting, in addition to determining glacier flow or mass transport directions, will allow scientists to more accurately reconstruct and interpret deposits and environments of the LPIA. This study is important as it is adding one more important tool to the arsenal for researchers working on such deposits.

My research objective in this study is to conduct a magnetic fabric analysis of glaciogenic deposits in the Paraná Basin, and compare results to previous studies, in hopes of delineating between different modes of deposition and to determine flow directions (ex: Rees, 1983; Gravenor, 1985; Eyles et al., 1987; Hailwood and Ding, 2000; Baas et al., 2007; Hooyer et al., 2008; Iverson et al., 2008).

1.4 Anisotropy of magnetic susceptibility

For decades, geologists have measured the magnetic fabrics in rocks to analyze the direction of stress during deposition or deformation (Ising, 1942; Rees, 1965; Hamilton and Rees, 1970, Tarling and Hrouda, 1993; Hrouda, 2007). In sedimentary fabrics, anisotropy of magnetic susceptibility (AMS) is a useful technique, which depicts the preferred orientation of magnetic particles during the final stages of transport. It has widely been recognized as an acceptable proxy to determine the preferred orientation of the constituent grains and therefore can be used to help determine mode of deposition and flow direction. Experimental and field-based studies over the past half-century have provided valuable insight about the magnetic signatures produced under a broad range of depositional and deformational settings. This information provides an ample amount of constraint in the interpretation of magnetic fabrics (Rees, 1965; Hamilton and Rees, 1970; Ellwood 1980; Taira and Scholle, 1979; Rees 1983; Taira, 1989; Tarling and Hrouda, 1993; Tauxe, 1998; Hailwood and Ding, 2000; Bass et al., 2007; Robion et al., 2007; Schwehr and Tauxe, 2007; Veloso et al., 2007; Hooyer et al., 2008; Tauxe et al., 2010).

1.4.1 Rock magnetism

1.4.1.1 Magnetic susceptibility

Magnetic susceptibility is a parameter used to describe the nature and intensity of a material's response to an external magnetic field (Petrovsky, 2007). All materials have a magnetic susceptibility, including those that do not carry permanent magnetization, because magnetic properties arise from the motion of electrically charged subatomic particles (Tarling and Hrouda, 1993; Tauxe et al., 2010). Susceptibility can be represented by the equation $M = \chi B$, where B is the strength of the applied magnetic field, M is the strength of the induced magnetization, and χ is a constant of proportionality defined as the susceptibility. Susceptibility can be treated as a scaler, or as a tensor where it is directionally dependent (see 2.2.3) as in studies of anisotropy of magnetic susceptibility.

1.4.1.2 Classes of magnetic materials

The derivation of magnetism stems from the orbital motions and spin properties of electrons around a nucleus and how those electrons interact with one another (Moskowitz, 1991). Depending upon the nature of magnetization, materials can be classified based on how they respond to an applied field either as diamagnetic, paramagnetic, or ferromagnetic (Moskowitz, 1991; Tarling and Hrouda, 1993; Tauxe et al., 2010). When the induced magnetization is in the opposite direction to that of the applied magnetic field and is lost upon removal of the field, the material is classified as diamagnetic (Fig 1-5a). Diamagnetic minerals (e.g., quartz and calcite) and have a magnetic susceptibility that is small and negative, typically on the order of 10^{-5} to 10^{-6} SI-units (Moskowitz, 1991; Tarling and Hrouda, 1993, Baas et al., 2007). When the induced magnetization is in the same direction as the applied magnetic field, and is lost immediately after removal, the material is paramagnetic (Fig 1-5b). Paramagnetic minerals (e.g., olivine, amphibole, pyroxene, and biotite) have a magnetic susceptibility that is positive and typically on the order of 10^{-2} to 10^{-4} SI-units (Moskowitz, 1991; Tarling and Hrouda, 1993, Baas et al., 2007). Some materials carry a strong magnetization even after an applied field has been removed. These ferromagnetic (*sensu lato*) minerals can carry a remanent (permanent) magnetization and may be ferromagnetic (*sensu stricto*) (e.g., Fe^0; Fig 1-5c), ferrimagnetic (e.g., magnetite), or antiferromagnetic (e.g., hematite). They typically have a very high susceptibility that is positive and on the order of 10^{-1} SI-units (Moskowitz, 1991; Tarling and Hrouda, 1993, Baas et al., 2007). Only a very small fraction of ferromagnetic minerals is needed (~0.1% volume of the whole rock), to control the susceptibility anisotropy of a sample (Tarling and Hrouda, 1993). In absence of these minerals, paramagnetic contributions tend to dominate over diamagnetic contributions provided they comprise more than 1% of the rock (Tarling and Hrouda, 1993).

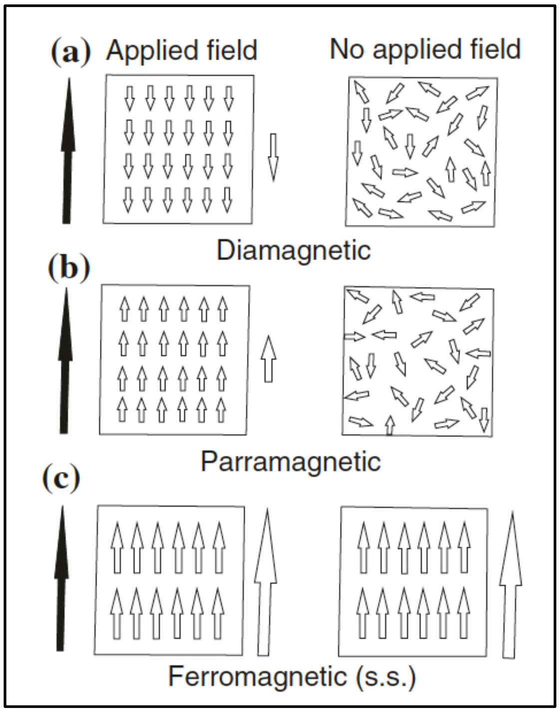

Fig 1-5. *Illustration depicting the three different classes of magnetization and arrangement of electron spins, both in the presence and absence of an applied field. Black arrows to the left of boxes show the orientation of the applied field, and white arrows to the right of boxes show the orientation of the resulting magnetization. Figure modified after Tarling and Hrouda (1993).*

1.4.1.3 Magnetic anisotropy

A material will always seek the most efficient configuration of electron spins to minimize its total energy (Tauxe et al., 2010). At the grain (or crystal) level, certain directions of magnetization are at a lower energy than others, resulting in an “easy axis” of magnetization. This preferred direction of magnetization referred to as magnetic anisotropy, is influenced by either the crystal lattice or crystal shape (Moskowitz, 1991). Magnetocrystalline anisotropy results from lattice forces acting on the electron spin configurations, resulting in magnetization along a specific crystallographic axis or plane (Tarling and Hrouda, 1993). Shape anisotropy arises from the interaction between magnetization and an internal demagnetizing field. This interaction results in the alignment of poles (surface charges) at opposite ends on each grain (Butler, 1992). In shape anisotropy, the preferred magnetization is normally oriented along the long axis of the grain to minimize its total energy. Both magnetocrystaline anisotropy and shape anisotropy are dependent upon a material’s magnetic mineralogy and grain size (Potter and Stephenson, 1988).

1.4.1.4 Domain states

Ferromagnetic grains can range in size (volume), which affects how they configure their electron spins (Dunlop and Özdemir, 1997). A large single ferromagnetic crystal can be broken down into smaller regions known as magnetic domains. Within a domain, the alignment of the electron spins is in the same direction. Within the next domain it may be opposite or different. By creating domains, the crystal minimizes magnetostatic energy by decreasing the spatial extent of the demagnetizing field (Moskowitz, 1991). As energy is required to produce and maintain these regions of transition referred to as a domain wall (Fig 1-6c), this subdivision cannot continue indefinitely (Moskowitz, 1991). Ferromagnetic particles with more than one domain are referred to as multi-domain (MD) (Fig 1-6b).

As grain size decreases, a threshold will be reached where the crystal will no longer create a domain wall because it is not energetically favorable (Moskowitz, 1991; Butler, 1992). Below this critical limit, the crystal contains a single-domain (SD) and is uniformly magnetized (Fig 1-6a). There is no precise boundary that defines the grain size transition between single- and multi-domain grains. In magnetite, the upper size limit for pure SD behavior is ~0.05 – 0.08 µm (Dunlop and Ozdemir, 1997; and references therin). Between ~0.4 – 10 µm, magnetite has so-called pseudo-single domain (PSD) properties and in some ways behave as single-domain and in some ways as multi-domain (Dunlop, 2002). As grain size continues to decrease, another threshold will be reached where magnetization becomes unstable as the result of thermal energies. When this happens the grain becomes superparamagnetic (SP) and can lead to the easy rotation of spins across energy barriers.

The presence of domains is inferred by the observation that some magnetic properties vary greatly with grain size, in particular coercivity and remanence (Moskowitz, 1991; Tauxe, 1998). Coercivity can be broadly defined as the resistance of a magnetic material to changes in magnetization. The process to change magnetization within a MD grain using low-strength fields is energetically easy, due to the preferential growth of domains with magnetization parallel to the field. Hence MD grains exhibit low values of coercivity and remanence. The process to change magnetization within a SD grain using a low-strength field is much more energetically difficult, as all spins must be coherently rotated together. Thus SD grains exhibit much higher values of coercivity and remanence. Coercivity values in SP grains also exhibit low values as a result of the unstable randomizing effects of thermal energy.

One caveat in interpreting AMS data is that SD grains exhibit what is referred to as an “inverse” fabric. The maximum susceptibility (easy axis) is parallel to the short axis, in contrast to a “normal” fabric where the maximum susceptibility is parallel to the long axis (Stephenson et al., 1986; Potter and Stephenson, 1988; Tarling and Hrouda, 1993). The inverse fabric arises from the fact that field required to switch the direction of magnetization in an SD grain (it’s coercivity) is considerably higher than the field applied in an AMS experiment. AMS fabrics produced from low-coercivity MD grains are normal fabrics. While the susceptibility of PSD grains needs further attention, past studies with PSD magnetite as the primary contribution to magnetic susceptibility tend to yield a normal fabric (Raposo, 1997; Rochette et al., 1999). This is supported by that fact that PSD grains tend to have low coercivity values.

Rocks are aggregations of ferromagnetic minerals distributed within a matrix of diamagnetic and paramagnetic contributions (Butler, 1992). As domain state and mineralogy can influence susceptibility, it is imperative to know the mineralogical composition and grain size distribution of the magnetic particles included in any AMS analysis.

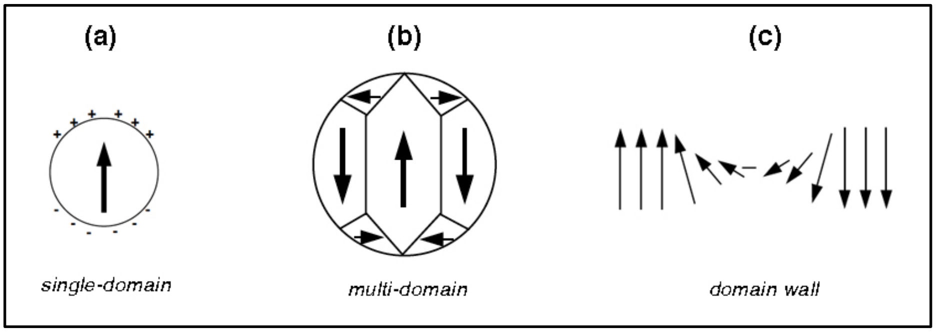

Fig 1-6. *Illustration outlining ferromagnetic domain states and components, black arrows show the direction of magnetization* ***(a)*** *single-domain with surface charges,* ***(b)*** *multi-domain,* ***(c)*** *rotation of magnetic moments within a domain wall. Figure modified after Butler (1992).*

1.4.2 Magnetic fabrics

During the deposition or deformation of sedimentary rock, the geometrical and spatial distributions of its constituent grains tend to show a preferential orientation of grain shapes referred to as an anisotropic fabric (Pettijohn, 1975; Lowrie, 1989). During deposition, referred to as a 'primary fabric,' the preferred alignment of grains is the result of gravitational, lift, or drag forces acting on the particle (Rees, 1965; Allen, 1982; Taira, 1989). The forces controlling grain orientation in turn depend on the physical properties of the grains, the transport medium, flow type, flow velocity, and morphology of the depositional surface (Reineck and Singh, 1973). A 'secondary fabric' may develop during post-depositional processes, as a result of compressional, tensional, or shear forces acting on the particles.

When an anisotropic fabric has an overlapping or shingling arrangement of grains, it is referred to as an imbricated fabric (Lindsey, 1972; Pettijohn, 1975; Potter and Pettijohn, 1977). The angle of imbrication can be defined as the angle at which grains lean away from a horizontal (a or b axis) or vertical (c-axis) position in the bedding plane (Fig1-7) (Hailwood and Ding, 2000; Baas et al, 2007). Imbrication results from grains orientating themselves into a position where they are hydrodynamically stable (minimum resistance to fluid shear), thus the mean orientation of imbrication within a deposit can be used as a reliable paleocurrent indicator (Hamilton and Rees, 1970; Lindsey, 1972; Potter and Pettijohn, 1977; Hailwood and Ding, 2000).

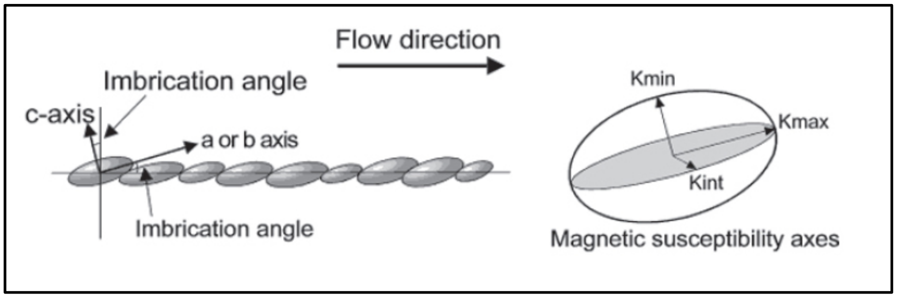

Fig 1-7. *Production of grain imbrication by fluid flow, showing imbrication angles both from horizontal and vertical positions in respect to the bedding plane; c-axis = short, b-axis = intermediate, a-axis = long. In 'normal fabrics' magnetic susceptibility axes are aligned with the imbricated grain axes. Figure modified after Hailwood and Ding (2000).*

1.4.2.1 Graphical representations of AMS

AMS is geometrically represented by a susceptibility ellipsoid with three principle axes: maximum ($\boldsymbol{k}_1$), intermediate ($\boldsymbol{k}_2$), and minimum ($\boldsymbol{k}_3$) known as eigenvectors and are used to describe the orientation of the ellipsoid, which can be used to classify direction of sediment transport (Fig 1-7). The magnitude of the susceptibility axes can be described by their eigenvalues (τ_1, τ_2, and τ_3 respectively) and are used to describe the shape of the ellipsoid. Directions of these principle axes are plotted on a lower hemisphere equal area (LHEA) stereonet projection. The axes of maximum, intermediate, and minimum susceptibility are plotted as red squares, blue triangles, and black circles respectively (Fig 1-8).

1.4.2.2 Fabric type and depositional process

Review of literature has identified four primary depositional fabric patterns: (1) horizontal fabric, (2) flow-aligned fabric, (3) flow-transverse fabric, (4) flow-oblique fabric (Fig 1-8).

When grains are deposited in a low energy environment and fall through a still column of water (or air), the dominant influence on particle orientation is gravity. If the surface of deposition is horizontal, the long ($\boldsymbol{k}_1$) and intermediate ($\boldsymbol{k}_2$) axes of the grains will be almost parallel to the plane, and the short axes ($\boldsymbol{k}_3$) will be perpendicular. As grains tend to fall thru suspension with their broadside perpendicular to the gravitational force (Allen, 1982), the orientation of $\boldsymbol{k}_1$ and $\boldsymbol{k}_2$ will be distributed randomly within the horizontal plane, and $\boldsymbol{k}_3$ will be clustered near vertical when projected on an equal-area stereonet. This 'horizontal fabric' is indicated by a strong foliation (Fig 1-8A).

When grains are deposited in a moderate-energy environment, transported by low to medium velocity flows, grains tend to be imbricated up-current with their long axes parallel to flow (Fig 1-7). The outcome is a tight cluster of $\boldsymbol{k}_3$ slightly off from vertical (10-30°), with a tight cluster of $\boldsymbol{k}_1$ dipping slightly from the bedding plane on an equal-area stereonet. This 'flow-aligned fabric' is indicated by a strong lineation (Fig 1-8B). Flow direction is indicated by the imbrication of $\boldsymbol{k}_3$ eigenvectors deflected from the vertical when projected in a LHEA stereonet.

When grains are deposited in high-energy environments, transported by high velocity flows, and/or sometimes sheared dispersion, grains are hydrodynamically stable with their long axes perpendicular to flow. The result is a split cluster of $\boldsymbol{k}_1$ along the bedding plane, and a tight cluster of $\boldsymbol{k}_3$ imbricated up to 30° off from vertical, orthogonal to the alignment of $\boldsymbol{k}_1$ on an equal-area stereonet. This 'flow-transverse fabric' is commonly referred to as a 'rolling fabric' (Fig 1-8C). Flow direction is indicated by the imbrication of $\boldsymbol{k}_3$ eigenvectors deflected from the vertical when projected in a LHEA stereonet.

Flow-oblique fabrics have not been thoroughly explored, and may occur more often than mentioned in literature. The term is often used when flow directions from AMS fabrics deviate from a secondary flow indicator by several tens of degrees. Baas et al. (2007) defines a flow-oblique fabric as when the $\boldsymbol{k}_1$ axes are oriented at a significant angle to the main flow direction. This would suggest flow-oblique fabrics cannot be identified without a secondary flow indicator (i.e., sedimentary structure). Causes for flow-oblique fabrics have been attributed to clast interactions in a viscous flow, spatial changes in current direction, changes in flow regime, changes in substrate roughness, and soft sediment deformation (Baas et al., 2007). For the purpose of this study, a flow-oblique fabric is defined as when the $\boldsymbol{k}_1$ and $\boldsymbol{k}_2$ axes are oriented at ~45° from the direction in which the $\boldsymbol{k}_3$ is deflected from the vertical (Fig 1-8D).

It should be noted that grain imbrication may or may not develop in flow-aligned, flow-transverse, and flow-oblique fabrics. Why imbrication may not occur has not been thoroughly explored, but suggested causes include sudden changes in flow regimes, and compaction.

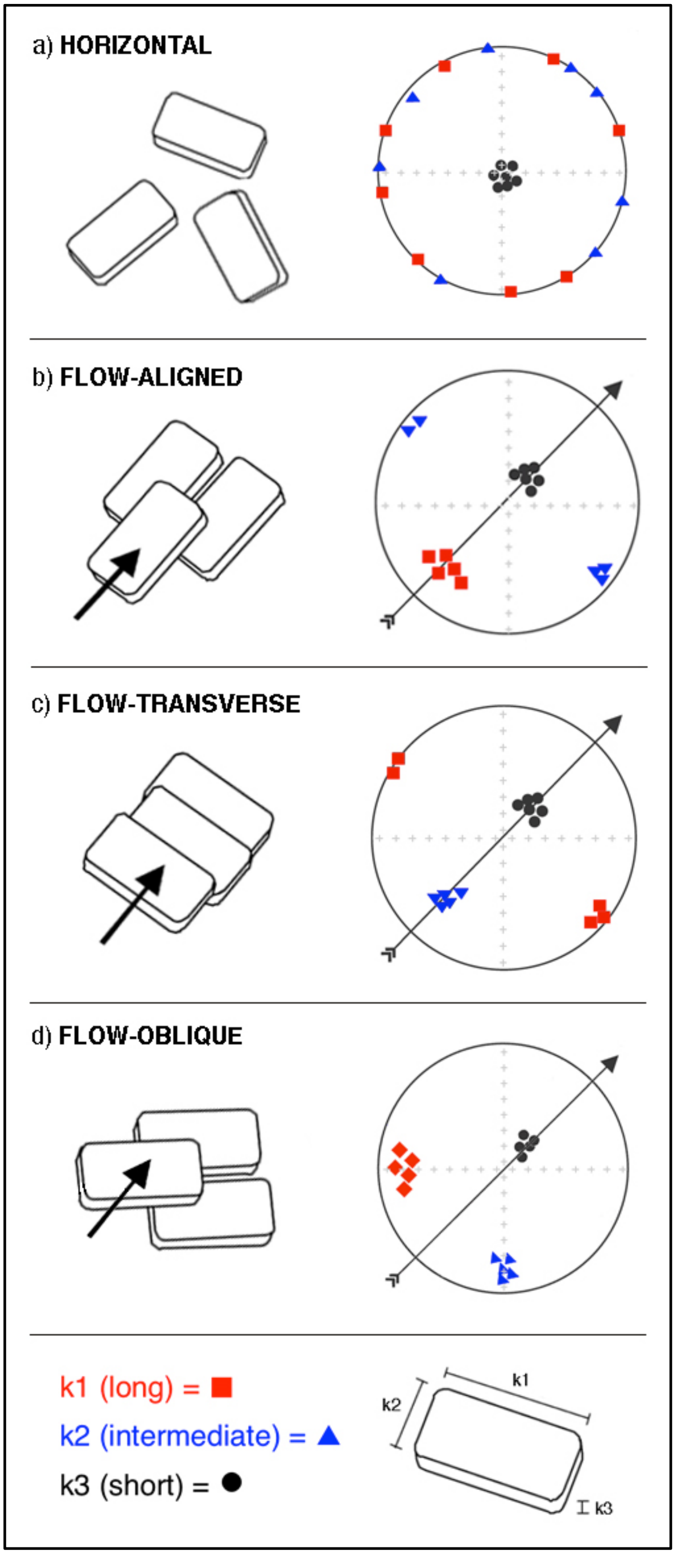

Fig 1-8. *Four primary depositional fabric patterns in lower hemisphere equal area stereonet projection. Imbricated subtypes shown in (b), (c) and (d). Horizontal fabric (a) is non-imbricated by definition. Black arrows in drawings and stereograms denote flow direction. Figure modified after Baas et al. (2007).*

1.4.2.3 Past Research

Over the years, AMS has been used to try and infer a variety of glaciogenic deposition including subglacial and subaqueous diamictites (e.g., Fuller, 1962; Gravenor et al., 1973; Stupavsky et al., 1974a, 1974b; Taira and Scholle, 1979, Gravenor, 1985; Eyles et al., 1987). Subglacial deposition includes lodgment at the base of a glacier, in situ melt-out below stagnant ice, and deformation of previously deposited sediment (Evans et al., 2007). Subaqueous deposition includes sediment gravity flows resulting from debris flows, density flows, turbidity currents, and/or slumps near the ice margin or distal areas within glaciomarine, glaciolacustrine, and proglacial environments, including rain-out deposition resulting from meltwater plumes and ice rafted debris (Gravenor, 1985; Eyles et al., 1987). It is generally agreed that rain-out deposition in a glaciogenic subaqueous environment typically results in a horizontal fabric (Hamilton and Rees, 1970; Gravenor 1985; Eyles et al., 1987). However, it should be made clear that weak to moderate currents on the basin floor can resediment these deposits into a flow-aligned fabric (Gravenor, 1985, Eyles et al., 1987). The structure and dispersion of sediment laden subaqueous debris/density flows and turbidity currents seem to vary depending upon multiple factors including the percentage of clasts and grains in suspension, the transport medium, and flow velocity (Rees, 1983; Pickering and Hiscott, 2015). While the exact nature of these deposits are still in question, there tends to be a general agreement that subaqueous mass transport deposits moving down a paleoslope typically result in either a flow-aligned or flow-transverse fabric (Taira and Scholle, 1979; Rees, 1983; Gravenor, 1985; Eyles et al., 1987), but flow-oblique fabrics have been observed (Rees, 1983). The planar and linear components may vary in MTDs depending upon the position within a vertical or horizontal succession (Taira and Scholle, 1979). It should be noted that sedimentation as mass transport may or may not be related to glacial activity. Such deposits occur along the margins of all sedimentary basins at all latitudes due to sedimentation on slopes. Such re-sedimentation typically produces diamictites, deformation, shearing and sediment gravity flows (Masson et al., 2013). It should also be noted that hyperpycnal flows originating at the mouths of rivers entering an ocean (including fjords) can produce turbidity flows which should not be classified as mass transport (Syvitski et al., 1987; Mulder and Syvitski 1995; Locat and Lee, 2002).

While past studies of AMS in subglacial tills have resulted in weakly developed fabrics, showing weak-moderate relation to ice flow direction (Fuller, 1962; Gravenor et al., 1973; Stupavsky et al., 1974a, 1974b; Eyles et al., 1987), Hooyer et al. (2008) and Iverson et al. (2008) recently applied AMS to tills with experimental data that link strain direction and magnitude using a ring shear device. Their studies indicate a weak relatively symmetric girdle of $\boldsymbol{k}_1$ can form from consolidation, which can strengthen with moderate shear strains of ~6, resulting in an up-glacier imbrication of grains with $\boldsymbol{k}_1$ and $\boldsymbol{k}_3$ orientations increasing in alignment in the direction of shear (Fig 1-9). At high shear strains of ~25, $\boldsymbol{k}_1$ orientations became more tightly clustered in the direction of shear. Based upon these experimental studies, then, tills can exhibit random fabrics, to weakly flow aligned fabrics, to strongly flow aligned fabrics depending upon the degree of shearing the till has undergone. Tills exhibiting random (disordered) fabrics are attributed to sub and supra -glacial melt-out processes.

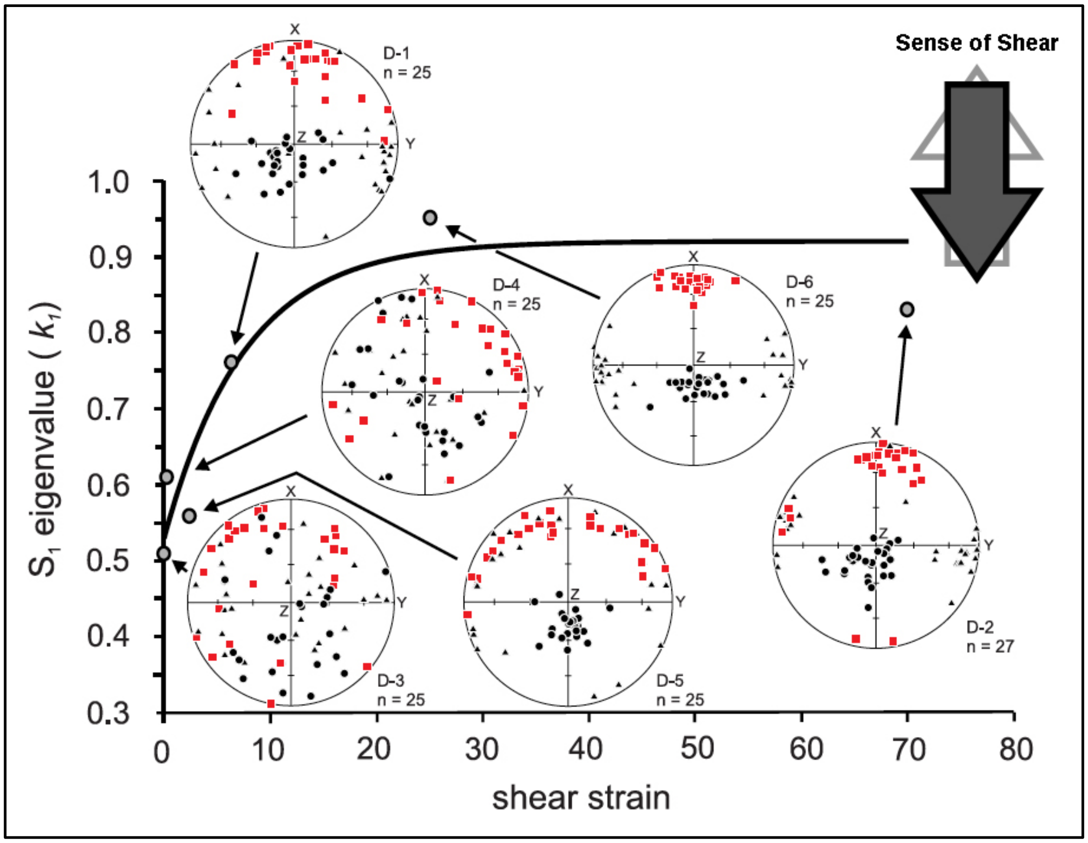

Fig 1-9. *Experimental data of sheared till that link strain direction and magnitude to AMS. Lower hemisphere stereonets accompany each data point showing the maximum (red squares), intermediate (grey triangles), and minimum (black circles) principal susceptibilities. Eigenvalue represents the degree of clustering; 0.33 indicates no alignment, 1.0 indicates perfect alignment. Tills can exhibit random fabrics, to weakly flow aligned fabrics, to strongly flow aligned fabrics, which are dependent upon the degree of shearing the till has undergone. Figure modified after Hooyer et al. (2008).*

CHAPTER 2. METHODS

2.1 Field methods

A sample collection scheme was adopted and modified from Butler (1992). A ‘location’ is referred to as a succession of sedimentary units at a specific place within a geographic region. A ‘site’ is an exposure of a particular unit within a sedimentary succession. A ‘sample’ is a separately oriented piece of rock from a site (i.e., a single core). A ‘specimen’ is a piece of a sample, which is measured. For the purpose of this study, it is expected that all samples from a site have similar mineralogy and magnetic behaviors.

Samples were collected from vertical and horizontal successions located within quarries, along road and railroad cuts, and from natural exposures on private property (which access was permitted). Sampling followed procedures that have been successful elsewhere (e.g., Tarling and Hrouda, 1993). A water-cooled Pomeroy DE-T3 electric rock core drill equipped with a Pomeroy BSS-1E diamond drill bit (2.86 cm) with stainless steel shank was used to extract the cores. A Pomeroy orienting device was used to find the magnetic azimuth and hade of a fiducial line scribed on the top of the core in the drill direction. To average out sampling errors, a minimum of four cores (2.5 cm in diameter by ~7-12 cm in length) were taken from each site and later processed into 8-19 specimens (2.5 cm in diameter and 2.2 cm in length) using a Hillquist 61 cm slab saw, with a 1.9 mm diamond blade. Drill bits and rock saw blades were cleaned and dressed before each use to avoid contamination.

In addition to collecting cores for magnetic fabric analysis, the following in-field measurements were recorded using a Brunton compass from each stratigraphic unit sampled, and/or neighboring beds, and/or horizontal/vertical successions: visible strike/dip and/or foliation/lineation, fault/fracture orientations, unit thickness, and note of any sedimentary structures with associated orientations (e.g. striated/grooved/plowed surfaces, deformational structures, cross-bedding). All measurements were corrected for locational variations in magnetic declination using an online magnetic field calculator (World Magnetic Model 2015) provided by the National Centers for Environmental Information (NCEI). All deposits were classified using a non-genetic classification of poorly sorted sediments (Fig 2-1) modified from Moncrieff (1989) by Hambrey and Glasser (2003). A classification to describe bed and laminae thickness was adopted from Boggs (2001): very thick-bedded (>100 cm), thick-bedded (30 cm to 100 cm), medium-bedded (10 cm to 30 cm), thin-bedded (3 cm to 10 cm), very thin-bedded (1 cm to 3 cm), laminated (0.3 cm to 1 cm), thinly laminated (<0.3 cm). A classification to interpret subaqueous sedimentary density flows (Fig 2-2) either as debris flows, hyperconcentrated density flows, concentrated density flow or turbidity flows was adopted from Mulder and Alexander (2001).

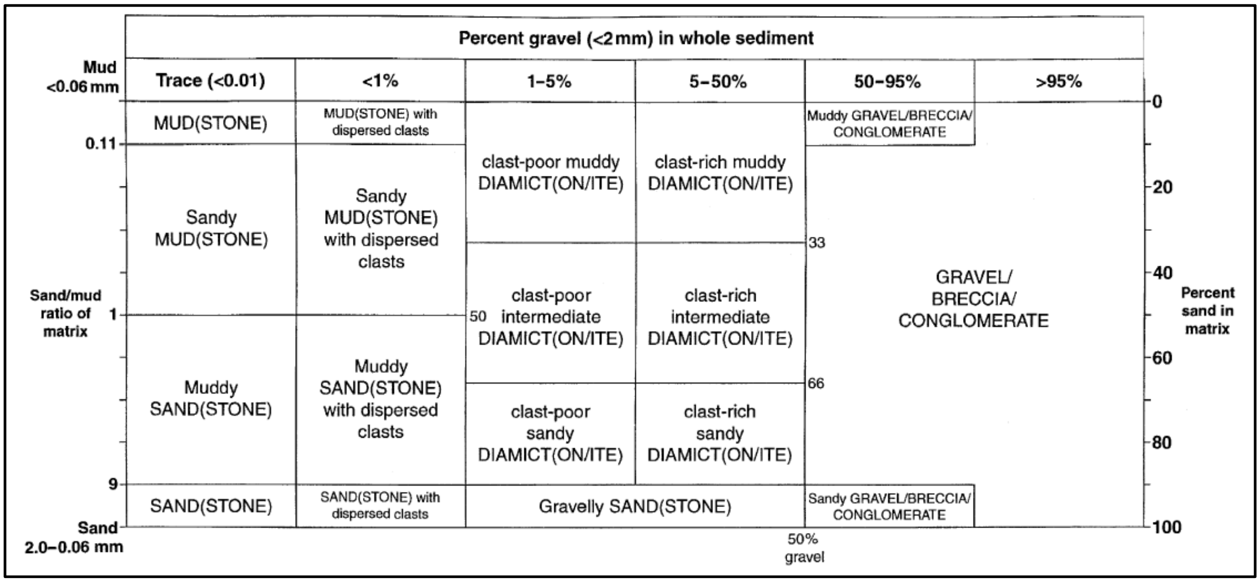

Fig 2-1. *Non-genetic classification of poorly sorted sediments. Figure from Hambrey and Glasser (2003); modified after Moncrieff (1989).*

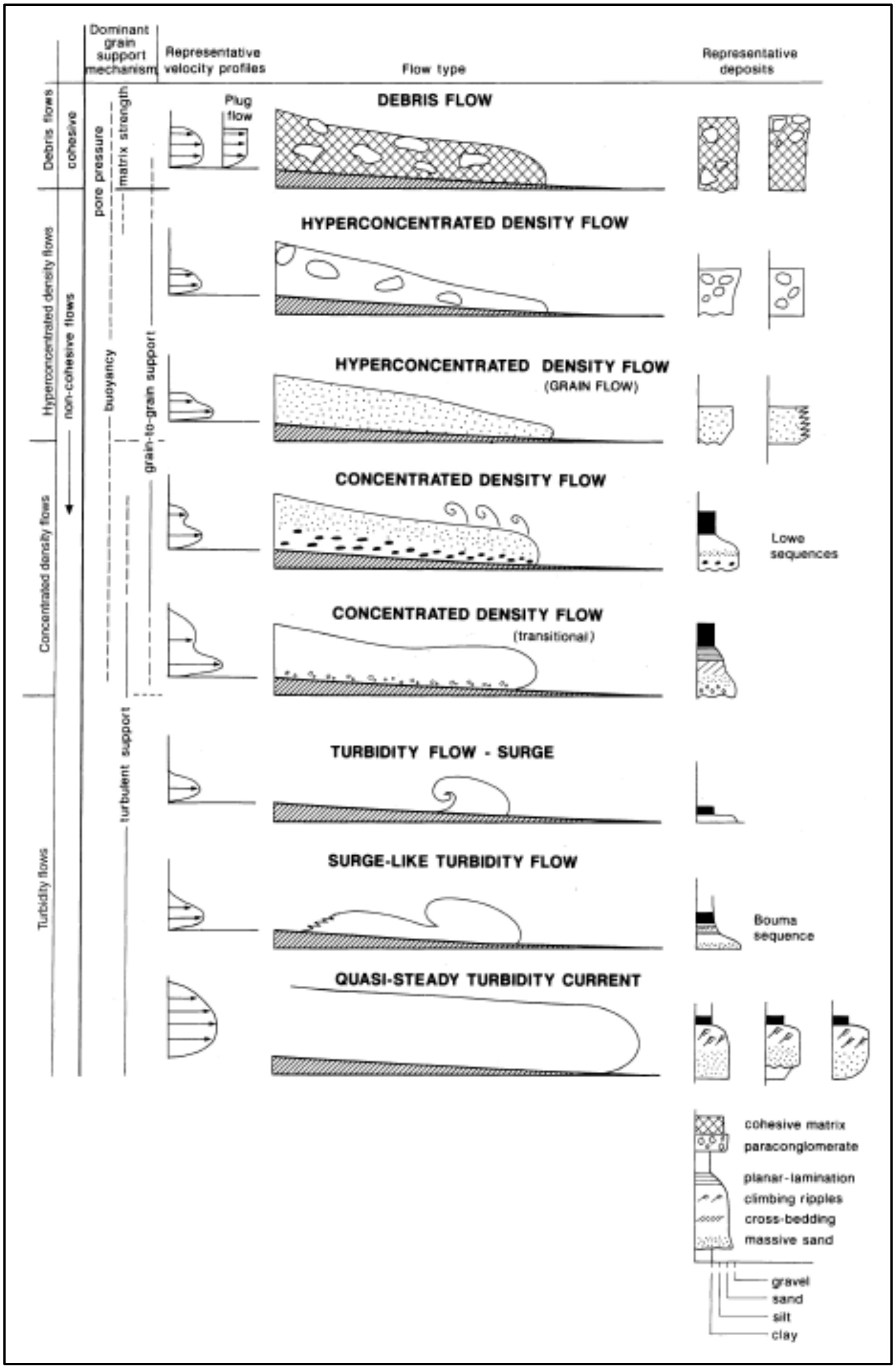

Fig 2-2. *Classification of subaqueous sedimentary density flows. Figure from Mulder and Alexander (2001).*

2.2 AMS and magnetic analyses

2.2.1 Susceptibility vs. temperature

A standard method to identify the dominant ferromagnetic (*s.l.*) mineralogy present in a sample is through the measurement of susceptibility as a function of temperature, $\chi(T)$ (Fig 2-2). (Hrouda, 1994). Ferromagnetic magnetization arises from the cooperative behavior among atoms exchanging electrons, referred to as exchange energy (Tarling and Hrouda, 1993). As temperature increases, magnetic crystals expand and exchange energy decreases (Tauxe at al., 2010). Eventually a critical temperature is reached referred to as the Curie (Néel) temperature (T_C), where thermal energy dominants over exchange energy and produces a randomizing effect on electron spins, causing a dramatic reduction in susceptibility. Curie temperature is an intrinsic property, and therefore is a good indicator of magnetic mineralogy (Petrovsky and Kapicka, 2006).

High-temperature susceptibility vs. temperature measurements were conducted using an AGICO MFK1-FA Multifunction Kappabridge with CS4 furnace attachment operated within the UWM Department of Geosciences using the Sufyte5W thermomagnetic curve control software (AGICO, 2011b). Crushed samples were heated under Ar atmosphere from room temperature to 700°C and then cooled while continuously measuring susceptibility. A cooling curve that sharply differs from the heating curve usually indicates the occurrence of mineralogical changes during initial heating. The temperature associated with the peak in the first derivative is taken to be the critical temperature. Curie temperatures for common magnetic minerals include: magnetite (580°C), titanomagnetite ($Fe_{3-x}Ti_xO_4$) (150°C for x = 0.6), and hematite (675-680°C) (Tarling and Hrouda, 1993; Tauxe et al., 2010).

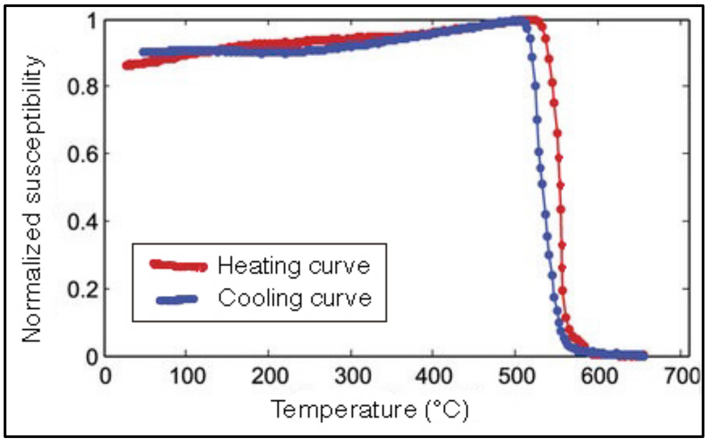

Fig 2-3. *Example of a thermomagnetic curve from a high-temperature susceptibility vs. temperature measurement; normalized susceptibility on the y-axis, temperature (°C) in the x-axis. The first derivative minima occurs ~580°C, indicating the presence of magnetite.*

2.2.2 Magnetic hysteresis

An integral property of ferromagnetic materials is their ability to record the direction of an applied magnetic field (Butler, 1992). During the removal of a magnetizing field, magnetization does not return to zero, but retains a memory of the external inducing field. The path of magnetization (M) as a function of applied field (B) is called a hysteresis loop (Butler, 1992). The shape of the loop is determined by several factors including the nature of magnetization (ferro- para- and diamagnetic), mineralogy, grain size, and concentration of each contributing mineral (Krasa, 2007).

Magnetic hysteresis is used to estimate magnetic grain size and ratios of magnetic contributions. Hysteresis loops were collected using a Princeton Applied Research Vibrating Sample Magnetometer (VSM) at room temperature located at the Institute for Rock Magnetism (IRM), University of Minnesota. A VSM measures the magnetization of a material in an applied field by mechanically vibrating the sample through a system of pickup coils (Krasa, 2007). B is cycled from zero to +1T, back to zero, up to -1T, and then back to +1T, while corresponding M values are measured (Fig 2-3) (Krasa, 2007). Through these measurements, several magnetic parameters can be determined including: saturation magnetization (M_s), the maximum magnetization attainable; saturation remanent magnetization (M_r), the maximum magnetization under no applied field; and coercivity (B_c), the reverse applied field required to reduce the saturation magnetization to zero. A fourth parameter is determined from the so-called 'backfield curve': coercivity of remanence (B_{cr}), the counter field necessary to remove the saturation remanence measured in zero field. Backfield curve measurements begin by saturating the sample in a maximum, positive field and then measuring the sample's remanent magnetization in a zero field. A small, negative field (or backfield) is applied to the sample and increased in steps until the remanent magnetization (in a zero field) is reduced to zero (Krasa, 2007).

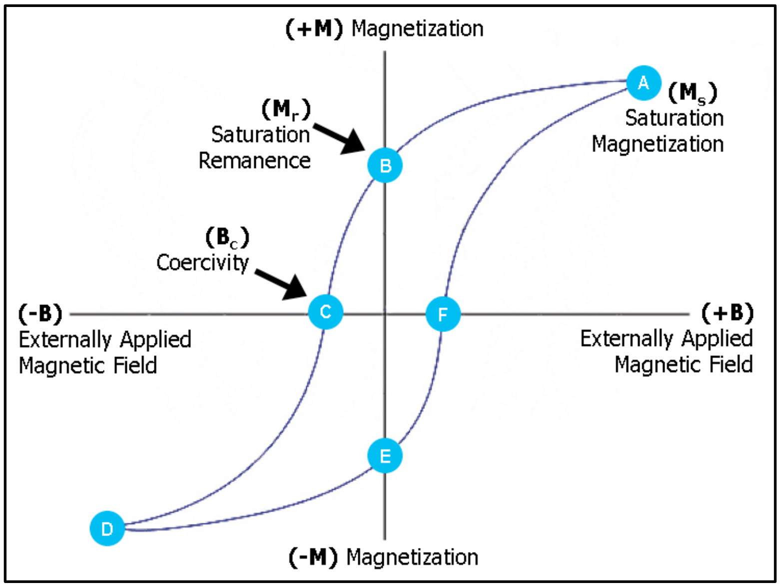

Fig 2-4. *Example of a hysteresis loop showing the relationship of magnetization (M) as a function of an applied magnetic field (B) in both positive and negative directions.* ***(A** and **D)*** *saturation magnetization* ($\boldsymbol{M_s}$)*, the maximum magnetization attainable,* ***(B** and **E)*** *the remanent saturated magnetization* ($\boldsymbol{M_r}$)*, the magnetization under no applied field,* ***(C** and **F)*** *coercivity* ($\boldsymbol{B_c}$)*, the reverse applied field required to reduce the saturation magnetism to zero.*

General information about the magnetic contributions of a sample can be observed from the shape of the hysteresis loop. Since diamagnetic and paramagnetic minerals do not carry remanent magnetization, they have null values of coercivity and saturation remanent magnetization, thus they have no magnetic hysteresis and only show negative (Fig 2-4a) and positive (Fig 2-4b) relationships respectively. On the other hand, as all ferromagnetic minerals carry remanent magnetization, they all retain magnetization in zero field and their values of coercivity are dependent upon grain size and composition. As SD grains possess high values of coercivity, their loops tend to be much larger (more open) than those of PSD and MD grains (Fig 2-4c).

As many rocks and sediments contain combinations of para- dia- and ferromagnetic contributions, many hysteresis loops will contain mixtures of shapes (i.e., paramagnetic and ferromagnetic). We can use a hysteresis loop to estimate the ratios of magnetic contributions. Unlike ferromagnetic constituents, which eventually reach a maximum magnetization attainable under increasing high-field strengths, paramagnetic and diamagnetic components will continue to increase indefinitely (Moskowitz, 1991; Tauxe et al., 2010). By subtracting high-field (X_{hf}) contributions (paramagnetic and diamagnetic) from low-field (X_0) corrected contributions (ferromagnetic), we can approximate the respective ratios contributing to the magnetic susceptibility of the sample (Tauxe et al., 2010).

Hysteresis parameters are often summarized on a Day plot (Day et al., 1977) of M_r/M_s vs B_{cr}/B_c (Fig. 2-5). This provides some guidance on the average ferromagnetic grain size. Dunlop (2002) made theoretical calculations of hysteresis parameters for magnetite in different domain states (and mixtures of domain states) (Fig 2-5). The theoretical trends for these mixtures can be used to estimate the average domain state of a sample (Krasa, 2007).

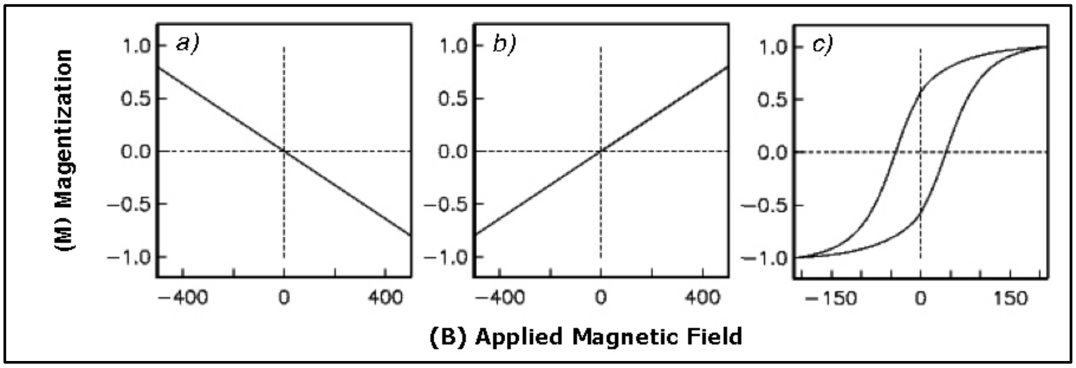

Fig 2-5. *Idealized hysteresis loops of end-member behaviors:* ***(a)*** *diamagnetic,* ***(b)*** *paramagnetic,* ***(c)*** *ferromagnetic. The size (thickness) of the loop in* ***(c)*** *reflects differences in ferromagnetic grain sizes. Figure modified after Tauxe et al. (2010).*

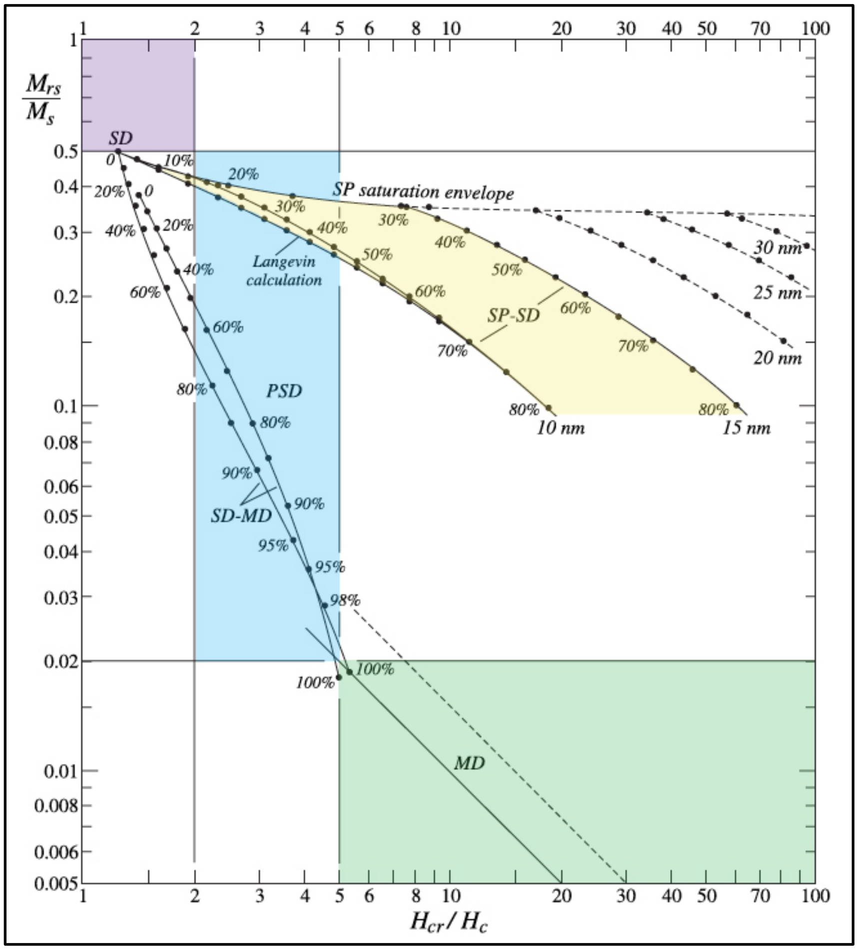

Fig 2-6. *Theoretical Day plot curves for magnetite showing regional locations for domain states and domain state mixtures; purple (SD), blue (PSD), green (MD), yellow (SP-SD). Figure modified after Dunlop (2002).*

2.2.3 Anisotropy of magnetic susceptibility measurements

All specimens were analyzed for AMS measurements using an AGICO Geophysika MFK1-FA Multifuction Kappabridge operated within the UWM Department of Geosciences using the Safyr6 control software (AGICO, 2011a). Measurements were conducted in a 976 Hz applied field at room temperature with a 200 Am^{-1} peak intensity, using the MFK1-A's spinning specimen method (Jelinek, 1995). The specimen is placed in the arm of the bridge in three orthogonal positions and is automatically rotated inside the pickup coils about each axis, X_1, X_2, and X_3 respectively (Fig 2-6) (Gee et al., 2008; AGICO, 2009). 192 measurements in total are made (64 about each axis), in addition to one bulk susceptibility measurement for each specimen (AGICO, 2009). The azimuth and dip of each sample recorded in-field is used to rotate data into geographic coordinates.

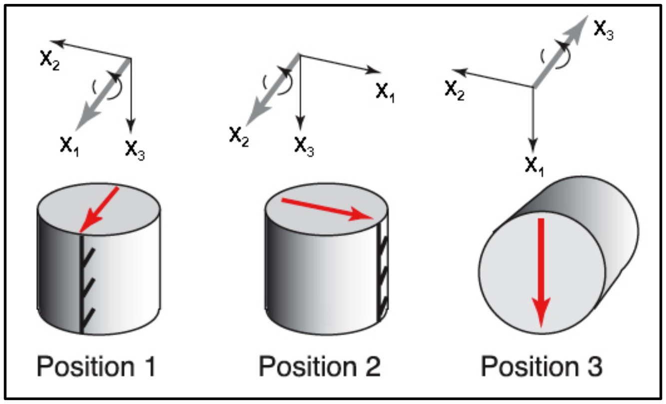

Fig 2-7. *Three specimen spin-positions used with the Kappabridge MFK1-FA. Heavy gray arrow illustrates the axis of rotation. Orientation of geographic coordinates indicated by the azimuth and plunge of the X_1 axis (red arrow). Figure modified after Gee et al. (2008).*

As susceptibility varies with direction, the Safyr6 control software calculates a second-rank tensor to characterize it (Jelinek, 1977, 1997; AGICO, 2011a). A tensor can be broadly defined as a way to describe the linear relationship(s) between vectors, scalars, and other tensors. Here, the susceptibility tensor describes the relationship between the applied field vector, $\boldsymbol{B}$, and the induced magnetization vector, $\boldsymbol{M}$. Following the coordinate system outlined in (Fig 2-6), the susceptibility tensor (χ_{ij}) may be expressed as follow.

$$\chi_{ij} = \begin{bmatrix} \chi_{11} & \chi_{12} & \chi_{13} \\ \chi_{21} & \chi_{22} & \chi_{23} \\ \chi_{31} & \chi_{32} & \chi_{33} \end{bmatrix}$$

The susceptibility tensor has 9 elements to account for magnetization in three orientations due to an applied field in the three orientations. However as the tensor is symmetric, there are only 6 independent matrix elements (i.e., $\chi_{21}= \chi_{12}$). The tensor is a three dimensional depiction of the specimen's magnetic susceptibility, geometrically represented by an ellipsoid with three principle axes: maximum or long ($\boldsymbol{k}_1$), intermediate ($\boldsymbol{k}_2$), and minimum or short ($\boldsymbol{k}_3$). As previously mentioned, these axes of magnetic susceptibility are referred to as eigenvectors and are used to describe the orientation of the ellipsoid. The magnitude of the susceptibility axes can be described by their eigenvalues (τ_1, τ_2, and τ3 respectively) and are used to describe the shape of the ellipsoid.

2.2.3.1 Anisotropy parameters

Past studies have used a wide range of shape and magnitude parameters to characterize AMS data. The eigenparameters of the susceptibility tensor are related to the statistical alignment and distribution of magnetic contributions within the rock (Tauxe et al., 1998). Some of the most widely used are the Hext (1963) *F* statistics to determine significance of eigenvalue ratios on the specimen level. The F statistics are calculated as follows:

$$F = 0.4\frac{(\tau_1^2 + \tau_2^2 + \tau_3^2 - 3\chi_b^2)}{{\sigma_v}^2}$$

$$F_{12} = 0.5\left(\frac{\tau_1 - \tau_2}{\sigma_v}\right)^2$$

$$F_{23} = 0.5\left(\frac{\tau_2 - \tau_3}{\sigma_v}\right)^2$$

where (χ_b) is the bulk susceptibility. $\sigma_v = \sqrt{\frac{S_o}{n_f}}$ is the estimated variance of the data, $n_f = 9$ (the number of degrees of freedom), and S_o is the residual sum of squares (Hext, 1963; Tauxe et al., 2010). The *F* parameter tests for significance of overall anisotropy (the tensor is statistically isotropic if $F < 3.4817$); the F_{12} parameter tests for significant difference between τ_1 and τ_2 (the tensor is statistically oblate if $F_{12} < 4.2565$). F_{23} parameter tests for significant difference between τ_2 and τ_3 (the tensor is statistically prolate if $F_{23} < 4.2565$) (Hext, 1963; Tauxe et al., 2010). If any specimen fell below the critical value of the *F* parameter test (at the 95% confidence level), the specimen was not included in the fabric analyses.

Other commonly used parameters to classify the shape of the anisotropy ellipsoid are lineation (P_1) and foliation (P_3), both functions of normalized susceptibility eigenvalues τ_1, τ_2, and τ_3 (Balsley and Buddington, 1960; Stacey et al., 1960; Tarling and Hrouda, 1993). Lineation and foliation are calculated (AGICO, 2011a) as follows

$$P_1 = \frac{\tau_1}{\tau_2}$$

$$P_3 = \frac{\tau_2}{\tau_3}$$

and can be plotted against each other in a Flinn-type plot (Flinn, 1962) to measure the degree of lineation or foliation at the specimen level (Tarling and Hrouda, 1993). Another useful parameter which provides a single measure of both lineation and foliation is the shape parameter (T), also functions of normalized susceptibility eigenvalues τ_1, τ_2, and τ_3 (Jelinek, 1981; Tarling and Hrouda, 1993). The shape parameter is calculated (AGICO, 2011a) as follows

$$T = \left[\frac{2\ln(\tau_2/\tau_3)}{\ln(\tau_1/\tau_3)}\right] - 1$$

where $0 < T \leq 1$ corresponds to an oblate shape, $-1 \leq T < 0$ corresponds to a prolate shape, and a value of 0 is neutral. The last commonly used anisotropy parameter is the corrected anisotropy degree (P_J), which is used to describe the magnitude (or strength) of anisotropy (Jelinek, 1981; Tarling and Hrouda, 1993). The corrected anisotropy degree is calculated (AGICO, 2011a) as follows, where $\eta_1 = lnk_1, \eta_2 = lnk_2, \eta_3 = lnk_3$, and $\eta_m = (\eta_1 + \eta_2 + \eta_3)/3$.

$$P_J = exp\sqrt{\{[(\eta_1 - \eta_m)^2 + (\eta_2 - \eta_m)^2 + (\eta_3 - \eta_m)^2]\}}$$

2.2.3.2 Bootstrap error analysis

Constraining flow directions within AMS data can be problematic, as the data in most magnetic analyses is much more poorly clustered then the ideal cases shown in (Fig 1-8). These weakly-developed fabrics can result from complicated flow regimes or post-depositional processes (Tauxe, 1998). Consequently, confidence in flow interpretations often depends upon some statistical evaluation of the data. A common approach to interpreting the distribution of vectors is the application of spherical probability density functions (PDF's) (Fisher, 1953; Bingham, 1974; Kent, 1982; Tauxe eat al., 2010). However, a different approach is required for tensors, where the three eigenvectors are not independent.

At the specimen level, it is common to use Hext statistics to describe how well a set of measurements describes the anisotropy of a given specimen. However, when combining results from multiple specimens, Hext statistics are not appropriate, as they do not follow the conditional presumption that the uncertainties in measurements are: small, have zero mean, and are normally distributed (Tauxe at al., 2010). To analyze uncertainty in principal mean orientations, 95% confidence ellipses were created using a bootstrap method for paleomagnetic tensors developed by Tauxe (1998). As majority of our sites contained fewer then 20 specimens, a parametric approach was taken. The parametric bootstrap method follows a similar methodology to a simple (naïve) bootstrap but assumes the data has an underlying distribution. The method proceeds as follows: (1) calculate the mean of N data points, (2) create a 'paradata set' by randomly selecting a list of N tensor elements from a normal distribution with the mean and standard deviation of the entire site (some points will be used more than once, other points will no be used at all), (3) from the paradata set, calculate the mean, (4) repeat the procedure of selecting paradata sets and calculating the mean N_b times (N_b equal to e.g., 10,000) (Tauxe et al., 1998). The 95% confidence interval is the surface that encloses 95% of the para-mean eigenvectors. To determine whether or not two axes are statistically distinct, we can additionally compare the cumulative distribution functions of the eigenvalues (Fig 2-7). We can then classify the AMS fabric as triaxial, oblate, prolate, or isotropic (Fig 2-7). Triaxial fabrics have statistically distinct $\boldsymbol{k}_1$, $\boldsymbol{k}_2$, and $\boldsymbol{k}_3$ orientation distributions (2-7d). Oblate fabrics have a distinct $\boldsymbol{k}_3$ distribution and indistinct $\boldsymbol{k}_1$ and $\boldsymbol{k}_2$ distribution (2-7b). Prolate fabrics have a distinct $\boldsymbol{k}_1$ distribution and indistinct $\boldsymbol{k}_2$ and $\boldsymbol{k}_3$ distribution (2-7c). If none of the orientation distributions are distinct, it is referred to as an isotropic fabric (2.7a). Parametric bootstraps along with cumulative distributions of the bootstrapped eigenvalues were calculated using PmagPy software with the aniso_magic.py plugin (Tauxe et al., 2016). The 95% confidence bounds of the cumulative distributions are plotted as vertical lines (Fig 2-7).

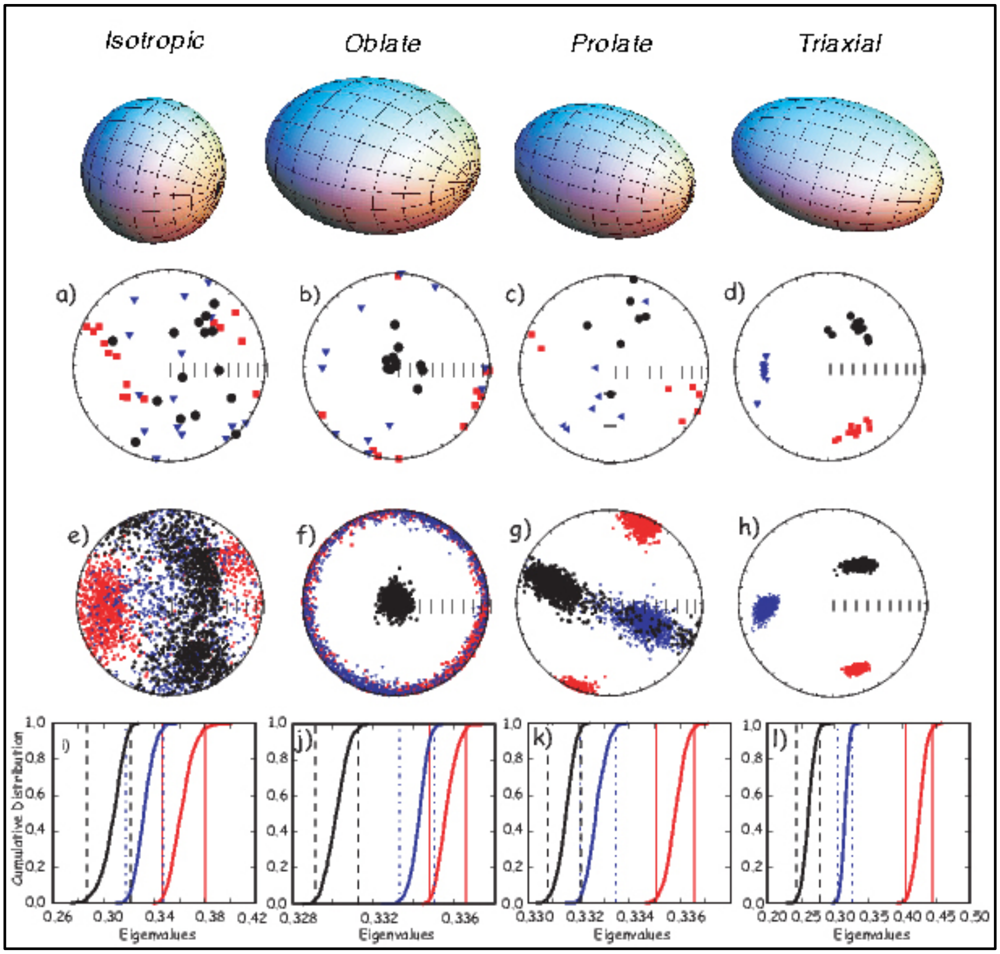

Fig 2-8. *Classification of AMS fabric using bootstrap confidence ellipses.* ***(a-d)*** *selected data sets plotted as eigenvector directions from individual specimens,* ***(e-h)*** *the bounds containing 95% of each eigenvalue are shown as vertical dashed dot line for* $\boldsymbol{\tau_3}$, *dashed for* $\boldsymbol{\tau_2}$ *and solid for* $\boldsymbol{\tau_1}$. *Figure modified after Tauxe et al. (2010).*

CHAPTER 3. FIELD LOCATIONS, FABRIC ANALYSIS, AND DISCUSSION

3.1 Introduction

This research project focused on collecting and interpreting AMS fabrics of late Carboniferous glaciogenic deposits within the Paraná Basin in order to better interpret depositional processes and determine the direction of sediment transport. Samples were collected from the outcrop belt along the southern and eastern margin of the basin in the states of Rio Grande do Sul, Santa Catarina, and Paraná (Fig 3-1). These areas are part of a collaborative study by Dr. John Isbell from UWM; Dr. Fernando Vesely from Universidade Federal do Paraná, Brazil (UFPR); Dr. Roberto Iannuzzi from Universidade Federal do Rio Grande do Sul (UFRGS); Dr. Isabel Montañez from the University of California, Davis; and Dr. Roland Mundl from the University of California, Berkeley. Nomenclature from Schneider et al. (1974) was used to classify outcrops according to formations of the Itararé Group.

In August of 2016, a total of 25 sample sets were collected from nine different locations, seven of which are included as the focus of this study. 13 samples sets were collected from four localities on the eastern margin of the basin in the states of Santa Catarina and Paraná: Alfredo Wagner (2), Aurora (1), Campo do Tenente (7), and Porto Amazonas (3). Six fabrics were collected from three localities on the southern margin of the basin in the states of Rio Grande do Sul: Cachoeira do Sul (3), Ibaré (2), and São Gabriel (1).

Specimen AMS measurements from these locations can be found in Appendix A and magnetic analyses in Appendix B. Brief field descriptions, AMS measurements (fabric and specimen), and magnetic analyses for locations not included in this study (Bassani and Mariana Pimentel) can be found in Appendix C and D. All sample sets from Bassani showed fabrics that were statistically isotropic except one. Additionally, two of the fabrics from Bassani showed evidence of inverse fabrics. The massive, red mudstone unit sampled at the Morro do Popoleau outcrop near Mariana Pimentel is correlated the Rio Bonito Formation which stratigraphically lies above the Itararé Group.

Fig 3-1. *Location map of sample sites along the eastern and southern margins of the Paraná Basin.*

3.2 Alfredo Wagner

3.2.1 Field description

In the state of Santa Catarina, a road cut exposure in the municipality of Alfredo Wagner along Highway BR-282 (km-89) was sampled (27°40'40.7"S, 49°13'00.7"W). The outcrop is correlated to the lower Rio do Sul Formation (Fig 1-4) and was first documented by Rocha-Campos et al. (1988) and later visited by Rosa et al. (2016) (Fig 3-2A). At the base of the exposure, a massive half meter thick diamictite (Fig 3-2B2) drapes relief cut on Precambrian granite, confined in a basement trough (Fig 3-2B1), which, in turn, is overlain by a meter thick stratified diamictite that drapes depositional relief on the underlying massive diamictite (Fig 3-2B3). Black shale blankets the outcrop (Fig 3-2B4). Both massive and stratified diamictites are laterally discontinuous and are classified as a 'clast-rich' and 'clast-poor intermediate' diamictite respectively. Striations and crescentic gouges on the surface of the granitic basement beneath the massive diamictite suggest a NW/SE ice paleoflow trend of 327/147° (Rocha-Campos et al., 1988).

3.2.2 AMS and magnetic analysis

Six cores were extracted from the massive diamictite (site B8) (Fig 3-3A), yielding 19 specimens (Table A-1). Five cores were extracted from the stratified diamictite (site R7) (Fig 3-3B), yielding 11 specimens (Table A-2). All specimens from both sites passed the *F* test and were included in the AMS analyses. Site B8 shows a flow-aligned fabric that is triaxial and imbricated, dipping at ~12° towards the SE suggesting flow towards the NW (Fig 3-4A). Site R7 shows a flow-oblique fabric that is triaxial and imbricated, dipping at ~23° towards the E suggesting flow towards the W (Fig 3-4B).

Magnetic analyses from sites B8 and R7 are included in Appendix B in detail, Fig B-1 and Fig B-2 respectively. Hysteresis measurements from both sites show loops characteristic of strong paramagnetic contributions. Susceptibility vs. temperature measurements indicate low-field ferromagnetic contributions from most likely magnetite (~580°C) at both sites, with additional phases occurring at 300°C and 400°C upon cooling, indicating that the sample underwent alteration during heating. Hysteresis parameters suggest the ferromagnetic grain size for both fabrics fall within PSD range. X_{hf} to X_0 ratios for both sites are 6:1, suggesting paramagnetic contributions dominate. All of the above suggests that the AMS is controlled by shape anisotropy, resulting in a normal fabric.

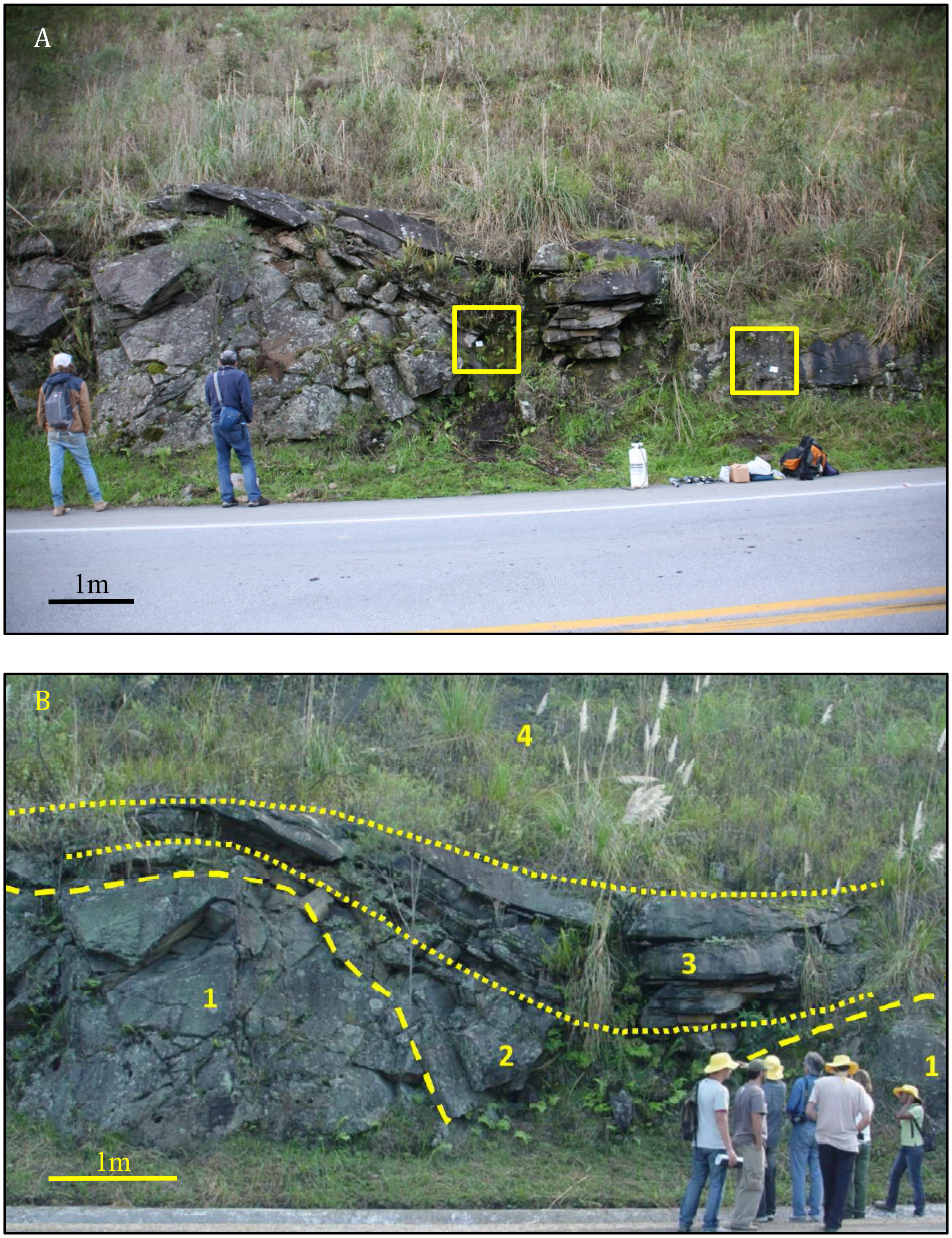

Fig 3-2. (A) *Alfredo Wagner road cut along Highway BR-282 in the state of Santa Catarina. Yellow boxes indicate approximate locations of sample sites.* ***(B1)*** *Precambrian granite,* ***(B2)*** *massive diamictite,* ***(B3)*** *stratified diamictite,* ***(B4)*** *black shale. Figure B modified after Rosa et al., (2016).*

Fig 3-3. *Sample sites at the Alfredo Wagner road cut in the state of Santa Catarina,* ***(A)*** *massive diamictite (site B8),* ***(B)*** *stratified diamictite (site R7)*

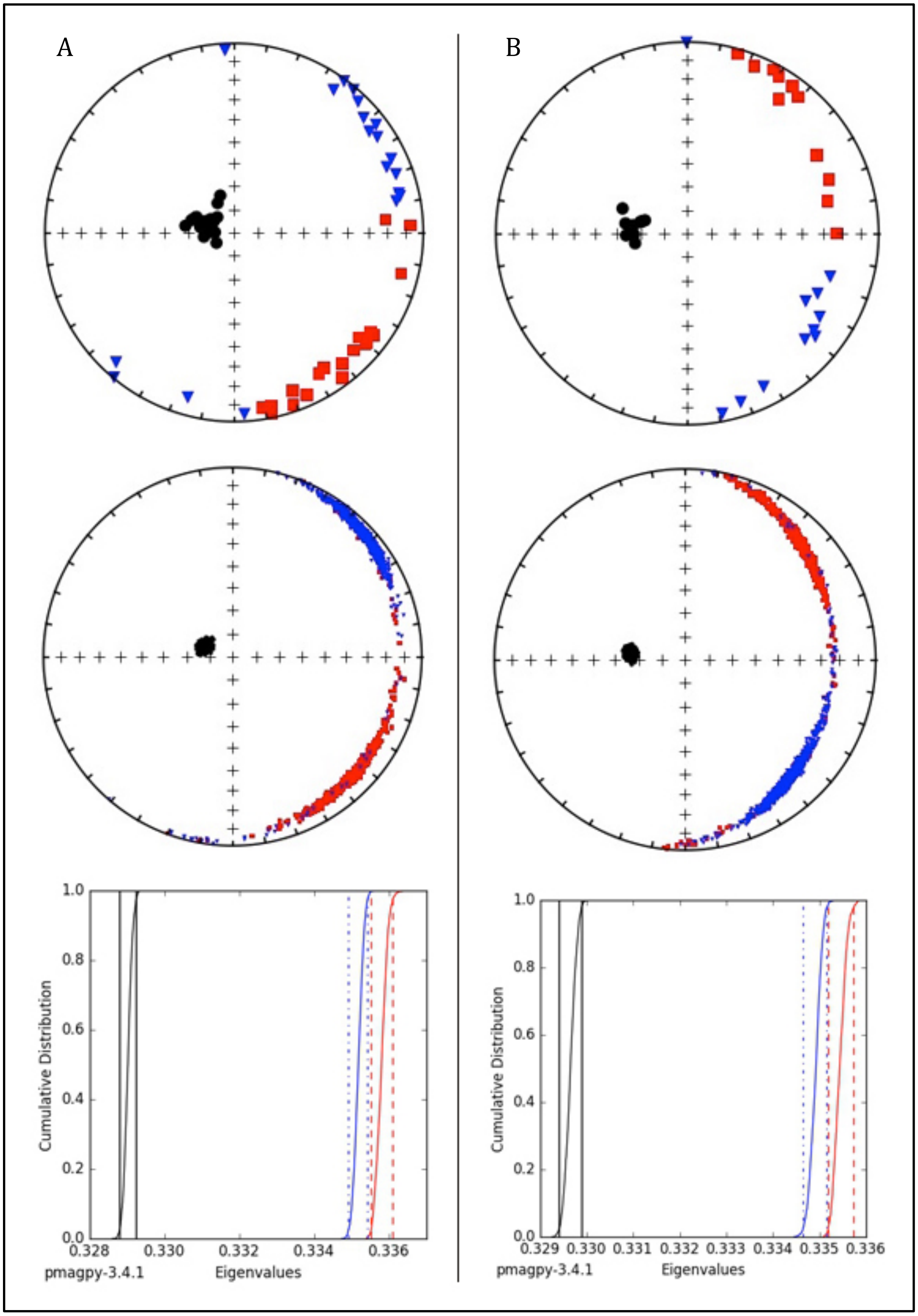

Fig 3-4. *Measured eigenvectors for each specimen (top), bootstrapped eigenvectors (center), and bootstrapped eigenvalue cumulative distribution graphs (bottom) for sites at Alfredo Wagner road cut* ***(A)*** *B8 (massive diamictite),* ***(B)*** *R7 (stratified diamictite). Maximum eigenvector indicated by red squares, intermediate by blue triangles, and minimum by black circles.*

3.2.3 Location discussion

Rocha Campos et al. (1988) interpreted this succession to include both subglacial and subaqueous facies. The undulating, striated, gouged, and scoured surface cut on the granitic basement indicates the occurrence of subglacial erosion (Evans et al. 2007). Deposition of the massive diamcitite directly on this surface suggest deposition as a subglacial traction till. Stratified diamictites are often attributed to stacked debris flows, common in glaciomarine environments (Eyles et al., 1993), but it should be noted that stacked debris flows can also operate subglacially if you have troughs or cavities at the ice-bed interface. According to Rocha Campos et al. (1988), crescentic gouges on the striated surface allowed them to infer ice–flow towards the NW, however Rosa et al. (2016) reported that due to weathering, those structures no longer existed.

Past studies have reported subglacial tills exhibiting isotropic to weakly developed flow-aligned fabrics (Fuller, 1962; Gravenor et al., 1973; Stupavsky et al., 1974a, 1974b; Eyles et al., 1987). Hooyer et al. (2008) experimentally demonstrated that tills with an isotropic fabric can develop a weak-to-strong flow-aligned fabric (imbricated up-glacier, dipping 10-30°) based upon the degree of shearing the till has undergone. The sample set from the massive diamictite shows a strong, flow-aligned fabric that is imbricated, dipping towards the SE thus suggesting a NW flow direction (Fig 3-4A). This data supports Rocha Campos et al. (1988) claim of ice flow to the NW determined from crescentic gauges on the striated basement. It should be noted that strong, flow-aligned fabrics can also develop subglacially by other processes which include: flowing water at the ice-bed contact, or plowing of particles through subglacial lodgment (Hooyer at al., 2008). The striations suggest that water was present at the ice-granite interface at the time the basement was overridden by ice.

The stacking of 10-30cm thick clast-poor, mud-rich deposits with sharp contacts would suggest that the stratified diamictites are most likely is the result of subaqueous debris flows (cf. Eyles et al., 1993; Mulder and Alexander, 2001). The sample set from the stratified diamictite (site R7) shows a flow-oblique fabric that is imbricated towards the E, which suggests a W flow direction (Fig 3-4B). While flow –aligned, -transverse fabrics are most commonly observed in debris flows, Rees (1983) experimentally demonstrated flow-oblique fabrics could develop in viscous (non-Newtonian) flows as a result of clast interactions between varying percentages of clasts and grains in suspension.

3.3 Aurora

3.3.1 Field description

In the state of Santa Catarina, a quarry in the municipality of Aurora along Highway SC-35, ~6 km north of Ituporanga was sampled (27°21'09.2"S, 49°36'45.4"W). The excavated exposure (Fig 3-5A) is interpreted to be part of the upper Rio do Sul Formation (Fig 1-4). Majority of the exposure consists of a massive diamictite classified as a ‘clast-poor muddy diamictite’ ~24 m thick, showing soft-sediment deformation features (i.e., folds, faults, shear planes and allochthonous sandstone bodies). Rodrigues et al. (2017) interpreted flow of the massive diamictite to the NW based on fold orientations. Massive sandstone 6-8 m thick overlies the very top of the succession. Access to the exposure was limited due to the vertical quarry walls (Fig 3-5A).

3.3.2 AMS and magnetic analysis

Five cores were extracted from the lower, sheared segment of the massive diamictite body (site Q1) (Fig 3-5B), yielding a total of 19 specimens for AMS analysis, all of which passed the F test (Table A-3). Site Q1 shows a strong, flow-aligned fabric that is triaxial and imbricated, dipping at ~20° towards the SSE suggesting flow towards the NNW (Fig 3-6).

Magnetic analysis from site Q1 is included in Appendix B in detail Fig B-3. Hysteresis measurements show a loop characteristic of strong paramagnetic contributions. Susceptibility vs. temperature measurement indicates low-field ferromagnetic contributions from most likely magnetite (~580°C) with an additional phase occurring at 400°C upon cooling, indicating that the sample underwent alteration during heating. Hysteresis parameters suggest the ferromagnetic grain size of the fabric falls within PSD range. X_{hf} to X_0 ratio for the site is 10:1, suggesting paramagnetic contributions dominate. All of the above suggests that the AMS is controlled by shape anisotropy, resulting in a normal fabric.

3.3.3 Location discussion

Fernando Vesely interpreted this succession as a glaciomarine slope complex; suggesting that it represented an unstable glaciogenic shelf that resulted in subaqueous mass transport (pers. comm., August 2016). The clast-poor muddy diamictite is interpreted to be the result of subaqueous slumps and debris flows suggested by the large-scale cohesive concentration of mud and other slump like deformational features (cf. Mulder and Alexander, 2001). The massive sandstone that overlies the very top of the succession is interpreted to be a slide block from a delta margin. Both flow -aligned, -transverse fabrics are common in subaqueous debris flow

(Rees, 1983; Gravenor, 1985; Eyles et al., 1987). The sample set from the massive diamictite shows a strong, flow-aligned fabric that is imbricated towards the SSE suggesting a NNW flow direction (Fig 3-6), which is consistent with the NW measurements of Rodrigues et al. (2017).

Fig 3-5. (A) *Exposure at the Aurora quarry located along Highway SC-35 in the state of Santa Catarina. Yellow box indicates approximate location of* ***(B)*** *sample site of massive diamictite (site Q1).*

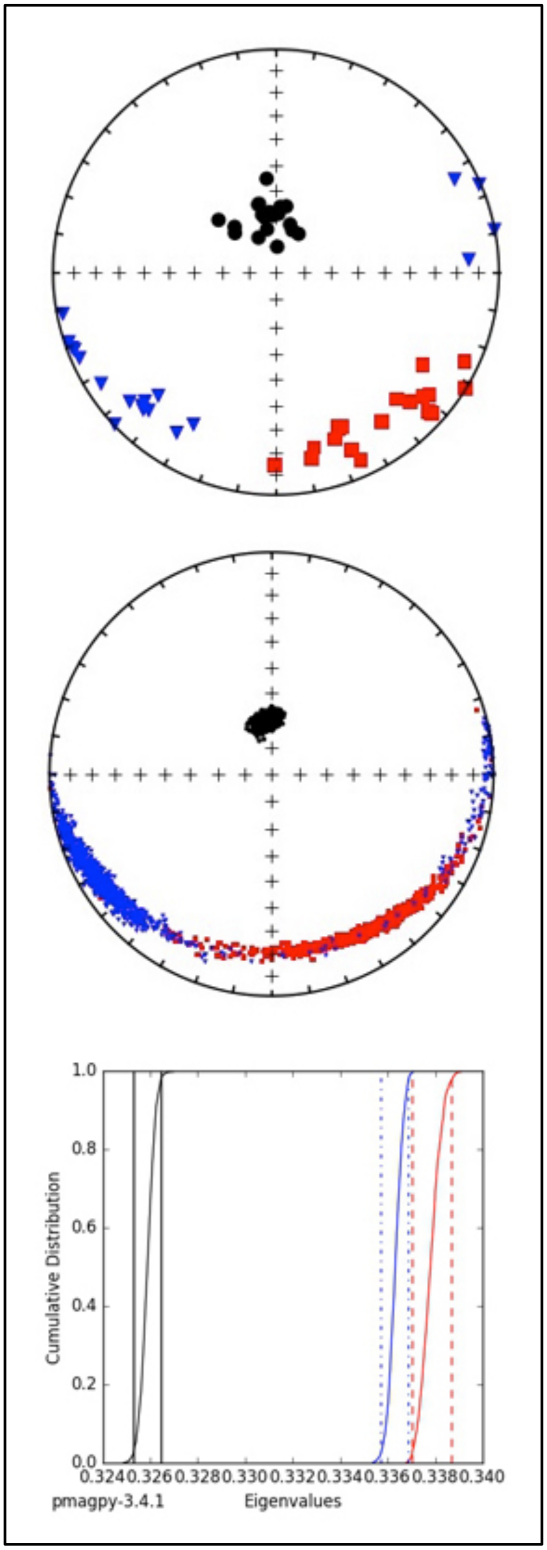

Fig 3-6. *Measured eigenvectors for each specimen (top), bootstrapped eigenvectors (center), and bootstrapped eigenvalue cumulative distribution graph (bottom) for site Q1 (massive diamictite) at the Aurora quarry. Maximum eigenvector indicated by red squares, intermediate by blue triangles, and minimum by black circles.*

3.4 Campo Do Tenente

3.4.1 Field description

In the state of Paraná, a quarry located ~1.5 km northeast of Campo do Tenente was sampled (25°58'12.1"S, 49°40'29.2"W) (Fig 3-8A). An exposure discussed by Suss et al. (2014) and interpreted to be part of the upper Campo do Tenente Formation (Fig 1-4). The bottom of the succession begins with 5.5 m of a massive diamictite (Fig 3-8B1) classified as a 'clast-poor intermediate diamictite' with relatively large lenticular sandstone bodies up to 2.5 m in height contained within the diamictite (Fig 3-8B2). The sandstone bodies are fine- to medium-grained and some contain climbing ripples with foresets that dip towards the SE. Other sandstone bodies display internal folding and in places brecciation. On the East wall of the quarry, sandstone bodies occur in clusters along individual horizons. These bodies appear to be large-scale brecciation of a once continuous larger sandstone body. The contact between the sandstone units and the diamictite is diffusive showing the process of homogenization. Above 1.5 m is a combination of facies that begins with a distinct, thinly bedded siltstone with ripples which grades first into rhythmites, and then into a thinly bedded stratified diamictite (Fig 3-8B3). The overall 1.5 m facies grades from zero to abundant lonestones and diamictite pellets. The debris-rich, stratified diamictite towards the top, contains thin laminations of mudstone. Then the next 5 m above are composed primarily of clay and silt with graded ~10-30 cm intervals of lonestones and diamictite pellets, with occasional carbonate concretions ~20 cm in length (Fig 3-8B4). A 10 cm thick clast-poor sandy diamictite with abundant rip up clasts can be found towards the top of the succession. The diamictite is laterally continuous across the quarry and shows sharp contacts to the underlying and overlying graded shale. Stratigraphically above lies several meters of brown shale, free of lonestones and diamictite pellets. There are no known indicators of flow anywhere in the quarry. Measured section and field description provided by Eduardo Luiz Menozzo da Rosa of UFPR (pers. comm., August 2016).

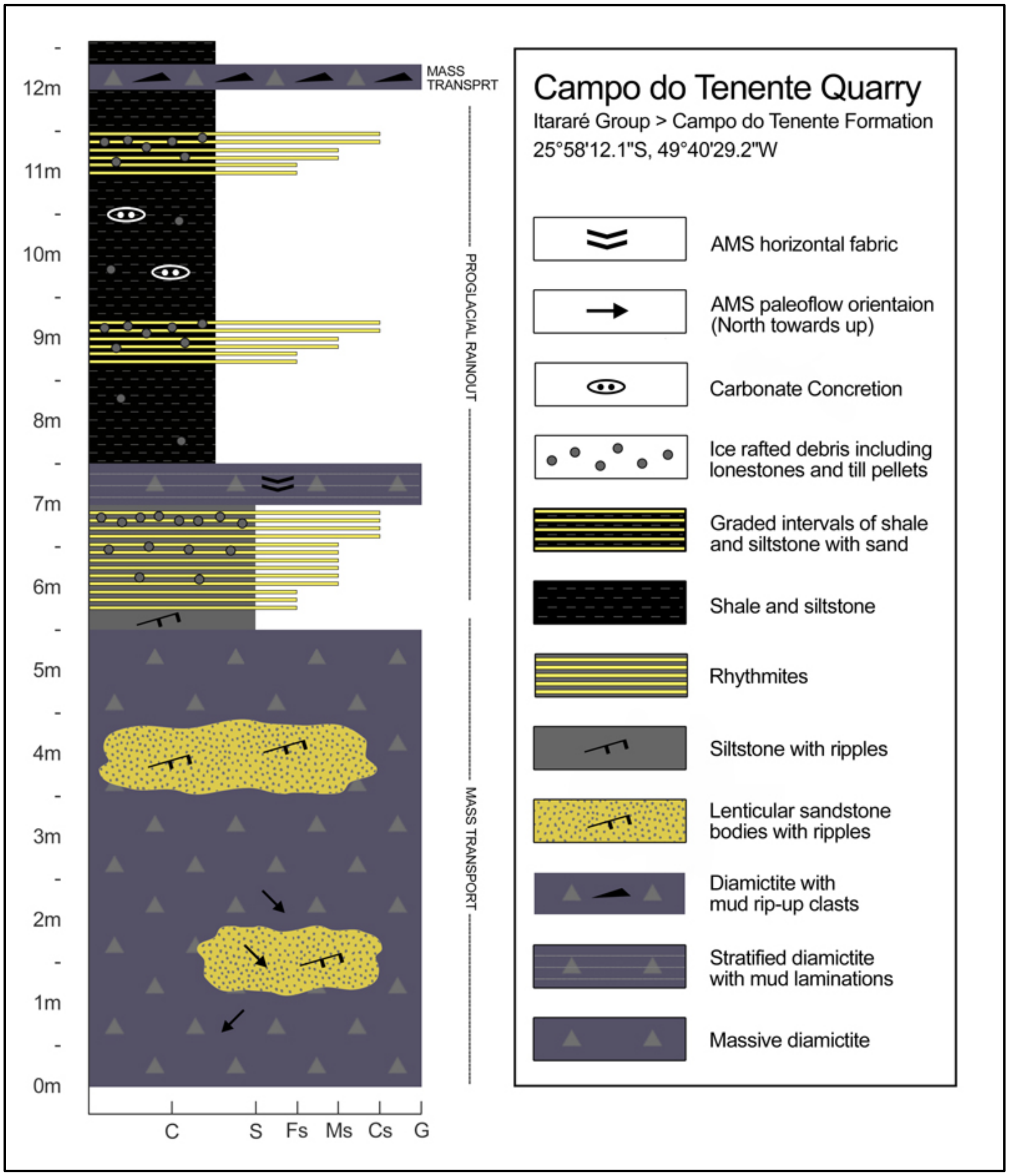

Fig 3-7. *Stratigraphic column of glacial marine succession at the Campo do Tenente quarry showing principle facies and AMS paleoflow orientaions (Measured section and field description provided by Eduardo Luiz Menozzo da Rosa of UFPR).*

3.4.2 AMS and magnetic analysis

Three sites were chosen within the massive diamictite to sample: below (site C3), above (site T5), and within (site D4) a sandstone body (Fig 3-9A). Ten cores were extracted from site D4, yielding 13 specimens (Table A-4). Six cores were extracted from site T5, yielding 15 specimens (Table A-5). Five cores were extracted from site D4, yielding 16 specimens (Table A-6). All specimens passed the *F* test and were included in the AMS analyses. Site C3 shows a flow-oblique fabric that is triaxial and imbricated, dipping at ~15° towards the NE suggesting flow towards the SW (Fig 3-11A); both the $\boldsymbol{k}_1$ and $\boldsymbol{k}_2$ axes are orientated ~45 in the direction of imbrication. Site T5 shows a weakly flow-aligned fabric that statistically triaxial but almost oblate. The fabric is imbricated, dipping ~15° towards the NW suggesting flow towards the SE (Fig 3-11B). Site D4 shows a strong, flow-aligned fabric that is triaxial and imbricated, dipping ~20° towards the NW, suggesting flow towards the SE (Fig 3-12A).

One site within the distinct, thinly bedded, siltstone (site D5) was sampled. Four cores were extracted, yielding 12 specimens for AMS analysis, all of which passed the *F* test (Table A-7). Site D5 shows a very strong, flow-aligned fabric that is triaxial and imbricated, dipping ~10° towards the W suggesting flow towards the E (Fig 3-12B).

Two sites were selected within the stratified diamictite to sample; both sets of samples were debris-rich, one of which contained a thin lamination of mud (site D3), and one of which did not (site C5) (Fig 3-10A). Seven cores were extracted from site C5, yielding 18 specimens (Table A-9). Six cores were extracted from site D3, yielding 17 specimens (Table A-8). All specimens passed the *F* test and were included in the AMS analyses. Site C5 shows an oblate, horizontal fabric (Fig 3-13B). Site D3 shows a triaxial, non-imbricated fabric making it difficult to distinguish between a flow- aligned or a transverse fabric (Fig 3-13A).

One site within the 10 cm thick clast-poor sandy diamictite with abundant rip up clasts (site FE1) towards the top of the 5 m of shale with graded intervals of dropstones and till pellets was sampled (Fig 3-10B). Five cores were extracted, yielding 16 specimens for AMS analysis, all of which passed the F test (Table A-10). Site FE1 statistically shows a triaxial fabric, that is weakly imbricated making it difficult to differentiate between a flow- aligned or a transverse fabric (Fig 3-14).

Magnetic analyses from sites C3, T5, D4, D5, D3, C5, and FE1 are included in Appendix B in detail; Fig B-4 thru Fig B-9 respectively. Hysteresis measurements from all sites show loops characteristic of both para- and ferromagnetic contributions. Susceptibility vs. temperature measurements indicate low-field ferromagnetic contributions from most likely magnetite (~580°C) at all sites, with one exception of a mineral phase occurring at 300°C upon cooling (site D5). Hysteresis parameters suggest the ferromagnetic grain size of the fabric falls within PSD range. X_{hf} to X_0 ratios for sites C3/T5, D4, D5, D3/C5, FE1 are ~ 1:2, 1:6, 1:0.5, 1:1, 1:0.5 respectively, suggesting an close-to-even para- and ferromagnetic contributions. All of the above strongly suggests that the AMS at the Campo do Tenente quarry is controlled by shape anisotropy, resulting in normal fabrics.

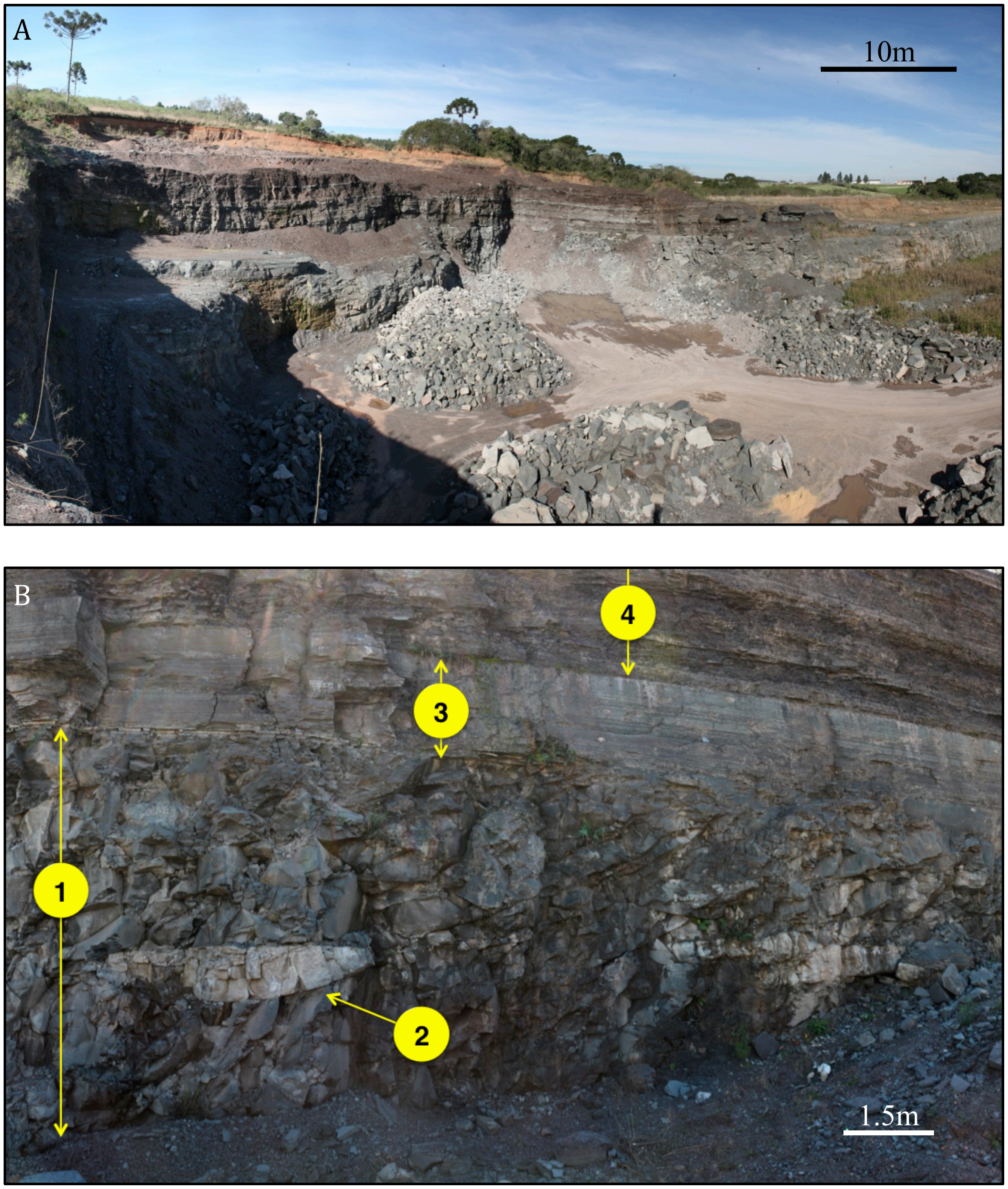

Fig 3-8. *Campo do Tenente quarry* ***(A)*** *NE view from the top of the quarry* ***(B)*** *exposure along the NW wall* ***(B1)*** *5.5 m of massive diamictite,* ***(B2)*** *sandstone body,* ***(B3)*** *1.5 m of rhythmites that grade into a stratified diamictite,* ***(B4)*** *5 m of clay/silt with graded intervals of dropstones and till pellets.*

Fig 3-9. *Bottom of succession at the Campo do Tenente quarry* ***(A)*** *massive diamictite (sites C3 and T5) with sandstone body (site D4),* ***(B)*** *thinly bedded, rippled unit that directly overlies massive diamictite (site D5).*

Fig 3-10. *Top of succession at the Campo do Tenente quarry* ***(A)*** *rhythmites that grade into a stratified diamictite (sites C5 and D3),* ***(B)*** *clast-poor sandy diamictite with abundant rip up clasts that lies towards the top of succession (site FE1).*

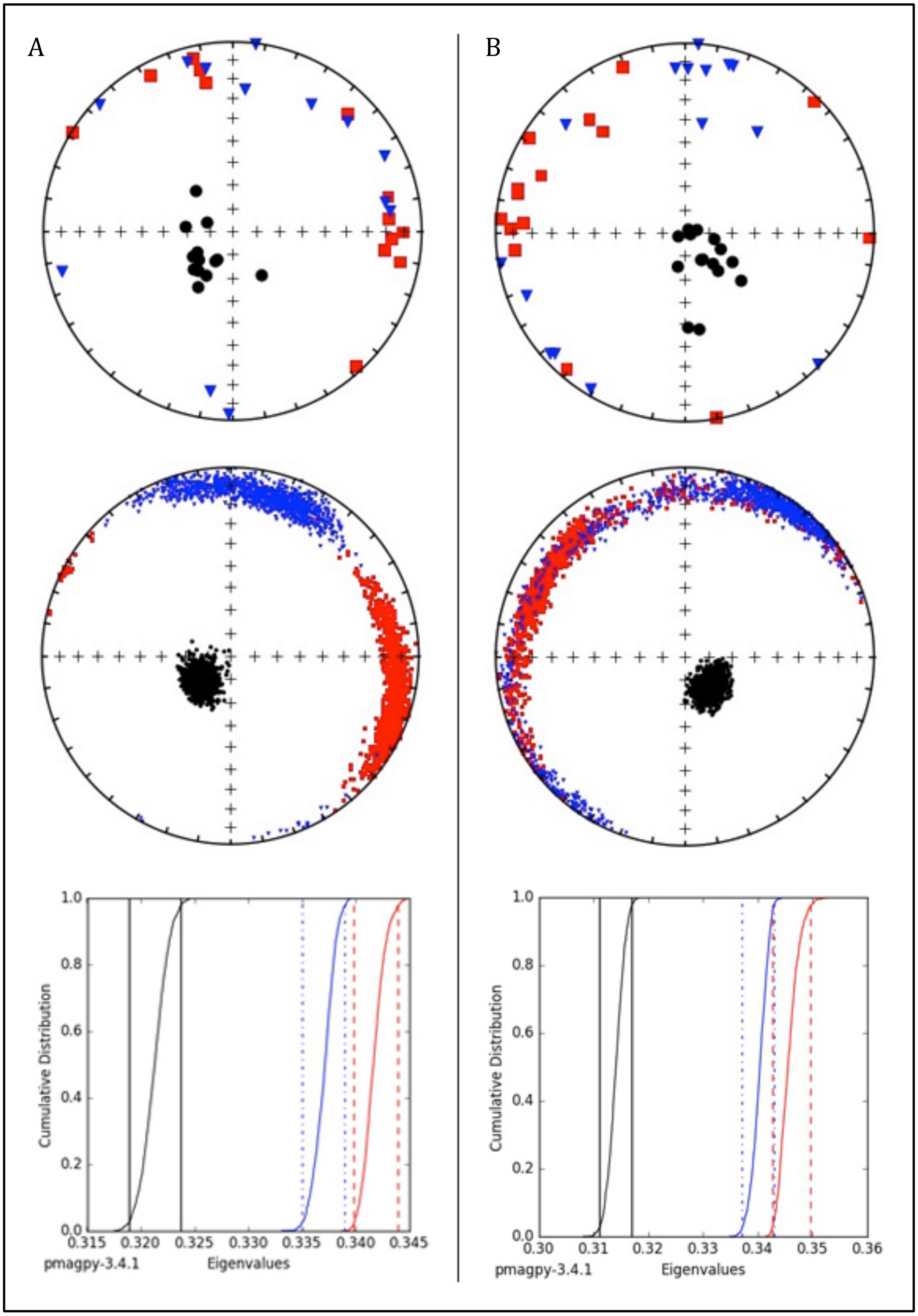

Fig 3-11. *Measured eigenvectors for each specimen (top), bootstrapped eigenvectors (center), and bootstrapped eigenvalue cumulative distribution graphs (bottom) for sites at the Campo do Tenente quarry* ***(A)*** *C3 (diamictite below),* ***(B)*** *T5 (diamictite above). Maximum eigenvector indicated by red squares, intermediate by blue triangles, and minimum by black circles.*

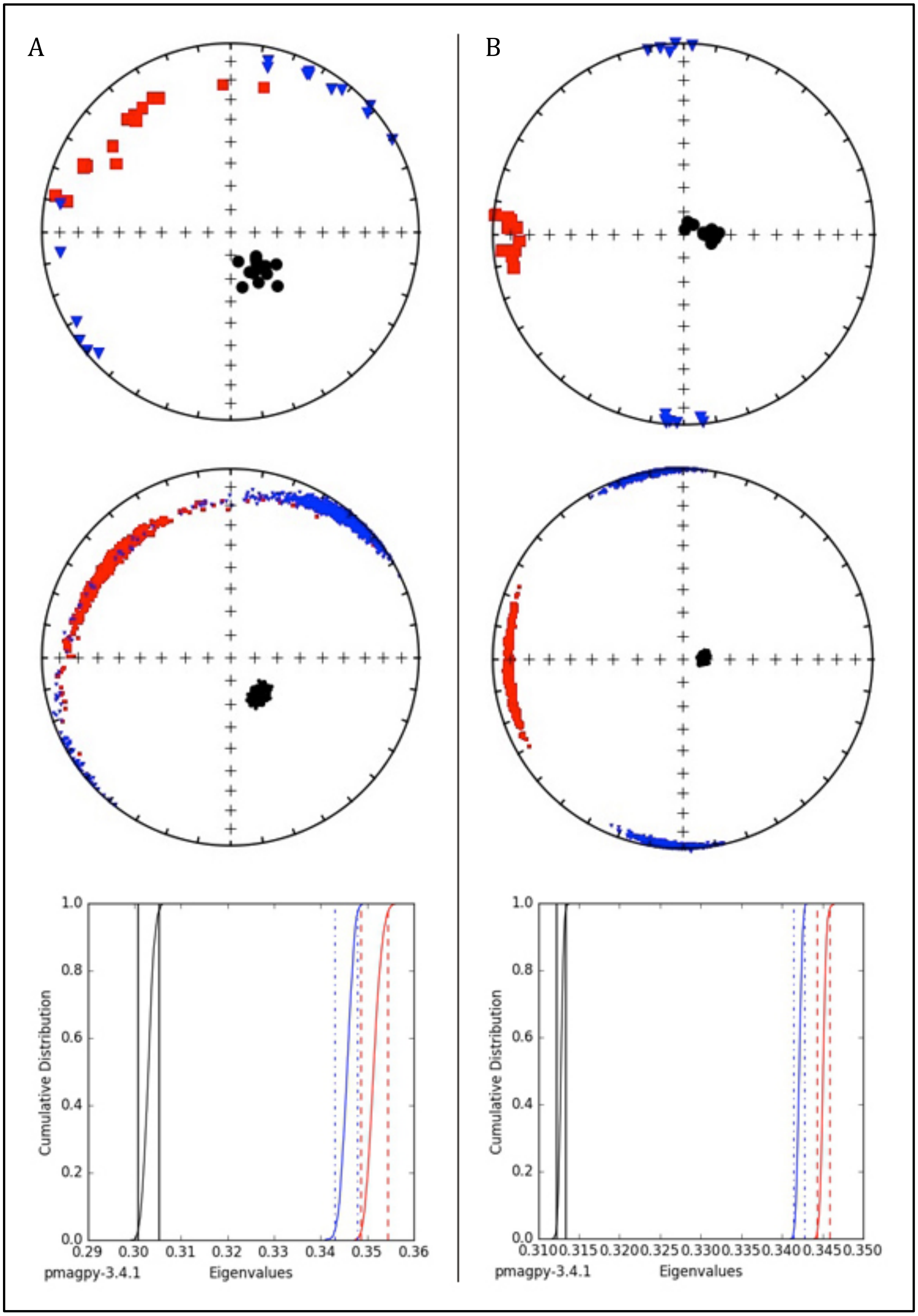

Fig 3-12. *Measured eigenvectors for each specimen (top), bootstrapped eigenvectors (center), and bootstrapped eigenvalue cumulative distribution graphs (bottom) for sites at the Campo do Tenente quarry* ***(A)*** *D4 (sandstone body),* ***(B)*** *D5 (thinly bedded, rippled unit). Maximum eigenvector indicated by red squares, intermediate by blue triangles, and minimum by black circles.*

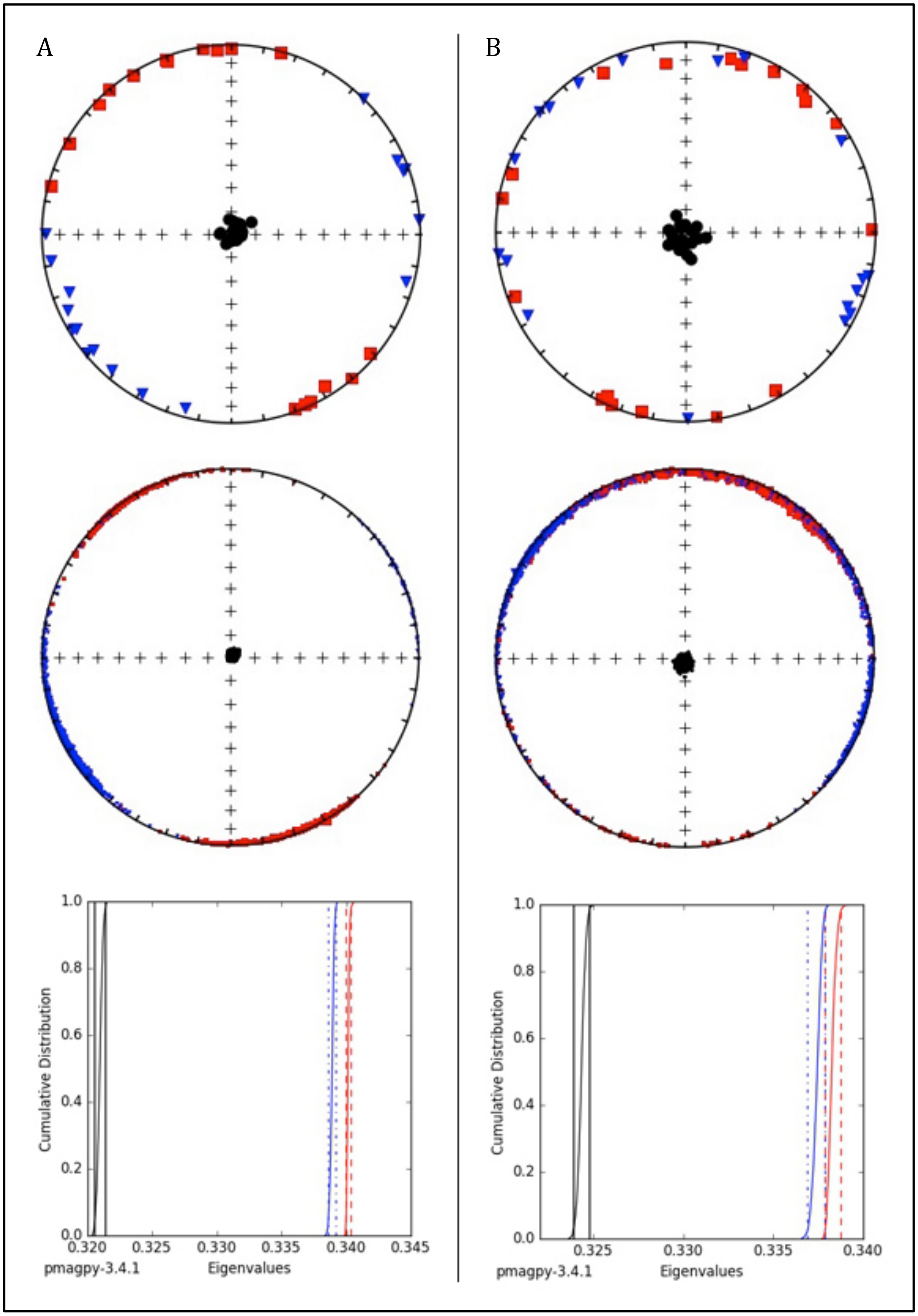

Fig 3-13. *Measured eigenvectors for each specimen (top), bootstrapped eigenvectors (center), and bootstrapped eigenvalue cumulative distribution graphs (bottom) for sites at the Campo do Tenente quarry **(A)** D3 (with lamination of mud), **(B)** C5 (without lamination of mud). Maximum eigenvector indicated by red squares, intermediate by blue triangles, and minimum by black circles.*

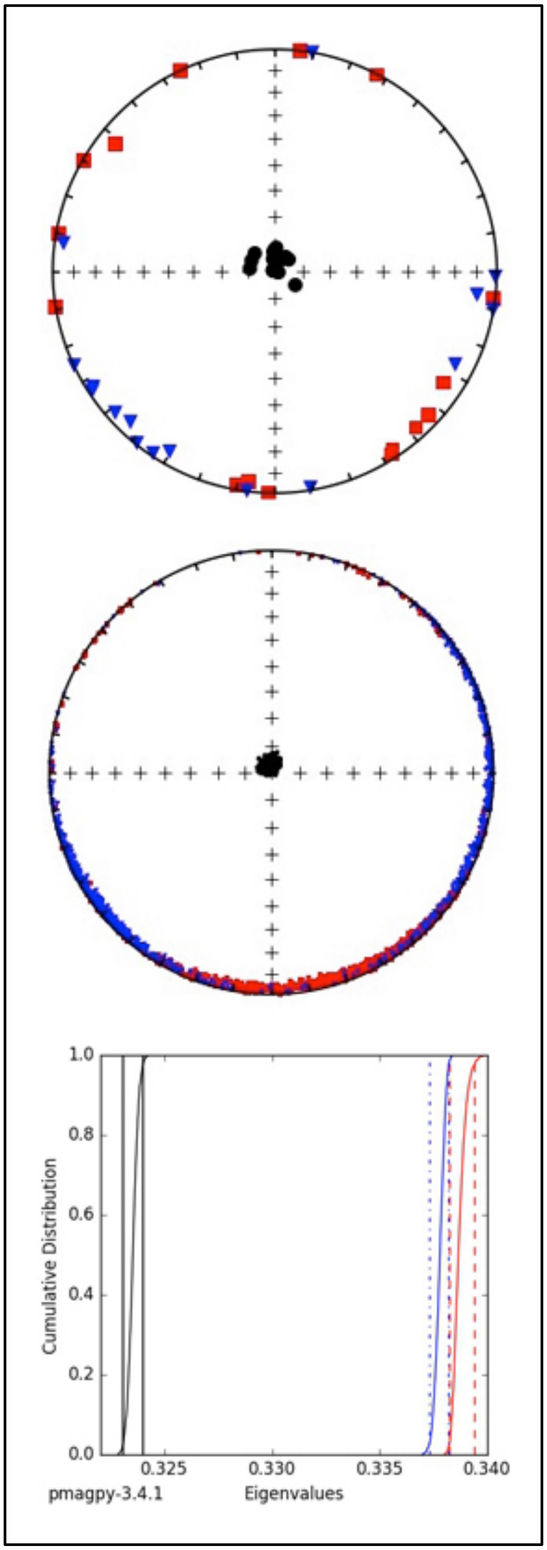

Fig 3-14. *Measured eigenvectors for each specimen (top), bootstrapped eigenvectors (center), and bootstrapped eigenvalue cumulative distribution graph (bottom) for site FE1 (thinly bedded sandstone) at the Campo do Tenente quarry. Maximum eigenvector indicated by red squares, intermediate by blue triangles, and minimum by black circles.*

3.4.3 Location discussion

Suss et al. (2014) interpreted this succession as a glaciomarine slope complex; deltaic progradation over a glaciogenic basin shelf, generating instability and subaqueous mass transport. The massive diamictite with relatively large lenticular sandstone bodies that comprise the bottom half of the succession is interpreted to be the result of subaqueous slumping and debris flows, indicated by the brecciation and homogenization of rafted sandstone slide blocks of deltaic origin. The upper half of the succession which includes both the unit of rhythmites that grade into a stratified diamictite, and the unit composed primarily of shale with graded intervals of lonestones and till pellets are interpreted to have recorded large influxes of fine-grained sediment and ice-rafted debris as the result of rain-out, indicated by the gradual and grading contacts of the facies. The influxes of sediment may represent the advances and retreats of a glacier margin, interludes of high and low discharge during summer and winter months respectively, or the presence/absence of sea ice (Dowdeswell et al., 2000).

As previously discussed both flow -aligned, -transverse fabrics are common in subaqueous debris flows, but flow-oblique fabric have been observed (Rees, 1983). While site T5 from the massive diamictite (above the sandstone body) shows a weakly flow-aligned fabric to the SE (Fig 3-11B), site C5 (below the sandstone body) shows an oblique-fabric flowing to the SW (Fig 3-11A). The ~90° difference in flow directions, could be the result of grains being displaced laterally (perpendicular to flow) beneath the block as it plowed (or rotated) its way through the underlying deposits. The sandstone block itself shows a strong flow-aligned fabric, with an inferred flow direction to the SE (Fig 3-12A). This supports the field observation of foresets contained within the block that also dip SE. While the flow direction of the sandstone block is similar to the flow direction of the massive diamictite above, the fabric contained within the block is inherited from the original deposits and should not be related to the resedimentation process of the slide block , as the ripples formed prior to any mass movement down a slope. The massive diamictite is most likely the result of subaqueous slumps and debris flows suggested by the large-scale cohesive concentration of mud, which include the brecciation and folding features of large sandstone bodies (cf. Mulder and Alexander, 2001).

Moving up the succession, the massive diamictite is overlain by a distinct, thinly bedded, siltstone with ripples, which then grades into rhythmites, and then into a stratified diamictite. The fabric from this siltstone shows a very strong, flow-aligned fabric to the E (Fig 3-12B). This unit could be interpreted as being genetically related to the massive diamictite. Often subaqueous sediment gravity flows will have a two-component system: a lower, dense laminar debris flow, and an upper, turbidity current (Postma et al., 1988; Shanmugam, 1996). The thin bed relative to the flow size (indicated by the continuous lateral extent of the deposit across the quarry) would suggest the deposit was the result of a 'surge-like turbidity flow' (Mulder and Alexander, 2001). The ~45° difference in flow directions could be the possibility of the turbidity current ponding on irregular topography, resulting in a deviation between the various current directions. Another possibility is that the unit is the result of rain-out deposition that has been reworked by moderate currents on the basin floor into a flow-aligned fabric.

Stratigraphically above, two sample sets were collected from a debris-rich stratified diamictite interpreted to be the result of rain-out deposition (Suss et al., 2014). One set of samples contains a very thin lamination of mud (site D3), and the other does not (site C5). Horizontal (or oblate) fabrics are most common in rain-out deposition, a two component system of fines settling from meltwater plumes and clast transported as ice rafted debris (Hamilton and Rees, 1970; Gravenor 1985; Eyles et al., 1987). The C5 fabric does show a horizontal fabric; the orientation of $\boldsymbol{k}_1$ and $\boldsymbol{k}_2$ are distributed randomly within the horizontal plane, and $\boldsymbol{k}_3$ is clustered near vertical (Fig 3-13B). By contrast, site D3 has $\boldsymbol{k}_3$ axes clustered near the vertical, but the orientation of $\boldsymbol{k}_1$ and $\boldsymbol{k}_2$ have a preferred distribution within the horizontal plane (Fig 3-13A). The mean $\boldsymbol{k}_3$ direction is slightly imbricated, dipping ~3° to the SW suggesting flow to the NE which would classify the fabric as flow-transverse, but because the 95% confidence interval defined by the bootstrapped $\boldsymbol{k}_3$ eigenvectors includes the vertical, technically the fabric is not imbricated, making it statistically difficult to correctly classify the fabric and determine the direction of sediment transport. The very thin laminations of mud are likely the result of deposition by distal, dilute, low-density turbidity currents. The fabric could be the result of rain-out deposition that has been reworked to some degree by these very small turbidity currents, too weak to cause significant imbrication but strong enough to show a preferred orientation of $\boldsymbol{k}_1$ and $\boldsymbol{k}_2$ in the horizontal plane.

The last fabric collected was from a 10-cm-thick clast-poor sandy diamictite with abundant rip-up clasts found towards the top of the succession contained with the unit composed primarily of shale with graded intervals of dropstones and till pellets. Here I interpret this unit to be the result of a small ‘concentrated debris flow,’ suggested by the sharp contact and erosive nature of abundant rip-up clasts (Mulder and Alexander, 2001). The fabric is statistically oblate, but does show a somewhat preferred distribution of $\boldsymbol{k}_1$ and $\boldsymbol{k}_2$ within the horizontal plane (Fig 3-14), similar to the fabric collected from the stratified diamictite at site D3. The mean $\boldsymbol{k}_3$ direction is slightly imbricated, dipping ~3° to the SSE suggesting flow towards NNW which would classify the fabric as flow-aligned, but because the 95% confidence interval defined by the bootstrapped $\boldsymbol{k}_3$ eigenvectors includes the vertical, technically the fabric is not imbricated, once again making it statistically difficult to correctly classify the fabric and determine the direction of sediment transport. The lack of significant imbrication could be the result of sudden changes in flow regimes or the result of a secondary fabric formed due to compaction. An alternative idea would be the fabric is showing a variation of two components: a flow-aligned fabric resulting from the diamictite, and a horizontal fabric resulting from the rip-up clasts contained within the facies.

3.5 Porto Amazonas

3.5.1 Field description

In the state of Paraná, a road cut exposure located ~700 m south of Porto Amazonas off Highway PR-427 was sampled (25°33'00.6"S, 49°53'08.7"W) (Fig 3-13A), an outcrop discussed by Vesely et al. (2015) as correlated to the lower Campo do Tenente Formation (Fig 1-4). The facies include rhythmites interbedded with sandstones. The rhythmites are comprised of thickly laminated, graded beds from fine sand to mud. Sandstones are structureless, thick- to very thick-bedded, tabular to lenticular in nature, moderately sorted, fine- to medium-grained. Rip-up mudstone clasts were observed at the base of these sandstones. The exposure contains no sedimentary structures that indicate flow direction. The only paleoflow information is from cross-stratified sandstones interpreted to be outwash about 20 m stratigraphically below the sampled unit that displays paleocurrent orientations to the west (log number 6) (Vesely et al., 2015).

3.5.2 AMS and magnetic analysis

A vertical succession of three sites, contained within a single sandstone bed was selected for sampling bottom (O5), middle (M6), and top (H7) (Fig3-14B). Six cores were extracted from site O5, yielding 18 specimens, 17 of which passed the *F* test and were included in the analysis (Table A-13). Five cores were extracted from site M6, yielding 16 specimens, 15 of which passed the *F* test and were included in the analysis (Table A-12). Five cores were extracted from site H7, yielding 16 specimens, 8 of which passed the *F* test and were included in the AMS analysis (Table A-11). Site O5 shows a flow-transverse fabric that is statistically triaxial but weakly developed (Fig 3-15A). Site M6 shows a strong, flow-transverse fabric that is triaxial and imbricated, dipping ~65° towards the SW (Fig 3-15B). Site H7 shows a flow-transverse fabric that is statistically triaxial but borders on being prolate (Fig 3-15C).

Magnetic analysis from sites O5, M6, and H7 is included in Appendix B in detail (Fig B-10). The hysteresis measurement shows a loop characteristic of both para- and ferromagnetic contributions. Susceptibility vs. temperature measurements indicate low-field ferromagnetic contributions from mineral phases occurring at 400°C and 500°C upon cooling. X_{hf} to X_0 ratios are ~2:1 suggesting even para- and ferromagnetic contributions. All of the above most likely suggests that the AMS is controlled by shape anisotropy, resulting in a normal fabric.

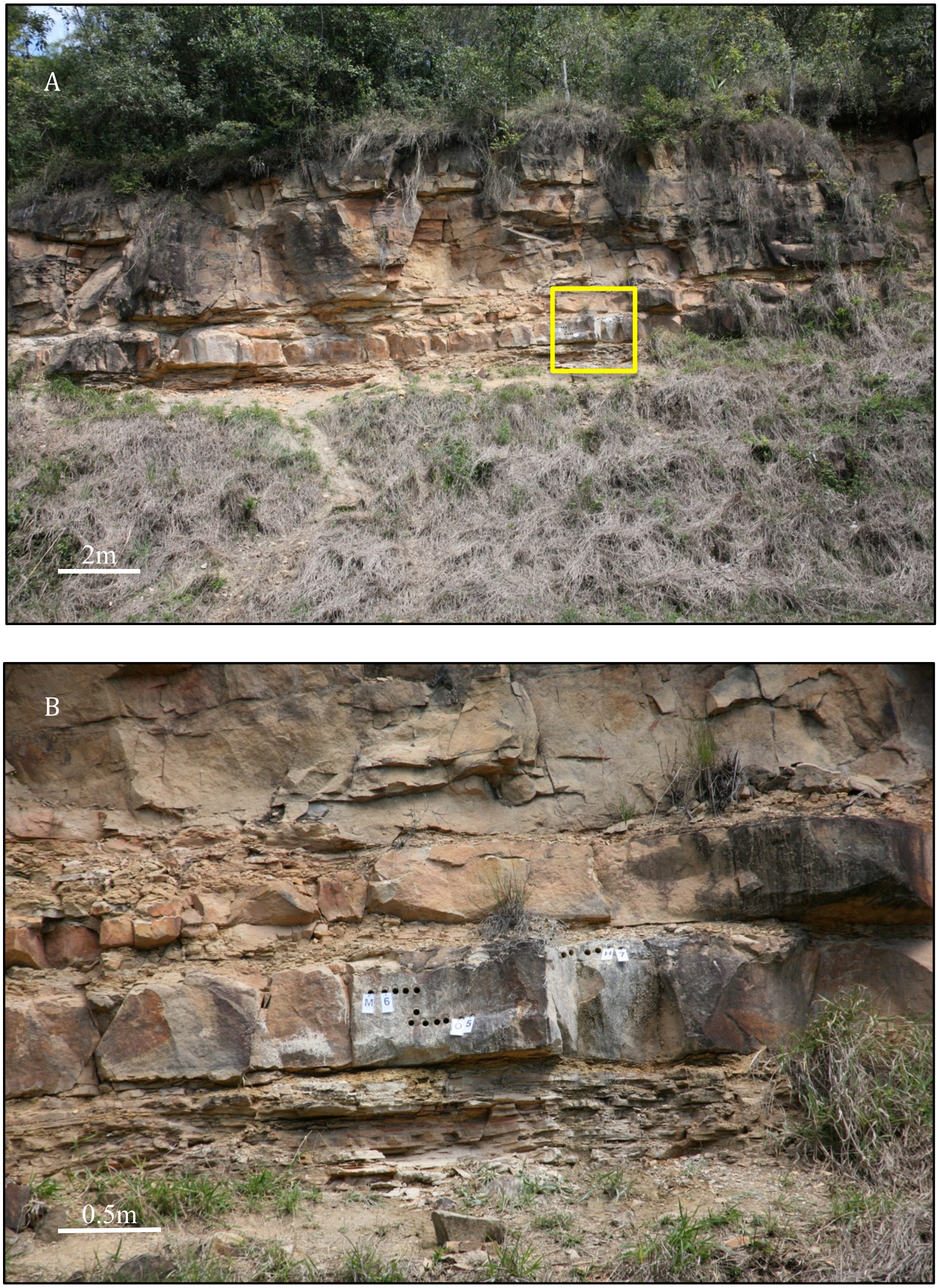

Fig 3-15. (A) *Porto Amazonas road cut exposure located off Highway PR-427 in the state of Paraná. Yellow box indicates approximate location of* ***(B)*** *sample sites within a structureless sandstone (sites O5, M6, and H7).*

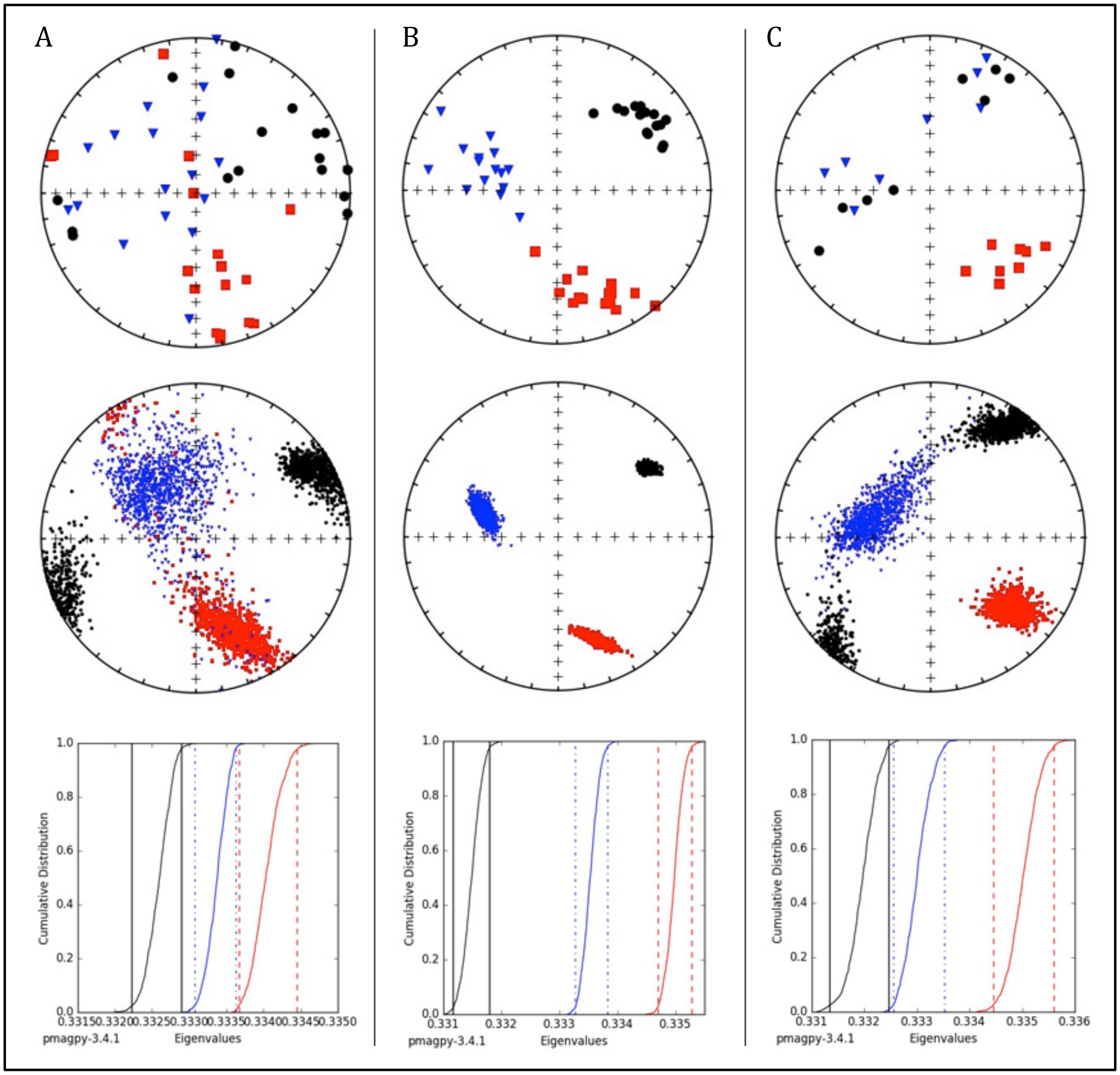

Fig 3-16*. Measured eigenvectors for each specimen (top), bootstrapped eigenvectors (center), and bootstrapped eigenvalue cumulative distribution graphs (bottom) for sites at the Porto Amazonas road cut exposure* ***(A)*** *O5 (bottom of sandstone unit,* ***(B)*** *M6 (middle of sandstone unit),* ***(C)*** *H7 (top of sandstone unit). Maximum eigenvector indicated by red squares, intermediate by blue triangles, and minimum by black circles.*

3.5.3 Location discussion

Vesely et al. (2015) interpreted these deposits to be part of a glaciomarine slope complex; high–density turbidity deposits, resulting from a collapsed grounding line fan or proglacial delta. The term 'high–density turbidity deposits' was first coined by Lowe, (1982), later redefined by Shanmugam (1996) as 'sandy debris flow deposits' which we define as a 'hyperconcentrated density flow (grain flow) deposits' using the nomenclature of Mulder and Alexander (2001). While the exact nature and classification of these deposits vary in the literature (Enos, 1977; Taira and Scholle, 1979; Lowe, 1982; Shanmugam, 1996; Sakai et al., 2002; Talling et al. 2012), massive, structureless sandstones are often attributed to Bouma's T_a division (Bouma, 1962; Eyles, 1993). The T_a interval is deposited under fast flow regimes when fluid turbulence is able to keep coarse material and high concentrations of sediment in suspension (Pickering and Hiscott, 2015). Eventually the energy dissipates and the grains tend to settle out or freeze all at once to create a massive bed (Pickering and Hiscott, 2015).

Both flow-aligned, and flow-transverse fabrics have been observed in these types of deposits in addition to isotropic fabrics (Rees, 1968; Hiscott and Middleton 1980; Rees, 1983). Isotropic or weakly developed fabrics (Fig 3-16A) may develop as a result of high apparent viscosity due to high near-bed sediment concentrations combined with frequent clast collisions during rapid settling from suspension (Hiscott and Middleton, 1980; Rees, 1983; Baas et al., 2007). Enos (1977) found weakly flow-aligned clasts in the basal shearing zone of debris flows.

Flow-transverse fabrics are indicative of deposition occurring under high flow velocities that are sufficient to entrain particles (Tauxe, 1998; Hailwood and Ding, 2000). These fabrics are characterized by triaxial fabrics (Fig 3-15B), or prolate fabrics (Fig 3-15C) where the distribution of $\boldsymbol{k}_3$ is streaked (Tauxe, 1998) indicating the rolling of grains, perpendicular to flow. Deposition occurring under high flow velocities is supported by field observations of rip-up clasts towards the base of the bed suggesting an erosive nature of fast, turbulent flow (Allen, 1982; Kano and Takeuchi, 1989).

In normal flow-transverse fabrics, the flow direction is indicated by the deflection of $\boldsymbol{k}_3$ eigenvectors from the vertical in a LHEA stereonet (up-current grain imbrication), which would indicate that flow direction within these deposits is to the NE. However, it should be noted that down-current grain imbrication has been observed in T_a divisions (Bouma, 1962; Hiscott and Middleton, 1980; Sakai et al., 2002), which might explain the relatively large imbrication of $\boldsymbol{k}_3$ ~65° (Fig 3-15B). If the grains are imbricated down-current, the inferred flow direction would be to the SW in a lower hemisphere stereonet and would be in agreement with the westward paleoflow information from cross-stratified sandstones located 20 m stratigraphically below the sampled sandstone bed (Vesely et al., 2015).

The sample sets collected from the vertical succession demonstrates how a depositional fabric can change upward within a deposit due to changing flow rheology and dynamics but still indicate a uniform flow direction. The weakly developed fabric found at the base of the bed, is most likely the result of high near-bed sediment concentrations combined with frequent clast collisions during rapid settling from suspension. The triaxial fabric found in the middle of the bed could be the result of grains rapidly freezing as the energy in the flow dissipates and the grains settle out all at once. The streaked distribution of $\boldsymbol{k}_3$ towards the top of the bed indicates the rolling of grains (long axes perpendicular to flow) during the final stages of transport (Tauxe, 1998). Despite the differences between the three fabrics, they all show a uniform flow direction trending SW/NE.

3.6 Cachoeira do Sul

3.6.1 Field description

In the state of Rio Grande do Sul, a surface exposure located on private land ~60 km southwest of Cachoeira do Sul was sampled (30°26'13.1"S, 53°05'38.2"W). The outcrop was first documented by Tomazelli & Soliani (1982) and is correlated to the very top of the Itararé Group (Fig 1-4). The outcrop shows a series of soft sediment grooved and ploughed surfaces composed of a clast-rich sandy diamictite (Rosa et al., 2016). A large granitic boulder ~40 cm in diameter is entrenched at the end of a large groove (Fig 3-18). Both the ploughed and grooved surfaces indicate an ice paleoflow direction to the N at 358°.

3.6.2 AMS and magnetic analysis

Three sample sets were collected from the surface exposure, all within the same unit but within different proximities to each other. Seven oriented cores were extracted from a ploughed surface (site P5) (Fig 3-18), yielding a total of 7 specimens, all of which passed the *F* test and were included in the analysis. (Table A-16). Five oriented cores were extracted from a river cut (site P7) (Fig 3-19A), yielding a total of 8 specimens, 7 of which passed the *F* test and were included in the analysis (Table A-17). Nine oriented cores were extracted from a grooved surface next to a road cut (site P9) (Fig 3-19B), yielding a total of 9 specimens, all of which passed the *F* test and were included in the analysis (Table A-18). All sample sets show flow-aligned fabrics, site P7 more weakly developed then the others. All fabrics are triaxial and imbricated, dipping ~20° towards the SSE suggesting paleo-iceflow towards NNW (Fig 3-20).

Magnetic analyses from sites P5, P7 and P9 are included in Appendix B in detail Fig B-12. Hysteresis measurements show a loop characteristic of both para- and ferromagnetic contributions. Susceptibility vs. temperature measurements indicates low-field ferromagnetic contributions from most likely magnetite (580°C), and an additional phase occurring at 480°C upon cooling, indicating that the sample underwent alteration during heating. Hysteresis parameters suggest the ferromagnetic grain size for the fabric falls within PSD range. X_{hf} to X_0 ratio is 1:1, suggesting even para- and ferromagnetic contributions. All of the above suggests that the AMS is controlled by shape anisotropy, resulting in a normal fabric.

Fig 3-17. *Ploughed surface located on private land southwest of Cachoeira do Sul. Samples extracted from (site P5) within close proximity.*

Fig 3-18. *Soft sediment grooved surfaced located on private land southwest of Cachoeira do Sul. Samples extracted from **(A)** river cut (site P7), and **(B)** road cut (site P9).*

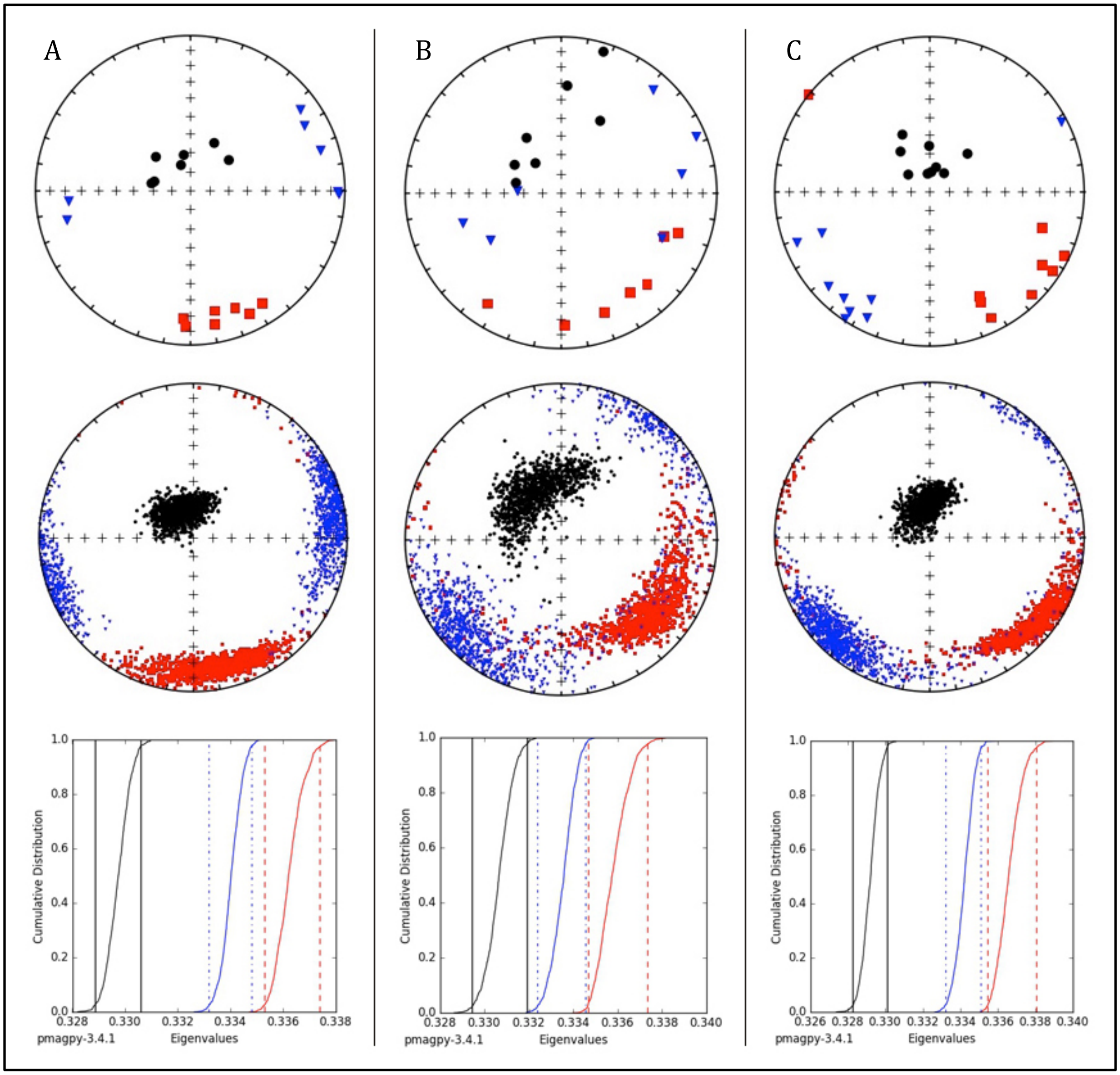

Fig 3-19. *Measured eigenvectors for each specimen (top), bootstrapped eigenvectors (center), and bootstrapped eigenvalue cumulative distribution graphs (bottom) for sites near Cachoeira do Sul* ***(A)*** *P5 (ploughed surface),* ***(B)*** *P7 (river cut), and* ***(C)*** *P9 (road cut). Maximum eigenvector indicated by red squares, intermediate by blue triangles, and minimum by black circles.*

3.6.3 Location discussion

Soft-sediment grooved surfaces are common in the Paraná Basin (Rosa et al., 2016) and can form subglacially, at the basal zone of a tidewater glacier, or as ice keel scours generated by free floating ice in a glaciomarine , glaciolacustrine setting (Woodworth-Lynas and Dowdesweell, 1994; Rosa et al., 2016).). In a subglacial environment, glaciers produce grooves and ridges through ploughing and deformation of unconsolidated beds (Benn and Evans, 2010). The presence of compression ridges at the boulder/bed interface, strongly suggests that the boulder ploughed its way through the soft substrate. This observation in conjunction with the lateral extent of grooved surfaces and presence of small flutes across the locality strongly suggests subglacial conditions. All three sample sets collected from the surface exposure near Cachoeira do Sul, show flow-aligned fabrics that are imbricated suggesting a NNW flow direction (Fig 3-20) and supports the inferred N ice paleoflow obtained from in-field measurements of the ploughed boulder and grooved surfaces. The ring-shear experiments of Hooyer et al. (2008) supports the interpretation of this fabric as the deposits and deformation of subglacial materials.

3.7 Ibaré

3.7.1 Field description

In the state of Rio Grande do Sul, an exposure located along railroad tracks ~6 km northwest of Ibaré was sampled (30°44'56.5"S, 54°17'37.5"W). The area was documented by Tomazelli & Soliani (1982/1997) and is correlated to the very top of the Itararé Group. The 2 m-thick exposure consists of thinly bedded, mildly deformed, fine-grained sandstones which, in turn, are overlain by thinly bedded, coarse-grained sandstones with dispersed clasts containing lenses of gravel up to 12cm thick and some striated clasts (angular to rounded). This is overlain by thinly bedded, fine-grained sandstones with minimal gravel, which, in turn, is overlain by a 10 cm thick clast-rich muddy diamictite, containing rafts of dislodged sedimentary bedding ~10 to 30 cm in length (Fig 3-21A). Multiple thrust sheets with internal overturned fold structures occur elsewhere along the exposure. The orientation of the axis of the fold suggest transport towards the NW (pers. comm., Nick Fedorchuk, August 2016).

3.7.2 AMS and magnetic analysis

Samples were collected from two sites within the first meter of the outcrop. Four oriented cores were extracted from the thinly bedded, mildly deformed, fine-grained sandstone (site E1) (Fig 3-21B), yielding a total of 14 specimens, all of which passed the *F* test and were included in the analysis. (Table A-19). Four oriented cores were extracted from the thinly bedded, coarse-grained sandstone with dispersed clasts (Site E2) (Fig 3-21B), yielding a total of 15 specimens, all of which passed the *F* test and were included in the analysis (Table A-20). Site E1 shows a weakly developed fabric that is statistically triaxial (Fig 3-22A). Site E2 shows a strong, flow-aligned fabric that is triaxial and imbricated ~15° NW (Fig 3-22B).

Magnetic analyses from sites E1 and E2 are included in Appendix B in detail Fig B-13. Hysteresis measurements show a loop characteristic of both para- and ferromagnetic contributions. Susceptibility vs. temperature measurements indicates low-field ferromagnetic contributions from most likely magnetite (580°C), and an additional phase occurring at 420°C upon cooling, indicating that the sample underwent alteration during heating. Hysteresis parameters suggest the ferromagnetic grain size for the fabric falls within PSD range. X_{hf} to X_0

ratio is 2:1, suggesting close-to-even para- and ferromagnetic contributions. All of the above suggests that the AMS is controlled by shape anisotropy, resulting in a normal fabric.

3.7.3 Location discussion

The exposure located along railroad tracks northwest of Ibaré, are most likely outwash deposits indicated by the abundant bedding of sandstones and gravel lenses. The mildly deformed fine-grain sandstones near the bottom of the succession may be the result of proximal subglacial shove as suggested by the abundance of thrust sheets elsewhere along the link of the exposure. The bootstrapped eigenvectors from the sample set collected from the mildly deformed, fine-grain sandstone (site E1) shows a fabric characteristic of a type IV deformation (Robion et al., 2007) indicated by the positions of $\boldsymbol{k}_3$ and $\boldsymbol{k}_1$ eigenvectors in the bedding plane. The AMS fabric supports the in-field observation of mildly deformed beds. The sample set collected from the coarse-grained sandstone with dispersed clasts (site E2) shows a strong, flow-aligned fabric that is imbricated, suggesting the direction of sediment transport was to the NW. This supports the in-field observation of multiple fold structures along the exposure overturning towards the NW.

***Fig 3-20. (A)** Exposure along railroad tracks located northwest of Ibaré. Yellow box indicates approximate location of **(B)** fine-grained sandstone unit (site E1), and coarse-grained sandstone unit above (site E2).*

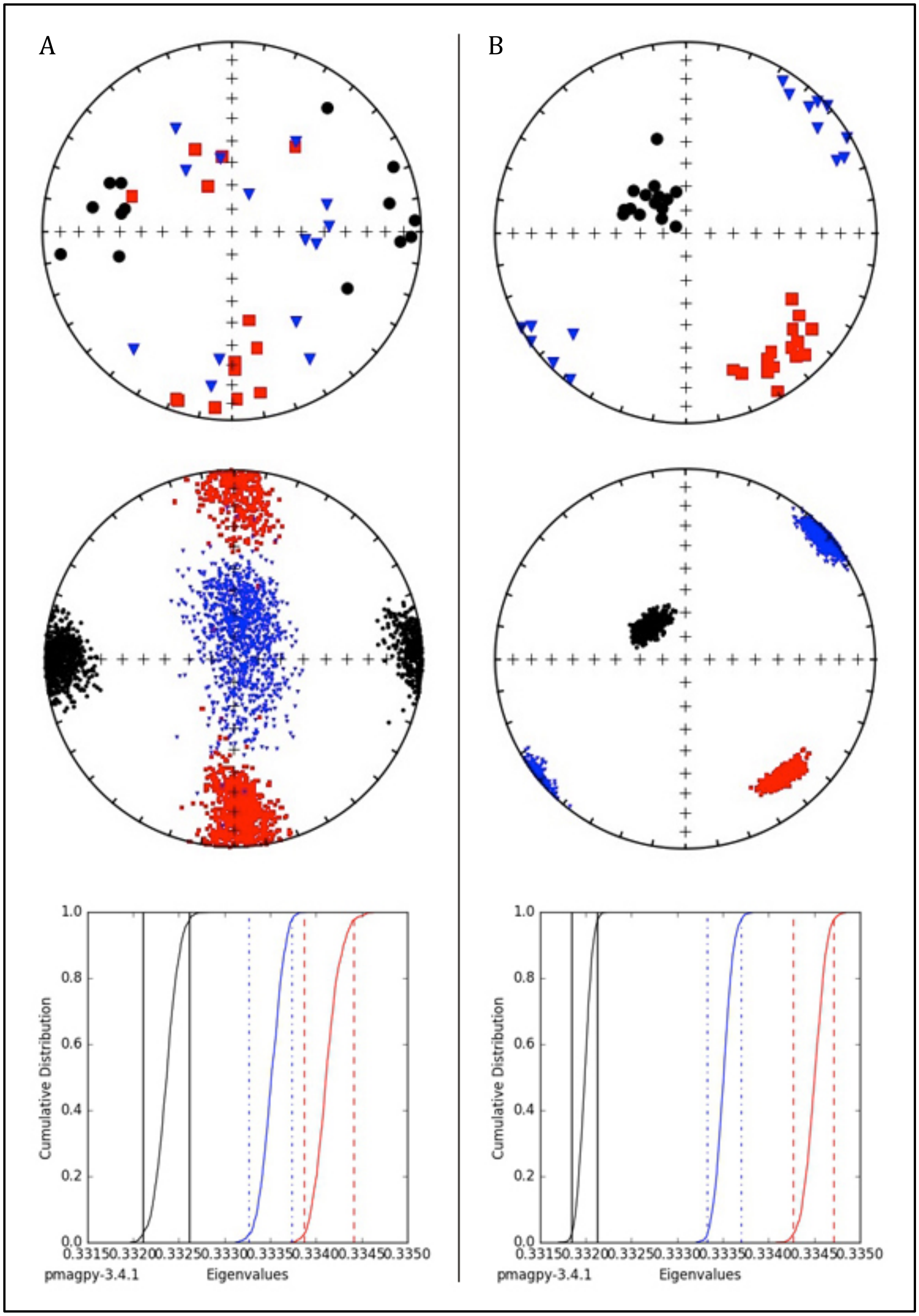

Fig 3-21. *Measured eigenvectors for each specimen (top), bootstrapped eigenvectors (center), and bootstrapped eigenvalue cumulative distribution graphs (bottom) for sites near Ibaré* ***(A)*** *E1 (fine-grained sandstone), and* ***(B)*** *E2 (coarse-grained sandstone). Maximum eigenvector indicated by red squares, intermediate by blue triangles, and minimum by black circles.*

3.8 São Gabriel

3.8.1 Field description

In the state of Rio Grande do Sul, a creek exposure located on private land ~25 km south of São Gabriel off Highway RS-630 was sampled (30°32'39.8"S, 54°26'50.0"W). An outcrop correlated to the very top of the Itararé Group (Fig 1-4) (cf. Tomazelli and Soliani, 1982). The meter thick succession of facies includes interbedded diamictites and sandstones with mudstone drapes (Fig 3-23). The medium-bedded diamictites are classified as 'clast-rich muddy diamictites.' The thin-bedded sandstones are moderately sorted, composed of medium- to fine-grained sand and are classified as a 'sandstone with dispersed clasts in Hambry and Glasser's (Fig 2-1) classification.' The sandstone beds are carpeted with asymmetric ripples showing a N/NE flow orientation of 020°. Semi-rounded cobbles of varying composition are dispersed throughout the deposits.

3.8.2 AMS and magnetic analysis

Five orientated cores were extracted from a sandstone bed (site S3) (Fig 3-23B), yielding a total of 12 specimens for AMS analysis, all of which passed the *F* test (Table A-21). Site S3 shows a strong, flow-aligned fabric that is triaxial and imbricated, dipping ~30° towards the SW suggesting flow towards the NE (Fig. 3-24).

Magnetic analyses from site S3 is included in Appendix B in detail Fig B-14. Hysteresis measurements show a loop characteristic of both para- and ferromagnetic contributions. Susceptibility vs. temperature measurements indicates low-field ferromagnetic contributions from most likely magnetite (580°C), and an additional phase occurring at 450°C upon cooling, indicating that the sample underwent alteration during heating. Hysteresis parameters suggest the ferromagnetic grain size for the fabric falls within PSD range. X_{hf} to X_0 ratio is 2:1, suggesting roughly even para- and ferro-magnetic contributions. All of the above suggests that the AMS is controlled by shape anisotropy, resulting in a normal fabric.

3.8.3 Location discussion

Field observations suggest these diamictite and sandstone deposits are couplets, most likely the result of subaqueous 'concentrated density flows' indicated by the horizontal stacked facies. (Postma et al., 1988; Shanmugam, 1996; Mulder and Alexander, 2001). Couplets can be broadly defined as genetically related and occurring in a repeating series. As previously discussed, often subaqueous sediment gravity flows will have a two-component system: a lower, dense laminar debris flow, and an upper, turbidity current. The turbidity current develops as the result of friction on the top of the debris flow by fluid drag; sediment is stripped from the high-density flow generating a co-genetic turbidity current.

The stratified clast-rich muddy diamictite represents the lower laminar flow, while the moderately sorted, rippled sandstone with dispersed clasts represents the upper quasi-steady turbulent current (Mulder and Alexander, 2001). While the clay-rich diamictites were too water saturated to sample with means of a drill, the sandstone unit reveled a strong, flow-aligned fabric that is imbricated with a flow direction to the NE. The inferred flow direction from AMS supports the observed in-field flow directions from asymmetric ripples.

Fig 3-22. (A) *Interbedded diamictites and sandstones at São Gabriel creek exposure in the state of Rio Grande do Sul, Yellow box indicates location of* ***(B)*** *sandstone unit (site S3).*

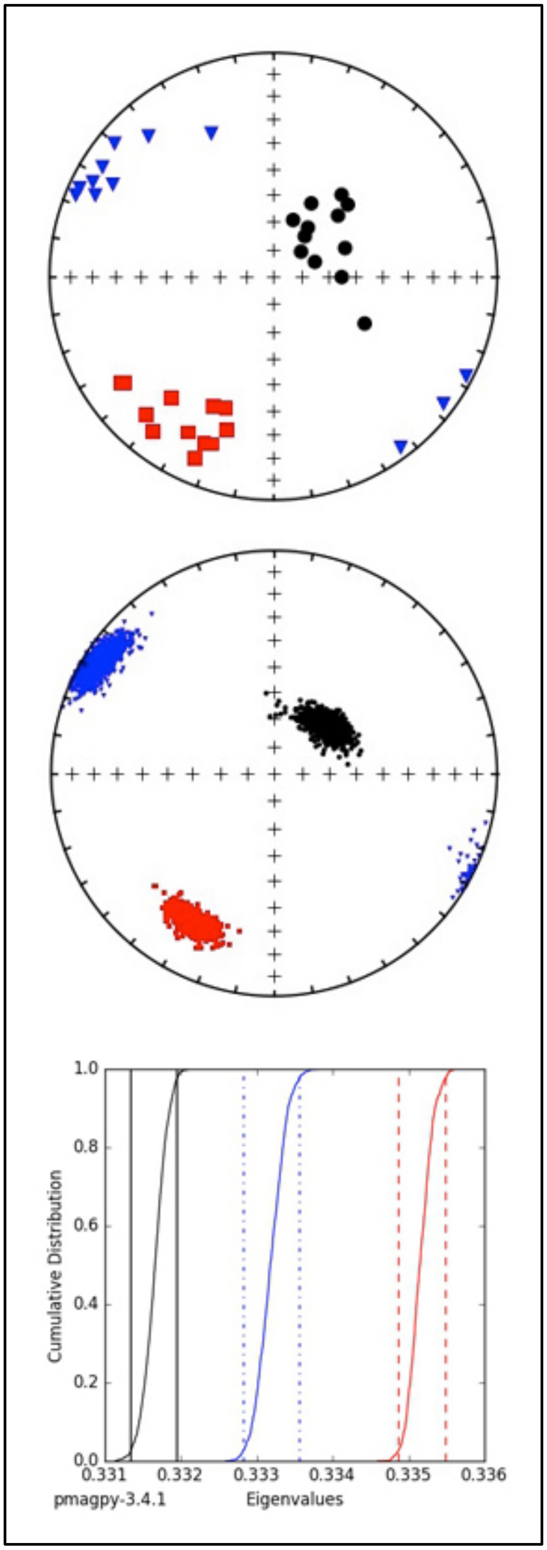

Fig 3-23. *Measured eigenvectors for each specimen (top), bootstrapped eigenvectors (center), and bootstrapped eigenvalue cumulative distribution graph (bottom) for site S3 (sandstone bed) at the São Gabriel creek exposure. Maximum eigenvector indicated by red squares, intermediate by blue triangles, and minimum by black circles.*

CHAPTER 4. DISCUSSION OF AMS IN RELATION TO FACIES

This study focuses on the collection and interpretation of magnetic fabrics from glaciogenic deposits of the Itararé Group that outcrop along the southern and eastern margins of the Paraná Basin in order to better differentiate subglacial processes from subaqueous mass transport, proglacial glaciomarine/glaciolacustrine rainout, and/or ice rafting, in addition to determining glacier flow or mass transport directions.

While in some cases (e.g., Campo do Tenente) AMS analyses allowed us to clearly delineate between the origins of diamictites (horizontal fabrics resulting from rainout vs flow - aligned, -oblique fabrics resulting from mass transport), in other cases (e.g., Alfredo Wagner) differentiating between flow-aligned fabrics resulting from mass transport and subglacial processes proved difficult without the aid of secondary structures (e.g., striated, gouged, and scoured surface indicating subglacial erosion). Presumably one should be able to differentiate between an MTD and subglacial traction till if a flow –transverse, -oblique fabric is observed (cf. Hooyer et al., 2008).

At two locations (Alfredo Wagner and Campo do Tenente) sample sets collected from stratified and massive diamictites (sites R7 and C3 respectively) interpreted to be the result of subaqueous mass transport showed flow-oblique fabrics (indicated by the 95% confidence interval), where the mean $\boldsymbol{k}_1$ and $\boldsymbol{k}_2$ eigenvectors were oriented ~45° from the direction in which the mean $\boldsymbol{k}_3$ eigenvector is deflected from the vertical. As previously discussed, the depositional kinematics of flow-oblique fabrics have not been thoroughly explored in literature, but have been attributed to clast interactions in a viscous flow, spatial changes in current direction, changes in flow regime, changes in substrate roughness, and soft sediment deformation (Baas et al., 2007).

Both of these clast-poor diamictites were classified as 'debris flows' based on the their high concentrations of cohesive material (mud) (cf. Mulder and Alexander, 2001). As a result of cohesive strength, debris flows exhibit a pseudoplastic rheology (non-Newtonian) and behave very different from all other types of subaqueous sedimentary density flows (Mulder and Alexander, 2001). Jeffery's (1922) theory of the motion of ellipsoidal particles immersed in a viscous (non-Newtonian) fluid states that particles will spend most of their time with their long axis parallel to flow, resulting in a statistically flow-aligned fabric when the flow comes to rest, as observed in other diamictites classified as debris flows based on their high concentrations of mud (site Q1 at Aurora and site T5 at Campo do Tenente). Rees (1983) experimentally demonstrated that flow–transverse (and flow-oblique) fabrics could develop in similar viscous flows (non-Newtonian) as a result of clast interactions between varying percentages of clasts and grains in suspension.

At two localities (Aurora and Campo Do Tenente), massive diamictites (site Q1 and sites C3/T5 respectively) were interpreted to be the result of subaqueous debris flows and slumping based on the large-scale cohesive concentration of mud, brecciation and homogenization of sandstone bodies, and other slump like deformational features. As a slump is a coherent mass of loosely consolidated material, which moves a short distance down a slope, some fabrics in these types of deposits could be inherited (i.e., fabric related to the deposit prior to failure) as opposed to a debris flow where the primary fabric is erased during the resedimentation of material thru a laminar flow moving downslope. In slumps we would expect to see internal deformation as a result of compressional strain, in debris flows lack thereof. If internal deformation becomes pervasive, a secondary fabric develops as a result of the deformation. This can be seen in the deformed sandstone bed at Ibaré (site E1). This facies was interpreted to be proglacial outwash reworked by sublglacial shove (compressional strain), and showed a type IV fabric (Robion et al., 2007) where $\boldsymbol{k}_1$ and $\boldsymbol{k}_3$ axes were parallel to the bedding plane at right angles. As compressional strain increases, you will see the gradual shift of $\boldsymbol{k}_1$ axes move from a near horizontal bedding plane toward a vertical position, while simultaneously $\boldsymbol{k}_3$ axes move from a vertical position towards a near horizontal (Robion et al., 2007). As mass transport processes can be complex, evolving from one form to another (i.e., debris flows are the result of flow transformation as sediment within slides, then slumps, begin to dissagregate into fluidizes flows), the above methodology may not always prove correct, but may assist in the interpretation of such deposits.

In almost all cases, AMS analyses were beneficial in determining the direction of sediment transport when $\boldsymbol{k}_3$ eigenvectors were deflected from the vertical. In outcrops where sedimentary flow structures were present, AMS results consistently agreed with the inferred flow direction (Alfredo Wagner, Cachoeira do Sul, and São Gabriel). In outcrops where flow structures were absent, AMS provided useful insight to paleoslope (i.e., Campo do Tenente and Porto Amazonas).

Lastly, the sample sets collected at Porto Amazonas from the vertical succession contained within a single, massive, structureless sandstone bed interpreted to be the result of a hyperconcentrated density flow (grain flow), demonstrates how a depositional fabric can change upward within a deposit due to changing flow rheology and dynamics but still indicate a uniform flow direction. The weakly developed fabric found at the base of the bed, is most likely the result of high viscosity due to high near-bed sediment concentrations combined with frequent clast collisions during rapid settling from suspension (Hiscott and Middleton, 1980; Rees, 1983; Baas et al., 2007). The triaxial fabric found in the middle of the bed could be the result of grains rapidly freezing as the energy in the flow dissipates and the grains settle out all at once. The streaked distribution of $\boldsymbol{k}_3$ towards the top of the bed indicates the rolling of grains (long axes perpendicular to flow) during the final stages of transport (Tauxe, 1998). Despite the difference between the three fabrics, they all show a uniform flow direction trending SW/NE. As both up-current and down-current grain imbrication has been observed in similar deposits associated with Bauma's T_a divisions, further petrofabric analysis is required to correctly interpret the direction of sediment transport. It should be noted that the only flow-transverse fabrics observed within this study were from these 'hyperconcentrated density flow (grain flow)' deposits classified using the nomenclature of Mulder and Alexander (2001) also referred to as 'high–density turbidity deposits' (Lowe, 1982) and 'sandy debris flow deposits' (Shanmugam ,1996). It is inferred that hyperconcentrated density flows differ from debris flows as a result of either lesser proportions of cohesive grains (mud) or cohesion is overcome as an effect of increased shear rate by high flow velocities (Mulder and Alexander, 2001).

In summary, results from this study were consistent with past studies, which used AMS to characterize a variety of glaciogenic deposits including subglacial and subaqueous diamictites. Fabrics collected from diamictites in a proglacial, subaqueous environment as a result of rainout deposition (meltwater plumes and ice rafted debris) showed a horizontal fabric. Fabrics collected from diamictites in subaqueous environments as a result of mass transport showed both flow-aligned and flow-transverse fabrics but resulting from different types of density flows (Newtonian vs non-Newtonian). Flow-oblique fabrics were additionally observed in mass transport deposits, but only in debris flows (non-Newtonian). Fabrics collected from diamictites in a subglacial environment, as a result of traction tills or grooved/ploughed surfaces showed a flow–aligned fabric strongly related to the direction of ice paleo-flow.

This study is important as it characterized a variety of glaciogenic deposits (diamictites and sandstones) of the Itararé Group in the Paraná Basin, unlike previous studies, which only focused on diamictites as a result of subaqueous debris flows (Gravenor and von Brunn, 1987; Archanjo et al., 2006). This study demonstrates and enforces that AMS can be a very useful tool to more accurately reconstruct and interpret deposits and environments not only of the LPIA, but other glaciated and mass movment related environments across time.

CHAPTER 5. SUMMARY AND DISCUSSION IN RELATION TO PAST STUDIES

This study collected samples for AMS analysis from two different regions within the Paraná Basin: three localities near the southern margin in the state of Rio Grande do Sul, and four localities along the eastern margin in the states of Santa Catarina and Paraná (Fig 5-1). Flow directions from localities along the southern margin (all correlated to the top of the Itararé Group) are uniform showing NW/NNW/NE flow directions (Fig 5-2) that are consistent with the N ice paleoflow indicators reported by Tomazelli and Soliani (1982) and Rosa et al. (2016). Flow directions from the eastern margin of the basin (correlated to the Rio do Sul Formation) in the area of Alfredo Wagner and Aurora are also uniform showing NNW/NW/W flow directions (Fig 5-1) and are also consistent with the inferred N/NW ice movement into the basin (Rosa et al., 2016). Flow directions obtained from mass transport deposits along the eastern margin of the basin (correlated to the Campo do Tenente Formation) in the area of Porto Amazonas and Campo do Tenente are also somewhat uniform, but showing flow directions to the SW/SE/E (Fig 5-1). These are not consistent with the inferred N/NW ice movement into the basin (Gesicki et al., 2002; Rosa et al., 2016), nor consistent with NW paleocurrents from cross-stratified sandstones reported by Vesely et al. (2015) and prograding, fluvial deltaic deposits reported by Carvalho and Vesely (2017) from nearby deposits and exposures. This might be explained as a result of meltwater input from an ice-margin to the SE combined with gravity flows deflecting to the SW because of tectonic subsidence or isostatic loading. It could also be due to the different scale of the geomorphic element producing paleoslope (e.g., ice lobes would result in a larger scale paleoslope that a smaller prograding delta front).

Gravenor and von Brunn (1987) described a glacial-marine succession at the Lapa quarry almost identical to the succession described ~30 km south at the Campo do Tenente quarry (both inferred to be part of the Campo do Tenente Formation). At the base of the succession, massive diamictite with sandstone bodies, interpreted to be the result of debris flows, are overlain by rhythmites, stratified diamictite, and shales with graded intervals of lonestones and till pellets interpreted to be the result of rain-out. Gravenor and von Brunn (1987) collected one sample set from the massive diamictite for AMS analysis and their results show a flow-aligned fabric to the SW. The direction of sediment transport obtained from AMS was consistent with their in-field observation of material flowing to the south based on the orientation of fold axes from deformed sandstones. Our SW/SE paleoflow directions of massive diamictites in the Campo do Tenente quarry obtained from AMS supports the work of Gravenor and von Brunn (1987) and strongly suggests that the regional topography between Lapa and Campo do Tenente during the early Pennsylvanian shows a paleoslope to the south.

Archanjo et al. (2006) conducted a magnetic fabric analysis on massive diamictites interpreted to be the result of subaqueous debris flows in the region between Mafra and Alredo Wagner, correlated to the Rio do Sul Formation. Their study supports the existence of a NW/SE trending, intrabasinal depression referred to as the Rio do Sul sub-basin (Santos, 1987; Canuto, 1993; Santo et al., 1996). This elongated depression, which extened from the southern region of Alfredo Wagner to just north of Mafra, is inferred from an isopach map (Fig 5-1) of the Rio do Sul Formation (Canuto, 1993). While Archanjo et al. (2006) found both flow-aligned and flow-transverse fabrics within these types of deposits that were similar to our study, his paleoflow directions in the Alfredo Wagner region are to the SE, inconsistent with the W/NNW paleoflow direction we obtained from AMS in Alfredo Wagner (Site R7) and Aurora (Site Q1) (all of which are correlated to the Rio du Sol Fm). Archanjo et al. (2006) also found many flow directions towards the SE in the region N/NW of Rio do Sul near Mafra (Fig-5-1), in the proximity of Campo do Tenente, Lapa and Porto Amazonas. While the time frame of deposition between the Campo do Tenente Formation and Rio do Sul Formations could span up to ~35 Ma years, flow directions from mass transport in the region stretching from Mafra to Porto Amazonas appear to be consistent between all studies, suggesting a southward paleoslope may have strongly influenced subaqueous deposition throughout the duration of the Itararé Group. The Rio do Sul sub-basin is traditionally considered as representative of the upper Itararé (Rio do Sul Fm.). This suggests that the sub-basin was possibly active earlier than previously reported or that multiple subsidence events may have been superimposed on top of each other (e.g., multiple loading events during glacial advance and retreat cyles).

Table 5-1. *Summary of flow directions obtained from AMS analyses. Paleoflow column includes AMS inferred cardinal direction of sediment and (sedimentary structure flow indicator).*

Location	**Site**	**Inferred Mode of Deposition**	**Paleoflow**	**Depositional Fabric**
Alfredo Wagner	(B8) Massive diamictite	Subglacial (traction till)	NW (327°)	Flow-aligned
Alfredo Wagner	(R7) Stratified diamictite	Mass transport (cohesive mudflow)	W	Flow-oblique
Aurora	(Q1) Massive diamictite	Mass transport (cohesive debris flow)	NNW	Flow-aligned
Cachoeira do Sul	(P5) Ploughed surface	Subglacial (grooved surface)	NNW (358°)	Flow-aligned
Cachoeira do Sul	(P7) River cut	Subglacial (grooved surface)	NNW (358°)	Flow-aligned
Cachoeira do Sul	(P9) Road cut	Subglacial (grooved surface)	NNW (358°)	Flow-aligned
Campo do Tenente	(C3) Massive diamictite below slide block	Mass transport (cohesive debris flow)	SW	Flow-oblique
Campo do Tenente	(T5) Massive diamictite above slide block	Mass transport (cohesive debris flow)	SE	Flow-aligned
Campo do Tenente	(D4) Sandstone body	Mass transport (slide block)	SE	Flow-aligned (Inherited fabric)
Campo do Tenente	(D5) Rippled siltstone	Mass transport (surge like tubidity flow) or reworked proglacial rainout	E	Flow-aligned
Campo do Tenente	(D3) Stratified diamictite w/ mud lamination	Proglacial rainout	-	(unclear)
Campo do Tenente	(C5) Stratified diamictite w/o mud lamination	Proglacial rainout	-	Horizontal
Campo do Tenente	(FE1) Diamictite	Mass transport (concentrated density flow)	-	(unclear)
Ibaré	(E1) Fine sandstone	Proglacial outwash	-	Deformational fabric
Ibaré	(E2) Coarse sandstone	Proglacial outwash	NW	Flow-aligned
Porto Amazonas	(O5) Massive structureless sandstone (bottom of unit)	Mass transport (hyperconcentrated density flow aka grain flow)	SW/NE	Flow-transverse
Porto Amazonas	(M6) Massive structureless sandstone (middle of unit)	Mass transport (hyperconcentrated density flow aka grain flow)	SW/NE	Flow-transverse
Porto Amazonas	(H7) Massive structureless sandstone (top of unit)	Mass transport (hyperconcentrated density flow aka grain flow)	SW/NE	Flow-transverse
São Gabriel	(S3) Sandstone couplet	Mass transport (concentrated density flow)	NE (020°)	Flow-aligned

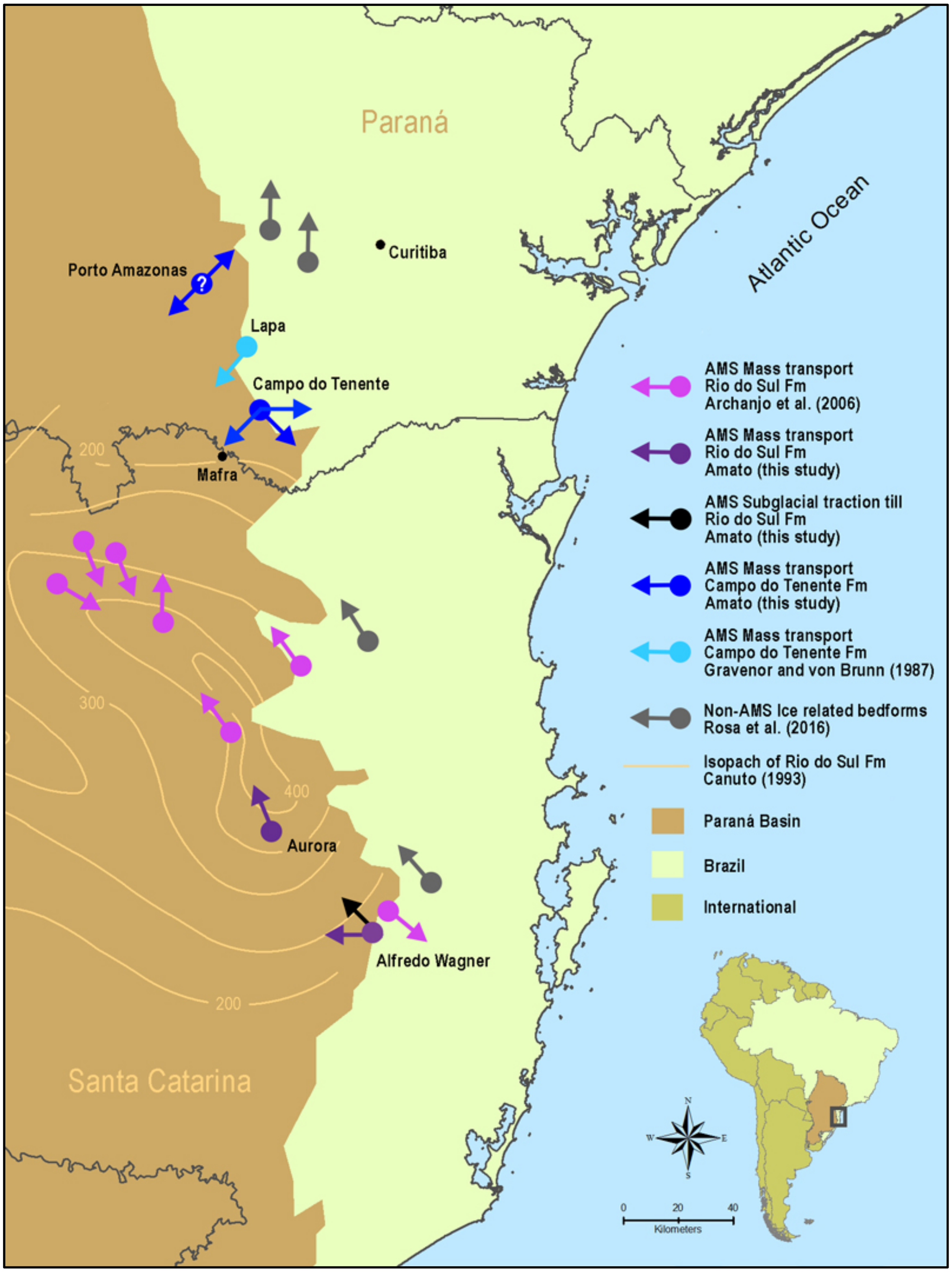

Fig 5-1. *Summary of flow directions obtained from AMS analyses along the eastern margin of the Paraná Basin pertaining to this study in addition to the studies of Gravenor and von Brunn (1987) and Archanjo et al. (2006), in relation to ice related features (non-AMS related) of Rosa et. al (2016) and Rio do Sul isopach of Canuto (1993). Purple shades denotes site localities correlated to the Rio do Sul Formation, blue shades denotes site localities correlated to the Campo do Tenente Formation.*

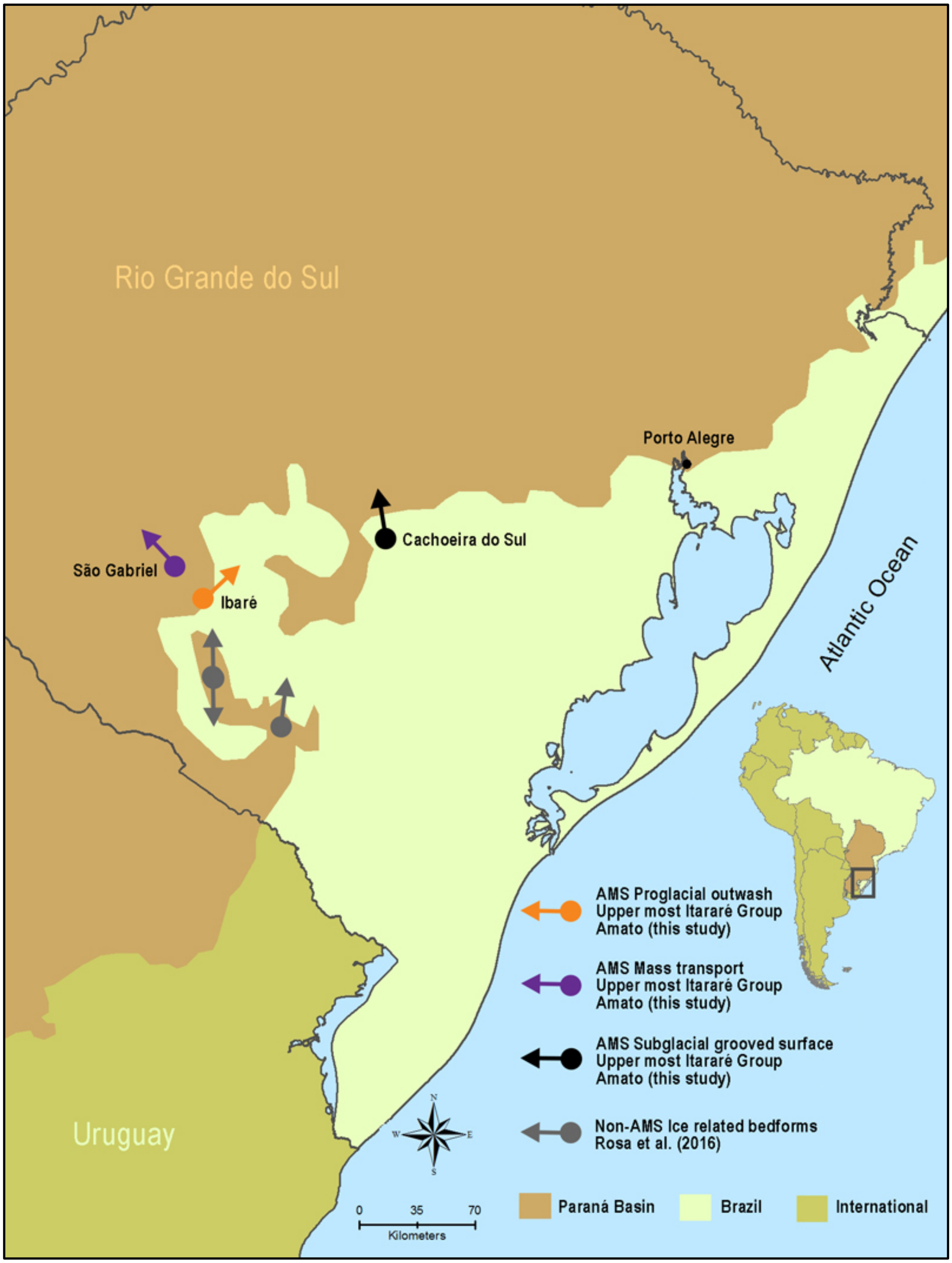

Fig 5-2. *Summary of flow directions obtained from AMS analyses along the southern margin of the Paraná Basin pertaining to this study in relation to ice related features (non-AMS related) of Rosa et. al (2016). All site localities correlated to the upper most Itararé Group.*

CHAPTER 6. CONCLUSION

This study focused on collecting and interpreting magnetic fabrics from glaciogenic deposits of the Itararé Group that outcrop along the south and east margins of the Paraná Basin in order to better interpret depositional processes of the LPIA and determine the direction of sediment transport. While in some cases, AMS analyses allowed us to delineate between the origins of the various diamictites (rainout from mass transport/subglacial), in other cases, differentiating between flow-aligned fabrics resulting from mass transport and subglacial processes proved difficult. In most cases, AMS measurements were beneficial in determining the direction of sediment transport. In outcrops where sedimentary flow structures were present, AMS results consistently agreed with the inferred flow direction. In outcrops where flow structures were absent, AMS provided useful insight to paleoslope. While flow directions along the southern margin of the basin are consistent with the inferred N/NW ice movement into the basin, some of the flow directions along the eastern margin are not, suggesting the existence of a southward paleoslope in the area stretching from Campo do Tenente to Porto Amazonas. While this observation is inconsistent with other studies in which cross-stratified sandstones nearby (stratigraphically equivalent) showed northward paleocurrent orientations, it is consistent with other AMS study of similar like deposits in the area (varying stratigraphically). This might be explained as a result of meltwater input from an ice-margin to the SE combined with gravity flows deflecting to the SW because of tectonic subsidence or isostatic loading, or due to the different scale of the geomorphic element producing paleoslope.

REFERENCES

AGICO, 2009, MKF1-FA/CS4/CSL, MFK1-A/CS4/CSL, MFK1-FB, MFK1-B, User's Guide, Advanced Geoscience Instruments Co.

-, 2011a, SAFYR4W MFK1 Kappabridge Control Software for Windows: User Manual, Volume Version 4.0.3.

-, 2011b, MFK1 Thermomagnetic Curve Control Software for Windows: User Manual, Volume Version 5.0.0.

Allen, J. R. L., 1982, Sedimentary structures, their character and physical basis; I, Elsevier Sci. Publ. Co., Amsterdam, 611 p.:

Archanjo, C. J., Silva, M. G., Castro, J. C., Launeau, P., Trindade, R. I. F., and Macedo, J. W. P., 2006, AMS and grain shape fabric of the late Palaeozoic diamictites of the southeastern Parana Basin, Brazil: Journal of the Geological Society of London, v. 163, no. 1, p. 95-106.

Baas, J. H., Hailwood, E. A., McCaffrey, W. D., Kay, M., and Jones, R., 2007, Directional petrological characterisation of deep-marine sandstones using grain fabric and permeability anisotropy; methodologies, theory, application and suggestions for integration: Earth-Science Reviews, v. 82, no. 1-2, p. 101-142.

Balsley, J. R., Jr., and Buddington, A. F., 1960, Magnetic susceptibility anisotropy and fabric of some Adirondack granites and orthogneisses [New York]: American Journal of Science, v. 258-A, p. 6-20.

Benn, D. I., and Evans, D. J. A., 2010, Glaciers and Glaciation, London, U.K., Arnold, 802 p.:

Bingham, C., 1974, An antipodally symmetric distribution on the sphere: The Annals of Statistics, v. 2, p. 1201–1225.

Blakey, R. C., 2008, Gondwana paleogeography from assembly to breakup--A 500 m.y. odyssey, in Fielding, C. R., Frank, T. D., and Isbell, J. L., eds., Resolving the Late Paleozoic Ice Age in Time and Space:: Boulder, CO, Geological Society of America Special Publication., p. 1-28.

Boggs, S., Jr., 1987, Principles of sedimentology and stratigraphy, Merrill Publ. Co., Columbus, OH, 784 p.:

Boulton, G. S., 1972, Modern Arctic glaciers as depositional models for former ice sheets: Journal of the Geological Society of London, v. 128, no. 4, p. 361-393.

Bouma, A. H., 1962, Sedimentology of some Flysch deposits; a graphic approach to facies interpretation, 168 p.:

Buggisch, W., Wang, X., Alekseev, A. S., and Joachimski, M. M., 2011, Carboniferous-Permian carbon isotope stratigraphy of successions from China (Yangtze platform), USA (Kansas) and Russia (Moscow Basin and Urals): Palaeogeography, Palaeoclimatology, Palaeoecology, v. 301, no. 1-4, p. 18-38.

Butler, R. F., 1992, Paleomagnetism; magnetic domains to geologic terranes, Blackwell Sci. Publ., Boston, MA, 319 p.:

Cagliari, J., Philipp, R. P., Buso, V. V., Netto, R. G., Klaus Hillebrand, P., da Cunha Lopes, R., Stipp Basei, M. A., and Faccini, U. F., 2016, Age constraints of the glaciation in the Parana Basin; evidence from new U-Pb dates: Journal of the Geological Society of London, v. 173, no. 6, p. 871-874.

Canuto, J. R., 1993, Facies e ambientes de sedimentação da formação Rio do Sul (Permiano), Bacia do Paraná, na região de Rio do Sul, Estado de Santa Catarina [Ph.D. Doctoral]: Universidade de São Paulo.

Canuto, J.R., Santos, P.R., Rocha-Campos, A.C., 2001. Estratigrafiade seqüências do Subgrupo Itararé (Neopaleozóico) no leste da Bacia do Paraná, nas regiões sul do Paraná e norte de Santa Catarina, Brasil. Rev. Bras. Geosci. 31, p. 107–116.

Caputo, M. V., and Crowell, J. C., 1985, Migration of glacial centers across Gondwana during Paleozoic Era: Geological Society of America Bulletin, v. 96, p. 1020-1036.

Carvalho, A. H., and Vesely, F. F., 2017, Facies relationships recorded in a late Paleozoic fluvio-deltaic system (Parana Basin, Brazil); insights into the timing and triggers of subaqueous sediment gravity flows: Sedimentary Geology, v. 352, p. 45-62.

Crowell, J. C., 1999, Pre-Mesozoic ice ages: their bearing on understanding the climate system: Geological Society of America Memoir, v. 192, p. 1-106.

Crowell, J. C., and Frakes, L. A., 1970, Ancient Gondwana glaciations, in Haughton, S. H., ed., Proceedings and Papers of the Second Gondwana Symposium, South Africa: Pretoria, CSIR, p. 469-476.

Dickins, J. M., 1997, Some problems of the Permian (Asselian) glaciation and the subsequent climate in the Permian, in Martini, I. P., ed., Late glacial and postglacial environmental changes: Quaternary, Carboniferous-Permian, and Proterozoic: Oxford, U.K., Oxford University Press, p. 243-245.

Day, R., M. Fuller, and V.A. Schmidt (1977), Hysteresis properties of titanomagnetites: Grain-size and compositional dependence, Physics of the Earth and Planetary Interiors, 13, 260-267.

Dowdeswell, J. A., Whittington, R. J., Jennings, A. E., Andrews, J. T., Mackensen, A., and Marienfeld, P., 2000, An origin for laminated glacimarine sediments through sea-ice build-up and suppressed iceberg rafting: Sedimentology, v. 47, no. 557-576.

Dunlop, D. J., 2002, Theory and application of the Day plot M_{rs}/M_s versus H_{cr}/H_c; 1, Theoretical curves and tests using titanomagnetite data: Journal of Geophysical Research, v. 107, no. B3, p. 22.

Dunlop, D. J., and Ozdemir, O., 1997, Rock magnetism; fundamentals and frontiers: Cambridge Studies in Magnetism, v. 3, 573 p.:

Ellwood, B. B., 1980, Application of the anisotropy of magnetic susceptibility method as an indicator of bottom-water flow direction: Marine Geology, v. 34, no. 3-4, p. M83-M90.

Enos, P., 1977, Flow regimes in debris flow: Sedimentology, v. 24, no. 1, p. 133-142.

Evans, D. J. A., Phillips, E. R., Hiemstra, J. F., and Auton, C. A., 2006, Subglacial till: Formation, sedimentary characteristics and classification: Earth-Science Reviews, v. 78, no. 1–2, p. 115-176.

Eyles, C. H., Eyles, N., and França, A. B., 1993, Glaciation and tectonics in an active intracratonic basin: the late Palaeozoic Itararé Group, Paraná Basin, Brazil: Sedimentology, v. 40, p. 1-25.

Eyles, N., Day, T. E., and Gavican, A., 1987, Depositional controls on the magnetic characteristics of lodgement tills and other glacial diamict facies: Canadian Journal of Earth Sciences = Revue Canadienne des Sciences de la Terre, v. 24, no. 12, p. 2436-2458.

Fallgatter, C., and Paim, P. S. G., 2017, On the origin of the Itararé Group basal nonconformity and its implications for the Late Paleozoic glaciation in the Paraná Basin, Brazil: Palaeogeography, Palaeoclimatology, Palaeoecology.

Felletti, F., Dall'Olio, E., and Muttoni, G., 2016, Determining flow directions in turbidites; an integrated sedimentological and magnetic fabric study of the Miocene Marnoso Arenacea Formation (Northern Apennines, Italy): Sedimentary Geology, v. 335, p. 197-215.

Fielding, C. R., Frank, T. D., Birgenheier, L. P., Rygel, M. C., Jones, A. T., and Roberts, J., 2008a, Stratigraphic imprint of the late Palaeozoic ice age in eastern Australia: a record of alternating glacial and nonglacial climate regime: Journal of the Geological Society, London, v. 165, p. 129-140.

Fielding, C. R., Frank, T. D., Birgenheier, L. P., Rygel, M. C., Jones, A. T., and Roberts, J., 2008d, Stratigraphic record and facies associations of the late Paleozoic ice age in eastern Australia (New South Wales and Queensland), in Fielding, C. R., Frank, T., and Isbell, J.

L., eds., Resolving the Late Paleozoic Ice Age in Time and Space: Boulder, Geological Society of America Special Paper 441, p. 41-57.

Fielding, C. R., Frank, T. D., and Isbell, J. L., 2008b, The late Paleozoic ice age--A review of current understanding and synthesis of global climate patterns, in Fielding, C. R., Frank, T. D., and Isbell, J. L., eds., Resolving the Late Paleozoic Ice Age in Time and Space: Boulder, CO, Geological Society of America Special Publication, p. 343-354.

Fielding, C. R., Frank, T. D., IsbeLL, J. L., and (Editors), 2008c, Resolving the Late Paleozoic Ice Age in Time and Space, Boulder, CO, Geological Society of America Special Publication 441, 354 p.:

Fisher, R. A., 1953, Dispersion on a sphere: Proceedings of the Royal Society of London, v. A217, p. 295–305.

Flint, R. F., Sanders, J. E., and Rodgers, J., 1960, Symmictite--A name for nonsorted terrigenous sedimentary rocks that contain a wide range of particle sizes: Bulletin of the Geological Society of America, v. 71, no. 4, p. 507-509.

Frakes, L. A., and Crowell, J. C., 1969, Late Paleozoic glaciation: I, South America: Geological Society of America Bulletin, v. 80, p. 1007-1042.

Frakes, L. A., and Francis, J. E., 1988, A guide to Phanerozoic cold polar climates from high-latitude ice-rafting in the Cretaceous: Nature, v. 333, p. 547-549.

Frakes, L. A., Francis, J. E., and Syktus, J. I., 1992, Climate modes of the Phanerozoic, Cambridge, Cambridge University Press, 274 p.:

Franca, A. B., and Potter, P. E., 1988, Estratigrafia, ambiente deposicional e analise de reservatorio do Grupo Itarare (Permocarbonifero), Bacia do Parana (Parte 1): Boletim de Geociencias da PETROBRAS, v. 2, no. 2-4, p. 147-191.

França, A. B., and Potter, P. E., 1991, Stratigraphy and reservoir potential of glacial deposits of the Itarare Group (Carboniferous-Permian), Parana Basin, Brazil: AAPG Bulletin, v. 75, no. 1, p. 62-85.

Fuller, M. D., 1962, A magnetic fabric in till: Geological Magazine, v. 99, no. 3, p. 233-237.

Gastaldo, R. A., DiMichele, W. A., and Pfefferkorn, H. W., 1996, Out of the icehouse into the greenhouse; a late Paleozoic analog for modern global vegetational change: GSA Today, v. 6, no. 10, p. 1-7.

Gee, J. S., Tauxe, L., and Constable, C., 2008, AMSSpin; a LabVIEW program for measuring the anisotropy of magnetic susceptibility with the Kappabridge KLY-4S: Geochemistry, Geophysics, Geosystems - G3, v. 9, no. 8, p. Citation Q08Y02.

Goldberg, K., and Humayun, M., 2010, The applicability of the Chemical Index of Alteration as a paleoclimatic indicator: An example from the Permian of the Parana Basin, Brazil: Palaeogeography, Palaeoclimatology, Palaeoecology, v. 293, no. 1-2, p. 175-183.

González, C. R., and Saravia, P. R., 2010, Bimodal character of the Late Paleozoic glaciations in Argentina and bipolarity of climatic changes: Palaeogeography, Palaeoclimatology, Palaeoecology, v. 298, no. 1-2, p. 101-111.

Gravenor, C. P., 1985, Magnetic and pebble fabrics of glaciomarine diamictons in the Champlain Sea, Ontario, Canada: Canadian Journal of Earth Sciences = Revue Canadienne des Sciences de la Terre, v. 22, no. 3, p. 422-434.

-, 1986, Magnetic and pebble fabrics in subaquatic debris-flow deposits: Journal of Geology, v. 94, no. 5, p. 683-698.

Gravenor, C. P., and Rocha-Campos, A. C., 1983, Patterns of late Paleozoic glacial sedimentation on the southeast side of the Paraná Basin, Brazil: Palaeogeography, Palaeoclimatology, Palaeoecology, v. 43, no. 1-2, p. 1-39.

Gravenor, C. P., Stupavsky, M., and Symons, D. T. A., 1973, Paleomagnetism and its Relationship to Till Deposition: Canadian Journal of Earth Sciences = Revue Canadienne des Sciences de la Terre, v. 10, no. 7, p. 1068-1078.

Gravenor, C. P., and von Brunn, V., 1987, Aspects of late Paleozoic glacial sedimentation in parts of the Paraná Basin, Brazil, and the Karoo Basin, South Africa, with special reference to th origin of massive diamictite, in McKenzie, G. D., ed., Gondwana Six: stratigraphy, sedimentology, and paleontology, Volume Geophysical Monograph 41: Washington, D.C., American Geophysical Union, p. 103-111.

Gulbranson, E. L., Montanez, I. P., Schmitz, M. D., Limarino, C. O., Isbell, J. L., Marenssi, S. A., and Crowley, J. L., 2010, High-precision U-Pb calibration of Carboniferous glaciation and climate history, Paganzo Group, NW Argentina: Geological Society of America Bulletin, v. 122, no. 9-10, p. 1480-1498.

Hailwood, E., and Ding, F., 2000, Sediment transport and dispersal pathways in the Lower Cretaceous sands of the Britannia Field, derived from magnetic anisotropy: Petroleum Geoscience, v. 6, no. 4, p. 369-379.

Hambrey, M. J., and Glasser, N. F., 2003, Glacial sediments; processes, environments and facies, in Middleton, G. V., eds., Encyclopedia of Sediments and Sedimentary Rocks. Kluwer Academic Publishers, Dordrecht., p. 316-331.

-, 2012, Discriminating glacier thermal and dynamic regimes in the sedimentary record: Sedimentary Geology, v. 251-252, p. 1-33.

Hamilton, N., and Rees, A. I., 1970, The use of magnetic fabric in palaeocurrent estimation, in Runcorn, S.K., eds., Palaeogeophysics: London and New York, Acad. Press., p. 445-464.

Hext, G. R., 1963, The Estimation of Second-Order Tensors, with Related Tests and Designs: Biometrika, v. 50, p. 353-373.

Hiscott, R. N., and Middleton, G. V., 1980, Fabric of coarse deep-water sandstones, Tourelle Formation, Quebec, Canada: Journal of Sedimentary Petrology, v. 50, no. 3, p. 703-721.

Holz, M., Souza, P. A., and Iannuzzi, R., 2008, Sequence stratigraphy and biostratigraphy of the Late Carboniferous to Early Permian glacial succession (Itararé subgroup) at the eastern-southeastern margin of the Paraná Basin, Brazil, in Fielding, C. R., Frank, T., and Isbell, J. L., eds., Resolving the Late Paleozoic Ice Age in Time and Space: Boulder, Geological Society of America Special Paper 441, p. 115-129.

Hooyer, T. S., Iverson, N. R., Lagroix, F., and Thomason, J. F., 2008, Magnetic fabric of sheared till; a strain indicator for evaluating the bed deformation model of glacier flow: Journal of Geophysical Research, v. 113, no. F2, p. Citation F02002.

Hrouda, F., 2007, Magnetic Susceptibility, Anisotropy, in Gubbins, D., and Herrero-Bervaer, E., eds., Encyclopedia of Geomagnetism and Paleomagnetism: Dordrecht, The Netherlands, Springer., p. 546-560.

Hughes, S. R., Alexander, J., and Druitt, T. H., 1995, Anisotropic grain fabric; volcanic and laboratory analogues for turbidites: Geological Society Special Publications, v. 94, p. 51-62.

Hyde, W. T., Crowley, T. J., Tarasov, L., and Peltier, W. R., 1999, The Pangean ice age; studies with a coupled climate-ice sheet model: Climate Dynamics, v. 15, no. 9, p. 619-629.

Isbell, J. L., Henry, L. C., Gulbranson, E. L., Limarino, C. O., Fraiser, M. L., Koch, Z. J., Ciccioli, P. L., and Dineen, A. A., 2012, Glacial paradoxes during the late Paleozoic ice age: Evaluating the equilibrium line altitude as a control on glaciation: Gondwana Research, v. 22, no. 1, p. 1-19.

Isbell, J. L., Lenaker, P. A., Askin, R. A., Miller, M. F., and Babcock, L. E., 2003, Reevaluation of the timing and extent of late Paleozoic glaciation in Gondwana: Role of the Transantarctic Mountains: Geology, v. 31, no. 11, p. 977-980.

Isbell, J. L., Miller, M. F., Wolfe, K. L., and Lenaker, P. A., 2003, Timing of late Paleozoic glaciation in Gondwana: was glaciation responsible for the development of northern hemisphere cyclothems?, in Chan, M. A., and Archer, A. W., eds., Extreme depositional environments: mega end members in geologic time, Volume 370: Boulder, Colorado, Geological Society of America Special Paper, p. 5-24.

Ising, G., 1942, Den varviga lerans magnetiska egenskaper: Geologiska Foreningens i Stockholm Forhandlingar, v. 64, no. 2, p. 126-142.

Iverson, N. R., Hooyer, T. S., Thomason, J. F., Graesch, M., and Shumway, J. R., 2008, The experimental basis for interpreting particle and magnetic fabrics of sheared till: Earth Surface Processes and Landforms, v. 33, no. 4, p. 627-645.

Jeffery, G. B., 1922, The motion of ellipsoidal particles immersed in a viscous fluid, Proc. R. Soc. London Ser. A, v. 102, p. 169 – 179.

Jelinek, V., 1977, The Statistical Theory of Measuring Anisotropy of Magnetic Susceptibility of Rocks and Its Application, Geofyzika.

-, 1995, Measuring Anisotropy of Magnetic Susceptibility on a Slowly Spinning Specimen - Basic Theory, in AGICO, ed., Print 10, p. 27.

Jenner, K. A., Piper, D. J. W., Campbell, D. C., and Mosher, D. C., 2007, Lithofacies and origin of late Quaternary mass transport deposits in submarine canyons, central Scotian Slope, Canada: Sedimentology, v. 54, no. 1, p. 19-38.

Kano, K., and Takeuchi, K., 1989, Origin of mudstone clasts in turbidites of the Miocene Ushikiri Formation, Shimane Peninsula, Southwest Japan: Sedimentary Geology, v. 62, no. 1, p. 79-87.

Kent, J. T., 1982, The Fisher-Bingham distribution on the sphere: Journal of the Royal Statistical Society: Series B, v. 44, p. 71–80.

Kilfeather, A. A., O'Cofaigh, C., Dowdeswell, J. A., Meer, J. J. M., and Evans, D. J. A., 2010, Micromorphological characteristics of glacimarine sediments: implications for distinguishing genetic processes of massive diamicts: Geo-Marine Letters, v. 30, no. 2, p. 77-97.

Krasa, D., and Fabian, K., 2007, Rock magnetism, hysteresis measurements, in Gubbins, D., and Herrero-Bervaer, E., eds., Encyclopedia of Geomagnetism and Paleomagnetism: Dordrecht, The Netherlands, Springer., p. 874-883.

Limarino, C. O., Césari, S. N., Spalletti, L. A., Taboada, A. C., Isbell, J. L., Geuna, S., and Gulbranson, E. L., 2014, A paleoclimatic review of southern South America during the late Paleozoic: A record from icehouse to extreme greenhouse conditions: Gondwana Research, v. 25, no. 4, p. 1396-1421.

Lindsey, D. A., 1972, Sedimentary petrology and paleocurrents of the Harebell Formation, Pinyon Conglomerate, and associated coarse clastic deposits, northwestern Wyoming: U. S. Geological Survey Professional Paper, p. B1-B68.

Locat, J., 2001, Instabilities along ocean margins; a geomorphological and geotechnical perspective: Marine and Petroleum Geology, v. 18, no. 4, p. 503-512.

Locat, J., and Lee, H. J., 2002, Submarine landslides: advances and challenges: Canadian Geotechnical Journal/Revue Canadienne de Geotechnique, v. 39, no. 1, p. 193-212.

López-Gamundí, O. R., 1997, Glacial-postglacial transition in the Late Paleozoic basins of southern South America, in Martini, I. P., ed., Late glacial and postglacial environmental changes: Quaternary, Carboniferous-Permian, and Proterozoic: Oxford, U.K., Oxford University Press, p. 147-168.

Lowe, D. R., 1982, Sediment gravity flows; II, Depositional models with special reference to the deposits of high-density turbidity currents: Journal of Sedimentary Petrology, v. 52, no. 1, p. 279-297.

Lowrie, W., 1989, Magnetic analysis of rock fabric, Geophysics: Boston, MA, Springer US, p. 698-706.

Masson, D. G., Arzola, R. G., Wynn, R. B., Hunt, J. E., and Weaver, P. P. E., 2011, Seismic triggering of landslides and turbidity currents offshore Portugal: Geochemistry, Geophysics, Geosystems - G3, v. 12, p. Citation Q12011.

Moncrieff, A. C. M., 1989, Classification of poorly-sorted sedimentary rocks: Sedimentary Geology, v. 65, no. 1-2, p. 191-194.

Montañez, I., Tabor, N. J., Niemeier, D., DiMichele, W. A., Frank, T., D., Fielding, C. R., Isbell, J. L., Birgenheier, L. P., and Rygel, M. C., 2007, CO2-forced climate and vegetation instability during late Paleozoic deglaciation: Science, v. 315, no. 5808, p. 87-91.

Montañez, I. P., and Poulsen, C. J., 2013, The late Paleozoic ice age: an evolving paradigm: Annual Review of Earth & Planetary Sciences, v. 41, no. 24, p. 1-28.

Moskowitz, B. M., 1991, Classes of Magnetic Minerals, Hitchhiker's Guide to Magnetism, Volume 2015, Institue of Rock Magnetism.

Moxiness, L. D., 2016, Sedimentology of the mid-carboniferous basal fill of the Olta paleovalley, Eastern Paganzo Basin, Argentina [M.S. Thesis]: University of Wisconsin-Milwaukee.

Mulder, T., and Alexander, J., 2001, The physical character of subaqueous sedimentary density flows and their deposits: Sedimentology, v. 48, no. 2, p. 269-299.

Mulder, T., and Syvitski, J. P. M., 1995, Turbidity currents generated at river mouths during exceptional discharges to the world oceans: Journal of Geology, v. 103, no. 3, p. 285-299.

Petrovsky, E., 2007, Susceptibility, in Gubbins, D., and Herrero-Bervaer, E., eds., Encyclopedia of Geomagnetism and Paleomagnetism: Dordrecht, The Netherlands, Springer., p. 931-937.

Petrovsky, E., Kapicka, A., Jackson, M. J., Williams, W., and Smirnov, A., 2006, On determination of the Curie point from thermomagnetic curves: Journal of Geophysical Research, v. 111, no. B12, p. B12S27.

Pettijohn, F. J., 1975, Sedimentary rocks, Harper & Row, Publ., New York, N.Y., 628 p.:

Pickering, K., and Hiscott, R., 2015, Deep marine systems: Processes, deposits, environments, tectonics and sedimentation, American Geophysical Union., 672 p.:

Pickering, K. T., and Corregidor, J., 2005, Mass-transport complexes (MTCs) and tectonic control on basin-floor submarine fans, middle Eocene, south Spanish Pyrenees: Journal of Sedimentary Research, v. 75, no. 5, p. 761-783.

Posamentier, H. W., and Martinsen, O. J., 2011, The character and genesis of submarine mass-transport deposits; insights from outcrop and 3D seismic data: Special Publication - Society for Sedimentary Geology, v. 96, p. 7-38.

Postma, G., Nemec, W., and Kleinspehn, K. L., 1988, Large floating clasts in turbidites; a mechanism for their emplacement: Sedimentary Geology, v. 58, no. 1, p. 47-61.

Potter, D. K., and Stephenson, A., 1988, Single-domain particles in rocks and magnetic fabric analysis: Geophysical Research Letters, v. 15, no. 10, p. 1097-1100.

Potter, P. E., and Pettijohn, F. J., 1977, Paleocurrents and basin analysis, New York, Springer-Verlag, 425 p.:

Raposo, M. I. B., 1997, Magnetic fabric and its significance in the Florianopolis dyke swarm, southern Brazil: Geophysical Journal International, v. 131, no. 1, p. 159-170.

Rees, A. I., 1965, The use of anisotropy of magnetic susceptibility in the estimation of sedimentary fabric: Sedimentology, v. 4, no. 4, p. 257-227.

-, 1983, Experiments on the production of transverse grain alignment in a sheared dispersion: Sedimentology, v. 30, no. 3, p. 437-448.

Reineck, H. E., and Singh, I. B., 1973, Depositional Sedimentary Environments; With Reference to Terrigenous Clastics, Springer-Verlag, 439 p.:

Ricci Lucci, F., 1970, Sedimentografia; atlante fotografico delle strutture primarie dei sedimenti, Zanichelli, 288 p.:

Robion, P., Grelaud, S., and Frizon de Lamotte, D., 2007, Pre-folding magnetic fabrics in fold-and-thrust belts; why the apparent internal deformation of the sedimentary rocks from the Minervois Basin (NE-Pyrenees, France) is so high compared to the Potwar Basin (SW-Himalaya, Pakistan): Sedimentary Geology, v. 196, no. 1-4, p. 181-200.

Rocha Campos, A. C., dos Santos, P. R., and Canuto, J. R., 2008, Late Paleozoic glacial deposits of Brasil: Paraná Basin, in Fielding, C. R., Frank, T. D., and Isbell, J. L., eds., Resolving the late Paleozoic Ice Age in time and space, Geological Society of America Special Paper 441, p. 97-114.

Rocha Campos, A. C., Machado, L. C. R., dos Santos, P. R., Canuto, J. R., and de Castro, J. C., 1988, Pavimento estriado da glaciacao neopaleozoica, em Alfredo Wagner, Santa Catarina, Brasil: Boletim IG-USP, Serie Cientifica, v. 19, p. 39-46.

Rocha-Campos, A. C., 1967, The Tubarao group in the Brazilian portion of the Parana Basin (1): Problems in Brazilian Gondwana geology, p. 27-102.

Rochette, P., Aubourg, C., and Perrin, M., 1999, Is this magnetic fabric normal?; a review and case studies in volcanic formations: Tectonophysics, v. 307, no. 1-2, p. 219-234.

Rodrigues, M. C. N. L., Trzaskos, B., Vesely, F. F., Mottin, T. E., Schemiko, D.C.B., 2017, Definição da orientação de paleotaludes a partir da análise cinemática de estruturas deformacionais em depósitos de transporte em massa. In: X Simpósio Sul-Brasileiro de Geologia, Curitiba. Anais.

Rosa, E. L. M. d., Vesely, F., and França, A. B., 2016, A review on late Paleozoic ice-related erosional landforms in the Paraná Basin: origin and paleogeographical implications: Brazilian Journal of Geology, v. 46.

Sakai, T., Yokokawa, M., Kubo, Y. s., Endo, N., and Masuda, F., 2002, Grain fabric of experimental gravity flow deposits: Sedimentary Geology, v. 154, no. 1-2, p. 1-10.

Santos, P. R. d., 1987, Facies e evolução paleogeográfica do Subgrupo Itararé/Grupo Aquidauana (Neopaleozoico) na Bacia do Paraná [Ph.D. Doctoral]: Universidade de São Paulo.

Santos, P. R. d., Rocha-Campos, A. C., and Canuto, J. R., 1996, Patterns of late Palaeozoic deglaciation in the Paraná Basin, Brazil: Palaeogeography, Palaeoclimatology, Palaeoecology, v. 125, no. 1-4, p. 165-184.

Schneider, R. L., Muehlmann, H., Tommazi, E., Medeiros, R. A., Daemon, R. F., and Nogueira, A. A., 1974, Revisao estratigrafica da Bacia do Parana: Anais do Congresso, no. 28, Vol. 1, p. 41-65.

Schwarzacher, W., 1951, Grain orientation in sands and sandstones: Journal of Sedimentary Petrology, v. 21, no. 3, p. 162-172.

Schwehr, K., Driscoll, N., and Tauxe, L., 2007, Origin of continental margin morphology; submarine-slide or downslope current-controlled bedforms, a rock magnetic approach: Marine Geology, v. 240, no. 1-4, p. 19-41.

Scotese, C. R., 1997, The PALEOMAP Project: paleogeographic atlas and plate tectonic software, The PALEOMAP Project: paleogeographic atlas and plate tectonic software, Department of Geology, University of Texas, TX.

Shanmugam, G., 1996, High-density turbidity currents; are they sandy debris flows?: Journal of Sedimentary Research, v. 66, no. 1, p. 2-10.

Shumway, J. R., and Iverson, N. R., 2009, Magnetic fabrics of the Douglas Till of the Superior Lobe; exploring bed-deformation kinematics: Quaternary Science Reviews, v. 28, no. 1-2, p. 107-119.

Souza, P. A., 2006, Late Carboniferous palynostratigraphy of the Itarare Subgroup, northeastern Parana Basin, Brazil: Review of Palaeobotany and Palynology, v. 138, no. 1, p. 9-29.

Stacey, F. D., Joplin, G., and Lindsay, J., 1960, Magnetic anisotropy of fabric of some foliated rocks demo S.E. Australia. GeoPhysica Pura Appl., v. 47, p. 30-40.

Stephenson, A., Sadikun, S., and Potter, D. K., 1986, A theoretical and experimental comparison of the anisotropies of magnetic susceptibility and remanence in rocks and minerals: Geophysical Journal of the Royal Astronomical Society, v. 84, no. 1, p. 185-200.

Stupavsky, M., Gravenor, C. P., and Symons, D. T. A., 1974a, Paleomagnetism and Magnetic Fabric of the Leaside and Sunnybrook Tills near Toronto, Ontario: Geological Society of America Bulletin, v. 85, no. 8, p. 1233-1236.

Stupavsky, M., Symons, D. T. A., and Gravenor, C. P., 1974b, Paleomagnetism of the Port Stanley Till, Ontario: Geological Society of America Bulletin, v. 85, no. 1, p. 141-144.

Suss, J. F. S., Vesely, F. F., Santa Catharina, A., Assine, M. L., and Paim, P. S. G., 2014, O Grupo Itararé (Neocarbonífero-Eopermiano) entre Porto Amazonas (Pr) e Mafra (Sc): sedimentação gravitacional em contexto marinho deltaico com influência glacia: Geociências, v. 33, no. 4, p. 701-719.

Syvitski, J. M., Burrell, D. C., and Skei, J. M., 1987, Fjords: processes and products, New York, Springer-Verlag, 379 p.:

Taira, A., 1989. Magnetic fabrics and depositional processes, in Taira, A., and Masuda, F., eds., Sedimentary Facies in the Active Plate Margins. Tokyo: Terra Science, p. 43-77.

Taira, A., and Scholle, P. A., 1979, Deposition of resedimented sandstone beds in the Pico Formation, Ventura Basin, California, as interpreted from magnetic fabric measurements: Geological Society of America Bulletin, v. 90, no. 10, p. 952-962.

Talling, P. J., Masson, D. G., Sumner, E. J., and Malgesini, G., 2012, Subaqueous sediment density flows; depositional processes and deposit types: Sedimentology, v. 59, no. 7, p. 1937-2003.

Tarling, D. H., and Hrouda, F., 1993, The magnetic anisotropy of rocks, Chapman & Hall, London, 217 p.:

Tarling, D. H., and Shi, H., 1995, Magnetic anisotropy of borehole core samples: Geological Society Special Publications, v. 98, p. 273-280.

Tauxe, L., 1998, Paleomagnetic principles and practice: Modern Approaches in Geophysics, v. 17, p. 299.

Tauxe, L., Butler, R. F., Van der Voo, R., and Banerjee, S. K., 2010, Essentials of paleomagnetism, University of California Press, Berkeley, CA, 489 p.:

Tauxe, L., Gee, J. S., and Staudigel, H., 1998, Flow directions in dikes from anisotropy of magnetic susceptibility data; the bootstrap way: Journal of Geophysical Research, v. 103, no. B8, p. 17-17,790.

Tauxe, L., Shaar, R., Jonestrask, L., Swanson-Hysell, N. L., Minnett, R., Koppers, A. A. P., Constable, C. G., Jarboe, N., Gaastra, K., and Fairchild, L., 2016, PmagPy; software package for paleomagnetic data analysis and a bridge to the Magnetics Information Consortium (MagIC) database: Geochemistry, Geophysics, Geosystems - G3, v. 17, no. 6, p. 2450-2463.

Tomazelli, L., and Soliani, E., 1982, Evidências de atividade glacial no Paleozoico Superior do Rio Grande do Sul, In: SBG, XXXII Congresso Brasileiro de Geologia, 4, Anais, p. 1378-1391.

-, 1997, Sedimentary facies and depositional environments related to Gondwana glaciation in Batovi and Suspiro regions, Rio Grande Do Sul, Brazil: Journal of South American Earth Sciences, v. 10(3), p. 295-303.

Torsvik, T. H., and Cocks, L. R. M., 2013, Gondwana from top to base in space and time: Gondwana Research, v. 24, no. 3-4, p. 999-1030.

Veevers, J. J., and Powell, C. M., 1987, Late Paleozoic glacial episodes in Gondwanaland reflected in transgressive-regressive depositional sequences in Euramerica: Geological Society of America Bulletin, v. 98, p. 475-487.

Veloso, E. E., Anma, R., Ota, T., Komiya, T., Kagashima, S.-i., and Yamazaki, T., 2007, Paleocurrent patterns of the sedimentary sequence of the Taitao Ophiolite constrained by anisotropy of magnetic susceptibility and paleomagnetic analyses: Sedimentary Geology, v. 201, no. 3-4, p. 446-460.

Vesely, F. F., and Assine, M. L., 2006, Deglaciation sequences in the Permo-Carboniferous Itarare Group, Paraná Basin, southern Brazil: Journal of South American Earth Sciences, v. 22, no. 3-4, p. 156-168.

Vesely, F., Trzaskos, B., Kipper, F., Assine, M. L., and Souza, P. A., 2015, Sedimentary record of a fluctuating ice margin from the Pennsylvanian of western Gondwana: Paraná Basin, southern Brazil: Sedimentary Geology, v. 326, p. 45-63.

Visser, J. N. J., 1987, The influence of topography on the Permo-Carboniferous glaciation in the Karoo Basin and adjoining areas, Southern Africa: Geophysical Monograph, v. 41, p. 123-129.

Woodworth-Lynas, C. M. T., Dowdeswell, J. A., and Anonymous, 1994, Soft-sediment striated surfaces and massive diamicton facies produced by floating ice: Program with Abstracts - Geological Association of Canada; Mineralogical Association of Canada: Joint Annual Meeting, v. 19, p. 126.

Ziegler, A. M., Bambach, R. K., Scotese, C. R., McKerrow, W. S., and Johnson, M. E., 1979, Paleozoic paleogeography, in Donath, F. A., ed., Annual review of earth and planetary sciences, Vol. 7, Annual Reviews Inc, p. 473-502.

Ziegler, A. M., Hulver, M. L., and Rowley, D. B., 1997, Permian World topography and climate, in Martini, I. P., ed., Late glacial and postglacial environmental changes: Quaternary, Carboniferous-Permian, and Proterozoic: Oxford, U.K., Oxford University Press, p. 111-146.

APPENDIX A: SPECIMEN AMS MEASUREMENTS FOR (CH3) LOCATIONS

Appendix A includes specimen AMS measurements for samples collected from localities included within this study (Alfredo Wagner, Aurora, Campo do Tenente, Porto Amazonas, Cachoeira do Sul, Ibaré, and São Gabriel) outlined in Ch3.

Table A-1. *Specimen AMS measurements for site B8 at Alfredo Wagner road cut exposure. Summary of column headers:* $\boldsymbol{\chi_b}$ *= bulk susceptibility, SE = standard error,* $\boldsymbol{\tau_1}$ *= normalized maximum eigenvalue,* $\boldsymbol{\tau_2}$ *= normalized intermediate eigenvalue,* $\boldsymbol{\tau_3}$ *= normalized minimum eigenvalue,* $\boldsymbol{P_1}$ *= lineation,* $\boldsymbol{P_3}$ *= foliation,* $\boldsymbol{P_j}$ *= corrected degree of anisotropy, T = shape parameter,* $\boldsymbol{k_1}$ *= maximum eigenvector,* $\boldsymbol{k_2}$ *= intermediate eigenvector,* $\boldsymbol{k_3}$ *= minimum eigenvector, DEC = declination, INC = inclination, F = Hext F statistic.*

ID	Specimen	χ_b	χ_b (SE)	τ_1	τ_1 (SE)	τ_2	τ_2 (SE)	τ_3	τ_3 (SE)	P_1	P_3	P_j	T	k_1 (Dec)	k_1 (Inc)	k_2 (Dec)	k_2 (Inc)	k_3 (Dec)	k_3 (Inc)	F
1	BR01-1	1.36E-04	3.56E-04	1.0073	0.00030	1.0058	0.00030	0.9869	0.00020	1.001	1.019	1.023	0.857	90.0	7.3	359.4	4.1	240.3	81.6	603.9
2	BR01-2	1.35E-04	3.29E-04	1.0085	0.00030	1.0062	0.00030	0.9853	0.00020	1.002	1.021	1.026	0.808	80.7	20.4	172.8	5.7	277.7	68.8	821.0
3	BR01-3	1.28E-04	1.80E-04	1.0075	0.00010	1.0063	0.00010	0.9862	0.00010	1.001	1.020	1.024	0.884	164.2	3.4	73.6	10.1	272.5	79.4	2595.5
4	BR02-1	1.31E-04	1.53E-04	1.0068	0.00010	1.0053	0.00010	0.9879	0.00010	1.002	1.018	1.021	0.842	139.7	5.8	49.0	6.3	271.8	81.5	2819.2
5	BR02-2	1.45E-04	1.19E-04	1.0045	0.00010	1.0034	0.00010	0.9921	0.00010	1.001	1.011	1.014	0.828	165.4	2.6	74.8	10.9	268.8	78.8	1972.7
6	BR02-3	1.43E-04	2.07E-04	1.0060	0.00020	1.0034	0.00010	0.9907	0.00010	1.003	1.013	1.017	0.663	147.0	14.2	54.5	10.0	290.7	72.5	855.5
7	BR02-4	1.40E-04	2.91E-04	1.0084	0.00020	1.0054	0.00020	0.9862	0.00020	1.003	1.020	1.024	0.739	136.8	12.4	45.4	6.2	289.6	76.1	972.2
8	BR03-1	1.52E-04	3.49E-04	1.0079	0.00030	1.0047	0.00030	0.9874	0.00020	1.003	1.018	1.022	0.691	171.3	7.2	79.5	14.0	287.7	74.2	553.7
9	BR03-2	1.45E-04	3.01E-04	1.0091	0.00020	1.0046	0.00020	0.9863	0.00020	1.004	1.019	1.025	0.610	146.6	14.9	53.3	12.0	286.0	70.7	860.7
10	BR03-3	1.41E-04	3.90E-04	1.0081	0.00030	1.0052	0.00030	0.9867	0.00030	1.003	1.019	1.024	0.732	157.1	12.5	64.2	13.0	289.6	71.8	479.1
11	BR03-4	1.44E-04	2.46E-04	1.0071	0.00020	1.0051	0.00020	0.9878	0.00020	1.002	1.018	1.022	0.796	145.2	10.5	53.3	10.1	280.3	75.4	1054.6
12	BR04-1	1.35E-04	3.44E-04	1.0089	0.00030	1.0079	0.00030	0.9833	0.00020	1.001	1.025	1.030	0.922	163.0	7.8	71.5	10.9	287.8	76.5	1013.7
13	BR04-2	1.37E-04	2.99E-04	1.0081	0.00020	1.0074	0.00020	0.9846	0.00020	1.001	1.023	1.027	0.940	154.3	6.8	63.2	8.9	281.3	78.8	1162.9
14	BR04-3	1.39E-04	2.49E-04	1.0074	0.00020	1.0060	0.00020	0.9866	0.00020	1.001	1.020	1.024	0.866	130.7	8.5	39.2	9.8	260.8	76.9	1245.8
15	BR05-1	1.35E-04	2.15E-04	1.0076	0.00020	1.0052	0.00020	0.9873	0.00020	1.002	1.018	1.022	0.765	102.6	10.0	194.4	10.4	329.7	75.5	1349.4
16	BR05-2	1.42E-04	2.74E-04	1.0090	0.00020	1.0055	0.00020	0.9855	0.00020	1.003	1.020	1.026	0.708	129.3	14.9	221.5	8.1	339.3	72.9	1041.3
17	BR06-1	1.40E-04	4.21E-04	1.0075	0.00030	1.0053	0.00030	0.9872	0.00030	1.002	1.018	1.023	0.780	126.1	11.3	35.9	1.0	300.7	78.6	386.6
18	BR06-2	1.26E-04	3.21E-04	1.0075	0.00020	1.0050	0.00020	0.9875	0.00020	1.002	1.018	1.022	0.758	129.4	9.4	39.1	1.8	298.3	80.4	646.5
19	BR06-3	1.40E-04	2.87E-04	1.0090	0.00020	1.0060	0.00020	0.9850	0.00020	1.003	1.021	1.027	0.746	127.5	9.9	217.7	1.0	313.2	80.0	1144.0
	MEAN	1.39E-04	1.439E-06	1.0077	0.00026	1.0055	0.00025	0.9869	0.00046	1.002	1.019	1.023	0.786							

Table A-2. *Specimen AMS measurements for site R7 at Alfredo Wagner road cut exposure. Summary of column headers:* $\boldsymbol{\chi_b}$ *= bulk susceptibility, SE = standard error,* $\boldsymbol{\tau_1}$ *= normalized maximum eigenvalue,* $\boldsymbol{\tau_2}$ *= normalized intermediate eigenvalue,* $\boldsymbol{\tau_3}$ *= normalized minimum eigenvalue,* $\boldsymbol{P_1}$ *= lineation,* $\boldsymbol{P_3}$ *= foliation,* $\boldsymbol{P_j}$ *= corrected degree of anisotropy, T = shape parameter,* $\boldsymbol{k_1}$ *= maximum eigenvector,* $\boldsymbol{k_2}$ *= intermediate eigenvector,* $\boldsymbol{k_3}$ *= minimum eigenvector, DEC = declination, INC = inclination, F = Hext F statistic.*

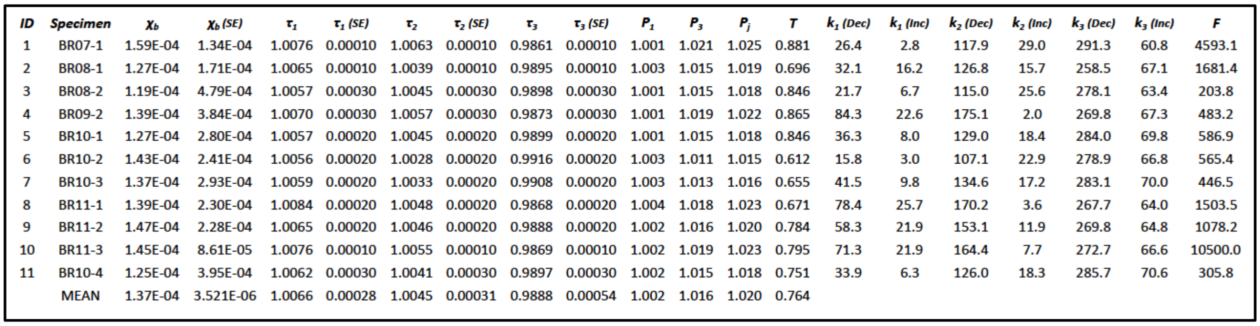

ID	Specimen	χ_b	χ_b (SE)	τ_1	τ_1 (SE)	τ_2	τ_2 (SE)	τ_3	τ_3 (SE)	P_1	P_3	P_j	T	k_1 (Dec)	k_1 (Inc)	k_2 (Dec)	k_2 (Inc)	k_3 (Dec)	k_3 (Inc)	F
1	BR07-1	1.59E-04	1.34E-04	1.0076	0.00010	1.0063	0.00010	0.9861	0.00010	1.001	1.021	1.025	0.881	26.4	2.8	117.9	29.0	291.3	60.8	4593.1
2	BR08-1	1.27E-04	1.71E-04	1.0065	0.00010	1.0039	0.00010	0.9895	0.00010	1.003	1.015	1.019	0.696	32.1	16.2	126.8	15.7	258.5	67.1	1681.4
3	BR08-2	1.19E-04	4.79E-04	1.0057	0.00030	1.0045	0.00030	0.9898	0.00030	1.001	1.015	1.018	0.846	21.7	6.7	115.0	25.6	278.1	63.4	203.8
4	BR09-2	1.39E-04	3.84E-04	1.0070	0.00030	1.0057	0.00030	0.9873	0.00030	1.001	1.019	1.022	0.865	84.3	22.6	175.1	2.0	269.8	67.3	483.2
5	BR10-1	1.27E-04	2.80E-04	1.0057	0.00020	1.0045	0.00020	0.9899	0.00020	1.001	1.015	1.018	0.846	36.3	8.0	129.0	18.4	284.0	69.8	586.9
6	BR10-2	1.43E-04	2.41E-04	1.0056	0.00020	1.0028	0.00020	0.9916	0.00020	1.003	1.011	1.015	0.612	15.8	3.0	107.1	22.9	278.9	66.8	565.4
7	BR10-3	1.37E-04	2.93E-04	1.0059	0.00020	1.0033	0.00020	0.9908	0.00020	1.003	1.013	1.016	0.655	41.5	9.8	134.6	17.2	283.1	70.0	446.5
8	BR11-1	1.39E-04	2.30E-04	1.0084	0.00020	1.0048	0.00020	0.9868	0.00020	1.004	1.018	1.023	0.671	78.4	25.7	170.2	3.6	267.7	64.0	1503.5
9	BR11-2	1.47E-04	2.28E-04	1.0065	0.00020	1.0046	0.00020	0.9888	0.00020	1.002	1.016	1.020	0.784	58.3	21.9	153.1	11.9	269.8	64.8	1078.2
10	BR11-3	1.45E-04	8.61E-05	1.0076	0.00010	1.0055	0.00010	0.9869	0.00010	1.002	1.019	1.023	0.795	71.3	21.9	164.4	7.7	272.7	66.6	10500.0
11	BR10-4	1.25E-04	3.95E-04	1.0062	0.00030	1.0041	0.00030	0.9897	0.00030	1.002	1.015	1.018	0.751	33.9	6.3	126.0	18.3	285.7	70.6	305.8
	MEAN	1.37E-04	3.521E-06	1.0066	0.00028	1.0045	0.00031	0.9888	0.00054	1.002	1.016	1.020	0.764							

Table A-3. *Specimen AMS measurements for site Q1 at the Aurora quarry. Summary of column headers:* $\boldsymbol{\chi_b}$ *= bulk susceptibility, SE = standard error,* $\boldsymbol{\tau_1}$ *= normalized maximum eigenvalue,* $\boldsymbol{\tau_2}$ *= normalized intermediate eigenvalue,* $\boldsymbol{\tau_3}$ *= normalized minimum eigenvalue,* $\boldsymbol{P_1}$ *= lineation,* $\boldsymbol{P_3}$ *= foliation,* $\boldsymbol{P_j}$ *= corrected degree of anisotropy, T = shape parameter,* $\boldsymbol{k_1}$ *= maximum eigenvector,* $\boldsymbol{k_2}$ *= intermediate eigenvector,* $\boldsymbol{k_3}$ *= minimum eigenvector, DEC = declination, INC = inclination, F = Hext F statistic.*

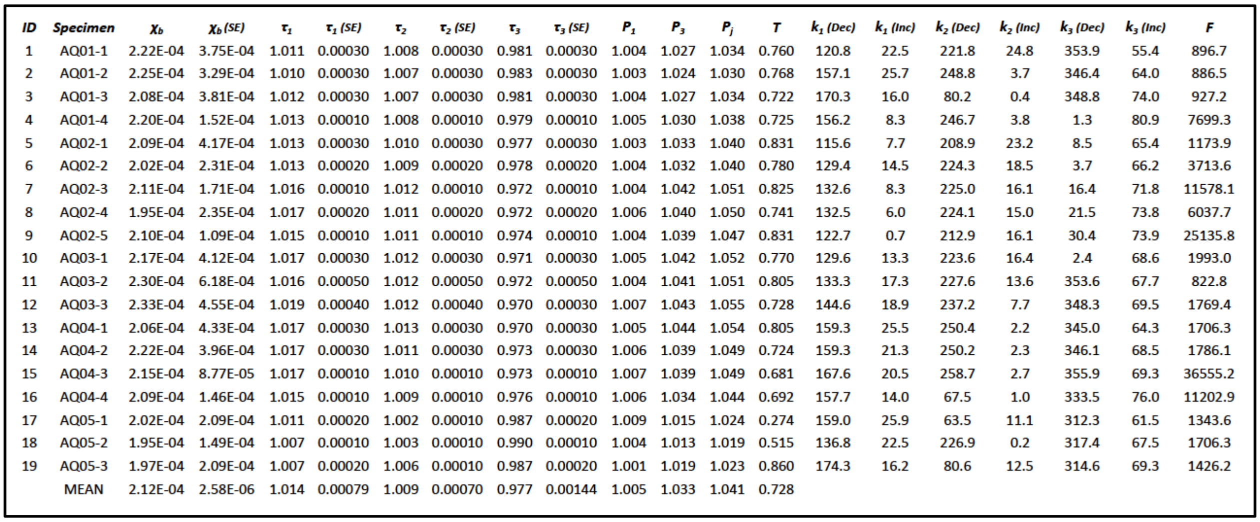

ID	Specimen	χ_b	χ_b (SE)	τ_1	τ_1 (SE)	τ_2	τ_2 (SE)	τ_3	τ_3 (SE)	P_1	P_3	P_j	T	k_1 (Dec)	k_1 (Inc)	k_2 (Dec)	k_2 (Inc)	k_3 (Dec)	k_3 (Inc)	F
1	AQ01-1	2.22E-04	3.75E-04	1.011	0.00030	1.008	0.00030	0.981	0.00030	1.004	1.027	1.034	0.760	120.8	22.5	221.8	24.8	353.9	55.4	896.7
2	AQ01-2	2.25E-04	3.29E-04	1.010	0.00030	1.007	0.00030	0.983	0.00030	1.003	1.024	1.030	0.768	157.1	25.7	248.8	3.7	346.4	64.0	886.5
3	AQ01-3	2.08E-04	3.81E-04	1.012	0.00030	1.007	0.00030	0.981	0.00030	1.004	1.027	1.034	0.722	170.3	16.0	80.2	0.4	348.8	74.0	927.2
4	AQ01-4	2.20E-04	1.52E-04	1.013	0.00010	1.008	0.00010	0.979	0.00010	1.005	1.030	1.038	0.725	156.2	8.3	246.7	3.8	1.3	80.9	7699.3
5	AQ02-1	2.09E-04	4.17E-04	1.013	0.00030	1.010	0.00030	0.977	0.00030	1.003	1.033	1.040	0.831	115.6	7.7	208.9	23.2	8.5	65.4	1173.9
6	AQ02-2	2.02E-04	2.31E-04	1.013	0.00020	1.009	0.00020	0.978	0.00020	1.004	1.032	1.040	0.780	129.4	14.5	224.3	18.5	3.7	66.2	3713.6
7	AQ02-3	2.11E-04	1.71E-04	1.016	0.00010	1.012	0.00010	0.972	0.00010	1.004	1.042	1.051	0.825	132.6	8.3	225.0	16.1	16.4	71.8	11578.1
8	AQ02-4	1.95E-04	2.35E-04	1.017	0.00020	1.011	0.00020	0.972	0.00020	1.006	1.040	1.050	0.741	132.5	6.0	224.1	15.0	21.5	73.8	6037.7
9	AQ02-5	2.10E-04	1.09E-04	1.015	0.00010	1.011	0.00010	0.974	0.00010	1.004	1.039	1.047	0.831	122.7	0.7	212.9	16.1	30.4	73.9	25135.8
10	AQ03-1	2.17E-04	4.12E-04	1.017	0.00030	1.012	0.00030	0.971	0.00030	1.005	1.042	1.052	0.770	129.6	13.3	223.6	16.4	2.4	68.6	1993.0
11	AQ03-2	2.30E-04	6.18E-04	1.016	0.00050	1.012	0.00050	0.972	0.00050	1.004	1.041	1.051	0.805	133.3	17.3	227.6	13.6	353.6	67.7	822.8
12	AQ03-3	2.33E-04	4.55E-04	1.019	0.00040	1.012	0.00040	0.970	0.00030	1.007	1.043	1.055	0.728	144.6	18.9	237.2	7.7	348.3	69.5	1769.4
13	AQ04-1	2.06E-04	4.33E-04	1.017	0.00030	1.013	0.00030	0.970	0.00030	1.005	1.044	1.054	0.805	159.3	25.5	250.4	2.2	345.0	64.3	1706.3
14	AQ04-2	2.22E-04	3.96E-04	1.017	0.00030	1.011	0.00030	0.973	0.00030	1.006	1.039	1.049	0.724	159.3	21.3	250.2	2.3	346.1	68.5	1786.1
15	AQ04-3	2.15E-04	8.77E-05	1.017	0.00010	1.010	0.00010	0.973	0.00010	1.007	1.039	1.049	0.681	167.6	20.5	258.7	2.7	355.9	69.3	36555.2
16	AQ04-4	2.09E-04	1.46E-04	1.015	0.00010	1.009	0.00010	0.976	0.00010	1.006	1.034	1.044	0.692	157.7	14.0	67.5	1.0	333.5	76.0	11202.9
17	AQ05-1	2.02E-04	2.09E-04	1.011	0.00020	1.002	0.00010	0.987	0.00020	1.009	1.015	1.024	0.274	159.0	25.9	63.5	11.1	312.3	61.5	1343.6
18	AQ05-2	1.95E-04	1.49E-04	1.007	0.00010	1.003	0.00010	0.990	0.00010	1.004	1.013	1.019	0.515	136.8	22.5	226.9	0.2	317.4	67.5	1706.3
19	AQ05-3	1.97E-04	2.09E-04	1.007	0.00020	1.006	0.00010	0.987	0.00020	1.001	1.019	1.023	0.860	174.3	16.2	80.6	12.5	314.6	69.3	1426.2
	MEAN	2.12E-04	2.58E-06	1.014	0.00079	1.009	0.00070	0.977	0.00144	1.005	1.033	1.041	0.728							

Table A-4. *Specimen AMS measurements for site C3 at the Campo do Tenente quarry. Summary of column headers:* $\boldsymbol{\chi_b}$ *= bulk susceptibility, SE = standard error,* $\boldsymbol{\tau_1}$ *= normalized maximum eigenvalue,* $\boldsymbol{\tau_2}$ *= normalized intermediate eigenvalue,* $\boldsymbol{\tau_3}$ *= normalized minimum eigenvalue,* $\boldsymbol{P_1}$ *= lineation,* $\boldsymbol{P_3}$ *= foliation,* $\boldsymbol{P_j}$ *= corrected degree of anisotropy, T = shape parameter,* $\boldsymbol{k_1}$ *= maximum eigenvector,* $\boldsymbol{k_2}$ *= intermediate eigenvector,* $\boldsymbol{k_3}$ *= minimum eigenvector, DEC = declination, INC = inclination, F = Hext F statistic.*

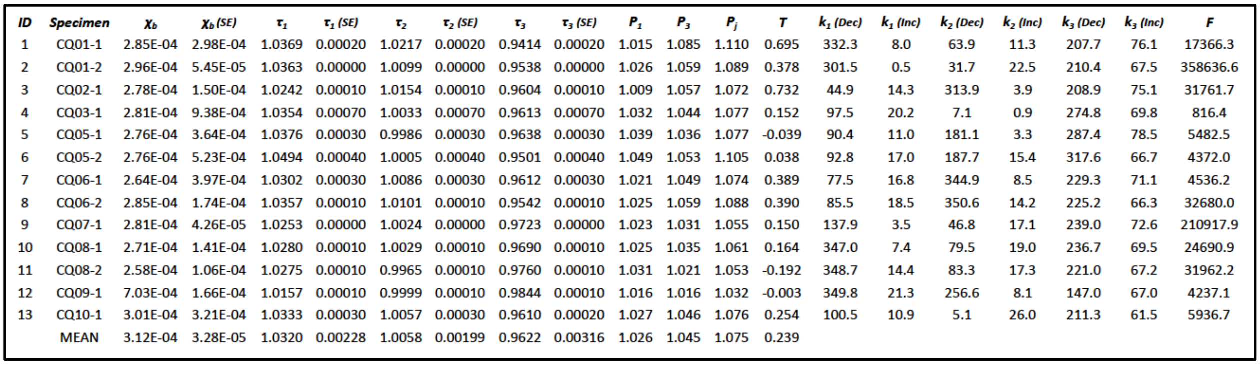

ID	Specimen	χ_b	χ_b (SE)	τ_1	τ_1 (SE)	τ_2	τ_2 (SE)	τ_3	τ_3 (SE)	P_1	P_3	P_j	T	k_1 (Dec)	k_1 (Inc)	k_2 (Dec)	k_2 (Inc)	k_3 (Dec)	k_3 (Inc)	F
1	CQ01-1	2.85E-04	2.98E-04	1.0369	0.00020	1.0217	0.00020	0.9414	0.00020	1.015	1.085	1.110	0.695	332.3	8.0	63.9	11.3	207.7	76.1	17366.3
2	CQ01-2	2.96E-04	5.45E-05	1.0363	0.00000	1.0099	0.00000	0.9538	0.00000	1.026	1.059	1.089	0.378	301.5	0.5	31.7	22.5	210.4	67.5	358636.6
3	CQ02-1	2.78E-04	1.50E-04	1.0242	0.00010	1.0154	0.00010	0.9604	0.00010	1.009	1.057	1.072	0.732	44.9	14.3	313.9	3.9	208.9	75.1	31761.7
4	CQ03-1	2.81E-04	9.38E-04	1.0354	0.00070	1.0033	0.00070	0.9613	0.00070	1.032	1.044	1.077	0.152	97.5	20.2	7.1	0.9	274.8	69.8	816.4
5	CQ05-1	2.76E-04	3.64E-04	1.0376	0.00030	0.9986	0.00030	0.9638	0.00030	1.039	1.036	1.077	-0.039	90.4	11.0	181.1	3.3	287.4	78.5	5482.5
6	CQ05-2	2.76E-04	5.23E-04	1.0494	0.00040	1.0005	0.00040	0.9501	0.00040	1.049	1.053	1.105	0.038	92.8	17.0	187.7	15.4	317.6	66.7	4372.0
7	CQ06-1	2.64E-04	3.97E-04	1.0302	0.00030	1.0086	0.00030	0.9612	0.00030	1.021	1.049	1.074	0.389	77.5	16.8	344.9	8.5	229.3	71.1	4536.2
8	CQ06-2	2.85E-04	1.74E-04	1.0357	0.00010	1.0101	0.00010	0.9542	0.00010	1.025	1.059	1.088	0.390	85.5	18.5	350.6	14.2	225.2	66.3	32680.0
9	CQ07-1	2.81E-04	4.26E-05	1.0253	0.00000	1.0024	0.00000	0.9723	0.00000	1.023	1.031	1.055	0.150	137.9	3.5	46.8	17.1	239.0	72.6	210917.9
10	CQ08-1	2.71E-04	1.41E-04	1.0280	0.00010	1.0029	0.00010	0.9690	0.00010	1.025	1.035	1.061	0.164	347.0	7.4	79.5	19.0	236.7	69.5	24690.9
11	CQ08-2	2.58E-04	1.06E-04	1.0275	0.00010	0.9965	0.00010	0.9760	0.00010	1.031	1.021	1.053	-0.192	348.7	14.4	83.3	17.3	221.0	67.2	31962.2
12	CQ09-1	7.03E-04	1.66E-04	1.0157	0.00010	0.9999	0.00010	0.9844	0.00010	1.016	1.016	1.032	-0.003	349.8	21.3	256.6	8.1	147.0	67.0	4237.1
13	CQ10-1	3.01E-04	3.21E-04	1.0333	0.00030	1.0057	0.00030	0.9610	0.00020	1.027	1.046	1.076	0.254	100.5	10.9	5.1	26.0	211.3	61.5	5936.7
	MEAN	3.12E-04	3.28E-05	1.0320	0.00228	1.0058	0.00199	0.9622	0.00316	1.026	1.045	1.075	0.239							

Table A-5. *Specimen AMS measurements for site T5 at the Campo do Tenente quarry. Summary of column headers:* $\boldsymbol{\chi_b}$ *= bulk susceptibility, SE = standard error,* $\boldsymbol{\tau_1}$ *= normalized maximum eigenvalue,* $\boldsymbol{\tau_2}$ *= normalized intermediate eigenvalue,* $\boldsymbol{\tau_3}$ *= normalized minimum eigenvalue,* $\boldsymbol{P_1}$ *= lineation,* $\boldsymbol{P_3}$ *= foliation,* $\boldsymbol{P_j}$ *= corrected degree of anisotropy, T = shape parameter,* $\boldsymbol{k_1}$ *= maximum eigenvector,* $\boldsymbol{k_2}$ *= intermediate eigenvector,* $\boldsymbol{k_3}$ *= minimum eigenvector, DEC = declination, INC = inclination, F = Hext F statistic.*

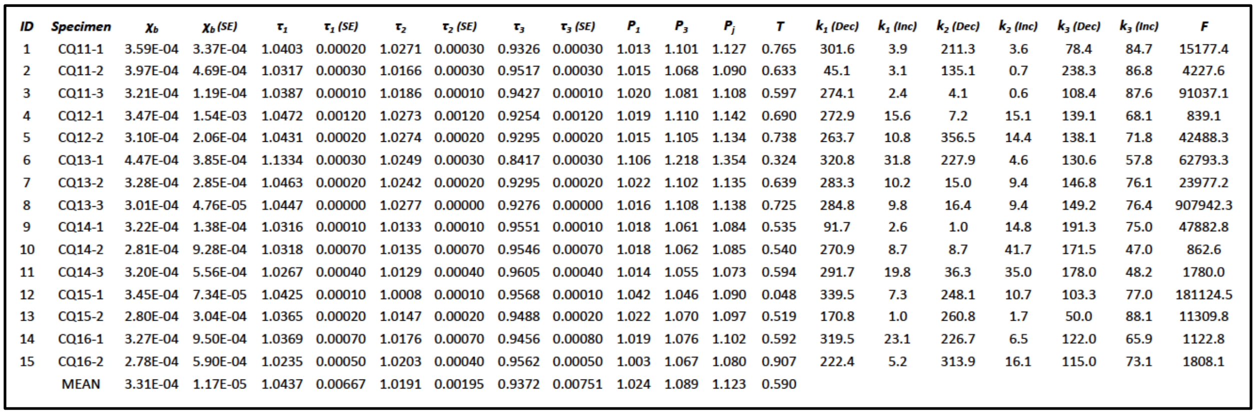

ID	Specimen	χ_b	χ_b (SE)	τ_1	τ_1 (SE)	τ_2	τ_2 (SE)	τ_3	τ_3 (SE)	P_1	P_3	P_j	T	k_1 (Dec)	k_1 (Inc)	k_2 (Dec)	k_2 (Inc)	k_3 (Dec)	k_3 (Inc)	F
1	CQ11-1	3.59E-04	3.37E-04	1.0403	0.00020	1.0271	0.00030	0.9326	0.00030	1.013	1.101	1.127	0.765	301.6	3.9	211.3	3.6	78.4	84.7	15177.4
2	CQ11-2	3.97E-04	4.69E-04	1.0317	0.00030	1.0166	0.00030	0.9517	0.00030	1.015	1.068	1.090	0.633	45.1	3.1	135.1	0.7	238.3	86.8	4227.6
3	CQ11-3	3.21E-04	1.19E-04	1.0387	0.00010	1.0186	0.00010	0.9427	0.00010	1.020	1.081	1.108	0.597	274.1	2.4	4.1	0.6	108.4	87.6	91037.1
4	CQ12-1	3.47E-04	1.54E-03	1.0472	0.00120	1.0273	0.00120	0.9254	0.00120	1.019	1.110	1.142	0.690	272.9	15.6	7.2	15.1	139.1	68.1	839.1
5	CQ12-2	3.10E-04	2.06E-04	1.0431	0.00020	1.0274	0.00020	0.9295	0.00020	1.015	1.105	1.134	0.738	263.7	10.8	356.5	14.4	138.1	71.8	42488.3
6	CQ13-1	4.47E-04	3.85E-04	1.1334	0.00030	1.0249	0.00030	0.8417	0.00030	1.106	1.218	1.354	0.324	320.8	31.8	227.9	4.6	130.6	57.8	62793.3
7	CQ13-2	3.28E-04	2.85E-04	1.0463	0.00020	1.0242	0.00020	0.9295	0.00020	1.022	1.102	1.135	0.639	283.3	10.2	15.0	9.4	146.8	76.1	23977.2
8	CQ13-3	3.01E-04	4.76E-05	1.0447	0.00000	1.0277	0.00000	0.9276	0.00000	1.016	1.108	1.138	0.725	284.8	9.8	16.4	9.4	149.2	76.4	907942.3
9	CQ14-1	3.22E-04	1.38E-04	1.0316	0.00010	1.0133	0.00010	0.9551	0.00010	1.018	1.061	1.084	0.535	91.7	2.6	1.0	14.8	191.3	75.0	47882.8
10	CQ14-2	2.81E-04	9.28E-04	1.0318	0.00070	1.0135	0.00070	0.9546	0.00070	1.018	1.062	1.085	0.540	270.9	8.7	8.7	41.7	171.5	47.0	862.6
11	CQ14-3	3.20E-04	5.56E-04	1.0267	0.00040	1.0129	0.00040	0.9605	0.00040	1.014	1.055	1.073	0.594	291.7	19.8	36.3	35.0	178.0	48.2	1780.0
12	CQ15-1	3.45E-04	7.34E-05	1.0425	0.00010	1.0008	0.00010	0.9568	0.00010	1.042	1.046	1.090	0.048	339.5	7.3	248.1	10.7	103.3	77.0	181124.5
13	CQ15-2	2.80E-04	3.04E-04	1.0365	0.00020	1.0147	0.00020	0.9488	0.00020	1.022	1.070	1.097	0.519	170.8	1.0	260.8	1.7	50.0	88.1	11309.8
14	CQ16-1	3.27E-04	9.50E-04	1.0369	0.00070	1.0176	0.00070	0.9456	0.00080	1.019	1.076	1.102	0.592	319.5	23.1	226.7	6.5	122.0	65.9	1122.8
15	CQ16-2	2.78E-04	5.90E-04	1.0235	0.00050	1.0203	0.00040	0.9562	0.00050	1.003	1.067	1.080	0.907	222.4	5.2	313.9	16.1	115.0	73.1	1808.1
	MEAN	3.31E-04	1.17E-05	1.0437	0.00667	1.0191	0.00195	0.9372	0.00751	1.024	1.089	1.123	0.590							

Table A-6. *Specimen AMS measurements for site D4 at the Campo do Tenente quarry. Summary of column headers:* $\boldsymbol{\chi_b}$ *= bulk susceptibility, SE = standard error,* $\boldsymbol{\tau_1}$ *= normalized maximum eigenvalue,* $\boldsymbol{\tau_2}$ *= normalized intermediate eigenvalue,* $\boldsymbol{\tau_3}$ *= normalized minimum eigenvalue,* $\boldsymbol{P_1}$ *= lineation,* $\boldsymbol{P_3}$ *= foliation,* $\boldsymbol{P_j}$ *= corrected degree of anisotropy, T = shape parameter,* $\boldsymbol{k_1}$ *= maximum eigenvector,* $\boldsymbol{k_2}$ *= intermediate eigenvector,* $\boldsymbol{k_3}$ *= minimum eigenvector, DEC = declination, INC = inclination, F = Hext F statistic.*

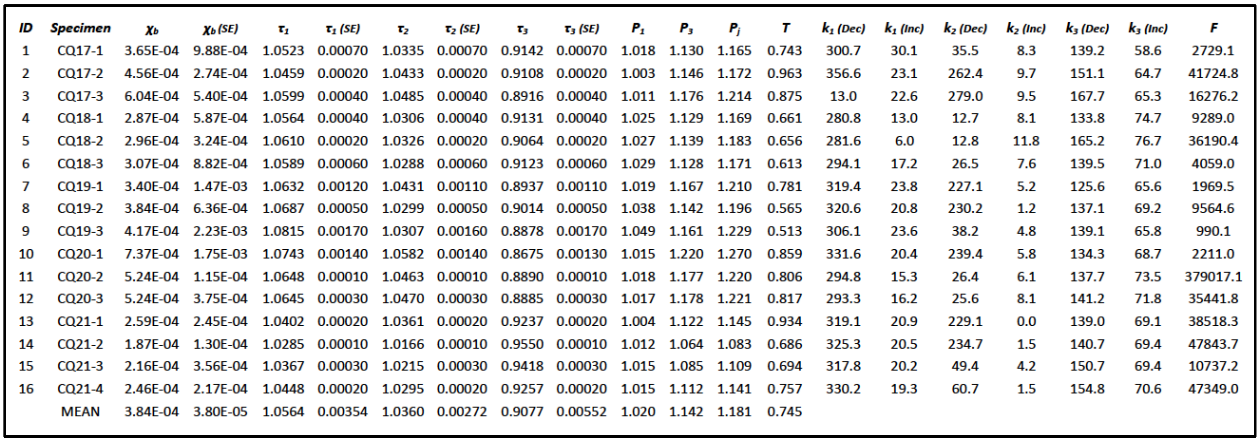

ID	Specimen	χ_b	χ_b (SE)	τ_1	τ_1 (SE)	τ_2	τ_2 (SE)	τ_3	τ_3 (SE)	P_1	P_3	P_j	T	k_1 (Dec)	k_1 (Inc)	k_2 (Dec)	k_2 (Inc)	k_3 (Dec)	k_3 (Inc)	F
1	CQ17-1	3.65E-04	9.88E-04	1.0523	0.00070	1.0335	0.00070	0.9142	0.00070	1.018	1.130	1.165	0.743	300.7	30.1	35.5	8.3	139.2	58.6	2729.1
2	CQ17-2	4.56E-04	2.74E-04	1.0459	0.00020	1.0433	0.00020	0.9108	0.00020	1.003	1.146	1.172	0.963	356.6	23.1	262.4	9.7	151.1	64.7	41724.8
3	CQ17-3	6.04E-04	5.40E-04	1.0599	0.00040	1.0485	0.00040	0.8916	0.00040	1.011	1.176	1.214	0.875	13.0	22.6	279.0	9.5	167.7	65.3	16276.2
4	CQ18-1	2.87E-04	5.87E-04	1.0564	0.00040	1.0306	0.00040	0.9131	0.00040	1.025	1.129	1.169	0.661	280.8	13.0	12.7	8.1	133.8	74.7	9289.0
5	CQ18-2	2.96E-04	3.24E-04	1.0610	0.00020	1.0326	0.00020	0.9064	0.00020	1.027	1.139	1.183	0.656	281.6	6.0	12.8	11.8	165.2	76.7	36190.4
6	CQ18-3	3.07E-04	8.82E-04	1.0589	0.00060	1.0288	0.00060	0.9123	0.00060	1.029	1.128	1.171	0.613	294.1	17.2	26.5	7.6	139.5	71.0	4059.0
7	CQ19-1	3.40E-04	1.47E-03	1.0632	0.00120	1.0431	0.00110	0.8937	0.00110	1.019	1.167	1.210	0.781	319.4	23.8	227.1	5.2	125.6	65.6	1969.5
8	CQ19-2	3.84E-04	6.36E-04	1.0687	0.00050	1.0299	0.00050	0.9014	0.00050	1.038	1.142	1.196	0.565	320.6	20.8	230.2	1.2	137.1	69.2	9564.6
9	CQ19-3	4.17E-04	2.23E-03	1.0815	0.00170	1.0307	0.00160	0.8878	0.00170	1.049	1.161	1.229	0.513	306.1	23.6	38.2	4.8	139.1	65.8	990.1
10	CQ20-1	7.37E-04	1.75E-03	1.0743	0.00140	1.0582	0.00140	0.8675	0.00130	1.015	1.220	1.270	0.859	331.6	20.4	239.4	5.8	134.3	68.7	2211.0
11	CQ20-2	5.24E-04	1.15E-04	1.0648	0.00010	1.0463	0.00010	0.8890	0.00010	1.018	1.177	1.220	0.806	294.8	15.3	26.4	6.1	137.7	73.5	379017.1
12	CQ20-3	5.24E-04	3.75E-04	1.0645	0.00030	1.0470	0.00030	0.8885	0.00030	1.017	1.178	1.221	0.817	293.3	16.2	25.6	8.1	141.2	71.8	35441.8
13	CQ21-1	2.59E-04	2.45E-04	1.0402	0.00020	1.0361	0.00020	0.9237	0.00020	1.004	1.122	1.145	0.934	319.1	20.9	229.1	0.0	139.0	69.1	38518.3
14	CQ21-2	1.87E-04	1.30E-04	1.0285	0.00010	1.0166	0.00010	0.9550	0.00010	1.012	1.064	1.083	0.686	325.3	20.5	234.7	1.5	140.7	69.4	47843.7
15	CQ21-3	2.16E-04	3.56E-04	1.0367	0.00030	1.0215	0.00030	0.9418	0.00030	1.015	1.085	1.109	0.694	317.8	20.2	49.4	4.2	150.7	69.4	10737.2
16	CQ21-4	2.46E-04	2.17E-04	1.0448	0.00020	1.0295	0.00020	0.9257	0.00020	1.015	1.112	1.141	0.757	330.2	19.3	60.7	1.5	154.8	70.6	47349.0
	MEAN	3.84E-04	3.80E-05	1.0564	0.00354	1.0360	0.00272	0.9077	0.00552	1.020	1.142	1.181	0.745							

Table A-7. *Specimen AMS measurements for site D5 at the Campo do Tenente quarry. Summary of column headers:* $\boldsymbol{\chi_b}$ *= bulk susceptibility, SE = standard error,* $\boldsymbol{\tau_1}$ *= normalized maximum eigenvalue,* $\boldsymbol{\tau_2}$ *= normalized intermediate eigenvalue,* $\boldsymbol{\tau_3}$ *= normalized minimum eigenvalue,* $\boldsymbol{P_1}$ *= lineation,* $\boldsymbol{P_3}$ *= foliation,* $\boldsymbol{P_j}$ *= corrected degree of anisotropy, T = shape parameter,* $\boldsymbol{k_1}$ *= maximum eigenvector,* $\boldsymbol{k_2}$ *= intermediate eigenvector,* $\boldsymbol{k_3}$ *= minimum eigenvector, DEC = declination, INC = inclination, F = Hext F statistic.*

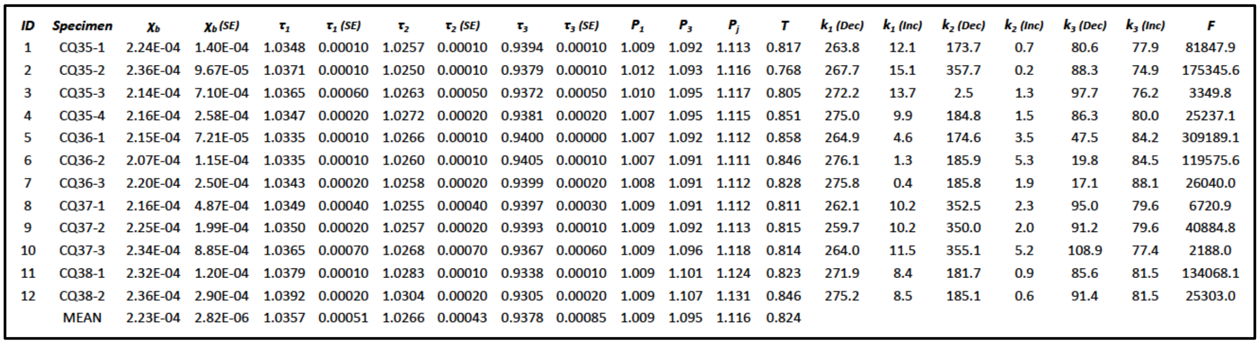

ID	Specimen	χ_b	χ_b (SE)	τ_1	τ_1 (SE)	τ_2	τ_2 (SE)	τ_3	τ_3 (SE)	P_1	P_3	P_j	T	k_1 (Dec)	k_1 (Inc)	k_2 (Dec)	k_2 (Inc)	k_3 (Dec)	k_3 (Inc)	F
1	CQ35-1	2.24E-04	1.40E-04	1.0348	0.00010	1.0257	0.00010	0.9394	0.00010	1.009	1.092	1.113	0.817	263.8	12.1	173.7	0.7	80.6	77.9	81847.9
2	CQ35-2	2.36E-04	9.67E-05	1.0371	0.00010	1.0250	0.00010	0.9379	0.00010	1.012	1.093	1.116	0.768	267.7	15.1	357.7	0.2	88.3	74.9	175345.6
3	CQ35-3	2.14E-04	7.10E-04	1.0365	0.00060	1.0263	0.00050	0.9372	0.00050	1.010	1.095	1.117	0.805	272.2	13.7	2.5	1.3	97.7	76.2	3349.8
4	CQ35-4	2.16E-04	2.58E-04	1.0347	0.00020	1.0272	0.00020	0.9381	0.00020	1.007	1.095	1.115	0.851	275.0	9.9	184.8	1.5	86.3	80.0	25237.1
5	CQ36-1	2.15E-04	7.21E-05	1.0335	0.00010	1.0266	0.00010	0.9400	0.00000	1.007	1.092	1.112	0.858	264.9	4.6	174.6	3.5	47.5	84.2	309189.1
6	CQ36-2	2.07E-04	1.15E-04	1.0335	0.00010	1.0260	0.00010	0.9405	0.00010	1.007	1.091	1.111	0.846	276.1	1.3	185.9	5.3	19.8	84.5	119575.6
7	CQ36-3	2.20E-04	2.50E-04	1.0343	0.00020	1.0258	0.00020	0.9399	0.00020	1.008	1.091	1.112	0.828	275.8	0.4	185.8	1.9	17.1	88.1	26040.0
8	CQ37-1	2.16E-04	4.87E-04	1.0349	0.00040	1.0255	0.00040	0.9397	0.00030	1.009	1.091	1.112	0.811	262.1	10.2	352.5	2.3	95.0	79.6	6720.9
9	CQ37-2	2.25E-04	1.99E-04	1.0350	0.00020	1.0257	0.00020	0.9393	0.00010	1.009	1.092	1.113	0.815	259.7	10.2	350.0	2.0	91.2	79.6	40884.8
10	CQ37-3	2.34E-04	8.85E-04	1.0365	0.00070	1.0268	0.00070	0.9367	0.00060	1.009	1.096	1.118	0.814	264.0	11.5	355.1	5.2	108.9	77.4	2188.0
11	CQ38-1	2.32E-04	1.20E-04	1.0379	0.00010	1.0283	0.00010	0.9338	0.00010	1.009	1.101	1.124	0.823	271.9	8.4	181.7	0.9	85.6	81.5	134068.1
12	CQ38-2	2.36E-04	2.90E-04	1.0392	0.00020	1.0304	0.00020	0.9305	0.00020	1.009	1.107	1.131	0.846	275.2	8.5	185.1	0.6	91.4	81.5	25303.0
	MEAN	2.23E-04	2.82E-06	1.0357	0.00051	1.0266	0.00043	0.9378	0.00085	1.009	1.095	1.116	0.824							

Table A-8. *Specimen AMS measurements for site D3 at the Campo do Tenente quarry. Summary of column headers:* χ_b *= bulk susceptibility, SE = standard error,* τ_1 *= normalized maximum eigenvalue,* τ_2 *= normalized intermediate eigenvalue,* τ_3 *= normalized minimum eigenvalue,* P_1 *= lineation,* P_3 *= foliation,* P_j *= corrected degree of anisotropy, T = shape parameter,* k_1 *= maximum eigenvector,* k_2 *= intermediate eigenvector,* k_3 *= minimum eigenvector, DEC = declination, INC = inclination, F = Hext F statistic.*

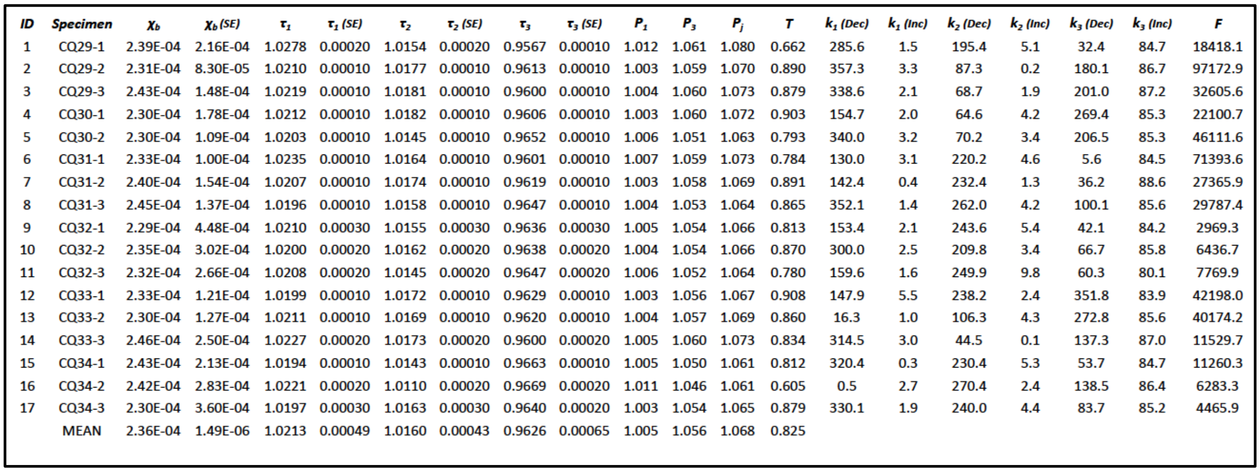

ID	Specimen	χ_b	χ_b (SE)	τ_1	τ_1 (SE)	τ_2	τ_2 (SE)	τ_3	τ_3 (SE)	P_1	P_3	P_j	T	k_1 (Dec)	k_1 (Inc)	k_2 (Dec)	k_2 (Inc)	k_3 (Dec)	k_3 (Inc)	F
1	CQ29-1	2.39E-04	2.16E-04	1.0278	0.00020	1.0154	0.00020	0.9567	0.00010	1.012	1.061	1.080	0.662	285.6	1.5	195.4	5.1	32.4	84.7	18418.1
2	CQ29-2	2.31E-04	8.30E-05	1.0210	0.00010	1.0177	0.00010	0.9613	0.00010	1.003	1.059	1.070	0.890	357.3	3.3	87.3	0.2	180.1	86.7	97172.9
3	CQ29-3	2.43E-04	1.48E-04	1.0219	0.00010	1.0181	0.00010	0.9600	0.00010	1.004	1.060	1.073	0.879	338.6	2.1	68.7	1.9	201.0	87.2	32605.6
4	CQ30-1	2.30E-04	1.78E-04	1.0212	0.00010	1.0182	0.00010	0.9606	0.00010	1.003	1.060	1.072	0.903	154.7	2.0	64.6	4.2	269.4	85.3	22100.7
5	CQ30-2	2.30E-04	1.09E-04	1.0203	0.00010	1.0145	0.00010	0.9652	0.00010	1.006	1.051	1.063	0.793	340.0	3.2	70.2	3.4	206.5	85.3	46111.6
6	CQ31-1	2.33E-04	1.00E-04	1.0235	0.00010	1.0164	0.00010	0.9601	0.00010	1.007	1.059	1.073	0.784	130.0	3.1	220.2	4.6	5.6	84.5	71393.6
7	CQ31-2	2.40E-04	1.54E-04	1.0207	0.00010	1.0174	0.00010	0.9619	0.00010	1.003	1.058	1.069	0.891	142.4	0.4	232.4	1.3	36.2	88.6	27365.9
8	CQ31-3	2.45E-04	1.37E-04	1.0196	0.00010	1.0158	0.00010	0.9647	0.00010	1.004	1.053	1.064	0.865	352.1	1.4	262.0	4.2	100.1	85.6	29787.4
9	CQ32-1	2.29E-04	4.48E-04	1.0210	0.00030	1.0155	0.00030	0.9636	0.00030	1.005	1.054	1.066	0.813	153.4	2.1	243.6	5.4	42.1	84.2	2969.3
10	CQ32-2	2.35E-04	3.02E-04	1.0200	0.00020	1.0162	0.00020	0.9638	0.00020	1.004	1.054	1.066	0.870	300.0	2.5	209.8	3.4	66.7	85.8	6436.7
11	CQ32-3	2.32E-04	2.66E-04	1.0208	0.00020	1.0145	0.00020	0.9647	0.00020	1.006	1.052	1.064	0.780	159.6	1.6	249.9	9.8	60.3	80.1	7769.9
12	CQ33-1	2.33E-04	1.21E-04	1.0199	0.00010	1.0172	0.00010	0.9629	0.00010	1.003	1.056	1.067	0.908	147.9	5.5	238.2	2.4	351.8	83.9	42198.0
13	CQ33-2	2.30E-04	1.27E-04	1.0211	0.00010	1.0169	0.00010	0.9620	0.00010	1.004	1.057	1.069	0.860	16.3	1.0	106.3	4.3	272.8	85.6	40174.2
14	CQ33-3	2.46E-04	2.50E-04	1.0227	0.00020	1.0173	0.00020	0.9600	0.00020	1.005	1.060	1.073	0.834	314.5	3.0	44.5	0.1	137.3	87.0	11529.7
15	CQ34-1	2.43E-04	2.13E-04	1.0194	0.00010	1.0143	0.00010	0.9663	0.00010	1.005	1.050	1.061	0.812	320.4	0.3	230.4	5.3	53.7	84.7	11260.3
16	CQ34-2	2.42E-04	2.83E-04	1.0221	0.00020	1.0110	0.00020	0.9669	0.00020	1.011	1.046	1.061	0.605	0.5	2.7	270.4	2.4	138.5	86.4	6283.3
17	CQ34-3	2.30E-04	3.60E-04	1.0197	0.00030	1.0163	0.00030	0.9640	0.00020	1.003	1.054	1.065	0.879	330.1	1.9	240.0	4.4	83.7	85.2	4465.9
	MEAN	2.36E-04	1.49E-06	1.0213	0.00049	1.0160	0.00043	0.9626	0.00065	1.005	1.056	1.068	0.825							

Table A-9. *Specimen AMS measurements for site C5 at the Campo do Tenente quarry. Summary of column headers:* χ_b *= bulk susceptibility, SE = standard error,* τ_1 *= normalized maximum eigenvalue,* τ_2 *= normalized intermediate eigenvalue,* τ_3 *= normalized minimum eigenvalue,* P_1 *= lineation,* P_3 *= foliation,* P_j *= corrected degree of anisotropy, T = shape parameter,* k_1 *= maximum eigenvector,* k_2 *= intermediate eigenvector,* k_3 *= minimum eigenvector, DEC = declination, INC = inclination, F = Hext F statistic.*

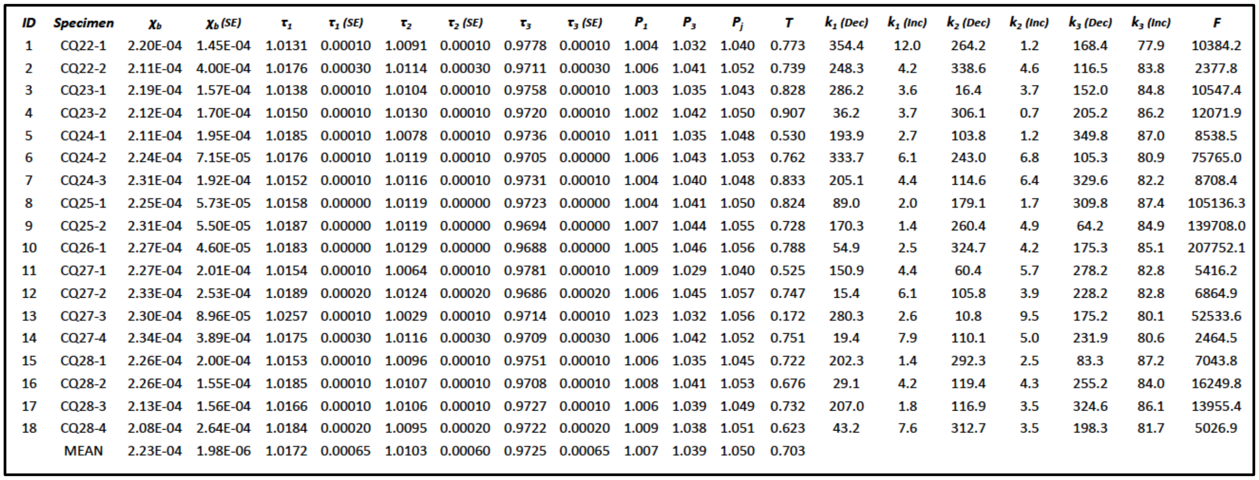

ID	Specimen	χ_b	χ_b (SE)	τ_1	τ_1 (SE)	τ_2	τ_2 (SE)	τ_3	τ_3 (SE)	P_1	P_3	P_j	T	k_1 (Dec)	k_1 (Inc)	k_2 (Dec)	k_2 (Inc)	k_3 (Dec)	k_3 (Inc)	F
1	CQ22-1	2.20E-04	1.45E-04	1.0131	0.00010	1.0091	0.00010	0.9778	0.00010	1.004	1.032	1.040	0.773	354.4	12.0	264.2	1.2	168.4	77.9	10384.2
2	CQ22-2	2.11E-04	4.00E-04	1.0176	0.00030	1.0114	0.00030	0.9711	0.00030	1.006	1.041	1.052	0.739	248.3	4.2	338.6	4.6	116.5	83.8	2377.8
3	CQ23-1	2.19E-04	1.57E-04	1.0138	0.00010	1.0104	0.00010	0.9758	0.00010	1.003	1.035	1.043	0.828	286.2	3.6	16.4	3.7	152.0	84.8	10547.4
4	CQ23-2	2.12E-04	1.70E-04	1.0150	0.00010	1.0130	0.00010	0.9720	0.00010	1.002	1.042	1.050	0.907	36.2	3.7	306.1	0.7	205.2	86.2	12071.9
5	CQ24-1	2.11E-04	1.95E-04	1.0185	0.00010	1.0078	0.00010	0.9736	0.00010	1.011	1.035	1.048	0.530	193.9	2.7	103.8	1.2	349.8	87.0	8538.5
6	CQ24-2	2.24E-04	7.15E-05	1.0176	0.00010	1.0119	0.00010	0.9705	0.00000	1.006	1.043	1.053	0.762	333.7	6.1	243.0	6.8	105.3	80.9	75765.0
7	CQ24-3	2.31E-04	1.92E-04	1.0152	0.00010	1.0116	0.00010	0.9731	0.00010	1.004	1.040	1.048	0.833	205.1	4.4	114.6	6.4	329.6	82.2	8708.4
8	CQ25-1	2.25E-04	5.73E-05	1.0158	0.00000	1.0119	0.00000	0.9723	0.00000	1.004	1.041	1.050	0.824	89.0	2.0	179.1	1.7	309.8	87.4	105136.3
9	CQ25-2	2.31E-04	5.50E-05	1.0187	0.00000	1.0119	0.00000	0.9694	0.00000	1.007	1.044	1.055	0.728	170.3	1.4	260.4	4.9	64.2	84.9	139708.0
10	CQ26-1	2.27E-04	4.60E-05	1.0183	0.00000	1.0129	0.00000	0.9688	0.00000	1.005	1.046	1.056	0.788	54.9	2.5	324.7	4.2	175.3	85.1	207752.1
11	CQ27-1	2.27E-04	2.01E-04	1.0154	0.00010	1.0064	0.00010	0.9781	0.00010	1.009	1.029	1.040	0.525	150.9	4.4	60.4	5.7	278.2	82.8	5416.2
12	CQ27-2	2.33E-04	2.53E-04	1.0189	0.00020	1.0124	0.00020	0.9686	0.00020	1.006	1.045	1.057	0.747	15.4	6.1	105.8	3.9	228.2	82.8	6864.9
13	CQ27-3	2.30E-04	8.96E-05	1.0257	0.00010	1.0029	0.00010	0.9714	0.00010	1.023	1.032	1.056	0.172	280.3	2.6	10.8	9.5	175.2	80.1	52533.6
14	CQ27-4	2.34E-04	3.89E-04	1.0175	0.00030	1.0116	0.00030	0.9709	0.00030	1.006	1.042	1.052	0.751	19.4	7.9	110.1	5.0	231.9	80.6	2464.5
15	CQ28-1	2.26E-04	2.00E-04	1.0153	0.00010	1.0096	0.00010	0.9751	0.00010	1.006	1.035	1.045	0.722	202.3	1.4	292.3	2.5	83.3	87.2	7043.8
16	CQ28-2	2.26E-04	1.55E-04	1.0185	0.00010	1.0107	0.00010	0.9708	0.00010	1.008	1.041	1.053	0.676	29.1	4.2	119.4	4.3	255.2	84.0	16249.8
17	CQ28-3	2.13E-04	1.56E-04	1.0166	0.00010	1.0106	0.00010	0.9727	0.00010	1.006	1.039	1.049	0.732	207.0	1.8	116.9	3.5	324.6	86.1	13955.4
18	CQ28-4	2.08E-04	2.64E-04	1.0184	0.00020	1.0095	0.00020	0.9722	0.00020	1.009	1.038	1.051	0.623	43.2	7.6	312.7	3.5	198.3	81.7	5026.9
	MEAN	2.23E-04	1.98E-06	1.0172	0.00065	1.0103	0.00060	0.9725	0.00065	1.007	1.039	1.050	0.703							

Table A-10. *Specimen AMS measurements for site FE1 at the Campo do Tenente quarry. Summary of column headers:* χ_b *= bulk susceptibility, SE = standard error,* τ_1 *= normalized maximum eigenvalue,* τ_2 *= normalized intermediate eigenvalue,* τ_3 *= normalized minimum eigenvalue,* P_1 *= lineation,* P_3 *= foliation,* P_j *= corrected degree of anisotropy, T = shape parameter,* k_1 *= maximum eigenvector,* k_2 *= intermediate eigenvector,* k_3 *= minimum eigenvector, DEC = declination, INC = inclination, F = Hext F statistic.*

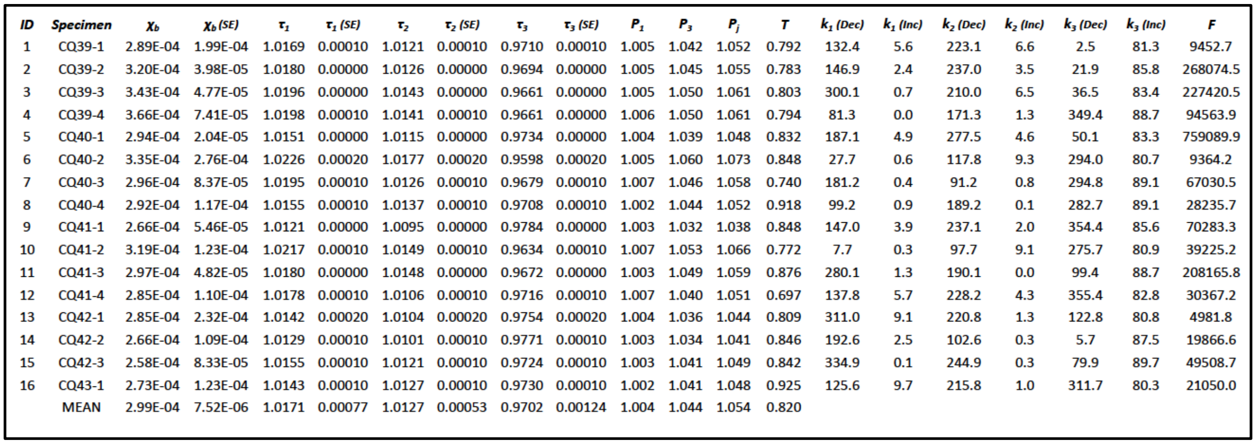

ID	Specimen	χ_b	χ_b (SE)	τ_1	τ_1 (SE)	τ_2	τ_2 (SE)	τ_3	τ_3 (SE)	P_1	P_3	P_j	T	k_1 (Dec)	k_1 (Inc)	k_2 (Dec)	k_2 (Inc)	k_3 (Dec)	k_3 (Inc)	F
1	CQ39-1	2.89E-04	1.99E-04	1.0169	0.00010	1.0121	0.00010	0.9710	0.00010	1.005	1.042	1.052	0.792	132.4	5.6	223.1	6.6	2.5	81.3	9452.7
2	CQ39-2	3.20E-04	3.98E-05	1.0180	0.00000	1.0126	0.00000	0.9694	0.00000	1.005	1.045	1.055	0.783	146.9	2.4	237.0	3.5	21.9	85.8	268074.5
3	CQ39-3	3.43E-04	4.77E-05	1.0196	0.00000	1.0143	0.00000	0.9661	0.00000	1.005	1.050	1.061	0.803	300.1	0.7	210.0	6.5	36.5	83.4	227420.5
4	CQ39-4	3.66E-04	7.41E-05	1.0198	0.00010	1.0141	0.00010	0.9661	0.00000	1.006	1.050	1.061	0.794	81.3	0.0	171.3	1.3	349.4	88.7	94563.9
5	CQ40-1	2.94E-04	2.04E-05	1.0151	0.00000	1.0115	0.00000	0.9734	0.00000	1.004	1.039	1.048	0.832	187.1	4.9	277.5	4.6	50.1	83.3	759089.9
6	CQ40-2	3.35E-04	2.76E-04	1.0226	0.00020	1.0177	0.00020	0.9598	0.00020	1.005	1.060	1.073	0.848	27.7	0.6	117.8	9.3	294.0	80.7	9364.2
7	CQ40-3	2.96E-04	8.37E-05	1.0195	0.00010	1.0126	0.00010	0.9679	0.00010	1.007	1.046	1.058	0.740	181.2	0.4	91.2	0.8	294.8	89.1	67030.5
8	CQ40-4	2.92E-04	1.17E-04	1.0155	0.00010	1.0137	0.00010	0.9708	0.00010	1.002	1.044	1.052	0.918	99.2	0.9	189.2	0.1	282.7	89.1	28235.7
9	CQ41-1	2.66E-04	5.46E-05	1.0121	0.00000	1.0095	0.00000	0.9784	0.00000	1.003	1.032	1.038	0.848	147.0	3.9	237.1	2.0	354.4	85.6	70283.3
10	CQ41-2	3.19E-04	1.23E-04	1.0217	0.00010	1.0149	0.00010	0.9634	0.00010	1.007	1.053	1.066	0.772	7.7	0.3	97.7	9.1	275.7	80.9	39225.2
11	CQ41-3	2.97E-04	4.82E-05	1.0180	0.00000	1.0148	0.00000	0.9672	0.00000	1.003	1.049	1.059	0.876	280.1	1.3	190.1	0.0	99.4	88.7	208165.8
12	CQ41-4	2.85E-04	1.10E-04	1.0178	0.00010	1.0106	0.00010	0.9716	0.00010	1.007	1.040	1.051	0.697	137.8	5.7	228.2	4.3	355.4	82.8	30367.2
13	CQ42-1	2.85E-04	2.32E-04	1.0142	0.00020	1.0104	0.00020	0.9754	0.00020	1.004	1.036	1.044	0.809	311.0	9.1	220.8	1.3	122.8	80.8	4981.8
14	CQ42-2	2.66E-04	1.09E-04	1.0129	0.00010	1.0101	0.00010	0.9771	0.00010	1.003	1.034	1.041	0.846	192.6	2.5	102.6	0.3	5.7	87.5	19866.6
15	CQ42-3	2.58E-04	8.33E-05	1.0155	0.00010	1.0121	0.00010	0.9724	0.00010	1.003	1.041	1.049	0.842	334.9	0.1	244.9	0.3	79.9	89.7	49508.7
16	CQ43-1	2.73E-04	1.23E-04	1.0143	0.00010	1.0127	0.00010	0.9730	0.00010	1.002	1.041	1.048	0.925	125.6	9.7	215.8	1.0	311.7	80.3	21050.0
	MEAN	2.99E-04	7.52E-06	1.0171	0.00077	1.0127	0.00053	0.9702	0.00124	1.004	1.044	1.054	0.820							

Table A-11. *Specimen AMS measurements for site H7 at the Porto Amazonas road cut exposure. Summary of column headers:* χ_b *= bulk susceptibility, SE = standard error,* τ_1 *= normalized maximum eigenvalue,* τ_2 *= normalized intermediate eigenvalue,* τ_3 *= normalized minimum eigenvalue,* P_1 *= lineation,* P_3 *= foliation,* P_j *= corrected degree of anisotropy, T = shape parameter,* k_1 *= maximum eigenvector,* k_2 *= intermediate eigenvector,* k_3 *= minimum eigenvector, DEC = declination, INC = inclination, F = Hext F statistic.*

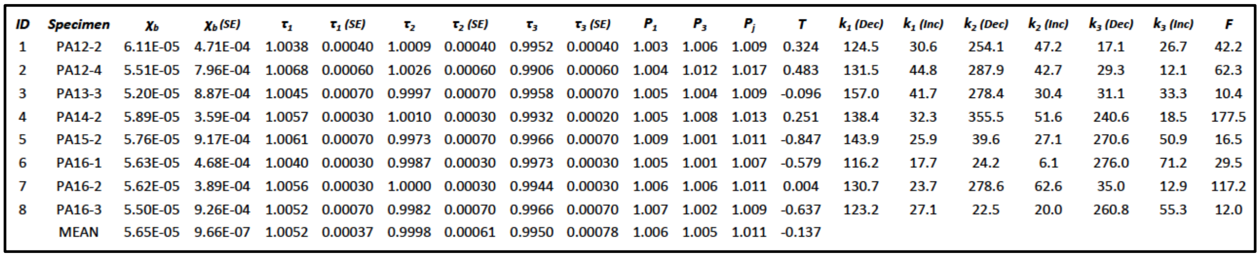

ID	Specimen	χ_b	χ_b (SE)	τ_1	τ_1 (SE)	τ_2	τ_2 (SE)	τ_3	τ_3 (SE)	P_1	P_3	P_j	T	k_1 (Dec)	k_1 (Inc)	k_2 (Dec)	k_2 (Inc)	k_3 (Dec)	k_3 (Inc)	F
1	PA12-2	6.11E-05	4.71E-04	1.0038	0.00040	1.0009	0.00040	0.9952	0.00040	1.003	1.006	1.009	0.324	124.5	30.6	254.1	47.2	17.1	26.7	42.2
2	PA12-4	5.51E-05	7.96E-04	1.0068	0.00060	1.0026	0.00060	0.9906	0.00060	1.004	1.012	1.017	0.483	131.5	44.8	287.9	42.7	29.3	12.1	62.3
3	PA13-3	5.20E-05	8.87E-04	1.0045	0.00070	0.9997	0.00070	0.9958	0.00070	1.005	1.004	1.009	-0.096	157.0	41.7	278.4	30.4	31.1	33.3	10.4
4	PA14-2	5.89E-05	3.59E-04	1.0057	0.00030	1.0010	0.00030	0.9932	0.00020	1.005	1.008	1.013	0.251	138.4	32.3	355.5	51.6	240.6	18.5	177.5
5	PA15-2	5.76E-05	9.17E-04	1.0061	0.00070	0.9973	0.00070	0.9966	0.00070	1.009	1.001	1.011	-0.847	143.9	25.9	39.6	27.1	270.6	50.9	16.5
6	PA16-1	5.63E-05	4.68E-04	1.0040	0.00030	0.9987	0.00030	0.9973	0.00030	1.005	1.001	1.007	-0.579	116.2	17.7	24.2	6.1	276.0	71.2	29.5
7	PA16-2	5.62E-05	3.89E-04	1.0056	0.00030	1.0000	0.00030	0.9944	0.00030	1.006	1.006	1.011	0.004	130.7	23.7	278.6	62.6	35.0	12.9	117.2
8	PA16-3	5.50E-05	9.26E-04	1.0052	0.00070	0.9982	0.00070	0.9966	0.00070	1.007	1.002	1.009	-0.637	123.2	27.1	22.5	20.0	260.8	55.3	12.0
	MEAN	5.65E-05	9.66E-07	1.0052	0.00037	0.9998	0.00061	0.9950	0.00078	1.006	1.005	1.011	-0.137							

Table A-12. *Specimen AMS measurements for site M6 at the Porto Amazonas road cut exposure. Summary of column headers:* χ_b *= bulk susceptibility, SE = standard error,* τ_1 *= normalized maximum eigenvalue,* τ_2 *= normalized intermediate eigenvalue,* τ_3 *= normalized minimum eigenvalue,* P_1 *= lineation,* P_3 *= foliation,* P_j *= corrected degree of anisotropy, T = shape parameter,* k_1 *= maximum eigenvector,* k_2 *= intermediate eigenvector,* k_3 *= minimum eigenvector, DEC = declination, INC = inclination, F = Hext F statistic.*

ID	Specimen	χ_b	χ_b (SE)	τ_1	τ_1 (SE)	τ_2	τ_2 (SE)	τ_3	τ_3 (SE)	P_1	P_3	P_j	T	k_1 (Dec)	k_1 (Inc)	k_2 (Dec)	k_2 (Inc)	k_3 (Dec)	k_3 (Inc)	F
1	PA07-1	7.46E-05	6.49E-04	1.0042	0.00050	0.9987	0.00050	0.9971	0.00050	1.006	1.002	1.007	-0.559	149.8	29.8	273.0	43.7	39.2	31.7	15.8
2	PA07-2	5.58E-05	9.22E-04	1.0057	0.00060	1.0007	0.00070	0.9935	0.00070	1.005	1.007	1.012	0.184	154.6	15.5	273.4	60.1	57.2	24.9	24.4
3	PA07-3	5.01E-05	8.13E-04	1.0053	0.00060	1.0017	0.00060	0.9930	0.00060	1.004	1.009	1.013	0.416	142.0	16.3	263.0	60.5	44.6	23.9	30.5
4	PA08-1	5.46E-05	8.99E-04	1.0044	0.00070	0.9989	0.00070	0.9967	0.00070	1.006	1.002	1.008	-0.438	170.9	26.3	301.5	52.8	68.0	24.3	10.1
5	PA08-2	5.39E-05	6.53E-04	1.0039	0.00050	1.0012	0.00050	0.9950	0.00050	1.003	1.006	1.009	0.392	152.2	23.0	274.3	51.4	48.5	29.1	22.3
6	PA08-3	4.83E-05	1.60E-03	1.0058	0.00120	1.0018	0.00130	0.9924	0.00130	1.004	1.010	1.014	0.406	197.9	54.7	303.3	10.6	40.3	33.2	8.0
7	PA08-4	4.91E-05	9.42E-04	1.0052	0.00070	1.0006	0.00070	0.9942	0.00070	1.005	1.006	1.011	0.173	152.6	24.3	287.8	57.5	53.0	20.2	16.9
8	PA09-1	6.64E-05	9.67E-04	1.0048	0.00080	0.9995	0.00080	0.9957	0.00080	1.005	1.004	1.009	-0.149	175.4	40.6	279.2	15.6	25.6	45.2	9.4
9	PA09-2	6.01E-05	7.54E-04	1.0037	0.00050	1.0015	0.00060	0.9948	0.00050	1.002	1.007	1.009	0.491	157.0	19.2	285.8	61.0	59.3	20.9	20.7
10	PA09-3	5.04E-05	7.39E-04	1.0070	0.00060	0.9999	0.00060	0.9931	0.00060	1.007	1.007	1.014	-0.018	167.6	28.6	290.1	44.6	57.8	31.8	44.3
11	PA10-1	5.72E-05	1.14E-03	1.0053	0.00080	1.0007	0.00080	0.9940	0.00090	1.005	1.007	1.011	0.202	139.1	1.3	231.8	64.6	48.5	25.3	11.8
12	PA10-3	4.61E-05	1.22E-03	1.0042	0.00090	1.0015	0.00100	0.9943	0.00090	1.003	1.007	1.010	0.441	166.9	29.2	291.1	45.1	57.6	30.6	8.7
13	PA11-1	4.44E-05	4.98E-04	1.0051	0.00040	1.0024	0.00040	0.9925	0.00040	1.003	1.010	1.013	0.570	178.7	33.5	308.5	44.1	68.6	27.4	94.5
14	PA11-2	4.41E-05	1.40E-03	1.0087	0.00100	0.9984	0.00100	0.9930	0.00100	1.010	1.005	1.016	-0.312	154.1	21.0	289.9	61.8	57.0	18.0	17.2
15	PA11-3	4.15E-05	1.18E-03	1.0066	0.00090	0.9989	0.00100	0.9945	0.00090	1.008	1.004	1.012	-0.270	161.7	43.4	291.9	34.3	42.5	27.3	12.5
	MEAN	5.31E-05	2.30E-06	1.0053	0.00034	1.0004	0.00033	0.9943	0.00037	1.005	1.006	1.011	0.102							

Table A-13. *Specimen AMS measurements for site O5 at the Porto Amazonas road cut exposure. Summary of column headers:* χ_b *= bulk susceptibility, SE = standard error,* τ_1 *= normalized maximum eigenvalue,* τ_2 *= normalized intermediate eigenvalue,* τ_3 *= normalized minimum eigenvalue,* P_1 *= lineation,* P_3 *= foliation,* P_j *= corrected degree of anisotropy, T = shape parameter,* k_1 *= maximum eigenvector,* k_2 *= intermediate eigenvector,* k_3 *= minimum eigenvector, DEC = declination, INC = inclination, F = Hext F statistic.*

ID	Specimen	χ_b	χ_b (SE)	τ_1	τ_1 (SE)	τ_2	τ_2 (SE)	τ_3	τ_3 (SE)	P_1	P_3	P_j	T	k_1 (Dec)	k_1 (Inc)	k_2 (Dec)	k_2 (Inc)	k_3 (Dec)	k_3 (Inc)	F
1	PA01-1	4.46E-05	9.23E-04	1.0038	0.00070	0.9989	0.00070	0.9973	0.00070	1.005	1.002	1.007	-0.501	101.4	38.5	231.2	38.8	346.4	27.9	6.3
2	PA01-2	4.45E-05	3.26E-04	1.0050	0.00020	1.0003	0.00020	0.9947	0.00020	1.005	1.006	1.010	0.080	283.1	5.6	178.7	68.6	15.2	20.6	145.2
3	PA01-3	3.55E-05	1.86E-04	1.0041	0.00010	1.0010	0.00010	0.9949	0.00010	1.003	1.006	1.009	0.328	285.8	2.6	157.2	85.8	15.9	3.3	384.3
4	PA02-1	5.05E-05	2.02E-04	1.0034	0.00010	1.0000	0.00010	0.9966	0.00010	1.003	1.003	1.007	0.008	346.1	7.1	234.3	71.4	78.3	17.1	166.7
5	PA02-2	4.91E-05	4.78E-04	1.0029	0.00030	0.9997	0.00040	0.9974	0.00040	1.003	1.002	1.006	-0.159	169.2	9.5	263.9	26.1	60.9	62.0	19.0
6	PA02-3	4.99E-05	2.99E-04	1.0023	0.00020	1.0004	0.00020	0.9973	0.00020	1.002	1.003	1.005	0.226	182.0	39.8	293.4	23.7	45.8	40.9	30.3
7	PA03-1	5.06E-05	5.01E-04	1.0039	0.00040	1.0001	0.00040	0.9959	0.00030	1.004	1.004	1.008	0.054	161.4	37.8	323.2	50.8	64.4	9.0	35.0
8	PA03-2	4.54E-05	3.91E-04	1.0030	0.00030	1.0006	0.00030	0.9963	0.00030	1.002	1.004	1.007	0.285	184.9	48.4	331.0	36.4	74.3	17.4	41.6
9	PA04-1	5.48E-05	3.47E-04	1.0026	0.00020	0.9991	0.00030	0.9984	0.00030	1.003	1.001	1.004	-0.661	349.9	70.6	186.0	18.7	94.3	5.0	22.8
10	PA04-2	4.89E-05	3.88E-04	1.0033	0.00030	0.9995	0.00030	0.9972	0.00030	1.004	1.002	1.006	-0.247	159.1	46.5	302.8	37.4	48.0	18.8	30.7
11	PA04-3	4.38E-05	6.07E-04	1.0041	0.00040	1.0005	0.00040	0.9954	0.00040	1.004	1.005	1.009	0.162	155.0	6.5	272.0	76.0	63.6	12.4	30.0
12	PA04-4	4.38E-05	4.27E-04	1.0047	0.00030	0.9995	0.00030	0.9958	0.00030	1.005	1.004	1.009	-0.167	159.2	55.2	2.9	32.4	265.7	11.2	56.0
13	PA05-1	4.82E-05	2.74E-04	1.0046	0.00020	1.0003	0.00020	0.9951	0.00020	1.004	1.005	1.010	0.104	158.1	10.9	36.0	70.1	251.4	16.5	172.4
14	PA05-2	4.70E-05	6.51E-04	1.0037	0.00050	1.0003	0.00050	0.9960	0.00050	1.003	1.004	1.008	0.108	149.5	34.6	6.2	49.2	253.0	18.7	18.3
15	PA06-1	5.63E-05	3.83E-04	1.0036	0.00030	0.9998	0.00030	0.9967	0.00030	1.004	1.003	1.007	-0.093	170.5	7.4	357.1	82.5	260.6	0.9	48.8
16	PA06-3	4.52E-05	4.79E-04	1.0023	0.00030	1.0013	0.00030	0.9964	0.00030	1.001	1.005	1.006	0.644	349.2	87.7	189.2	2.1	99.2	0.8	23.5
17	PA06-2	5.68E-05	4.29E-04	1.0019	0.00030	0.9999	0.00030	0.9981	0.00030	1.002	1.002	1.004	-0.058	169.3	6.5	261.2	16.3	58.2	72.4	11.4
	MEAN	4.79E-05	1.27E-06	1.0035	0.00022	1.0001	0.00015	0.9964	0.00026	1.003	1.004	1.007	0.007							

Table A-14. *Specimen AMS measurements for site P5 near Cachoeira do Sul. Summary of column headers:* $\boldsymbol{\chi_b}$ *= bulk susceptibility, SE = standard error,* $\boldsymbol{\tau_1}$ *= normalized maximum eigenvalue,* $\boldsymbol{\tau_2}$ *= normalized intermediate eigenvalue,* $\boldsymbol{\tau_3}$ *= normalized minimum eigenvalue,* $\boldsymbol{P_1}$ *= lineation,* $\boldsymbol{P_3}$ *= foliation,* $\boldsymbol{P_j}$ *= corrected degree of anisotropy, T = shape parameter,* $\boldsymbol{k_1}$ *= maximum eigenvector,* $\boldsymbol{k_2}$ *= intermediate eigenvector,* $\boldsymbol{k_3}$ *= minimum eigenvector, DEC = declination, INC = inclination, F = Hext F statistic.*

ID	Specimen	χ_b	χ_b (SE)	τ_1	τ_1 (SE)	τ_2	τ_2 (SE)	τ_3	τ_3 (SE)	P_1	P_3	P_j	T	k_1 (Dec)	k_1 (Inc)	k_2 (Dec)	k_2 (Inc)	k_3 (Dec)	k_3 (Inc)	F
1	PS03-1	9.29E-05	5.87E-04	1.0077	0.00050	1.0031	0.00050	0.9892	0.00040	1.005	1.014	1.019	0.510	182.2	18.3	91.0	3.6	350.1	71.3	149.0
2	PS04-1	7.52E-05	9.92E-05	1.0045	0.00010	0.9994	0.00010	0.9962	0.00010	1.005	1.003	1.008	-0.228	160.5	19.8	258.5	21.3	31.5	60.2	729.7
3	PS05-1	7.52E-05	4.17E-04	1.0080	0.00030	1.0021	0.00030	0.9899	0.00030	1.006	1.012	1.019	0.356	154.8	12.4	61.3	15.5	281.9	69.9	278.9
4	PS05-2	6.68E-05	1.95E-04	1.0078	0.00020	1.0031	0.00010	0.9891	0.00010	1.005	1.014	1.020	0.492	168.5	21.4	73.0	13.6	312.8	64.3	1354.1
5	PS05-3	5.77E-05	2.23E-04	1.0164	0.00020	1.0071	0.00020	0.9766	0.00020	1.009	1.031	1.043	0.541	182.3	13.1	91.1	5.1	340.2	75.9	4977.1
6	PS06-1	6.22E-05	1.95E-04	1.0089	0.00020	1.0010	0.00010	0.9900	0.00020	1.008	1.011	1.019	0.165	169.8	12.3	264.9	21.8	52.4	64.6	971.2
7	PS07-1	8.31E-05	3.72E-04	1.0053	0.00030	1.0036	0.00030	0.9911	0.00030	1.002	1.013	1.016	0.761	148.3	13.7	55.0	13.2	282.5	70.8	246.4
	MEAN	7.33E-05	4.63E-06	1.0084	0.00146	1.0028	0.00091	0.9889	0.00225	1.006	1.014	1.021	0.371							

Table A-15. *Specimen AMS measurements for site P7 near Cachoeira do Sul. Summary of column headers:* $\boldsymbol{\chi_b}$ *= bulk susceptibility, SE = standard error,* $\boldsymbol{\tau_1}$ *= normalized maximum eigenvalue,* $\boldsymbol{\tau_2}$ *= normalized intermediate eigenvalue,* $\boldsymbol{\tau_3}$ *= normalized minimum eigenvalue,* $\boldsymbol{P_1}$ *= lineation,* $\boldsymbol{P_3}$ *= foliation,* $\boldsymbol{P_j}$ *= corrected degree of anisotropy, T = shape parameter,* $\boldsymbol{k_1}$ *= maximum eigenvector,* $\boldsymbol{k_2}$ *= intermediate eigenvector,* $\boldsymbol{k_3}$ *= minimum eigenvector, DEC = declination, INC = inclination, F = Hext F statistic.*

ID	Specimen	χ_b	χ_b (SE)	τ_1	τ_1 (SE)	τ_2	τ_2 (SE)	τ_3	τ_3 (SE)	P_1	P_3	P_j	T	k_1 (Dec)	k_1 (Inc)	k_2 (Dec)	k_2 (Inc)	k_3 (Dec)	k_3 (Inc)	F
1	PS08-1	4.32E-05	9.28E-04	1.0062	0.00070	0.9985	0.00070	0.9953	0.00070	1.008	1.003	1.011	-0.419	136.5	20.9	41.2	13.8	280.0	64.6	17.5
2	PS08-2	6.23E-05	5.31E-04	1.0114	0.00040	0.9996	0.00040	0.9890	0.00040	1.012	1.011	1.023	-0.048	178.6	16.4	81.6	22.4	301.7	61.7	219.3
3	PS09-1	5.33E-05	2.49E-04	1.0111	0.00020	1.0061	0.00020	0.9828	0.00020	1.005	1.024	1.031	0.648	213.1	15.8	114.0	29.2	328.0	56.0	1671.0
4	PS09-2	4.69E-05	6.90E-04	1.0054	0.00060	0.9988	0.00060	0.9958	0.00050	1.007	1.003	1.010	-0.366	145.7	23.0	253.9	36.3	30.7	44.8	21.3
5	PS09-3	4.25E-05	6.23E-04	1.0078	0.00050	0.9978	0.00050	0.9944	0.00050	1.010	1.003	1.014	-0.490	112.8	28.8	236.7	45.4	3.8	30.7	62.2
6	PS10-1	3.98E-05	6.94E-04	1.0140	0.00050	0.9983	0.00050	0.9877	0.00050	1.016	1.011	1.027	-0.186	109.0	21.3	272.0	67.8	16.7	5.9	206.8
7	PS12-1	3.86E-05	4.89E-04	1.0068	0.00040	1.0020	0.00040	0.9912	0.00040	1.005	1.011	1.016	0.384	161.0	19.2	68.7	6.4	321.0	69.7	136.5
	MEAN	4.67E-05	3.20E-06	1.0090	0.00122	1.0002	0.00112	0.9909	0.00179	1.009	1.009	1.019	-0.068							

Table A-16. *Specimen AMS measurements for site P9 near Cachoeira do Sul. Summary of column headers:* $\boldsymbol{\chi_b}$ *= bulk susceptibility, SE = standard error,* $\boldsymbol{\tau_1}$ *= normalized maximum eigenvalue,* $\boldsymbol{\tau_2}$ *= normalized intermediate eigenvalue,* $\boldsymbol{\tau_3}$ *= normalized minimum eigenvalue,* $\boldsymbol{P_1}$ *= lineation,* $\boldsymbol{P_3}$ *= foliation,* $\boldsymbol{P_j}$ *= corrected degree of anisotropy, T = shape parameter,* $\boldsymbol{k_1}$ *= maximum eigenvector,* $\boldsymbol{k_2}$ *= intermediate eigenvector,* $\boldsymbol{k_3}$ *= minimum eigenvector, DEC = declination, INC = inclination, F = Hext F statistic.*

ID	Specimen	χ_b	χ_b (SE)	τ_1	τ_1 (SE)	τ_2	τ_2 (SE)	τ_3	τ_3 (SE)	P_1	P_3	P_j	T	k_1 (Dec)	k_1 (Inc)	k_2 (Dec)	k_2 (Inc)	k_3 (Dec)	k_3 (Inc)	F
1	PS13-1	4.59E-05	7.81E-04	1.0069	0.00060	1.0017	0.00060	0.9914	0.00060	1.005	1.010	1.016	0.327	154.1	22.4	248.2	9.8	0.3	65.3	49.9
2	PS16-1	4.49E-05	8.36E-04	1.0054	0.00070	1.0024	0.00070	0.9922	0.00060	1.003	1.010	1.014	0.543	307.7	0.6	217.6	11.6	40.7	78.3	33.0
3	PS17-1	4.71E-05	3.25E-04	1.0087	0.00020	1.0001	0.00030	0.9912	0.00020	1.009	1.009	1.018	0.027	154.7	25.6	62.6	4.4	323.6	64.0	348.7
4	PS18-1	4.44E-05	8.34E-04	1.0079	0.00060	1.0017	0.00070	0.9903	0.00070	1.006	1.011	1.018	0.296	153.9	10.4	249.1	26.2	44.2	61.6	54.1
5	PS20-1	4.45E-05	1.28E-03	1.0104	0.00100	1.0024	0.00100	0.9873	0.00090	1.008	1.015	1.024	0.312	123.2	14.4	213.5	1.2	308.2	75.6	46.3
6	PS21-1	4.05E-05	1.35E-03	1.0097	0.00110	0.9995	0.00110	0.9908	0.00100	1.010	1.009	1.019	-0.078	123.1	6.0	213.9	7.4	354.2	80.5	23.0
7	PS22-1	4.65E-05	4.43E-04	1.0152	0.00030	1.0055	0.00040	0.9793	0.00040	1.010	1.027	1.038	0.463	107.5	24.0	207.7	21.5	334.7	56.7	776.3
8	PS23-1	4.19E-05	6.00E-04	1.0085	0.00040	1.0008	0.00050	0.9908	0.00050	1.008	1.010	1.018	0.137	114.7	3.4	205.2	9.9	5.8	79.5	109.0
9	PS24-1	6.41E-05	6.28E-04	1.0223	0.00050	1.0077	0.00050	0.9699	0.00050	1.014	1.039	1.056	0.453	134.8	6.4	226.2	11.5	16.1	76.8	891.3
	MEAN	4.67E-05	2.29E-06	1.0106	0.00173	1.0024	0.00087	0.9870	0.00252	1.008	1.016	1.025	0.276							

Table A-17. *Specimen AMS measurements for site E1 near Ibaré. Summary of column headers:* $\boldsymbol{\chi_b}$ *= bulk susceptibility, SE = standard error,* $\boldsymbol{\tau_1}$ *= normalized maximum eigenvalue,* $\boldsymbol{\tau_2}$ *= normalized intermediate eigenvalue,* $\boldsymbol{\tau_3}$ *= normalized minimum eigenvalue,* $\boldsymbol{P_1}$ *= lineation,* $\boldsymbol{P_3}$ *= foliation,* $\boldsymbol{P_j}$ *= corrected degree of anisotropy, T = shape parameter,* $\boldsymbol{k_1}$ *= maximum eigenvector,* $\boldsymbol{k_2}$ *= intermediate eigenvector,* $\boldsymbol{k_3}$ *= minimum eigenvector, DEC = declination, INC = inclination, F = Hext F statistic.*

ID	Specimen	χ_b	χ_b (SE)	τ_1	τ_1 (SE)	τ_2	τ_2 (SE)	τ_3	τ_3 (SE)	P_1	P_3	P_j	T	k_1 (Dec)	k_1 (Inc)	k_2 (Dec)	k_2 (Inc)	k_3 (Dec)	k_3 (Inc)	F
1	ERT01-1	1.04E-04	7.07E-04	1.0045	0.00050	1.0003	0.00050	0.9952	0.00050	1.004	1.005	1.009	0.088	169.5	13.2	27.8	73.4	261.9	9.9	19.3
2	ERT01-2	1.14E-04	3.52E-04	1.0035	0.00030	0.9991	0.00030	0.9974	0.00030	1.004	1.002	1.006	-0.432	179.3	31.9	345.8	57.4	85.4	6.1	33.1
3	ERT02-1	1.03E-04	3.26E-04	1.0033	0.00030	1.0001	0.00030	0.9966	0.00020	1.003	1.004	1.007	0.055	286.6	43.9	144.9	39.2	37.4	20.3	51.1
4	ERT02-2	1.02E-04	1.85E-04	1.0029	0.00010	1.0008	0.00010	0.9962	0.00010	1.002	1.005	1.007	0.378	338.5	50.7	220.2	21.2	116.6	31.3	144.1
5	ERT02-3	1.00E-04	3.34E-04	1.0053	0.00030	0.9995	0.00030	0.9952	0.00030	1.006	1.004	1.010	-0.146	352.4	57.9	185.7	31.4	92.0	6.0	111.1
6	ERT02-4	1.03E-04	6.45E-04	1.0047	0.00050	1.0029	0.00050	0.9924	0.00050	1.002	1.011	1.013	0.719	332.4	69.4	187.6	17.1	94.1	11.2	48.9
7	ERT03-1	9.92E-05	2.84E-04	1.0037	0.00020	1.0013	0.00020	0.9950	0.00020	1.002	1.006	1.009	0.454	35.6	43.2	148.9	22.8	258.2	38.1	101.1
8	ERT03-2	1.04E-04	1.68E-04	1.0021	0.00010	1.0005	0.00010	0.9974	0.00010	1.002	1.003	1.005	0.287	196.6	7.0	95.0	58.7	290.7	30.4	86.6
9	ERT03-3	1.01E-04	1.94E-04	1.0016	0.00020	1.0007	0.00020	0.9977	0.00020	1.001	1.003	1.004	0.551	158.0	45.0	27.8	32.8	278.7	27.0	46.7
10	ERT03-4	1.00E-04	3.20E-04	1.0039	0.00030	1.0013	0.00020	0.9948	0.00020	1.003	1.007	1.009	0.434	169.3	49.3	331.1	39.3	68.6	9.1	114.3
11	ERT04-1	1.01E-04	2.06E-04	1.0040	0.00020	1.0004	0.00020	0.9956	0.00020	1.004	1.005	1.008	0.152	178.7	11.5	76.5	46.3	279.0	41.4	186.5
12	ERT04-2	1.03E-04	5.52E-04	1.0036	0.00040	1.0006	0.00040	0.9958	0.00040	1.003	1.005	1.008	0.221	185.5	7.3	87.7	46.7	282.2	42.3	22.1
13	ERT04-3	1.07E-04	4.55E-04	1.0043	0.00040	0.9996	0.00030	0.9962	0.00030	1.005	1.003	1.008	-0.161	178.8	27.3	323.2	57.6	80.2	16.1	38.7
14	ERT04-4	1.17E-04	1.83E-04	1.0030	0.00010	1.0000	0.00010	0.9970	0.00010	1.003	1.003	1.006	-0.012	198.5	5.2	101.7	52.6	292.4	36.9	111.5
	MEAN	1.04E-04	1.41E-06	1.0036	0.00027	1.0005	0.00025	0.9959	0.00037	1.003	1.005	1.008	0.185							

Table A-18. *Specimen AMS measurements for site E2 near Ibaré. Summary of column headers:* $\boldsymbol{\chi_b}$ *= bulk susceptibility, SE = standard error,* $\boldsymbol{\tau_1}$ *= normalized maximum eigenvalue,* $\boldsymbol{\tau_2}$ *= normalized intermediate eigenvalue,* $\boldsymbol{\tau_3}$ *= normalized minimum eigenvalue,* $\boldsymbol{P_1}$ *= lineation,* $\boldsymbol{P_3}$ *= foliation,* $\boldsymbol{P_j}$ *= corrected degree of anisotropy, T = shape parameter,* $\boldsymbol{k_1}$ *= maximum eigenvector,* $\boldsymbol{k_2}$ *= intermediate eigenvector,* $\boldsymbol{k_3}$ *= minimum eigenvector, DEC = declination, INC = inclination, F = Hext F statistic.*

ID	Specimen	χ_b	χ_b (SE)	τ_1	τ_1 (SE)	τ_2	τ_2 (SE)	τ_3	τ_3 (SE)	P_1	P_3	P_j	T	k_1 (Dec)	k_1 (Inc)	k_2 (Dec)	k_2 (Inc)	k_3 (Dec)	k_3 (Inc)	F
1	ERT05-1	1.15E-04	2.03E-04	1.0035	0.00010	1.0010	0.00010	0.9954	0.00010	1.002	1.006	1.008	0.384	138.6	11.6	48.1	2.4	306.5	78.2	238.0
2	ERT05-2	1.19E-04	7.81E-05	1.0039	0.00010	1.0012	0.00010	0.9949	0.00010	1.003	1.006	1.009	0.389	138.1	14.9	48.1	0.1	317.8	75.1	1938.0
3	ERT05-3	1.15E-04	1.60E-04	1.0034	0.00010	0.9998	0.00010	0.9968	0.00010	1.004	1.003	1.007	-0.083	124.3	27.5	31.2	6.1	289.7	61.8	198.8
4	ERT05-4	1.16E-04	2.54E-04	1.0032	0.00020	1.0009	0.00020	0.9959	0.00020	1.002	1.005	1.008	0.387	148.1	4.2	58.0	1.7	305.9	85.5	129.0
5	ERT06-1	1.18E-04	3.36E-04	1.0033	0.00020	1.0003	0.00020	0.9964	0.00020	1.003	1.004	1.007	0.115	156.9	21.2	63.4	8.9	311.8	66.8	53.9
6	ERT06-2	1.18E-04	2.38E-04	1.0051	0.00020	1.0000	0.00020	0.9949	0.00020	1.005	1.005	1.010	-0.001	123.1	35.5	228.3	20.2	341.9	47.5	183.7
7	ERT06-3	1.13E-04	2.62E-04	1.0045	0.00020	1.0001	0.00020	0.9954	0.00020	1.004	1.005	1.009	0.021	147.9	22.4	52.2	13.4	293.7	63.5	148.9
8	ERT06-4	1.18E-04	1.76E-04	1.0034	0.00010	1.0010	0.00010	0.9956	0.00010	1.002	1.005	1.008	0.381	149.0	16.8	58.9	0.3	327.7	73.2	279.8
9	ERT07-1	1.22E-04	3.68E-04	1.0041	0.00030	1.0005	0.00030	0.9954	0.00030	1.004	1.005	1.009	0.166	161.2	25.1	65.0	12.9	310.3	61.3	65.8
10	ERT07-2	1.12E-04	3.68E-04	1.0041	0.00030	1.0002	0.00020	0.9957	0.00030	1.004	1.005	1.008	0.075	143.6	23.5	234.7	2.6	330.8	66.3	63.6
11	ERT07-3	1.07E-04	3.19E-04	1.0045	0.00020	1.0006	0.00020	0.9948	0.00020	1.004	1.006	1.010	0.201	136.7	18.6	227.4	2.0	323.4	71.2	123.4
12	ERT08-1	1.10E-04	4.78E-04	1.0045	0.00030	0.9997	0.00030	0.9958	0.00030	1.005	1.004	1.009	-0.103	148.3	16.2	239.8	5.2	347.0	73.0	44.4
13	ERT08-2	1.14E-04	3.58E-04	1.0029	0.00030	1.0008	0.00030	0.9963	0.00030	1.002	1.005	1.007	0.360	132.9	25.2	38.3	9.7	288.9	62.7	44.1
14	ERT08-3	1.11E-04	2.62E-04	1.0028	0.00020	0.9998	0.00020	0.9974	0.00020	1.003	1.002	1.005	-0.098	126.9	17.8	217.4	1.5	311.9	72.1	54.9
15	ERT08-4	1.11E-04	4.23E-04	1.0031	0.00030	1.0013	0.00030	0.9956	0.00030	1.002	1.006	1.008	0.533	136.1	18.1	43.4	8.1	290.2	70.0	45.5
	MEAN	1.15E-04	1.04E-06	1.0038	0.00018	1.0005	0.00014	0.9958	0.00019	1.003	1.005	1.008	0.182							

Table A-19. *Specimen AMS measurements for site S3 at the São Gabriel creek exposure. Summary of column headers:* $\boldsymbol{\chi_b}$ *= bulk susceptibility, SE = standard error,* $\boldsymbol{\tau_1}$ *= normalized maximum eigenvalue,* $\boldsymbol{\tau_2}$ *= normalized intermediate eigenvalue,* $\boldsymbol{\tau_3}$ *= normalized minimum eigenvalue,* $\boldsymbol{P_1}$ *= lineation,* $\boldsymbol{P_3}$ *= foliation,* $\boldsymbol{P_j}$ *= corrected degree of anisotropy, T = shape parameter,* $\boldsymbol{k_1}$ *= maximum eigenvector,* $\boldsymbol{k_2}$ *= intermediate eigenvector,* $\boldsymbol{k_3}$ *= minimum eigenvector, DEC = declination, INC = inclination, F = Hext F statistic.*

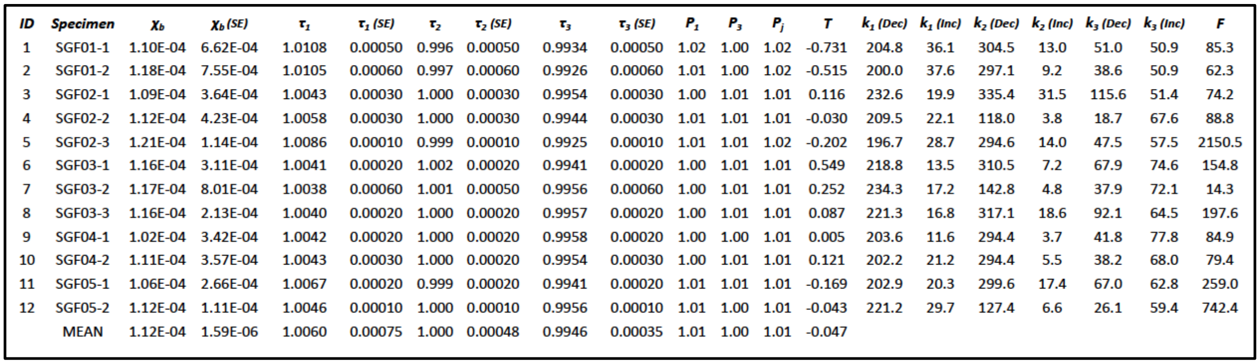

ID	Specimen	χ_b	χ_b (SE)	τ_1	τ_1 (SE)	τ_2	τ_2 (SE)	τ_3	τ_3 (SE)	P_1	P_3	P_j	T	k_1 (Dec)	k_1 (Inc)	k_2 (Dec)	k_2 (Inc)	k_3 (Dec)	k_3 (Inc)	F
1	SGF01-1	1.10E-04	6.62E-04	1.0108	0.00050	0.996	0.00050	0.9934	0.00050	1.02	1.00	1.02	-0.731	204.8	36.1	304.5	13.0	51.0	50.9	85.3
2	SGF01-2	1.18E-04	7.55E-04	1.0105	0.00060	0.997	0.00060	0.9926	0.00060	1.01	1.00	1.02	-0.515	200.0	37.6	297.1	9.2	38.6	50.9	62.3
3	SGF02-1	1.09E-04	3.64E-04	1.0043	0.00030	1.000	0.00030	0.9954	0.00030	1.00	1.01	1.01	0.116	232.6	19.9	335.4	31.5	115.6	51.4	74.2
4	SGF02-2	1.12E-04	4.23E-04	1.0058	0.00030	1.000	0.00030	0.9944	0.00030	1.01	1.01	1.01	-0.030	209.5	22.1	118.0	3.8	18.7	67.6	88.8
5	SGF02-3	1.21E-04	1.14E-04	1.0086	0.00010	0.999	0.00010	0.9925	0.00010	1.01	1.01	1.02	-0.202	196.7	28.7	294.6	14.0	47.5	57.5	2150.5
6	SGF03-1	1.16E-04	3.11E-04	1.0041	0.00020	1.002	0.00020	0.9941	0.00020	1.00	1.01	1.01	0.549	218.8	13.5	310.5	7.2	67.9	74.6	154.8
7	SGF03-2	1.17E-04	8.01E-04	1.0038	0.00060	1.001	0.00050	0.9956	0.00060	1.00	1.01	1.01	0.252	234.3	17.2	142.8	4.8	37.9	72.1	14.3
8	SGF03-3	1.16E-04	2.13E-04	1.0040	0.00020	1.000	0.00020	0.9957	0.00020	1.00	1.01	1.01	0.087	221.3	16.8	317.1	18.6	92.1	64.5	197.6
9	SGF04-1	1.02E-04	3.42E-04	1.0042	0.00020	1.000	0.00020	0.9958	0.00020	1.00	1.00	1.01	0.005	203.6	11.6	294.4	3.7	41.8	77.8	84.9
10	SGF04-2	1.11E-04	3.57E-04	1.0043	0.00030	1.000	0.00020	0.9954	0.00030	1.00	1.01	1.01	0.121	202.2	21.2	294.4	5.5	38.2	68.0	79.4
11	SGF05-1	1.06E-04	2.66E-04	1.0067	0.00020	0.999	0.00020	0.9941	0.00020	1.01	1.01	1.01	-0.169	202.9	20.3	299.6	17.4	67.0	62.8	259.0
12	SGF05-2	1.12E-04	1.11E-04	1.0046	0.00010	1.000	0.00010	0.9956	0.00010	1.01	1.00	1.01	-0.043	221.2	29.7	127.4	6.6	26.1	59.4	742.4
	MEAN	1.12E-04	1.59E-06	1.0060	0.00075	1.000	0.00048	0.9946	0.00035	1.01	1.00	1.01	-0.047							

APPENDIX B: MAGNETIC ANALYSES FOR (CH3) LOCATIONS

Appendix B includes magnetic analyses (hysteresis and susceptibility vs. temperature measurements) for site localities included within this study (Alfredo Wagner, Aurora, Campo do Tenente, Porto Amazonas, Cachoeira do Sul, Ibaré, and São Gabriel) outlined in Ch3.

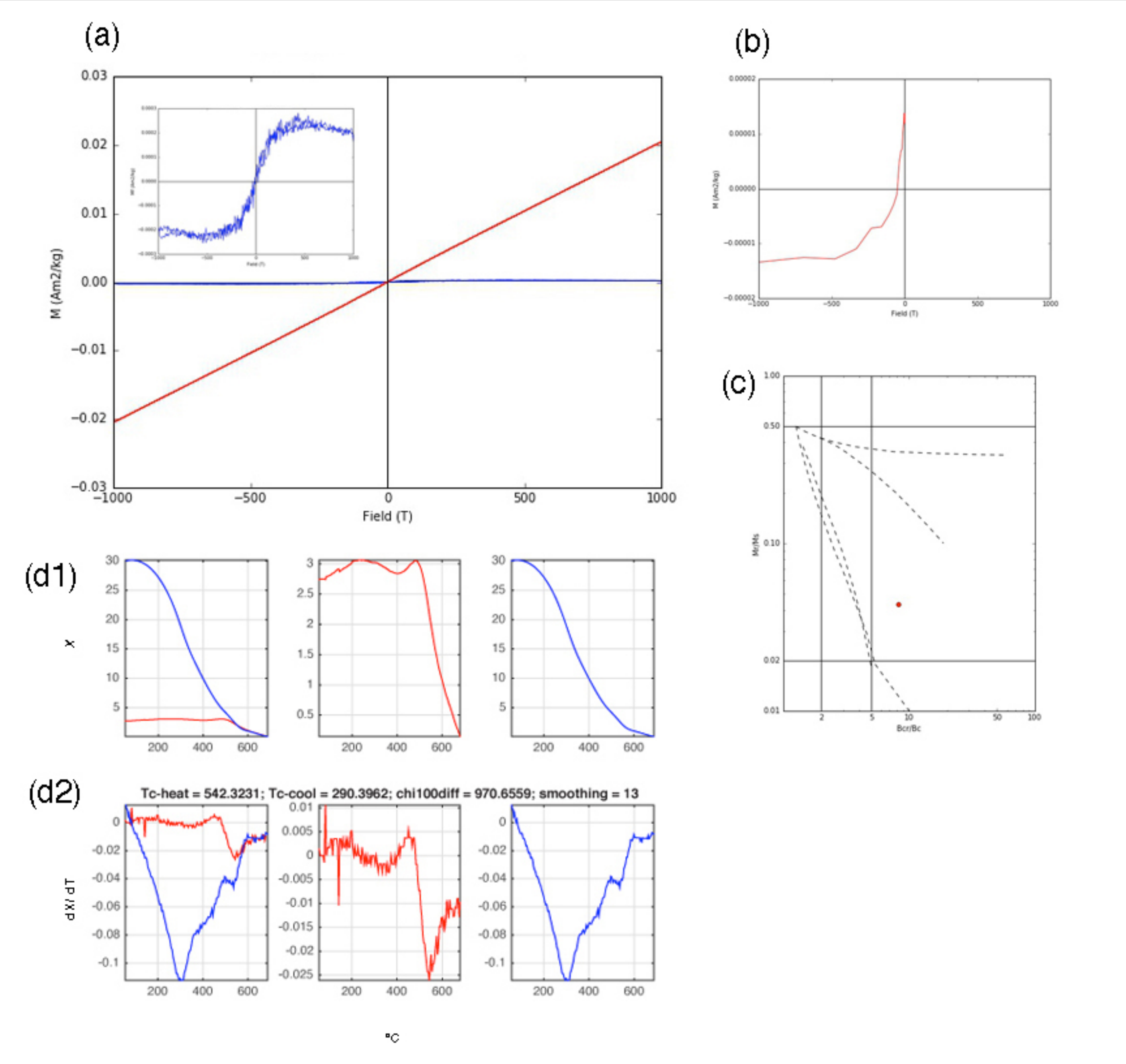

Fig B-1. *Magnetic analyses for site B8 at the Alfredo Wagner road cut* ***(a)*** *hysteresis measurement, red = raw data containing both para- and ferromagnetic contributions, blue = slope-corrected ferromagnetic loop* ***(b)*** *backfield measurement* ***(c)*** *Day plot* ***(d1)*** *susceptibility vs. temperature measurement, red = heating curve, blue = cooling curve* ***(d2)*** *calculated first derivatives for thermomagnetic curves.*

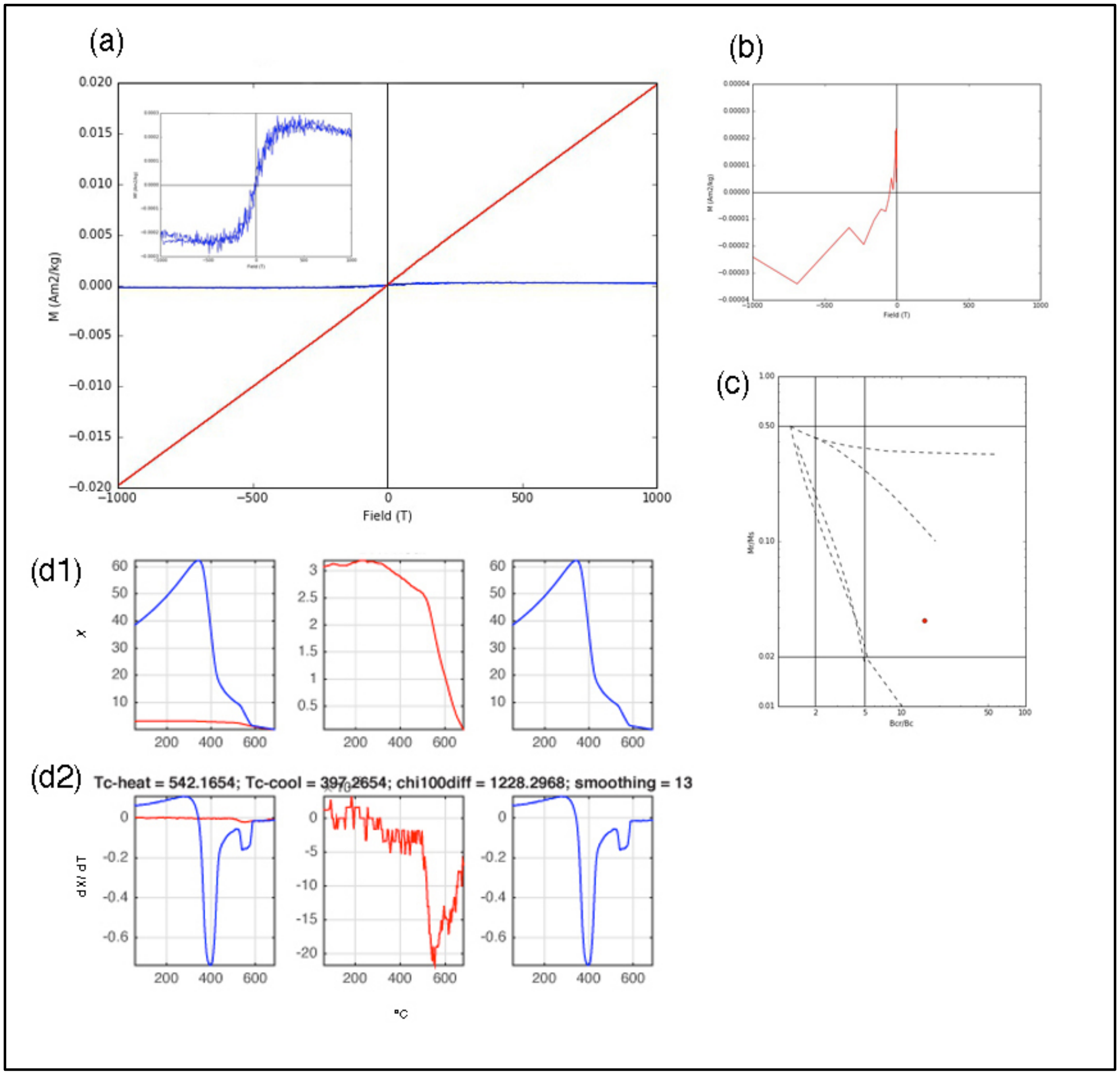

Fig B-2. *Magnetic analyses for site R7 at the Alfredo Wagner road cut* ***(a)*** *hysteresis measurement, red = raw data containing both para- and ferromagnetic contributions, blue = slope-corrected ferromagnetic loop* ***(b)*** *backfield measurement* ***(c)*** *Day plot* ***(d1)*** *susceptibility vs. temperature measurement, red = heating curve, blue = cooling curve* ***(d2)*** *calculated first derivatives for thermomagnetic curves.*

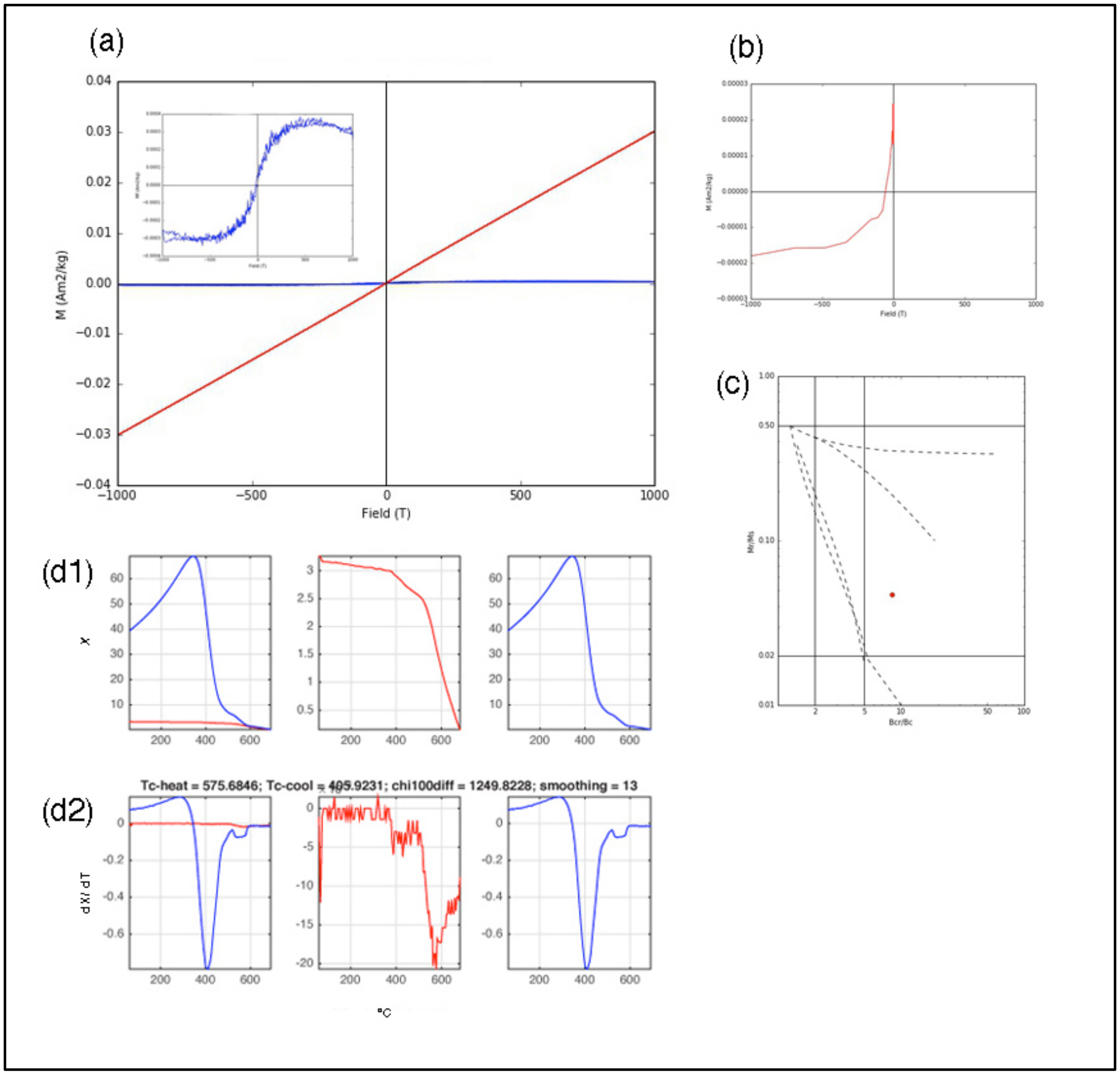

Fig B-3. *Magnetic analyses for site Q1 at the Aurora quarry* ***(a)*** *hysteresis measurement, red = raw data containing both para- and ferromagnetic contributions, blue = slope-corrected ferromagnetic loop* ***(b)*** *backfield measurement* ***(c)*** *Day plot* ***(d1)*** *susceptibility vs. temperature measurement, red = heating curve, blue = cooling curve* ***(d2)*** *calculated first derivatives for thermomagnetic curves.*

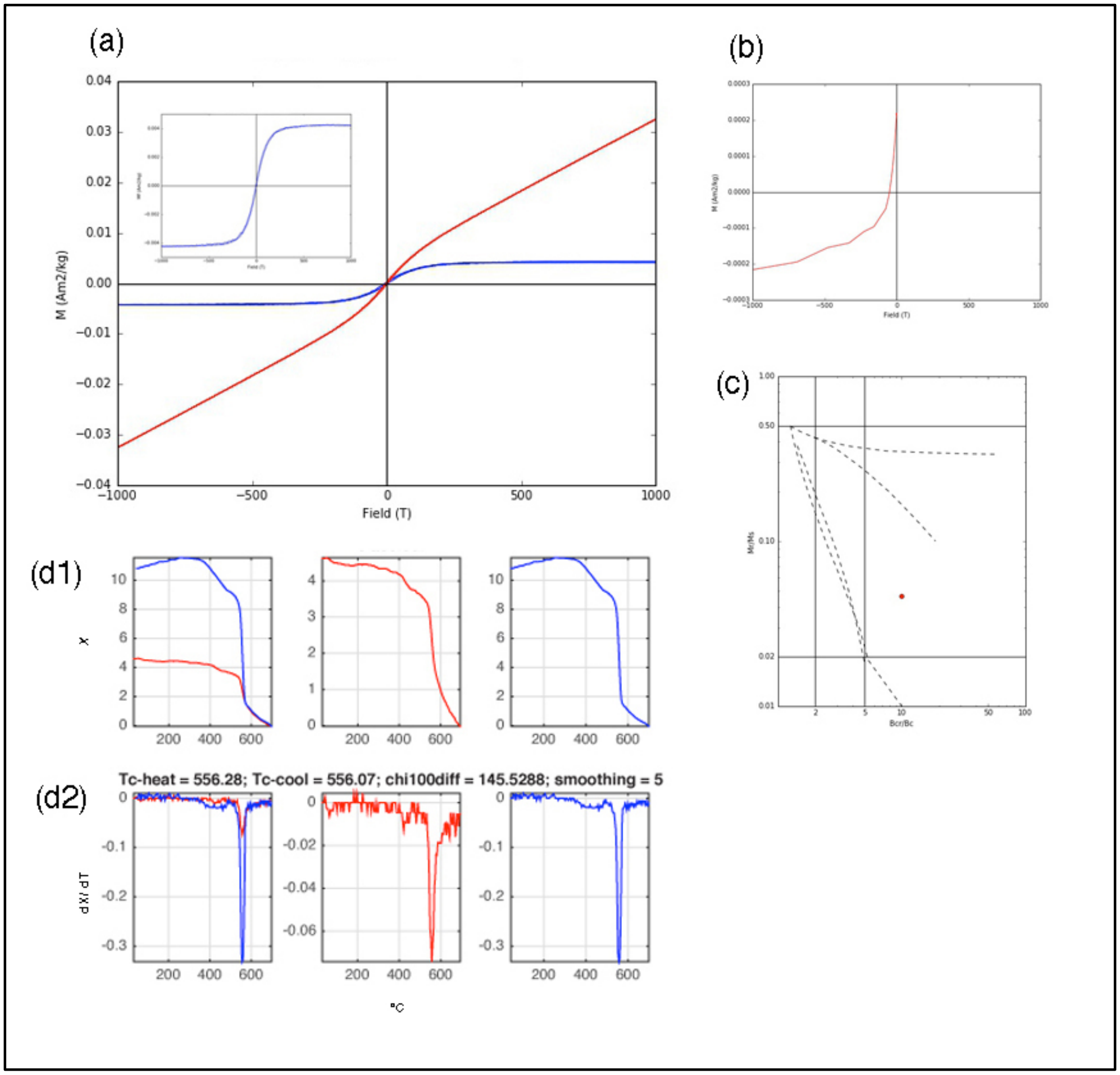

Fig B-4. Magnetic analyses for site C3 at the Campo do Tenente quarry *(a)* hysteresis measurement, red = raw data containing both para- and ferromagnetic contributions, blue = slope-corrected ferromagnetic loop *(b)* backfield measurement *(c)* Day plot *(d1)* susceptibility vs. temperature measurement, red = heating curve, blue = cooling curve *(d2)* calculated first derivatives for thermomagnetic curves.

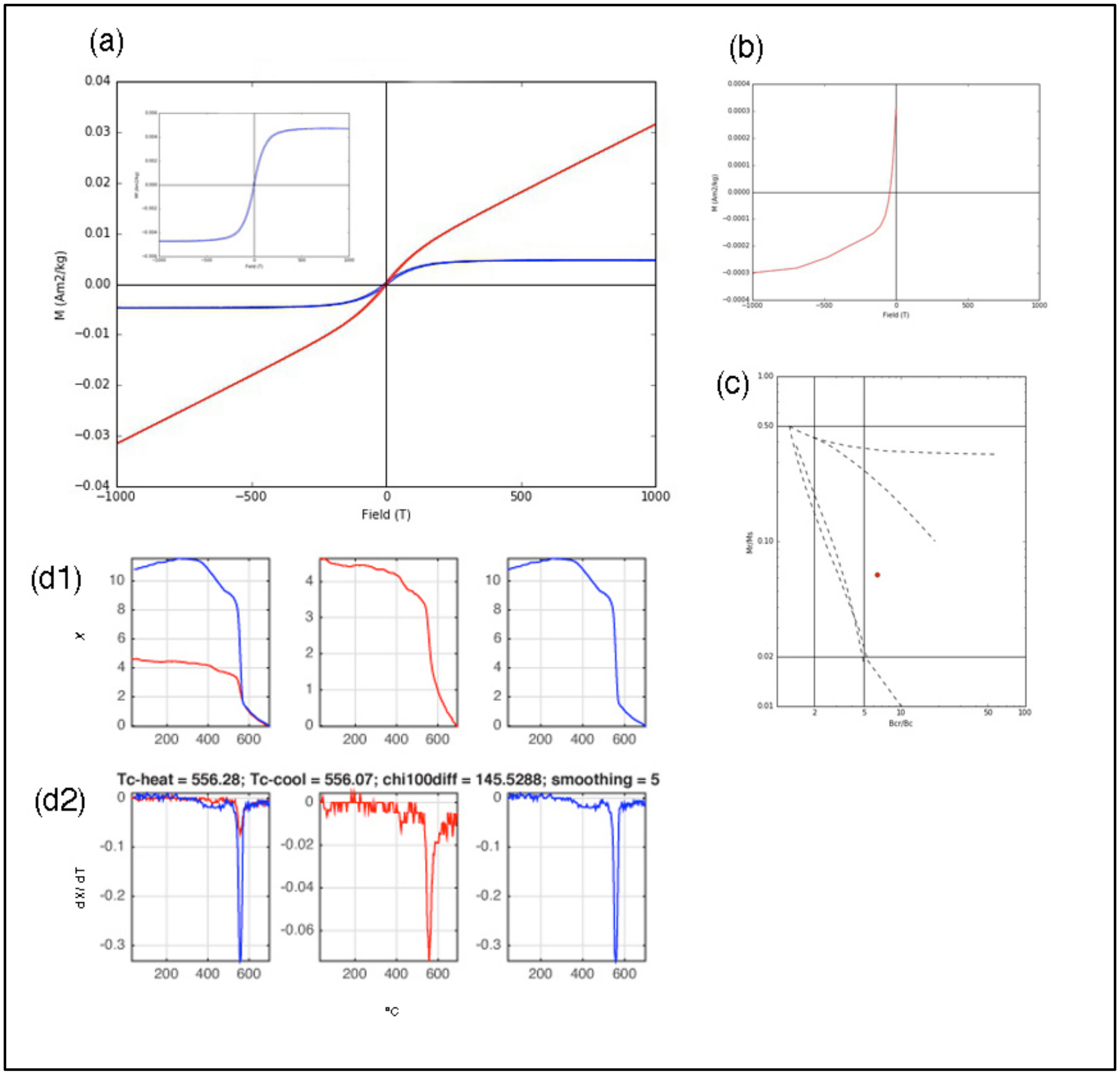

Fig B-5. Magnetic analyses site T5 at the Campo do Tenente quarry ***(a)*** hysteresis measurement, red = raw data containing both para- and ferromagnetic contributions, blue = slope-corrected ferromagnetic loop ***(b)*** backfield measurement ***(c)*** Day plot ***(d1)*** susceptibility vs. temperature measurement, red = heating curve, blue = cooling curve ***(d2)*** calculated first derivatives for thermomagnetic curves.

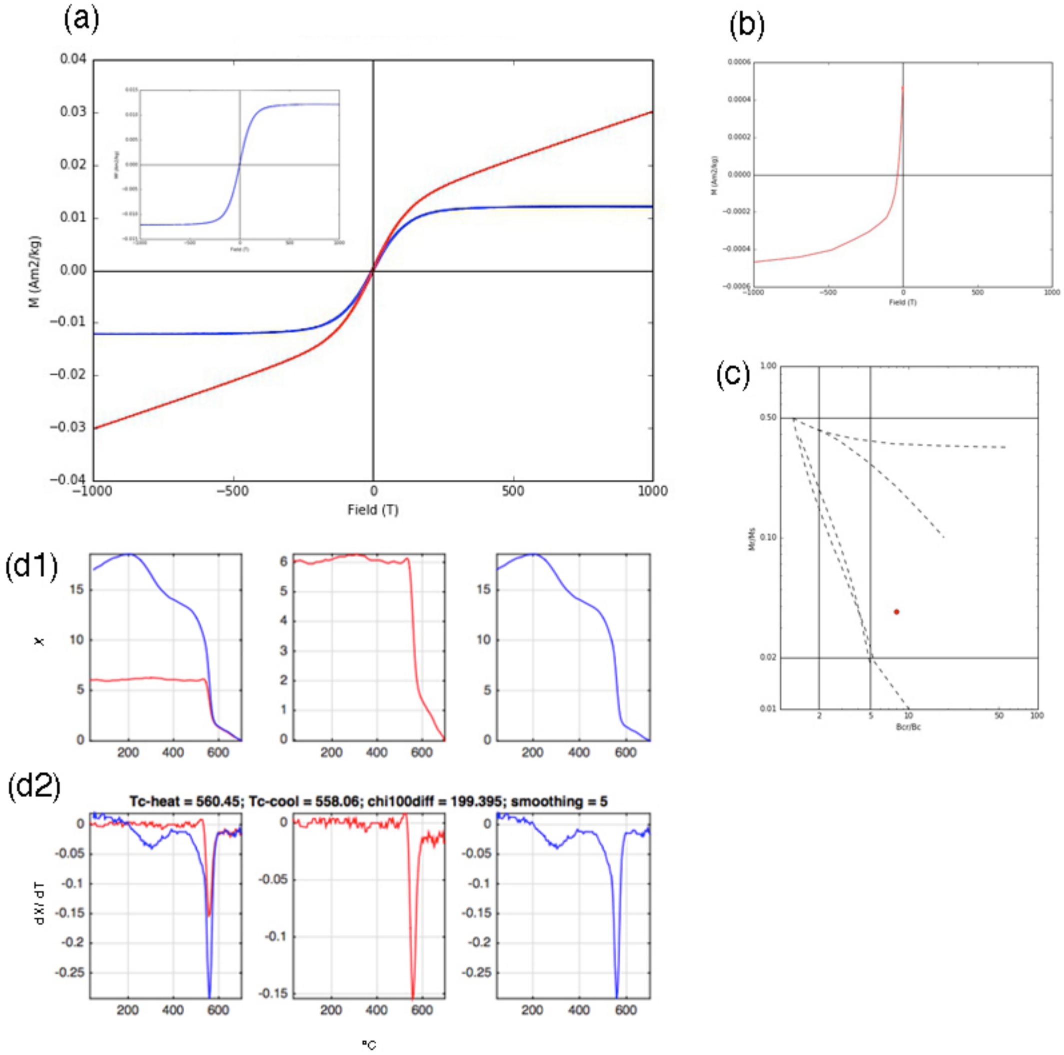

Fig B-6. *Magnetic analyses for site D4 at the Campo do Tenente quarry* ***(a)*** *hysteresis measurement, red = raw data containing both para- and ferromagnetic contributions, blue = slope-corrected ferromagnetic loop* ***(b)*** *backfield measurement* ***(c)*** *Day plot* ***(d1)*** *susceptibility vs. temperature measurement, red = heating curve, blue = cooling curve* ***(d2)*** *calculated first derivatives for thermomagnetic curves.*

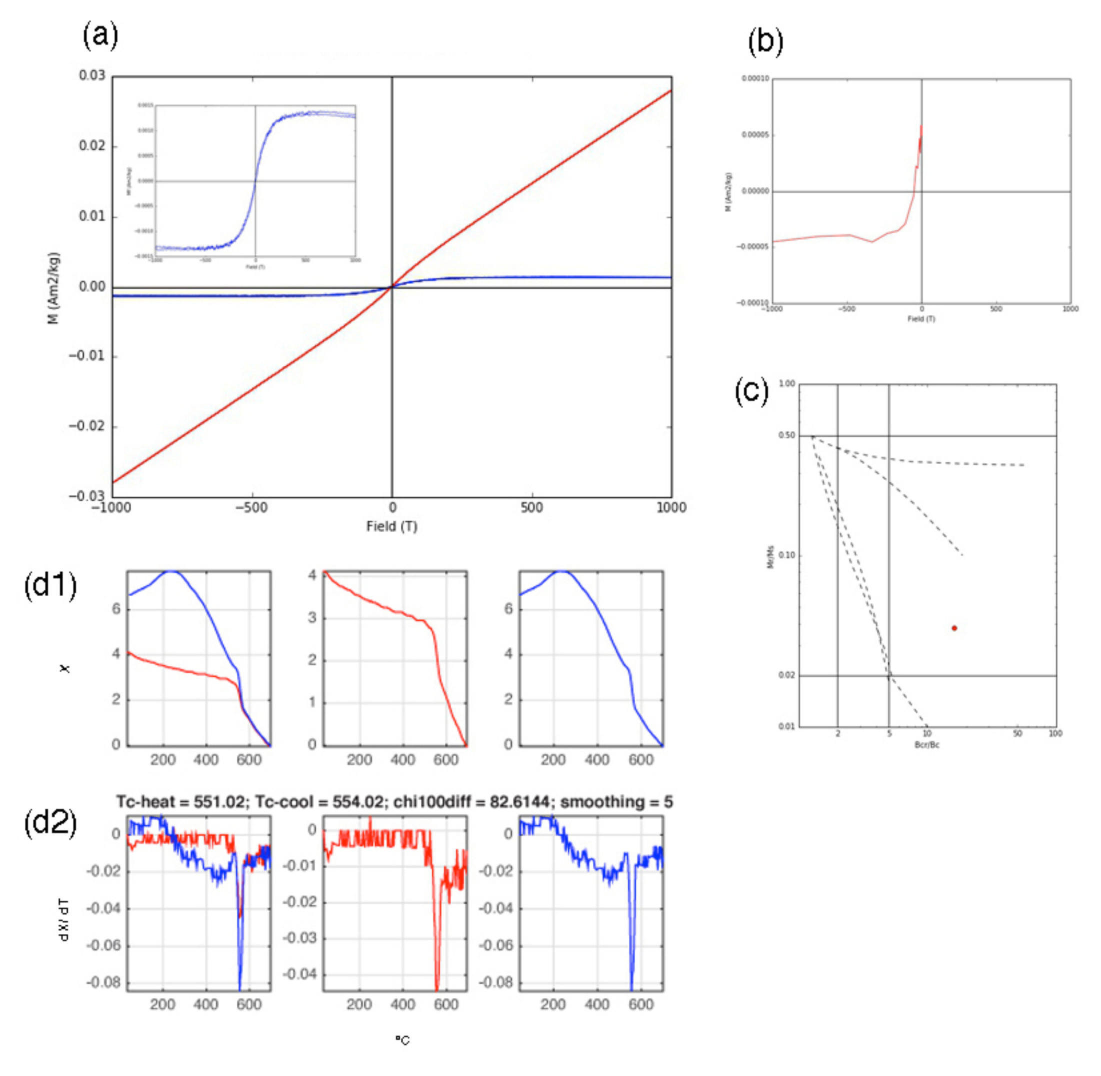

Fig B-7. *Magnetic analyses for site D5 at the Campo do Tenente quarry* ***(a)*** *hysteresis measurement, red = raw data containing both para- and ferromagnetic contributions, blue = slope-corrected ferromagnetic loop* ***(b)*** *backfield measurement* ***(c)*** *Day plot* ***(d1)*** *susceptibility vs. temperature measurement, red = heating curve, blue = cooling curve* ***(d2)*** *calculated first derivatives for thermomagnetic curves.*

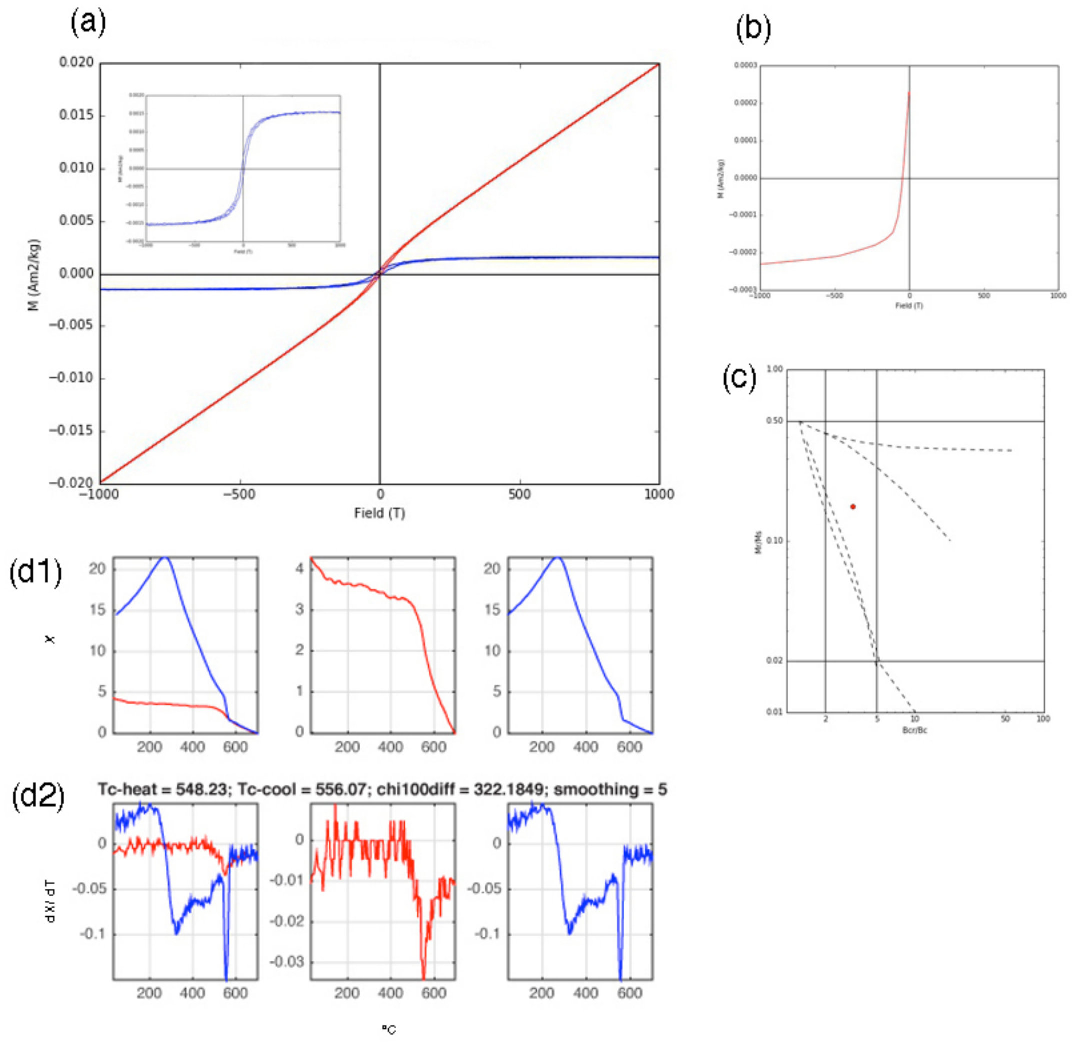

Fig B-8. *Magnetic analyses for sites D3 and C5 at the Campo do Tenente quarry* ***(a)*** *hysteresis measurement, red = raw data containing both para- and ferromagnetic contributions, blue = slope-corrected ferromagnetic loop* ***(b)*** *backfield measurement* ***(c)*** *Day plot* ***(d1)*** *susceptibility vs. temperature measurement, red = heating curve, blue = cooling curve* ***(d2)*** *calculated first derivatives for thermomagnetic curves.*

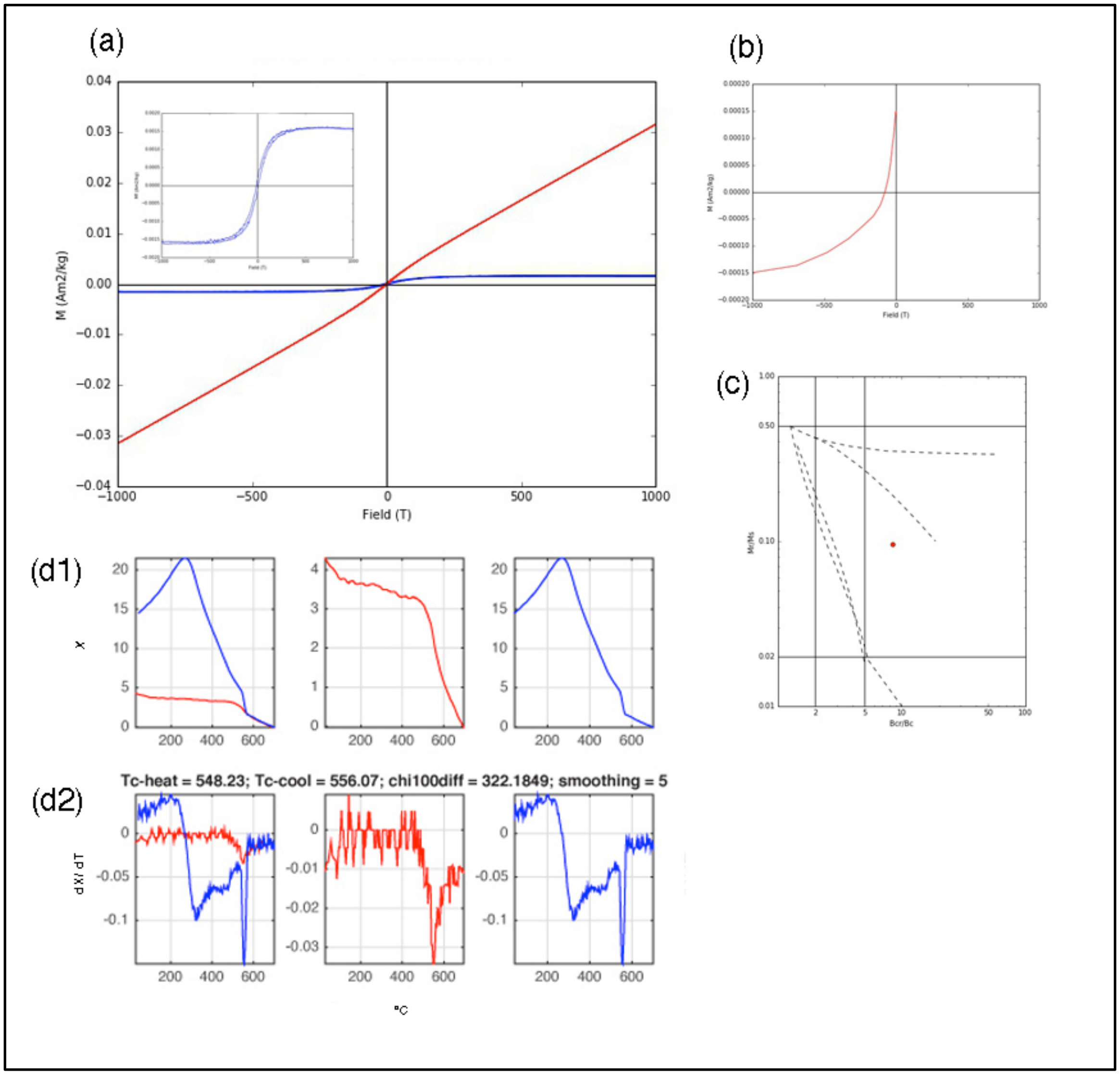

Fig B-9. Magnetic analyses for site FE1 at the Campo do Tenente quarry ***(a)*** hysteresis measurement, red = raw data containing both para- and ferromagnetic contributions, blue = slope-corrected ferromagnetic loop ***(b)*** backfield measurement ***(c)*** Day plot ***(d1)*** susceptibility vs. temperature measurement, red = heating curve, blue = cooling curve ***(d2)*** calculated first derivatives for thermomagnetic curves.

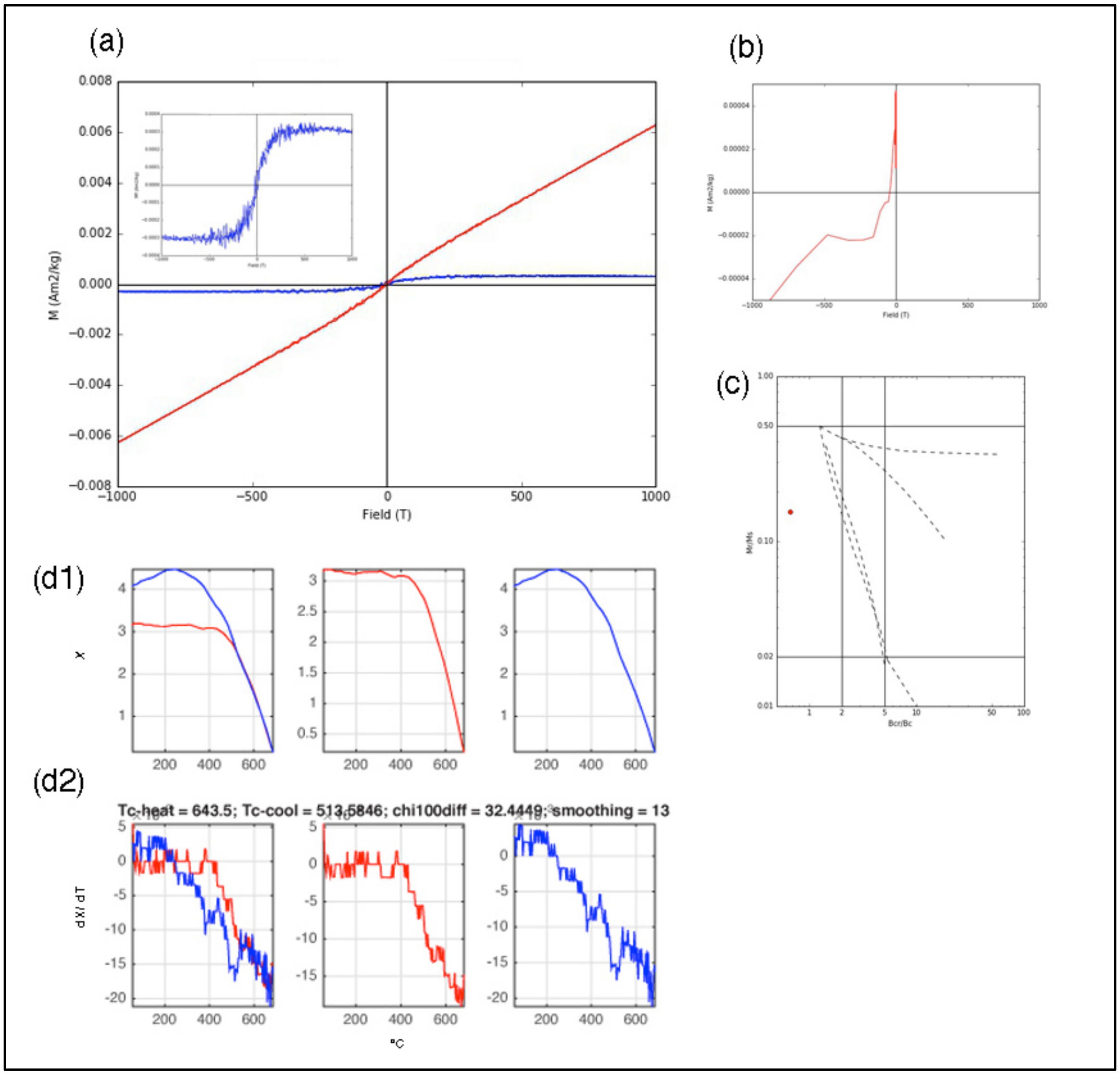

Fig B-10. *Magnetic analyses for sites H7, M6, and O5 at the Porto Amazonas road cut* ***(a)*** *hysteresis measurement, red = raw data containing both para- and ferromagnetic contributions, blue = slope-corrected ferromagnetic loop* ***(b)*** *backfield measurement* ***(c)*** *Day plot* ***(d1)*** *susceptibility vs. temperature measurement, red = heating curve, blue = cooling curve* ***(d2)*** *calculated first derivatives for thermomagnetic curves.*

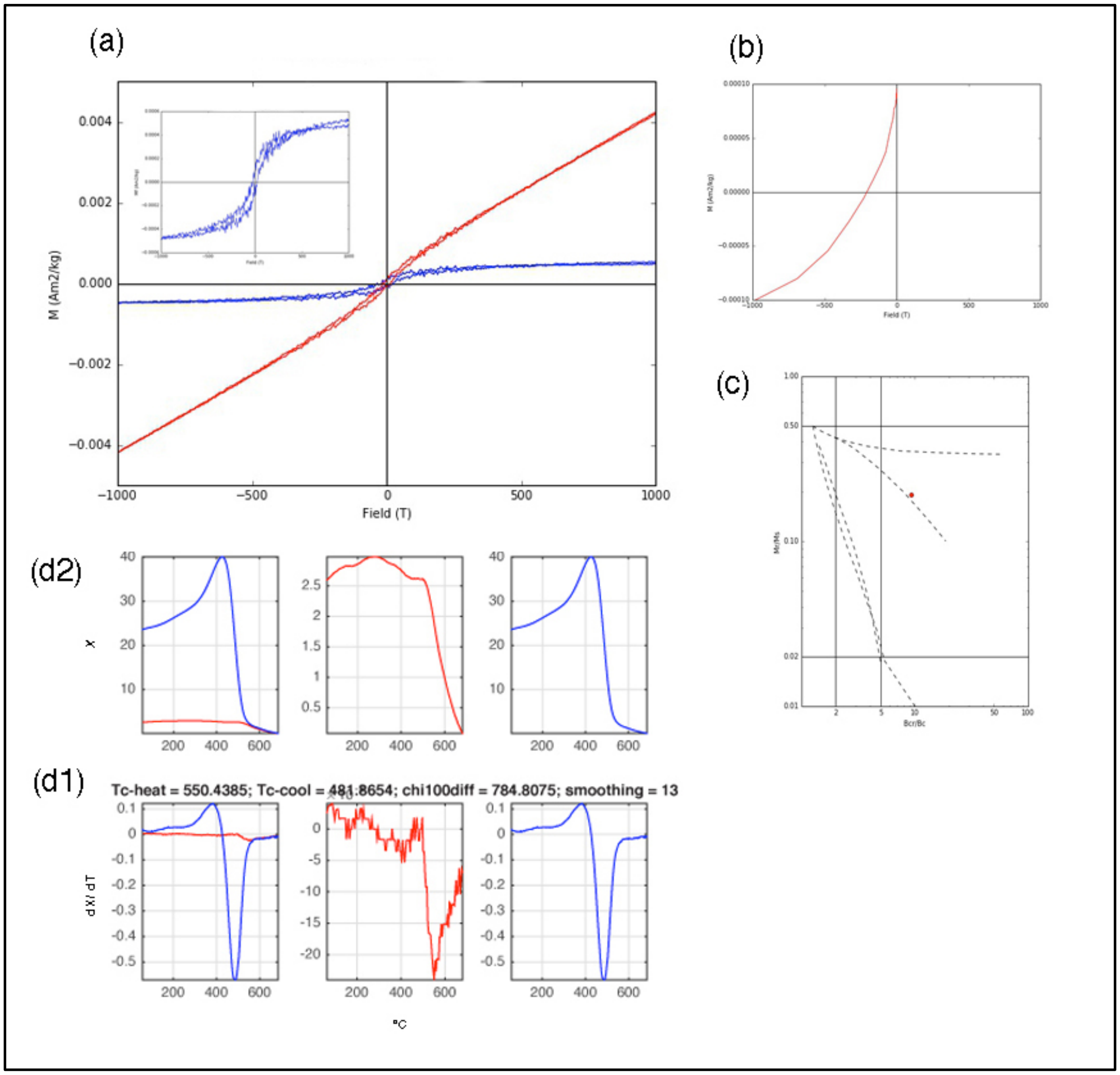

Fig B-11. *Magnetic analyses for sites P5, P7 and P9 near Cachoeira do Sul* ***(a)*** *hysteresis measurement, red = raw data containing both para- and ferromagnetic contributions, blue = slope-corrected ferromagnetic loop* ***(b)*** *backfield measurement* ***(c)*** *Day plot* ***(d1)*** *susceptibility vs. temperature measurement, red = heating curve, blue = cooling curve* ***(d2)*** *calculated first derivatives for thermomagnetic curves.*

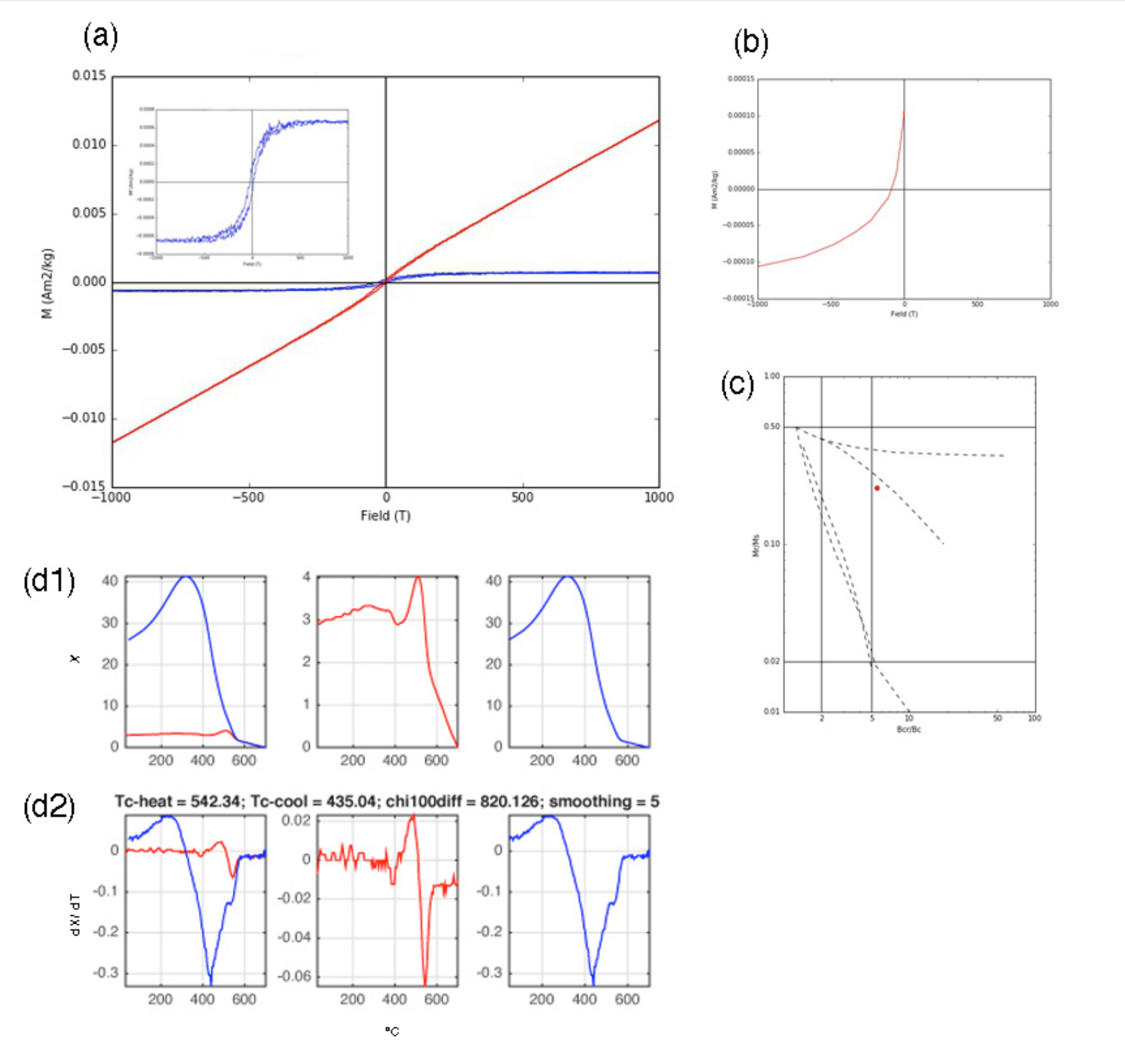

Fig B-12. *Magnetic analyses sites E1 and E2 near Ibaré* ***(a)*** *hysteresis measurement, red = raw data containing both para- and ferromagnetic contributions, blue = slope-corrected ferromagnetic loop* ***(b)*** *backfield measurement* ***(c)*** *Day plot* ***(d1)*** *susceptibility vs. temperature measurement, red = heating curve, blue = cooling curve* ***(d2)*** *calculated first derivatives for thermomagnetic curves.*

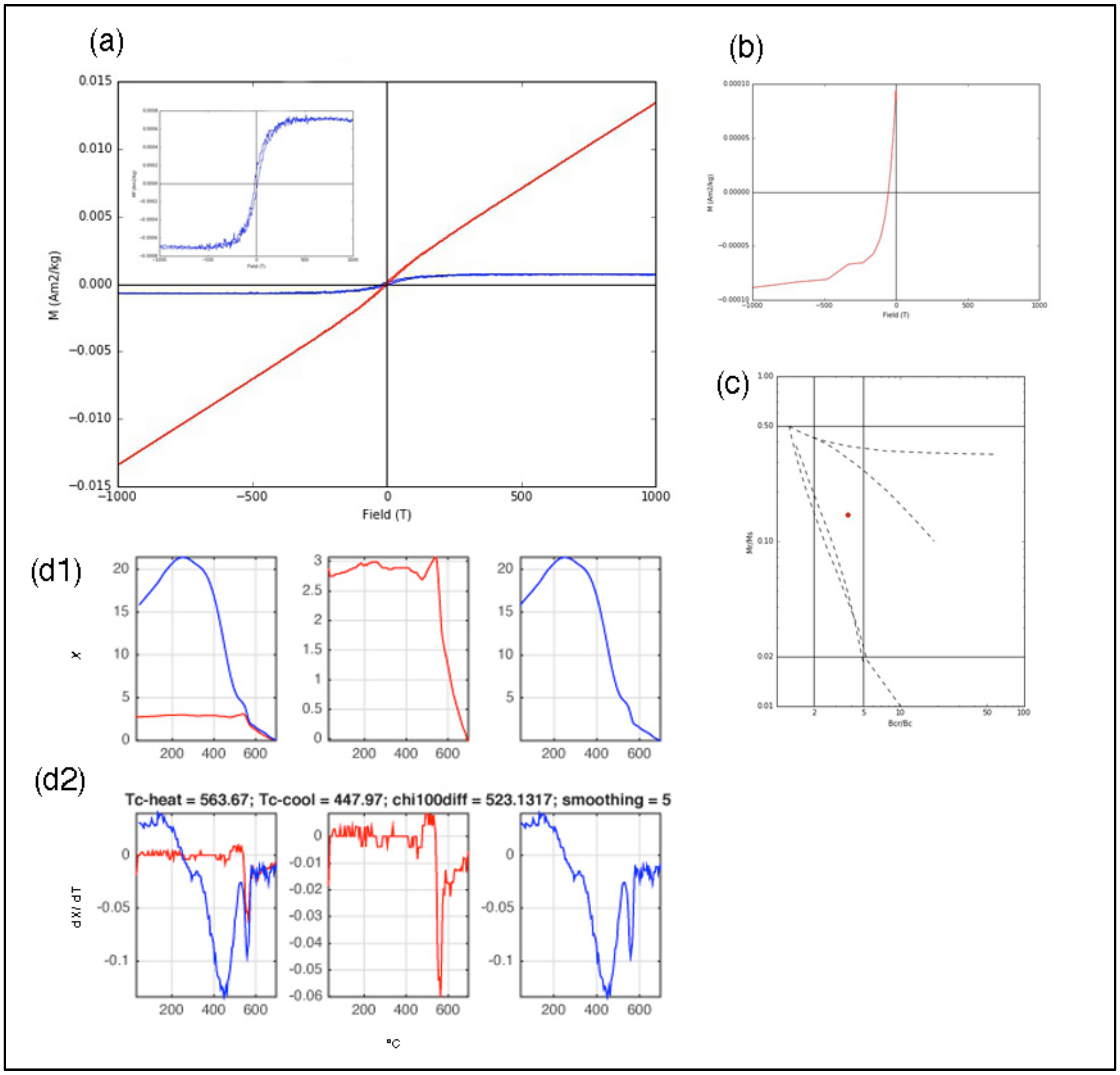

Fig B-13. *Magnetic analyses for site S3 at the São Gabriel creek exposure* ***(a)*** *hysteresis measurement, red = raw data containing both para- and ferromagnetic contributions, blue = slope-corrected ferromagnetic loop* ***(b)*** *backfield measurement* ***(c)*** *Day plot* ***(d1)*** *susceptibility vs. temperature measurement, red = heating curve, blue = cooling curve* ***(d2)*** *calculated first derivatives for thermomagnetic curves.*

APPENDIX C: ADDITIONAL LOCATION (BASSANI)

Appendix C includes a brief field description, photos, AMS fabric analyses, AMS specimen measurements, and magnetic analyses for samples collected from a locality near Bassani.

In the state of Paraná, samples were collected from the Bassani quarry west of Curitiba (W49°40'8.27", S25°30'27.70”) (Fig C-1). The exposure is correlated to the Itararé and consists of interbedded sandstones, conglomerates, and diamictites. Two fabrics were collected from a sandstone with dispersed clasts: ~2.5 cm (site A2) (Fig C-3A) and ~1 *m* (site A3) (Fig C-3B), below the surface of the bed respectively. Another fabric was collected from a white sandstone (site F2), and two fabrics were collected from a soft sediment grooved surface interpreted to be an ice-keel scour mark (site G3 - grove) and (site B2 - berm) (Fig C-2). All sample sets showed fabrics that were statistically isotropic, except one (site A3). Two fabrics showed evidence of inverse fabrics (sites G3 and B2) in the apparent swapping of the $\boldsymbol{k}_1$and $\boldsymbol{k}_3$ axes. The open loop of the hysteresis measurement (Fig. C-8) and red pigmentation in the rocks suggests the presence of hematite. It is not uncommon for authigenic hematite to be in a single-domain state, which would explain the inverse fabrics.

Fig C-1. *View of Bassani quarry, located west of Curitiba.*

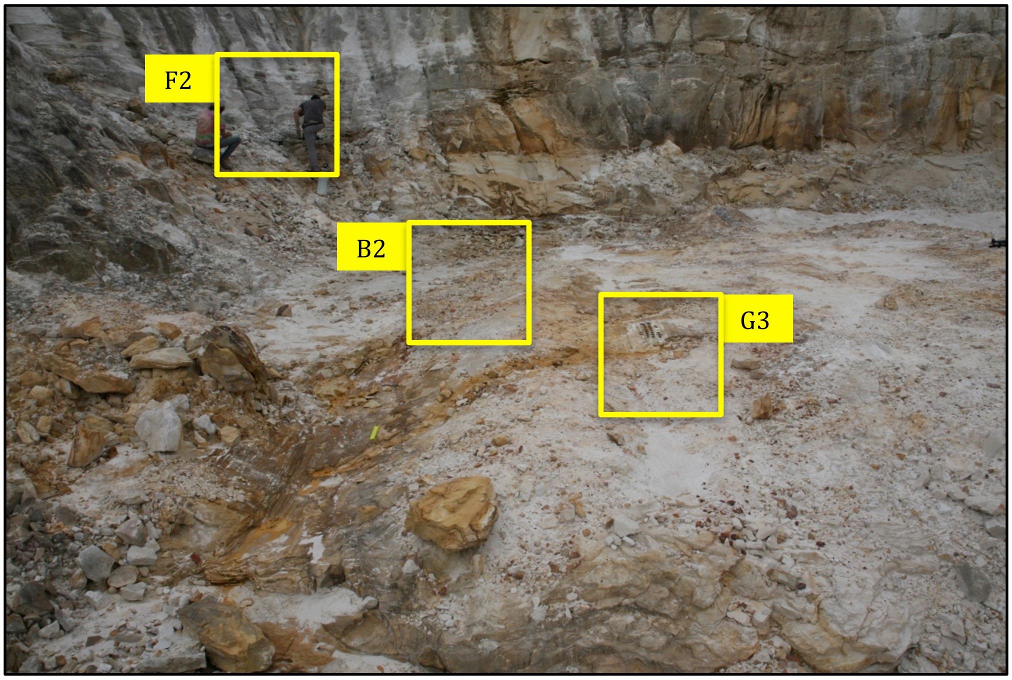

Fig C-2. *Samples extracted from white sandstone unit (site F2), and grooved surface (site G3 - groove) and (site B2 - berm) at the Bassani quarry. Yellow boxes indicate locations of sample sites.*

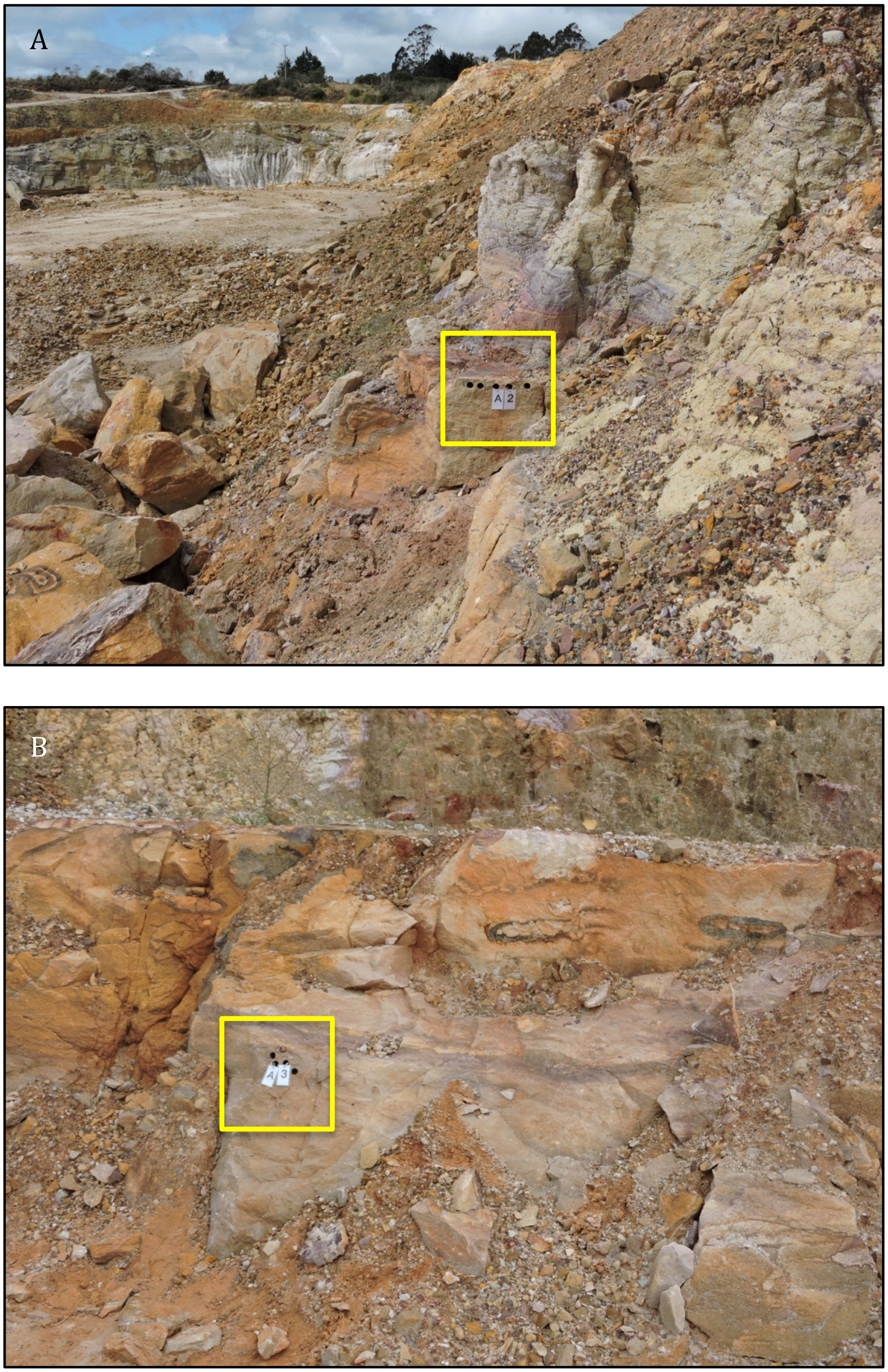

Fig C-3. *Sandstone with dispersed clasts at the Bassani quarry. Yellow boxes indicate locations of samples extracted from **(A)** (site A2) ~2.5 cm, and **(B)** (site A3) ~1 m below the surface of the bed respectively.*

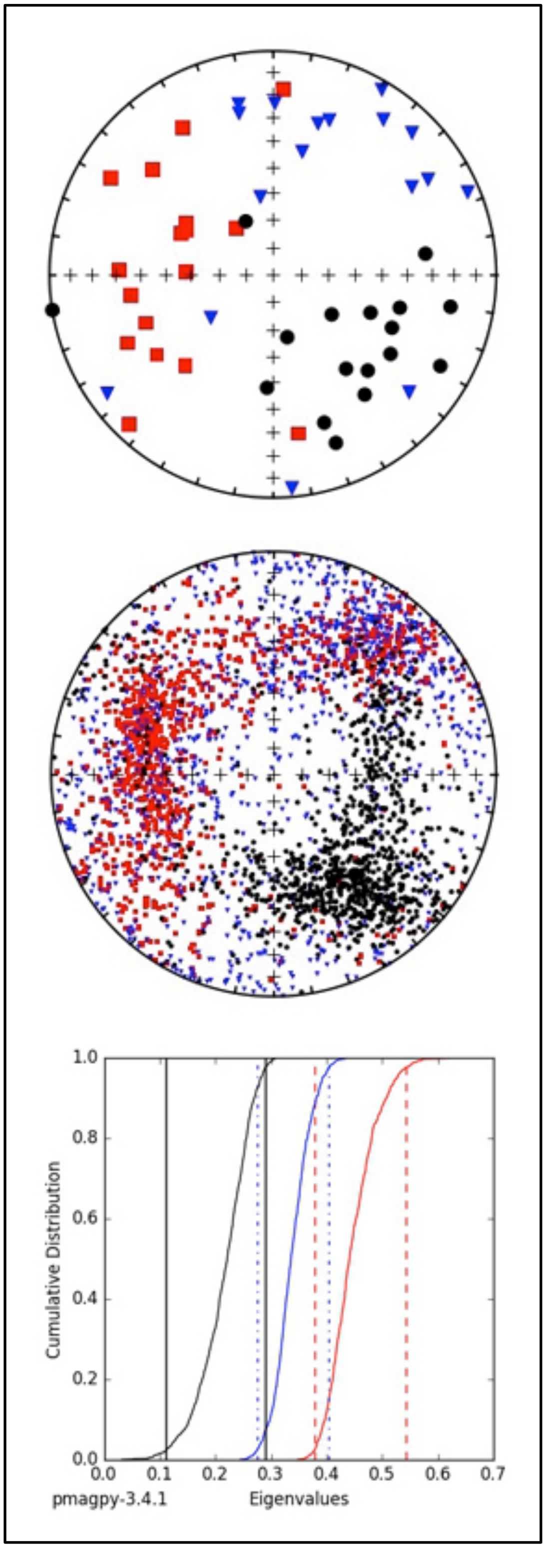

Fig C-4. *Measured eigenvectors for each specimen (top), bootstrapped eigenvectors (center), and bootstrapped eigenvalue cumulative distribution graph (bottom) for site F2 at the Bassani quarry. Maximum eigenvector indicated by red squares, intermediate by blue triangles, and minimum by black circles*

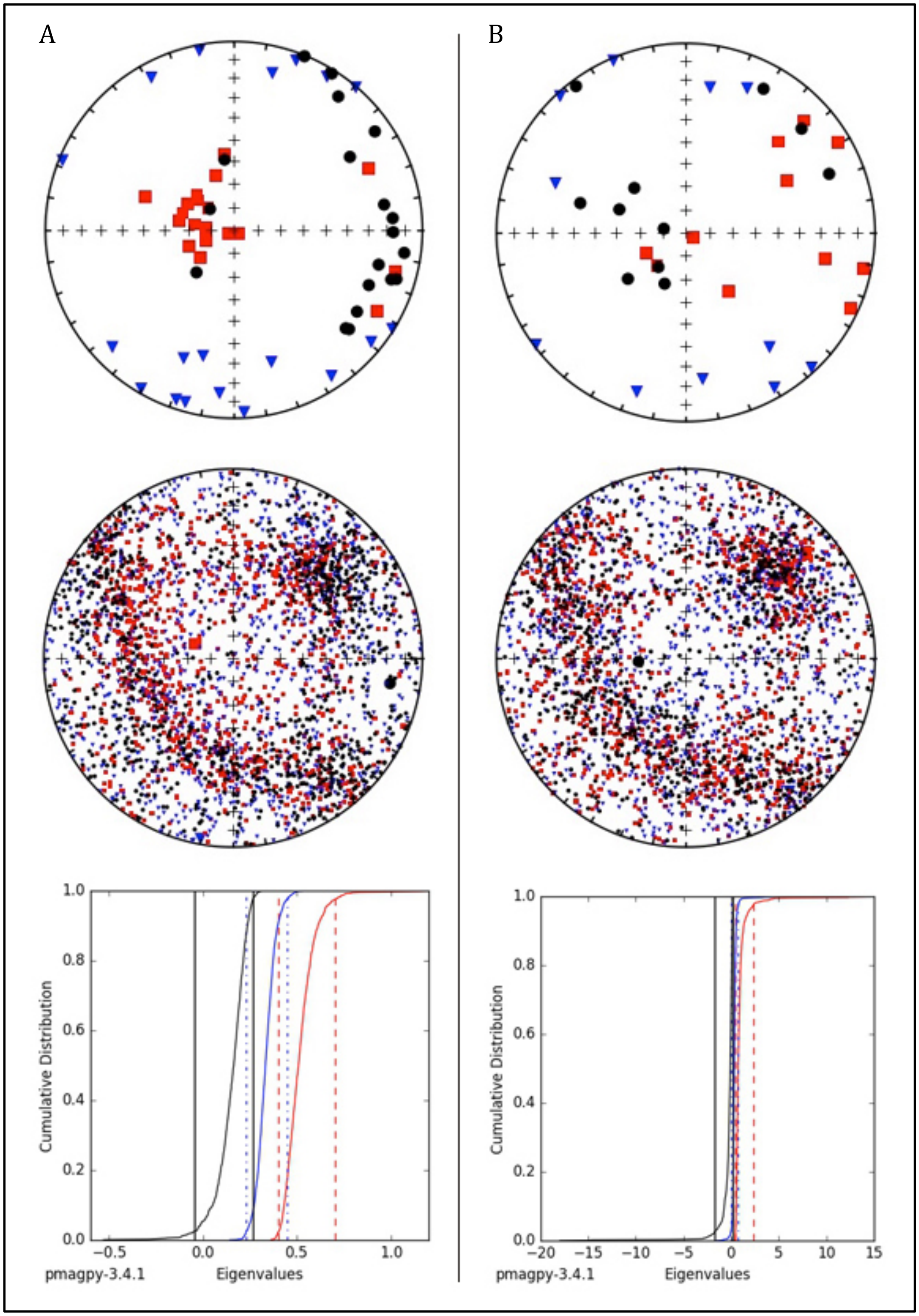

Fig C-5. *Measured eigenvectors for each specimen (top), bootstrapped eigenvectors (center), and bootstrapped eigenvalue cumulative distribution graphs (bottom) for sites at the Bassani quarry* ***(A)*** *B2 (berm)* ***(B)*** *G3 (groove). Maximum eigenvector indicated by red squares, intermediate by blue triangles, and minimum by black circles.*

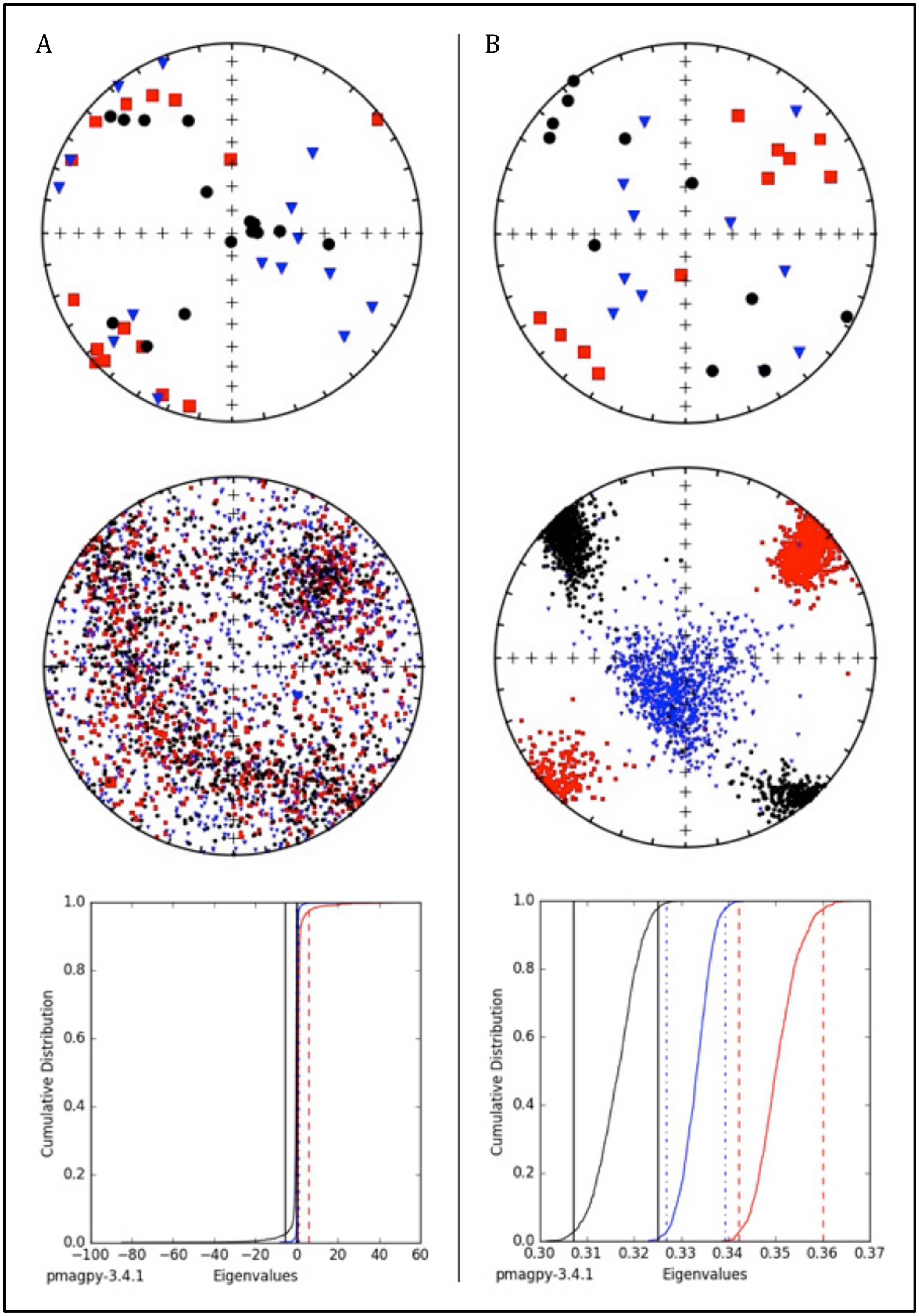

Fig C-6. *Measured eigenvectors for each specimen (top), bootstrapped eigenvectors (center), and bootstrapped eigenvalue cumulative distribution graphs (bottom) for sites at the Bassani quarry (A) A2 (~2.5 cm), and (B) A3 (~1 m). Maximum eigenvector indicated by red squares, intermediate by blue triangles, and minimum by black circles.*

Table C-1. *Specimen AMS measurements for site G3 at the Bassani quarry. Summary of column headers:* $\boldsymbol{\chi_b}$ *= bulk susceptibility, SE = standard error,* $\boldsymbol{\tau_1}$ *= normalized maximum eigenvalue,* $\boldsymbol{\tau_2}$ *= normalized intermediate eigenvalue,* $\boldsymbol{\tau_3}$ *= normalized minimum eigenvalue,* $\boldsymbol{P_1}$ *= lineation,* $\boldsymbol{P_3}$ *= foliation,* $\boldsymbol{P_j}$ *= corrected degree of anisotropy, T = shape parameter,* $\boldsymbol{k_1}$ *= maximum eigenvector,* $\boldsymbol{k_2}$ *= intermediate eigenvector,* $\boldsymbol{k_3}$ *= minimum eigenvector, DEC = declination, INC = inclination, F = Hext F statistic.*

ID	Specimen	χ_b	χ_b (SE)	τ_1	τ_1 (SE)	τ_2	τ_2 (SE)	τ_3	τ_3 (SE)	P_1	P_3	P_j	T	k_1 (Dec)	k_1 (Inc)	k_2 (Dec)	k_2 (Inc)	k_3 (Dec)	k_3 (Inc)	F
1	BQ01	4.11E-05	1.04E-03	1.0048	0.00080	1.0027	0.00080	0.9925	0.00070	1.002	1.010	1.013	0.654	46.2	32.0	137.1	1.4	229.4	57.9	21.8
2	BQ04	3.73E-05	6.85E-04	1.0027	0.00050	1.0008	0.00050	0.9966	0.00050	1.002	1.004	1.006	0.375	64.5	40.9	175.3	22.3	286.1	40.8	9.3
3	BR06	4.00E-05	1.03E-03	1.0070	0.00070	1.0012	0.00070	0.9918	0.00070	1.006	1.010	1.015	0.250	59.1	7.7	149.9	5.9	276.7	80.3	32.3
4	BQ09	2.53E-05	1.44E-03	1.0098	0.00110	1.0034	0.00110	0.9869	0.00100	1.006	1.017	1.024	0.448	101.3	5.1	9.1	23.1	203.0	66.2	36.8
5	BR10	3.06E-05	4.64E-04	1.0037	0.00040	1.0018	0.00040	0.9945	0.00030	1.002	1.007	1.010	0.587	114.6	4.6	23.0	19.5	217.3	70.0	63.5
6	BQ13	2.03E-05	1.30E-03	1.0105	0.00100	0.9998	0.00100	0.9897	0.00100	1.011	1.010	1.021	-0.031	101.1	26.1	197.6	12.9	311.5	60.4	31.9
7	BQ15	3.87E-05	8.44E-04	1.0029	0.00060	1.0007	0.00060	0.9965	0.00060	1.002	1.004	1.006	0.308	94.1	84.5	234.7	4.2	325.0	3.5	8.1
8	BQ04-2	-5.52E-06	4.35E-03	-0.9794	0.00290	-0.9968	0.00290	-1.0239	0.00290	1.027	1.018	1.046	-0.208	68.3	19.2	337.7	1.6	243.0	70.7	15.8
9	BQ05-2	-4.28E-06	5.69E-03	-0.9700	0.00410	-0.9835	0.00420	-1.0465	0.00390	1.064	1.014	1.084	-0.637	47.6	19.0	316.9	2.2	220.5	70.9	29.9
10	BQ08-2	-6.25E-06	4.14E-03	-0.9824	0.00310	-1.0026	0.00330	-1.0150	0.00320	1.012	1.021	1.034	0.249	28.2	14.7	290.5	27.1	143.6	58.6	7.8
11	BQ11-2	6.50E-07	5.00E-02	1.2094	0.03640	0.9596	0.03790	0.8310	0.03710	1.260	1.155	1.460	-0.233	46.4	15.0	143.8	25.8	289.2	59.6	7.8
	MEAN	1.98E-05	5.98E-06	0.4835	0.28347	0.4534	0.28037	0.4267	0.28218	1.036	1.025	1.065	0.160							

Table C-2. *Specimen AMS measurements for site B2 at the Bassani quarry. Summary of column headers:* $\boldsymbol{\chi_b}$ *= bulk susceptibility, SE = standard error,* $\boldsymbol{\tau_1}$ *= normalized maximum eigenvalue,* $\boldsymbol{\tau_2}$ *= normalized intermediate eigenvalue,* $\boldsymbol{\tau_3}$ *= normalized minimum eigenvalue,* $\boldsymbol{P_1}$ *= lineation,* $\boldsymbol{P_3}$ *= foliation,* $\boldsymbol{P_j}$ *= corrected degree of anisotropy, T = shape parameter,* $\boldsymbol{k_1}$ *= maximum eigenvector,* $\boldsymbol{k_2}$ *= intermediate eigenvector,* $\boldsymbol{k_3}$ *= minimum eigenvector, DEC = declination, INC = inclination, F = Hext F statistic.*

ID	Specimen	χ_b	χ_b (SE)	τ_1	τ_1 (SE)	τ_2	τ_2 (SE)	τ_3	τ_3 (SE)	P_1	P_3	P_j	T	k_1 (Dec)	k_1 (Inc)	k_2 (Dec)	k_2 (Inc)	k_3 (Dec)	k_3 (Inc)	F
1	BQ19	1.52E-05	4.43E-03	1.0217	0.00300	0.9946	0.00330	0.9836	0.00330	1.027	1.011	1.040	-0.415	104.5	13.0	201.4	27.5	351.9	59.1	11.4
2	BQ21	1.22E-05	2.16E-03	1.0145	0.00160	1.0044	0.00160	0.9811	0.00150	1.010	1.024	1.035	0.402	119.7	13.2	210.3	2.7	311.6	76.5	35.5
3	BQ30	1.18E-05	3.27E-03	1.0143	0.00230	0.9997	0.00230	0.9861	0.00230	1.015	1.014	1.029	-0.030	65.9	22.7	332.1	9.0	221.9	65.4	10.6
4	BQ17-2	-1.83E-06	2.64E-02	-0.8315	0.01790	-0.8752	0.01840	-1.2932	0.01810	1.478	1.053	1.621	-0.768	90.9	16.6	185.1	14.0	313.3	68.1	53.9
5	BQ18-2	-1.73E-06	3.03E-02	-0.9003	0.02070	-0.9630	0.02130	-1.1367	0.02110	1.180	1.070	1.271	-0.423	106.7	10.9	13.7	15.4	230.6	71.0	9.4
6	BQ21-2	-1.29E-06	2.89E-02	-0.8834	0.01990	-1.0184	0.02030	-1.0982	0.01980	1.078	1.153	1.247	0.307	103.5	22.1	195.8	5.5	299.0	67.2	8.2
7	BQ22-2	-3.11E-06	1.40E-02	-0.9608	0.01080	-0.9841	0.01090	-1.0551	0.00960	1.072	1.024	1.102	-0.489	130.6	20.4	40.4	0.5	309.0	69.6	7.0
8	BQ24-2	-4.12E-06	8.55E-03	-0.9548	0.00660	-1.0062	0.00690	-1.0390	0.00630	1.033	1.054	1.089	0.241	131.2	22.0	225.9	11.4	341.3	65.0	12.3
9	BQ25-2	-4.43E-06	1.05E-02	-0.9493	0.00810	-0.9818	0.00810	-1.0689	0.00700	1.089	1.034	1.130	-0.433	38.1	11.0	129.3	6.5	249.3	77.2	20.4
10	BQ28-2	-2.51E-06	1.14E-02	-0.9291	0.00770	-0.9958	0.00780	-1.0751	0.00770	1.080	1.072	1.157	-0.051	80.4	20.3	349.1	3.6	249.4	69.3	24.4
11	BQ17-3	-3.73E-06	5.17E-03	-0.9541	0.00350	-0.9909	0.00350	-1.0550	0.00350	1.065	1.039	1.107	-0.246	107.7	13.6	199.0	5.4	310.1	75.3	57.7
12	BQ18-3	-4.54E-06	3.84E-03	-0.9691	0.00260	-1.0003	0.00290	-1.0306	0.00290	1.030	1.032	1.063	0.030	97.8	9.8	194.0	31.8	352.7	56.4	35.4
13	BQ21-3	-4.39E-06	5.93E-03	-0.9370	0.00460	-0.9516	0.00460	-1.1114	0.00400	1.168	1.016	1.208	-0.819	54.8	9.6	146.1	7.5	273.3	77.7	158.0
14	BQ22-3	-4.33E-06	2.49E-03	-0.9258	0.00190	-0.9559	0.00190	-1.1183	0.00170	1.170	1.033	1.224	-0.661	123.6	22.6	31.3	5.5	288.4	66.6	1010.8
15	BQ24-3	-4.93E-06	2.99E-03	-0.9842	0.00210	-0.9997	0.00230	-1.0161	0.00220	1.016	1.016	1.032	-0.024	22.3	0.7	292.3	2.1	129.6	87.8	15.6
16	BQ25-3	-3.92E-06	4.56E-03	-0.9861	0.00350	-0.9945	0.00350	-1.0193	0.00310	1.025	1.009	1.035	-0.488	30.9	2.2	120.9	1.4	242.4	87.4	8.2
17	BQ26-3	-5.16E-06	2.42E-03	-0.9897	0.00190	-0.9988	0.00190	-1.0114	0.00180	1.013	1.009	1.022	-0.158	57.8	27.9	164.4	28.3	291.5	48.2	10.0
18	BQ28-3	-4.69E-06	5.75E-03	-0.9664	0.00390	-0.9888	0.00390	-1.0447	0.00380	1.056	1.023	1.083	-0.411	85.6	16.7	176.7	3.5	278.2	72.9	29.4
19	BQ29-3	-4.15E-06	4.70E-03	-0.9782	0.00350	-0.9995	0.00350	-1.0223	0.00320	1.023	1.022	1.045	-0.025	112.3	23.8	20.1	5.0	279.0	65.6	12.5
	MEAN	-1.03E-06	1.47E-06	-0.6342	0.16874	-0.6687	0.17042	-0.7497	0.17751	1.086	1.037	1.134	-0.235							

Table C-3. *Specimen AMS measurements for site F2 at the Bassani quarry. Summary of column headers:* χ_b *= bulk susceptibility, SE = standard error,* τ_1 *= normalized maximum eigenvalue,* τ_2 *= normalized intermediate eigenvalue,* τ_3 *= normalized minimum eigenvalue,* P_1 *= lineation,* P_3 *= foliation,* P_j *= corrected degree of anisotropy, T = shape parameter,* k_1 *= maximum eigenvector,* k_2 *= intermediate eigenvector,* k_3 *= minimum eigenvector, DEC = declination, INC = inclination, F = Hext F statistic.*

ID	Specimen	χ_b	χ_b (SE)	τ_1	τ_1 (SE)	τ_2	τ_2 (SE)	τ_3	τ_3 (SE)	P_1	P_3	P_j	T	k_1 (Dec)	k_1 (Inc)	k_2 (Dec)	k_2 (Inc)	k_3 (Dec)	k_3 (Inc)	F
1	BQ31-2	3.18E-06	3.10E-02	1.0829	0.02250	1.0594	0.02310	0.8577	0.02160	1.022	1.235	1.294	0.811	3.4	18.1	234.9	62.2	100.4	20.3	9.0
2	BQ31-3	1.95E-06	3.56E-02	1.1852	0.02410	1.0667	0.02580	0.7481	0.02550	1.111	1.426	1.619	0.542	271.6	58.0	174.9	4.2	82.3	31.6	22.4
3	BQ33-1	1.58E-06	3.96E-02	1.1685	0.02920	1.1045	0.03020	0.7271	0.02860	1.058	1.519	1.679	0.763	294.5	53.1	30.6	4.6	124.0	36.6	19.4
4	BQ33-2	1.10E-06	1.67E-02	1.3603	0.01210	1.1275	0.01130	0.5122	0.01230	1.207	2.201	2.820	0.616	321.8	68.5	67.2	6.0	159.5	20.5	344.4
5	BQ33-3	3.41E-06	1.86E-02	1.0935	0.01460	1.0367	0.01440	0.8698	0.01280	1.055	1.192	1.271	0.534	261.6	35.9	16.7	30.4	135.4	39.3	22.0
6	BQ34-1	4.54E-06	3.62E-03	1.0589	0.00290	1.0482	0.00290	0.8929	0.00270	1.010	1.174	1.211	0.880	223.9	43.3	13.8	42.5	118.7	15.6	338.2
7	BQ34-2	5.20E-06	4.83E-03	1.0247	0.00350	0.9970	0.00360	0.9783	0.00360	1.028	1.019	1.048	-0.180	223.9	7.5	131.1	20.6	332.9	67.9	12.1
8	BQ35-1	4.40E-06	2.22E-03	1.0812	0.00170	1.0554	0.00160	0.8634	0.00170	1.024	1.222	1.280	0.785	235.3	37.0	348.2	27.3	104.7	40.9	1377.0
9	BQ35-2	2.58E-06	4.64E-03	1.0571	0.00360	1.0168	0.00360	0.9262	0.00310	1.040	1.098	1.146	0.412	271.4	31.8	20.1	27.4	142.2	45.6	119.1
10	BQ35-3	3.17E-06	4.48E-03	1.1176	0.00330	1.0488	0.00310	0.8336	0.00320	1.066	1.258	1.361	0.566	296.8	54.5	44.6	12.3	142.6	32.7	570.5
11	BQ36-1	3.20E-06	1.06E-02	1.1242	0.00800	1.0539	0.00770	0.8219	0.00780	1.067	1.282	1.392	0.588	244.5	28.8	348.5	23.6	111.4	51.2	110.6
12	BQ36-2	2.89E-06	1.20E-02	1.0938	0.00860	1.0847	0.00900	0.8216	0.00860	1.008	1.320	1.385	0.942	310.0	28.6	56.9	28.0	183.0	47.9	89.8
13	BQ36-3	7.70E-07	2.37E-02	1.1374	0.01850	1.0110	0.01790	0.8516	0.01670	1.125	1.187	1.338	0.186	300.7	16.7	35.6	16.1	167.2	66.4	18.8
14	BQ37-1	3.28E-06	1.64E-02	1.1253	0.01190	1.0323	0.01170	0.8423	0.01200	1.090	1.226	1.346	0.404	300.7	52.5	58.6	19.8	160.9	30.4	40.0
15	BQ37-2	5.77E-07	1.51E-01	1.5941	0.12030	1.2940	0.11560	0.1119	0.11060	1.232	11.561	19.184	0.843	249.1	38.9	0.6	24.5	114.1	41.2	13.6
16	BQ38-1	9.65E-07	3.33E-02	1.4313	0.02520	1.1366	0.02270	0.4322	0.02550	1.259	2.630	3.564	0.615	328.4	24.0	234.2	9.4	124.3	64.0	106.6
17	BQ38-2	-3.87E-07	1.67E-01	-0.2056	0.12180	-0.6215	0.11550	-2.1729	0.11980	3.496	3.023	10.586	-0.062	260.8	0.0	350.8	61.4	170.8	28.6	20.3
	MEAN	2.49E-06	3.76E-07	1.0900	0.08889	0.9736	0.10107	0.5834	0.18003	1.229	2.093	3.148	0.544							

Table C-4. *Specimen AMS measurements for site A2 at the Bassani quarry. Summary of column headers:* χ_b *= bulk susceptibility, SE = standard error,* τ_1 *= normalized maximum eigenvalue,* τ_2 *= normalized intermediate eigenvalue,* τ_3 *= normalized minimum eigenvalue,* P_1 *= lineation,* P_3 *= foliation,* P_j *= corrected degree of anisotropy, T = shape parameter,* k_1 *= maximum eigenvector,* k_2 *= intermediate eigenvector,* k_3 *= minimum eigenvector, DEC = declination, INC = inclination, F = Hext F statistic.*

ID	Specimen	χ_b	χ_b (SE)	τ_1	τ_1 (SE)	τ_2	τ_2 (SE)	τ_3	τ_3 (SE)	P_1	P_3	P_j	T	k_1 (Dec)	k_1 (Inc)	k_2 (Dec)	k_2 (Inc)	k_3 (Dec)	k_3 (Inc)	F
1	BQ39-1	-2.77E-06	6.40E-03	-0.9129	0.00460	-1.0169	0.00480	-1.0702	0.00460	1.052	1.114	1.176	0.357	232.7	22.0	95.5	61.1	330.1	17.7	85.0
2	BQ39-2	1.73E-05	4.01E-03	1.0886	0.00270	1.0062	0.00270	0.9052	0.00270	1.082	1.112	1.203	0.147	52.2	2.7	322.1	3.0	184.1	86.0	314.3
3	BQ39-3	1.80E-05	5.17E-03	1.0225	0.00390	0.9995	0.00390	0.9780	0.00360	1.023	1.022	1.045	-0.023	218.1	24.3	68.8	62.3	313.8	12.5	10.0
4	BQ39-4	1.58E-05	1.33E-03	1.0283	0.00090	1.0069	0.00100	0.9648	0.00100	1.021	1.044	1.067	0.342	229.1	6.3	126.4	63.4	322.1	25.8	325.1
5	BQ40-1	-3.76E-06	8.86E-03	-0.9257	0.00710	-0.9405	0.00680	-1.1338	0.00670	1.206	1.016	1.253	-0.843	96.5	46.7	229.6	32.7	336.9	24.9	82.7
6	BQ40-2	5.44E-06	7.71E-03	1.0818	0.00600	1.0406	0.00590	0.8776	0.00520	1.040	1.186	1.249	0.628	193.6	6.4	284.3	6.5	59.3	80.9	113.2
7	BQ41-1	-3.33E-06	6.74E-03	-0.9573	0.00510	-1.0117	0.00500	-1.0310	0.00520	1.019	1.057	1.080	0.489	216.5	26.0	118.2	16.6	359.1	58.5	15.6
8	BQ41-2	4.22E-06	3.08E-02	1.1124	0.02050	1.0090	0.02190	0.8787	0.02190	1.102	1.148	1.267	0.173	226.3	0.1	135.9	71.2	316.3	18.8	8.3
9	BQ41-3	5.43E-06	8.20E-03	1.0437	0.00610	1.0059	0.00600	0.9503	0.00560	1.038	1.058	1.099	0.213	202.9	7.3	293.9	7.6	69.4	79.5	18.5
10	BQ42-1	-3.63E-06	1.47E-02	-0.8986	0.01150	-0.9561	0.01160	-1.1453	0.01040	1.198	1.064	1.287	-0.488	209.9	48.8	45.8	40.1	309.1	7.9	42.3
11	BQ42-2	1.98E-05	2.07E-03	1.0278	0.00160	1.0241	0.00160	0.9481	0.00140	1.004	1.080	1.095	0.912	293.5	7.8	203.0	3.7	87.5	81.4	279.4
12	BQ42-3	7.34E-06	6.63E-03	1.0336	0.00490	0.9928	0.00530	0.9736	0.00510	1.041	1.020	1.063	-0.347	228.6	24.7	113.2	42.9	338.8	36.9	11.0
13	BQ43-1	-3.84E-06	1.09E-02	-0.8953	0.00780	-0.9160	0.00790	-1.1887	0.00760	1.298	1.023	1.370	-0.839	88.7	69.2	227.0	15.8	320.8	13.1	126.3
14	BQ43-2	2.47E-05	7.90E-04	1.0105	0.00060	1.0007	0.00060	0.9888	0.00060	1.010	1.012	1.022	0.097	224.2	5.6	132.1	20.0	328.9	69.1	103.8
15	BQ43-3	2.09E-05	1.85E-03	1.0230	0.00130	0.9964	0.00120	0.9807	0.00130	1.027	1.016	1.044	-0.248	247.0	10.2	337.8	4.3	90.1	78.9	77.0
	MEAN	8.11E-06	2.69E-06	0.3922	0.24772	0.3494	0.24910	0.2585	0.25962	1.077	1.065	1.155	0.038							

Table C-5. *Specimen AMS measurements for site A3 at the Bassani quarry. Summary of column headers:* $\boldsymbol{\chi_b}$ *= bulk susceptibility, SE = standard error,* $\boldsymbol{\tau_1}$ *= normalized maximum eigenvalue,* $\boldsymbol{\tau_2}$ *= normalized intermediate eigenvalue,* $\boldsymbol{\tau_3}$ *= normalized minimum eigenvalue,* $\boldsymbol{P_1}$ *= lineation,* $\boldsymbol{P_3}$ *= foliation,* $\boldsymbol{P_j}$ *= corrected degree of anisotropy, T = shape parameter,* $\boldsymbol{k_1}$ *= maximum eigenvector,* $\boldsymbol{k_2}$ *= intermediate eigenvector,* $\boldsymbol{k_3}$ *= minimum eigenvector, DEC = declination, INC = inclination, F = Hext F statistic.*

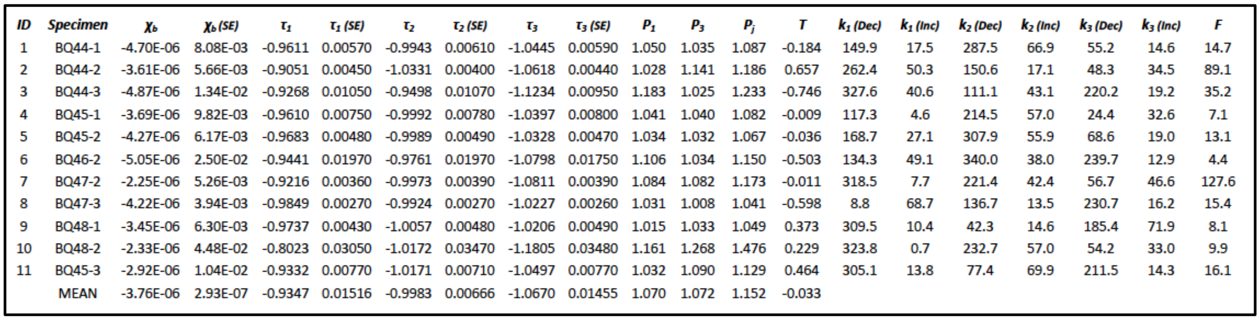

ID	Specimen	χ_b	χ_b (SE)	τ_1	τ_1 (SE)	τ_2	τ_2 (SE)	τ_3	τ_3 (SE)	P_1	P_3	P_j	T	k_1 (Dec)	k_1 (Inc)	k_2 (Dec)	k_2 (Inc)	k_3 (Dec)	k_3 (Inc)	F
1	BQ44-1	-4.70E-06	8.08E-03	-0.9611	0.00570	-0.9943	0.00610	-1.0445	0.00590	1.050	1.035	1.087	-0.184	149.9	17.5	287.5	66.9	55.2	14.6	14.7
2	BQ44-2	-3.61E-06	5.66E-03	-0.9051	0.00450	-1.0331	0.00400	-1.0618	0.00440	1.028	1.141	1.186	0.657	262.4	50.3	150.6	17.1	48.3	34.5	89.1
3	BQ44-3	-4.87E-06	1.34E-02	-0.9268	0.01050	-0.9498	0.01070	-1.1234	0.00950	1.183	1.025	1.233	-0.746	327.6	40.6	111.1	43.1	220.2	19.2	35.2
4	BQ45-1	-3.69E-06	9.82E-03	-0.9610	0.00750	-0.9992	0.00780	-1.0397	0.00800	1.041	1.040	1.082	-0.009	117.3	4.6	214.5	57.0	24.4	32.6	7.1
5	BQ45-2	-4.27E-06	6.17E-03	-0.9683	0.00480	-0.9989	0.00490	-1.0328	0.00470	1.034	1.032	1.067	-0.036	168.7	27.1	307.9	55.9	68.6	19.0	13.1
6	BQ46-2	-5.05E-06	2.50E-02	-0.9441	0.01970	-0.9761	0.01970	-1.0798	0.01750	1.106	1.034	1.150	-0.503	134.3	49.1	340.0	38.0	239.7	12.9	4.4
7	BQ47-2	-2.25E-06	5.26E-03	-0.9216	0.00360	-0.9973	0.00390	-1.0811	0.00390	1.084	1.082	1.173	-0.011	318.5	7.7	221.4	42.4	56.7	46.6	127.6
8	BQ47-3	-4.22E-06	3.94E-03	-0.9849	0.00270	-0.9924	0.00270	-1.0227	0.00260	1.031	1.008	1.041	-0.598	8.8	68.7	136.7	13.5	230.7	16.2	15.4
9	BQ48-1	-3.45E-06	6.30E-03	-0.9737	0.00430	-1.0057	0.00480	-1.0206	0.00490	1.015	1.033	1.049	0.373	309.5	10.4	42.3	14.6	185.4	71.9	8.1
10	BQ48-2	-2.33E-06	4.48E-02	-0.8023	0.03050	-1.0172	0.03470	-1.1805	0.03480	1.161	1.268	1.476	0.229	323.8	0.7	232.7	57.0	54.2	33.0	9.9
11	BQ45-3	-2.92E-06	1.04E-02	-0.9332	0.00770	-1.0171	0.00710	-1.0497	0.00770	1.032	1.090	1.129	0.464	305.1	13.8	77.4	69.9	211.5	14.3	16.1
	MEAN	-3.76E-06	2.93E-07	-0.9347	0.01516	-0.9983	0.00666	-1.0670	0.01455	1.070	1.072	1.152	-0.033							

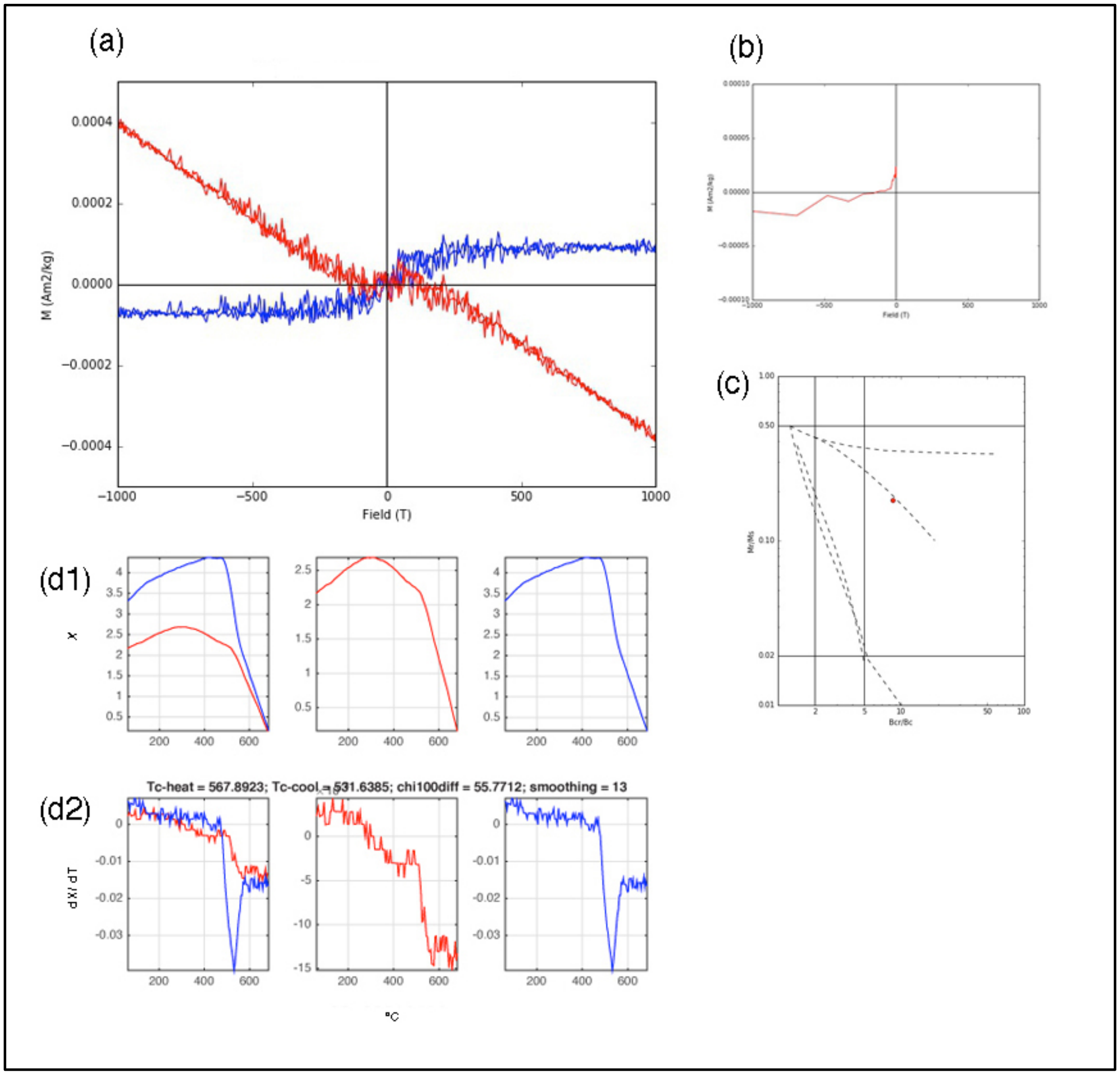

Fig C-7. *Magnetic analyses for site F2 at the Bassani quarry* ***(a)*** *hysteresis measurement, red = raw data containing both dia- and ferromagnetic contributions, blue = slope-corrected ferromagnetic loop* ***(b)*** *backfield measurement* ***(c)*** *Day plot* ***(d1)*** *susceptibility vs. temperature measurement, red = heating curve, blue = cooling curve* ***(d2)*** *calculated first derivatives for thermomagnetic curves.*

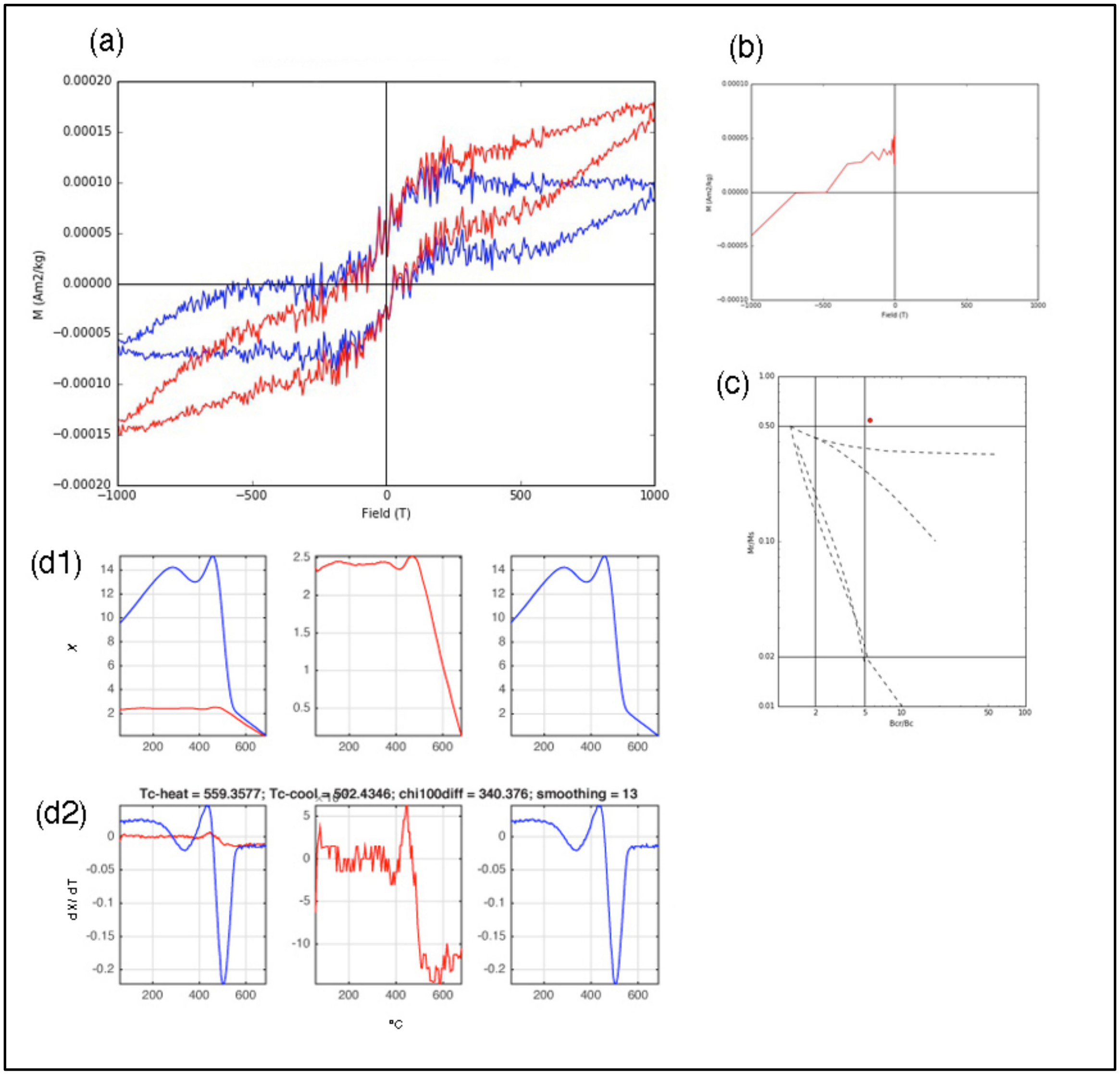

Fig C-8. *Magnetic analyses for sites G3 and B2 at the Bassani quarry* ***(a)*** *hysteresis measurement, red = raw data containing both para - and ferromagnetic contributions, blue = slope-corrected ferromagnetic loop* ***(b)*** *backfield measurement* ***(c)*** *Day plot* ***(d1)*** *susceptibility vs. temperature measurement, red = heating curve, blue = cooling curve* ***(d2)*** *calculated first derivatives for thermomagnetic curves.*

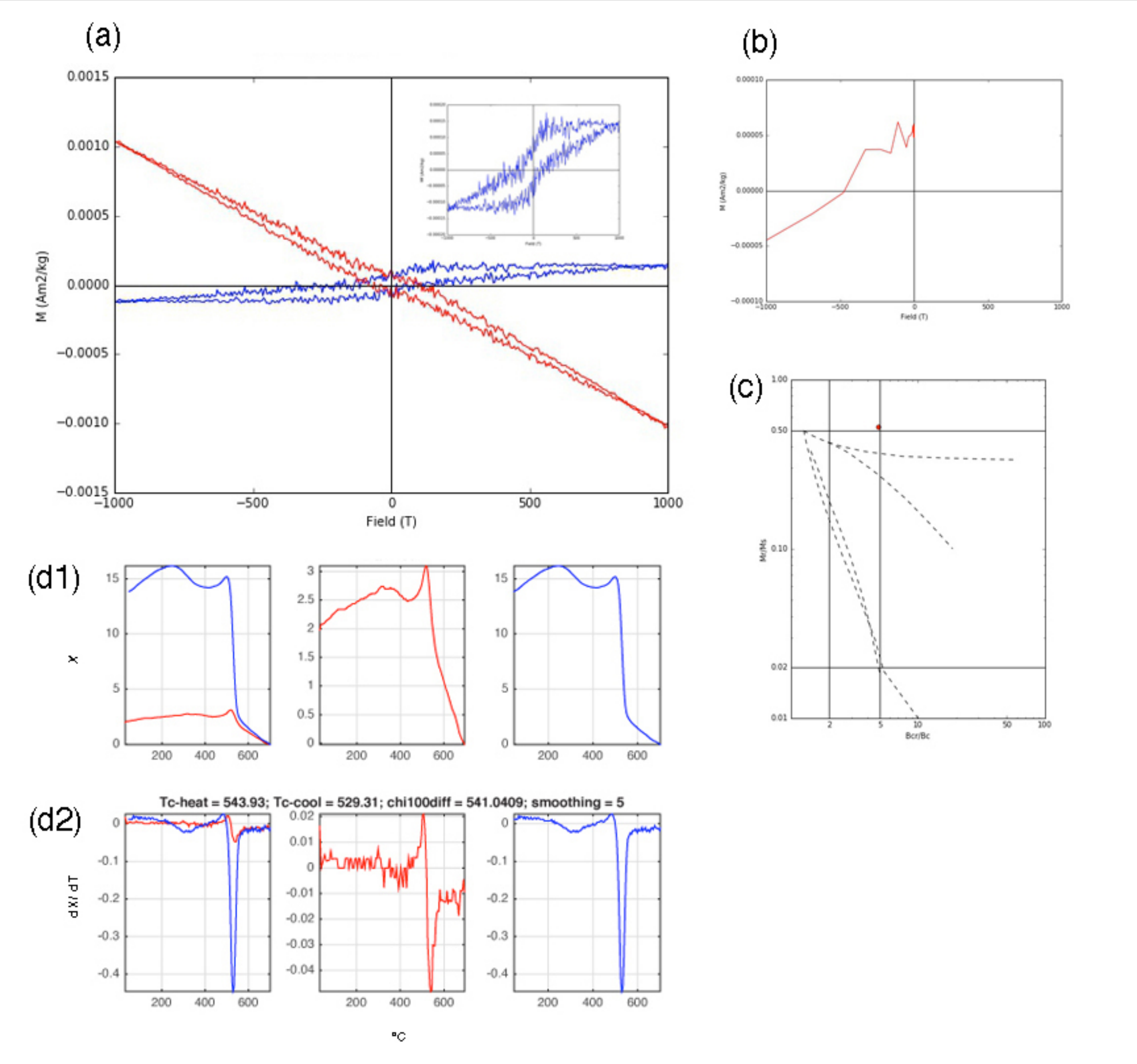

Fig C-9. *Magnetic analyses for sites A2 and A3 at the Bassani quarry* ***(a)*** *hysteresis measurement, red = raw data containing both dia- and ferromagnetic contributions, blue = slope-corrected ferromagnetic loop* ***(b)*** *backfield measurement* ***(c)*** *Day plot* ***(d1)*** *susceptibility vs. temperature measurement, red = heating curve, blue = cooling curve* ***(d2)*** *calculated first derivatives for thermomagnetic curves.*

APPENDIX D: ADDITIONAL LOCATION (MARIANA PIMENTEL)

Appendix D includes a brief field description, photo, AMS fabric analysis, AMS specimen measurements, and magnetic analyses for samples collected from a locality near Mariana Pimentel.

In the state of Rio Grande do Sul, an outcrop located northwest of Mariana Pimentel referred to as Morro do Popoleau was sampled (W51°38.587’, S30°18.463'). One sample set was collected from massive red mudstone (site M9) (Fig D-1) correlated to the Rio Bonito Formation, which stratigraphically lies above the Itararé Group.

Fig D-1. *Yellow boxes indicate locations of sample extracted from massive red mudstone (site M9) at Morro do Popoleau outcrop located northwest of Mariana Pimentel.*

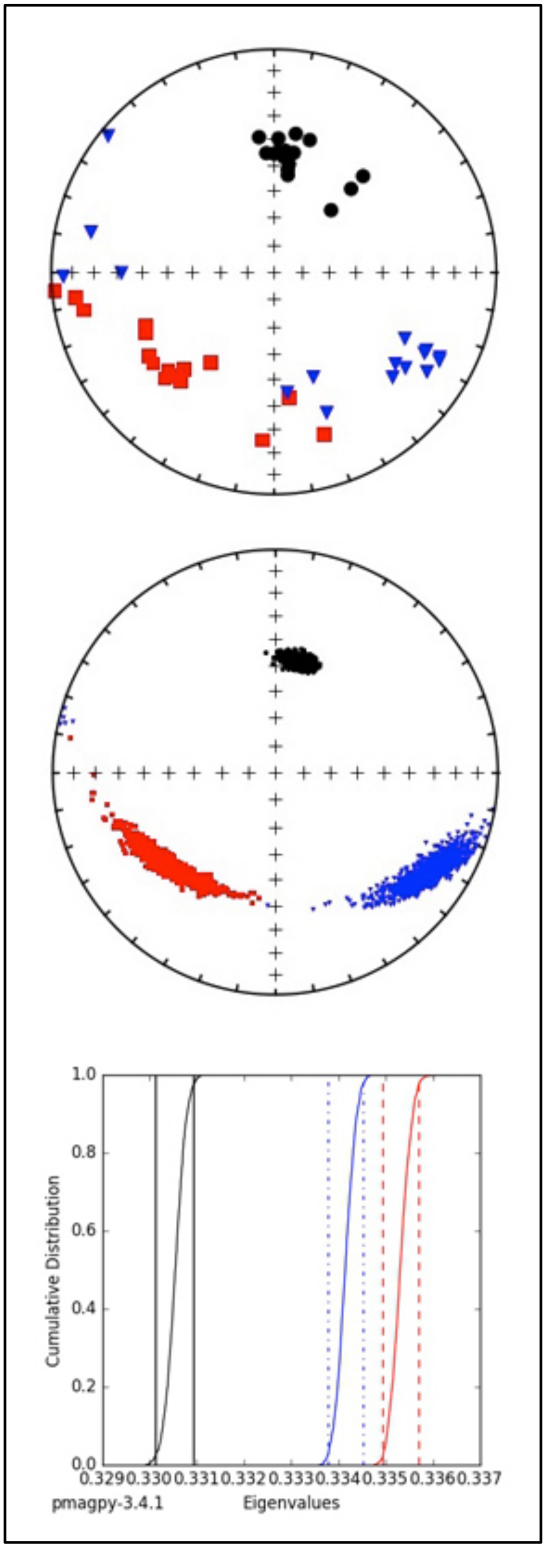

Fig D-2. *Measured eigenvectors for each specimen (top), bootstrapped eigenvectors (center), and bootstrapped eigenvalue cumulative distribution graph (bottom) for site M9 (Morro do Popoleau outcrop) near Mariana Pimentel. Maximum eigenvector indicated by red squares, intermediate by blue triangles, and minimum by black circles*

Table D-1. *Specimen AMS measurements for site M9 near Mariana Pimentel. Summary of column headers:* $\boldsymbol{\chi_b}$ *= bulk susceptibility, SE = standard error,* $\boldsymbol{\tau_1}$ *= normalized maximum eigenvalue,* $\boldsymbol{\tau_2}$ *= normalized intermediate eigenvalue,* $\boldsymbol{\tau_3}$ *= normalized minimum eigenvalue,* $\boldsymbol{P_1}$ *= lineation,* $\boldsymbol{P_3}$ *= foliation,* $\boldsymbol{P_j}$ *= corrected degree of anisotropy, T = shape parameter,* $\boldsymbol{k_1}$ *= maximum eigenvector,* $\boldsymbol{k_2}$ *= intermediate eigenvector,* $\boldsymbol{k_3}$ *= minimum eigenvector, DEC = declination, INC = inclination, F = Hext F statistic.*

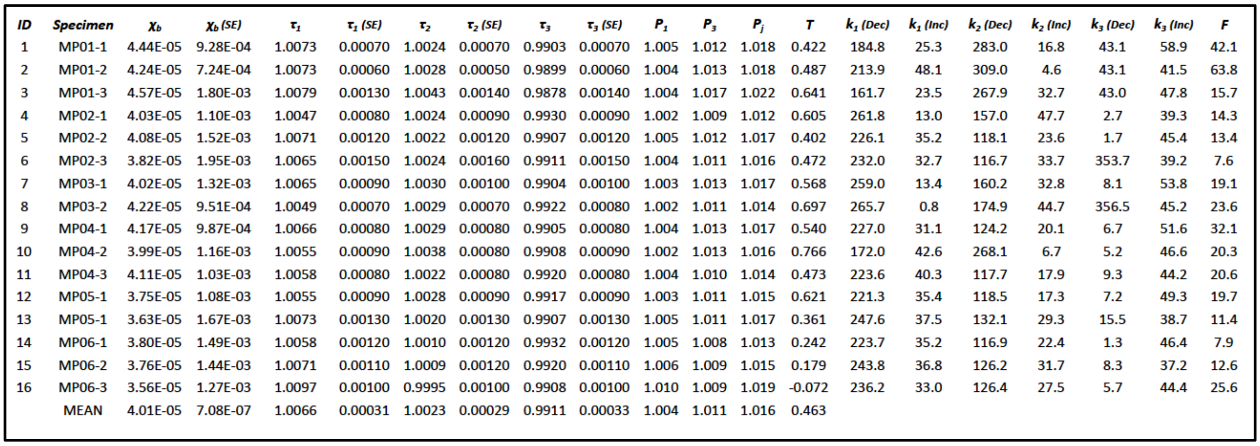

ID	Specimen	χ_b	χ_b (SE)	τ_1	τ_1 (SE)	τ_2	τ_2 (SE)	τ_3	τ_3 (SE)	P_1	P_3	P_j	T	k_1 (Dec)	k_1 (Inc)	k_2 (Dec)	k_2 (Inc)	k_3 (Dec)	k_3 (Inc)	F
1	MP01-1	4.44E-05	9.28E-04	1.0073	0.00070	1.0024	0.00070	0.9903	0.00070	1.005	1.012	1.018	0.422	184.8	25.3	283.0	16.8	43.1	58.9	42.1
2	MP01-2	4.24E-05	7.24E-04	1.0073	0.00060	1.0028	0.00050	0.9899	0.00060	1.004	1.013	1.018	0.487	213.9	48.1	309.0	4.6	43.1	41.5	63.8
3	MP01-3	4.57E-05	1.80E-03	1.0079	0.00130	1.0043	0.00140	0.9878	0.00140	1.004	1.017	1.022	0.641	161.7	23.5	267.9	32.7	43.0	47.8	15.7
4	MP02-1	4.03E-05	1.10E-03	1.0047	0.00080	1.0024	0.00090	0.9930	0.00090	1.002	1.009	1.012	0.605	261.8	13.0	157.0	47.7	2.7	39.3	14.3
5	MP02-2	4.08E-05	1.52E-03	1.0071	0.00120	1.0022	0.00120	0.9907	0.00120	1.005	1.012	1.017	0.402	226.1	35.2	118.1	23.6	1.7	45.4	13.4
6	MP02-3	3.82E-05	1.95E-03	1.0065	0.00150	1.0024	0.00160	0.9911	0.00150	1.004	1.011	1.016	0.472	232.0	32.7	116.7	33.7	353.7	39.2	7.6
7	MP03-1	4.02E-05	1.32E-03	1.0065	0.00090	1.0030	0.00100	0.9904	0.00100	1.003	1.013	1.017	0.568	259.0	13.4	160.2	32.8	8.1	53.8	19.1
8	MP03-2	4.22E-05	9.51E-04	1.0049	0.00070	1.0029	0.00070	0.9922	0.00080	1.002	1.011	1.014	0.697	265.7	0.8	174.9	44.7	356.5	45.2	23.6
9	MP04-1	4.17E-05	9.87E-04	1.0066	0.00080	1.0029	0.00080	0.9905	0.00080	1.004	1.013	1.017	0.540	227.0	31.1	124.2	20.1	6.7	51.6	32.1
10	MP04-2	3.99E-05	1.16E-03	1.0055	0.00090	1.0038	0.00080	0.9908	0.00090	1.002	1.013	1.016	0.766	172.0	42.6	268.1	6.7	5.2	46.6	20.3
11	MP04-3	4.11E-05	1.03E-03	1.0058	0.00080	1.0022	0.00080	0.9920	0.00080	1.004	1.010	1.014	0.473	223.6	40.3	117.7	17.9	9.3	44.2	20.6
12	MP05-1	3.75E-05	1.08E-03	1.0055	0.00090	1.0028	0.00090	0.9917	0.00090	1.003	1.011	1.015	0.621	221.3	35.4	118.5	17.3	7.2	49.3	19.7
13	MP05-1	3.63E-05	1.67E-03	1.0073	0.00130	1.0020	0.00130	0.9907	0.00130	1.005	1.011	1.017	0.361	247.6	37.5	132.1	29.3	15.5	38.7	11.4
14	MP06-1	3.80E-05	1.49E-03	1.0058	0.00120	1.0010	0.00120	0.9932	0.00120	1.005	1.008	1.013	0.242	223.7	35.2	116.9	22.4	1.3	46.4	7.9
15	MP06-2	3.76E-05	1.44E-03	1.0071	0.00110	1.0009	0.00120	0.9920	0.00110	1.006	1.009	1.015	0.179	243.8	36.8	126.2	31.7	8.3	37.2	12.6
16	MP06-3	3.56E-05	1.27E-03	1.0097	0.00100	0.9995	0.00100	0.9908	0.00100	1.010	1.009	1.019	-0.072	236.2	33.0	126.4	27.5	5.7	44.4	25.6
	MEAN	4.01E-05	7.08E-07	1.0066	0.00031	1.0023	0.00029	0.9911	0.00033	1.004	1.011	1.016	0.463							

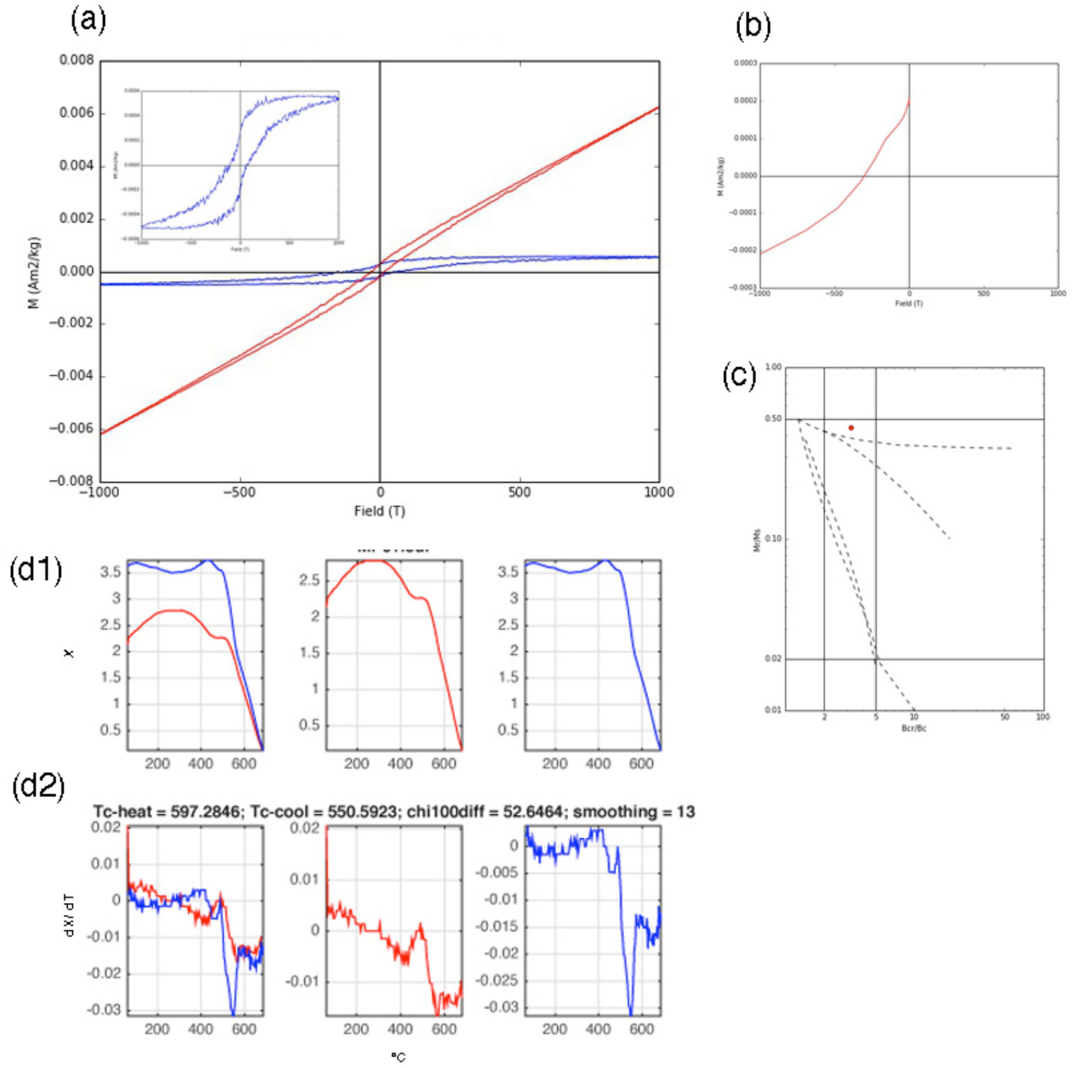

Fig D-3. *Magnetic analyses for site M9 near Mariana Pimentel* ***(a)*** *hysteresis measurement, red = raw data containing both para- and ferromagnetic contributions, blue = slope-corrected ferromagnetic loop* ***(b)*** *backfield measurement* ***(c)*** *Day plot* ***(d1)*** *susceptibility vs. temperature measurement, red = heating curve, blue = cooling curve* ***(d2)*** *calculated first derivatives for thermomagnetic curves.*